



AD A 097553

REPORT DOCUMENTATION PAGE		READ INSTRUCTIONS BEFORE COMPLETING FORM
1. REPORT NUMBER 15529.6-GS	2. GOVT ACCESSION NO. AD A097553	3. RECIPIENT'S CATALOG NUMBER
4. TITLE (and Subtitle) Low-Level Convergence and the Prediction of Convective Precipitation in South Florida		5. TYPE OF REPORT & PERIOD COVERED Technical
		6. PERFORMING ORG. REPORT NUMBER
7. AUTHOR(s) Andrew I. Watson                      Patrick T. Gannon Ronald L. Holle                         David O. Blanchard John B. Lunning		8. CONTRACT OR GRANT NUMBER(s) ARO MIPR 20-78
9. PERFORMING ORGANIZATION NAME AND ADDRESS University of Illinois Urbana, IL 61801		10. PROGRAM ELEMENT, PROJECT, TASK AREA & WORK UNIT NUMBERS
11. CONTROLLING OFFICE NAME AND ADDRESS U. S. Army Research Office Post Office Box 12211 Research Triangle Park, NC 27709		12. REPORT DATE Feb 81
14. MONITORING AGENCY NAME & ADDRESS (if different from Controlling Office)		13. NUMBER OF PAGES 228
		15. SECURITY CLASS. (of this report) Unclassified
16. DISTRIBUTION STATEMENT (of this Report) Approved for public release; distribution unlimited.		15a. DECLASSIFICATION/DOWNGRADING SCHEDULE
17. DISTRIBUTION STATEMENT (of the abstract entered in Block 20, if different from Report) NA		
18. SUPPLEMENTARY NOTES The view, opinions, and/or findings contained in this report are those of the author(s) and should not be construed as an official Department of the Army position, policy, or decision, unless so designated by other documentation.		
19. KEY WORDS (Continue on reverse side if necessary and identify by block number) convective precipitation                      storms south Florida                                    surface winds cloud development cloud duration		
20. ABSTRACT (Continue on reverse side if necessary and identify by block number) A reliable method is presented for the prediction of convective precipitation in south Florida. Total area divergence is statistically related to area rainfall as derived by radar in a mesoscale region on the order of 1400 km <sup>2</sup> . Various network grids and sizes are examined to find the best scale to measure total area divergence. The response of visible clouds to surface convergence is investigated with time-lapse photographs taken in the FACE mesonet. One case study of a convective storm complex as measured by Doppler radar and surface pressure data is presented. Finally, vertical adjustment factors are determined for surface winds		

**LEVEL**

DTIC  
ELECTE  
APR 8 1981  
S  
C

DTIC FILE COPY

175 550

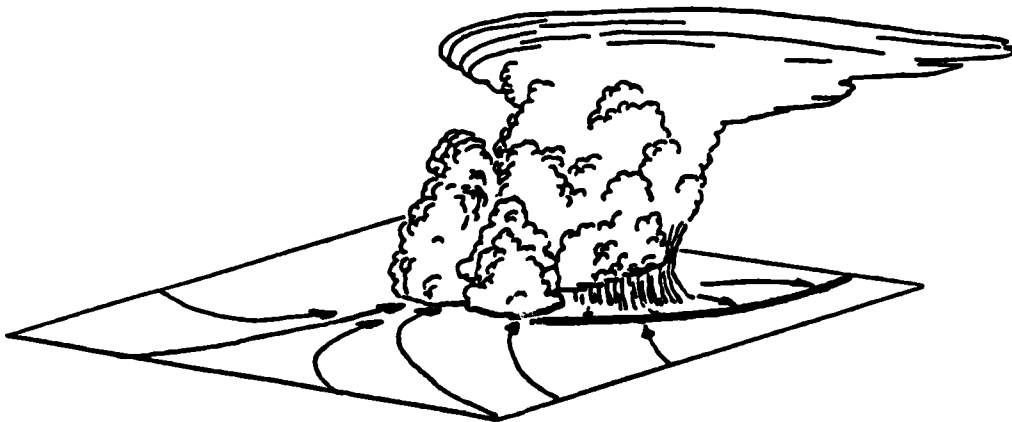
State Water Survey Division ✓  
METEOROLOGY SECTION  
AT THE  
UNIVERSITY OF ILLINOIS

Office of Weather Research  
and Modification  
NOAA Environmental Research Laboratories  
Boulder, Colorado

---

LOW-LEVEL CONVERGENCE AND THE PREDICTION  
OF CONVECTIVE PRECIPITATION IN SOUTH FLORIDA

*Andrew I. Watson*  
*Ronald L. Holle*  
*John B. Cuning*  
*Patrick T. Gannon*  
*David O. Blanchard*



Technical Report 4  
NSF Grant ATM 78-08865  
Low-Level Convergence and the  
Prediction of Convective Precipitation  
February 1981

81 4 7 019

The project "Low-level Convergence and the Prediction of Convective Precipitation" is a coordinated research effort by the State Water Survey Division of the Illinois Institute of Natural Resources, the Office of Weather Research and Modification in the National Oceanic and Atmospheric Administration, and the Department of Environmental Sciences of the University of Virginia. Support of this research has been provided to the State Water Survey by the Atmospheric Research Section, National Science Foundation, through grant ATM-78-08865. This award includes funds from the Army Research Office and the Air Force Office of Scientific Research of the Department of Defense.

12

Low-Level Convergence and the  
Prediction of Convective Precipitation  
in South Florida,

Andrew I. Watson  
Ronald L. Holle  
John B. Cuning  
Patrick T. Gannon  
David O. Blanchard

DTIC  
SELECTED  
APR 8 1981  
S D C

Office of Weather Research and Modification<sup>1</sup>  
Environmental Research Laboratories, NOAA  
Boulder, Colorado 80303

Technical Report<sup>4</sup>  
NSF Grant ATM 78-08865

Low Level Convergence and the  
Prediction of Convective Precipitation  
February 1981

<sup>1</sup> A major portion of this research was conducted while the authors were at the National Hurricane and Experimental Meteorology Laboratory, NOAA, Coral Gables, Florida.

**DISTRIBUTION STATEMENT A**  
Approved for public release;  
Distribution Unlimited

LOW-LEVEL CONVERGENCE AND THE PREDICTION OF CONVECTIVE PRECIPITATION IN SOUTH FLORIDA

1. INTRODUCTION	1
2. FACE 1975 MESONETWORK DATA-COLLECTION AND ANALYSIS METHODS	5
a. FACE 1975 Surface Network	5
b. Processing of Surface Data	5
c. Objective Analysis Scheme	8
d. Divergence Quantities	10
e. Radar-Derived Rainfall	12
f. Radar Rainfall Adjustment	14
g. Visible Cloud Analysis	15
3. INTERPRETATION OF DIVERGENCE-RAINFALL RELATIONSHIPS	18
a. Mean Conditions - August 1975	18
b. Background	22
c. Total Area Divergence Versus Area Rainfall	24
d. Weighted Convergence Versus Area Rainfall	27
e. Line Integral Divergence	29
f. Convective Outflow Versus Area Rainfall	30
g. Forecasting Test	32
h. Area Precipitation/Moisture Flux Ratios	34
i. Summary	39

Accession For	
NTIS GRA&I	<input checked="" type="checkbox"/>
DTIC TAB	<input type="checkbox"/>
Unannounced	<input type="checkbox"/>
Justification	
By _____	
Distribution/	
Availability Codes	
Dist	Special
A	

4. EFFECT OF INCREASED STATION SEPARATION AND VARIABLE NETWORK SIZE ON MESOSCALE WINDS AND DIVERGENCE ANALYSIS	40
a. Introduction	40
b. Variable Station Separation	41
(1) 16 August 1975	43
(2) 25 August 1975	106
(3) Discussion	129
c. Variable Network Size	136
d. Summary	142
5. ADDITIONAL RESEARCH BASED ON BOUNDARY LAYER FORCING MECHANISMS AND CUMULUS DEVELOPMENT	143
a. Visible Cloud Growth Related to Convergence	143
b. Time History of Storm Events Normalized to Duration	145
c. Merger of Radar Echoes and Visible Clouds	152
d. Interaction of Cloud-Scale Dynamics with Surface Convergence as Measured by Doppler Radar and Surface Pressure Data	169
e. Analysis of Boundary Layer Winds	180
6. CONCLUSIONS	186
ACKNOWLEDGMENTS	192
REFERENCES	193
APPENDIX	198

## ABSTRACT

A reliable method is presented for the prediction of convective precipitation in south Florida. Total area divergence is statistically related to area rainfall as derived by radar in a mesoscale region on the order of  $1400 \text{ km}^2$ . Data collected during the FACE 1975 field experiment are examined. It is found that for slow moving convective systems or when low-level winds are weak, there is three times the amount of rainfall per convergence event with only a 30% increase in convergence. When mid-level (850-500 mb) moisture is available (>52%), two and one-half times more precipitation is recorded for approximately the same amount of convergence than occurs during dry periods. Convective outflow and its reflection in total area divergence is examined and relationships are developed for determining the amount of precipitation for each convergence event. For the 38 rain events during August 1975, a correlation coefficient of .76 is found. Area precipitation efficiencies are calculated for 23 days of August 1975. On days when echo motion is weak or when mid-level moisture is available, significant improvement of efficiencies is observed.

Various network grids and sizes are examined to find the best scale to measure total area divergence. When three different distances between recording sites are used (6.4 km = "ground truth," 12.9 km and 19.3 km), all scales measure approximately the same total area divergence for the  $1400 \text{ km}^2$  region. It was also found that focusing on a convective event by decreasing the network area can improve the chance of total area divergence to describe the convective event and predict rainfall.

The response of visible clouds to surface convergence is investigated with time-lapse photographs taken in the FACE mesonet network. It is shown that the early

stages of cloud development are very good predictors of cloud duration, intensity and rainfall production. Visible clouds are also examined to determine, visually, the extent of cloud growth and interaction at the time of radar merger of two echoes. Several cases show, at radar merger, that visible clouds become joined into a solid mass up to 9 km or higher.

One case study of a convective storm complex as measured by Doppler radar and surface pressure data is presented. It is asserted that surface pressure may be the key that determines whether a storm evolves into a mesoscale system that produces or induces its own mesoscale convergence fields such that it is no longer dependent on the pre-existing convergence.

Finally, vertical adjustment factors are determined for surface winds under varying meteorological conditions and times of day. These adjustment factors are useful in accounting for the variation of boundary layer winds with height and permit a more accurate computation of fluxes from cloud base to the surface when only surface winds are available.

## 1. INTRODUCTION

This paper presents the NOAA results of the Florida work as performed under a grant awarded by the U.S. Army and the National Science Foundation (NSF) to NOAA, the Illinois State Water Survey (ISWS) and the University of Virginia (U.Va.). This is only the first portion of NOAA's contribution to this grant. To follow is a detailed analysis of work in a more complicated environment of the midwestern United States, namely Illinois. This report focuses entirely on the analysis of FACE data with a view towards verifying the relationship between surface convergence and convection in south Florida. Not only do the authors want to be able to predict the relationship between convergence and rainfall in a statistical sense, but it is hoped that this analysis can enhance, also, some physical understanding of the important processes of cumulus cloud development and interaction.

The idea that surface convergence and convective rainfall are related is not new. The classic Thunderstorm Project (Byers and Braham, 1949) reported a relationship between convergence and cumulus cloud development. They found, during the early cumulus stage, convergence at the surface up to 20 to 30 minutes before a radar echo appeared. Marked convergence was recorded at all levels around developing cumulus. When precipitation began and the downdraft spread out over the surface, strong divergence was found. The magnitude of maximum divergence was found to be directly related to the maximum rate of rainfall, although there may be a 5 minute lag of divergence behind the maximum rate of rainfall. It was also discovered that a new thunderstorm cell frequently developed on the downwind side of an existing cell, making the outflow instrumental in its development.

On a more subsynoptic scale, Copeland and Hexter (1957) recognized the relationship between convergence and rainfall in New England. In some cases the convergence pattern preceded the rainfall by approximately one half hour. They did not find a relationship between the intensity of convergence and concentration of precipitation. Anderson and Uccellini (1974) studied the association between surface convergence and hailstorms in northeast Colorado. They found lead times as large as 5 hours between maximum convergence and cell development. Little correlation was found between subsynoptic convergence and air mass thunderstorms. Achtemeier and Morgan (1975) used "cumulative lift," a parameter based on an integration with time of the surface divergence, as a predictor variable in a short-term forecast model for predicting the onset and location of thunderstorm areas in Illinois.

In Florida, Fernandez - Partagas (1973) studied three days during FACE 1971. He found a relationship that links convergence and divergence at three scales with peak rainfall. Maximum convergence occurred first at the peninsula scale followed by a maximum on the mesoscale (area-averaged convergence) and then at the cloud scale. After peak rainfall, maximum divergence occurred first at cloud scale and continued through the peninsula scales. He, too, recognized that convergence is a short-range forecasting tool for convective rainfall.

More recently, Holle et al. (1977) examined one case-study day during FACE 1975 in south Florida. They showed the importance of area-averaged divergence and its possibility as a forecast tool. Area-averaged divergence yielded a lead time of approximately one hour between maximum convergence and maximum area rainfall in their case.

Ulanski and Garstang (1978), using FACE 1971 and 1973 data, found readily

identifiable convergence zones that may precede the onset of precipitation by 60 to 90 minutes. They related the convergence gradient with maximum point rainfall when cells of convergence had contours  $\geq 600 \times 10^{-6} \text{ s}^{-1}$  and persisted for 15 min or more. Ulanski and Garstang, however, omitted days when rainfall totaled less than 0.2 cm and synoptic conditions were considered disturbed.

The main objective in this paper is to develop a relationship between convergence and rainfall on an area wide basis with a large set of data. It appears that total area divergence is sufficient to indicate surface convergence signatures prior to the onset of convective rainfall within a mesonetwork region. An ensemble approach is employed to document the total area divergence - area precipitation relationships. August 1975 FACE mesonetwork data are used to develop the initial statistical relationships; several days in July 1975 are used to test the capabilities of the system. All days but one in August 1975 are examined, and some no rain events are used in the ensemble. Precipitation volumes are derived by radar estimation and adjusted by a smaller rain gage network.

While the major emphasis of the NOAA research has been on rainfall response to surface convergence, important research has been undertaken also to examine the early development of cumulus convection with emphasis on cloud response to cloud seeding. With the aid of triple Doppler radar information and surface mesonetwork data collected during FACE 1975, some of the physical linkages between a developing cumulus and surface convergence may be clarified with recent research findings.

The association between visible clouds and surface convergence has also been investigated. In particular, the interval between the growth of visible

clouds and initial convergence has been examined. Very few, if any, previous studies have been made of this particular research topic.

Merger of cloud elements has been evaluated in the past with radar echoes only (Simpson et al., 1980; Westcott and Simpson, 1980), but the configuration and evolution of a merger detected by other parameters has not been addressed. In order to investigate the events accompanying radar echo mergers, visible clouds and rain-gage data for the same period have been examined. This has resulted in a better understanding of the dynamics of cloud systems during the radar echo merger period.

Finally, the representativeness of the surface winds to subcloud winds is explored under varying meteorological conditions and time of day. This adjustment can be useful and permits a more accurate computation of fluxes and divergence in the boundary layer when only surface winds are available.

## 2. FACE 1975 MESONETWORK DATA-COLLECTION AND ANALYSIS METHODS

### a. FACE 1975 Surface Network

The mesoscale program of FACE 1975 was a major field effort designed to help determine the interaction of both seeded and natural clouds with each other and with their environment. The mesonetwork instrumentation recorded surface quantities such as wind speed and direction, pressure, temperature, rainfall, and relative humidity.

The Doppler radar program obtained in-cloud kinematics from three Doppler radars within the mesonetwork. The upper-air program obtained measurements of pressure, temperature, relative humidity, and wind above the surface from a single location in the FACE mesonetwork. Upper-air data collected at the fixed rawinsonde site in Miami was also used in the analyses. Photography taken from the surface showed the evolution of cloud systems throughout the day in the field network.

The FACE 1975 project was conducted in the area shown in Fig. 1; a listing and description of all data collected in FACE 1975 is given in Staff, Cumulus Group (1976). The field network was divided into two coincident networks, the rain-gage and the mesoscale. The rain-gage network provided ground truth for daily radar rain-gage comparisons to calibrate the digitized WSR-57 radar data. The 66 rain-gages were laid out on a 3.2 km (2 st mi) spacing (Fig. 2) and covered 598 km<sup>2</sup>.

The mesoscale network measured surface wind, pressure, temperature, and relative humidity in an area generally coincident with the Doppler radar coverage. The network consisted of 46 surface wind stations on a 32 x 45 km area with one station every 6.4 km.

### b. Processing of Surface Data

One of the main aspects of NOAA's contribution to this grant has been the reduction and analysis of the 60-day FACE 1975 data set. Without the massive

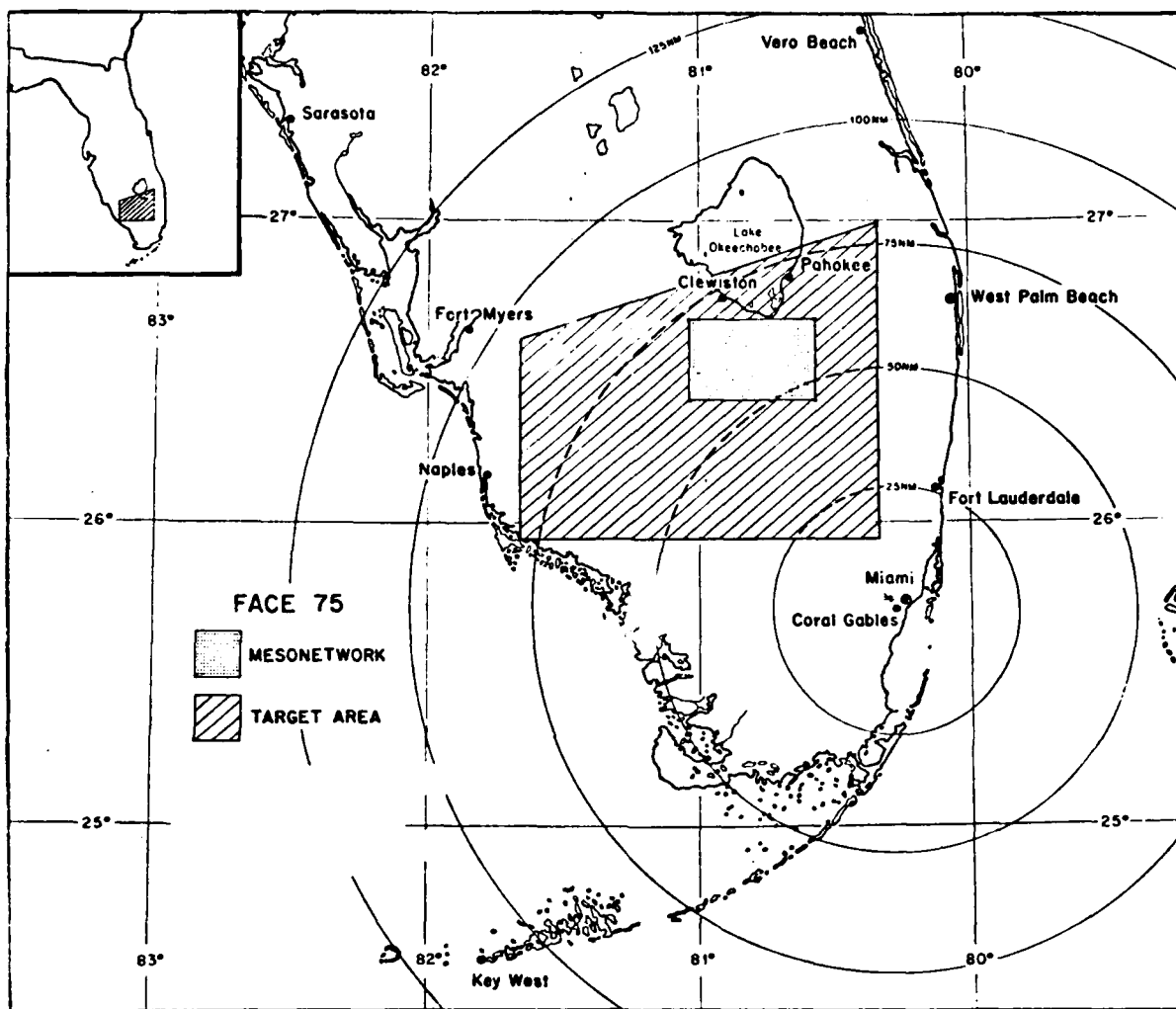


Figure 1. FACE 1975 operational regions. Hatched area is the FACE cloud seeding region, while the shaded area contains both the rain gage cluster and wind network.

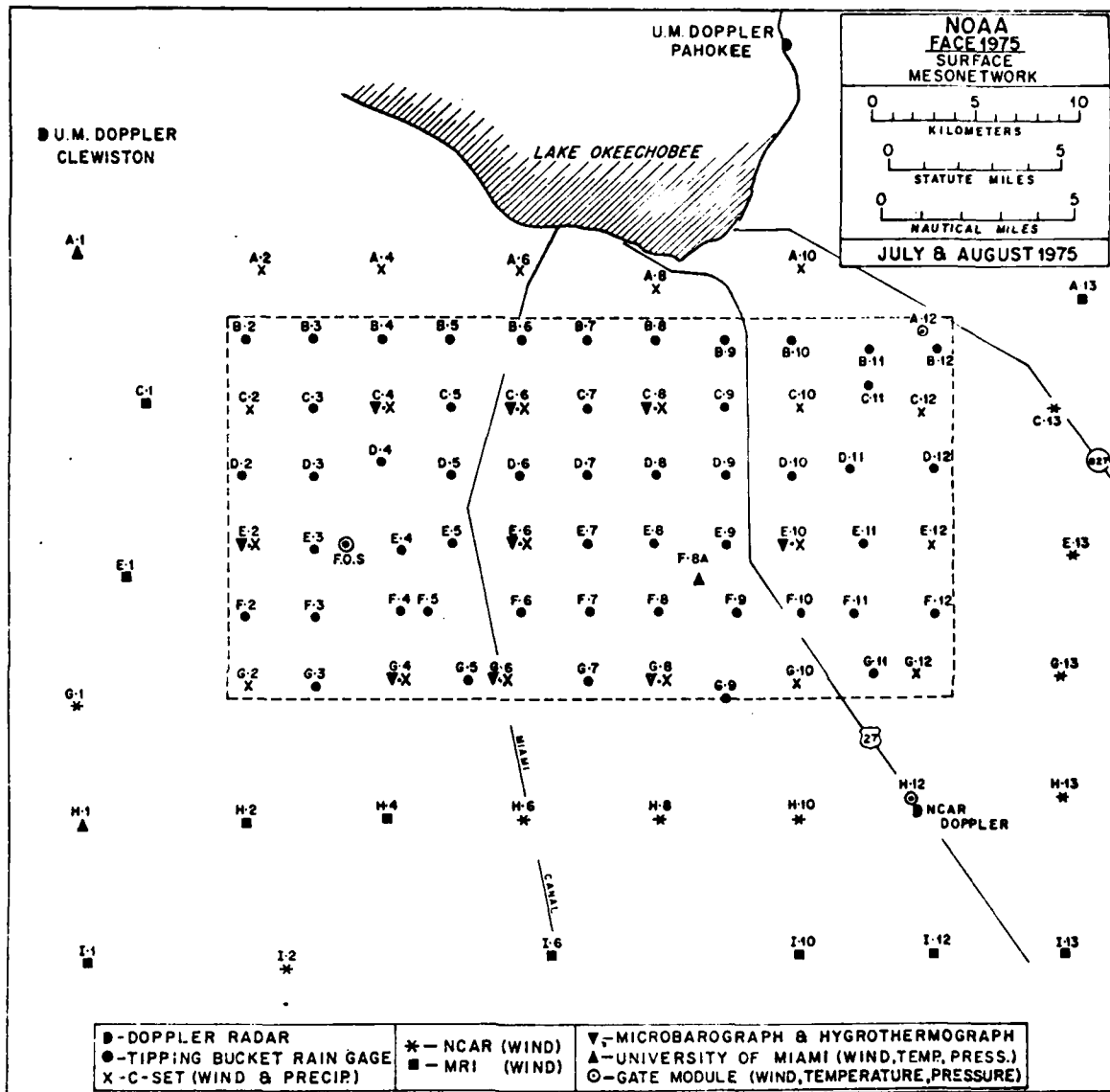


Figure 2. FACE 1975 mesonet network. The dashed line encloses the rain gage cluster. Locations of the Doppler radar sites and Field Observing Site (FOS) are also shown.

data reduction effort that was shared with the University of Virginia, the convergence-rainfall relationships could not have been investigated. NOAA assumed the processing of wind data recorded during August 1975, and this task was completed in August 1979.

Table 1 lists the eight types of instrumentation and the meteorological quantities they measure, their accuracy, and the data format. The wind information was recorded primarily on strip charts. The data were digitized in 5-minute time intervals from the raw analog wind records. Because of the persistent summertime nature of south Florida afternoon convection, only data from 0800 to 2000 EDT were digitized.

Despite frequent problems with several stations, 75% of all possible wind data were recorded. It has been estimated that this data processing effort has taken slightly more than 1 man year to complete the extraction of mesoscale wind data for 30 days. Pressure, temperature, and relative humidity information have been processed only for a few case study days. Doubtful accuracy of strip charts and ground truths have made these types of data of little use for large-scale bulk processing.

#### c. Objective Analysis Scheme

Through the use of an objective analysis scheme, the mesonetwork wind data are transformed into a uniform grid of divergence values. The objective analysis scheme is basically a Cressman (1959) technique. However, before this scheme is applied, the raw 5-min station data are subjected to a 15-min smoother. This temporal filtering is necessary to remove any high-frequency oscillations occurring at the individual stations, and it is helpful to smooth over any slight errors in station timing committed in data reduction or in field data collection.

Table 1. Instrumentation systems in the mesonet network

Instrument type	No. in field	Lender	Parameter Measured	Relative Accuracy	Recording Technique	Avg. duration of record (days)
C-set	21	U. of Va.	Wind speed Wind direction Rainfall	± 10% ± 11 deg ± 1%	Event recorder strip chart. 1 sample min <sup>-1</sup>	4 at 12 in/hr
Climet	9	NCAR	Wind speed Wind direction	± 10% ± 5 deg	Analog strip chart for each parameter	14
MRI	10	NCAR	Wind speed Wind direction Temperature	± 10% ± 5 deg unknown	Analog strip chart with all parameters on one chart	14
GATE module	3	GATE office	Wind speed Wind direction Pressure Temperature (mast) Temperature (soil) Radiation (1 site) All sky photography (2)	± 3% ± 2 deg ± 20 μbars ± 0.5° C ± 0.5° C	Digital incremental magnetic tape	7 with 1 sample min <sup>-1</sup>
Univ. of Miami	3	U. of Miami	Wind speed Wind direction Pressure Temperature (mast)	± 3% ± 2 deg ± 20 μbars ± 0.5° C	Digital incremental magnetic tape	7 with 1 sample min <sup>-1</sup>
Weather Measure rain gage (tipping bucket)	50		Rainfall	± 1%	24-hour drum-type recorder	2
Microbarograph	9	NCAR	Pressure	± 200 μbars	24-hour drum-type recorder	2
Hygrothermograph	9	NCAR	Humidity Temperature	± 5% ± 2° C	24-hour drum-type recorder	2

A grid of equally spaced (6.4 km) grid points (6 x 8) are superimposed upon the original network. There are 46 possible reporting stations, but no more than 33 to 35 of these stations provide usable data on any particular day. At any time, only half of the 9 Climets, 10 MRI's, and 6 digital systems were operational whereas the 21 C-sets were very reliable. The u- and v-components for each grid point are created from an initial guess derived from a distance-weighted average from the two closest reporting stations. The next step is to compute a deviation field by bilinear interpolation. Once the deviation field is computed, the Cressman scheme is then applied to the initial field. A single scan is made through the field of data with each grid point being considered. The value of the first guess at a grid point is corrected according to the value of the data at the reporting stations within the radius of influence ( $r = 6 \text{ st mi}/9.7 \text{ km}$ ). Once the corrective scheme is applied at each grid point, a second deviation field is computed to give an estimate of the mean square deviation. Since most of the reporting stations are at, or very close to, the grid points, only a single pass is made through the field of data with the objective analysis scheme. The values of u- and v-components at each of the grid points are then used to compute the divergence quantities.

#### d. Divergence Quantities

The primary objective of the work done under this contract is to determine if the convergence-rainfall relationships hold true for an entire mesoscale region. It appears that an averaged divergence over a small region is sufficient to indicate surface convergence signatures prior to the onset of convective rainfall within the mesonetwork region.

Several types of total area divergence are believed to be important for this study:

1. Total area divergence
  - a. The mean of all divergence values in the 6 x 8 mesoscale grid array as derived from the objective analysis scheme.
  - b. Line integral divergence as found by integration of the wind field along the border of the mesonet network with objective analysis data as input.
  - c. Line integral divergence with raw boundary mesonet network data as input.
2. Weighted convergence - The summation of convergence values at grid points divided by the total number of grid points.
3. Weighted divergence - The summation of divergence values at grid points divided by the total number of grid points. The sum of weighted divergence and weighted convergence is total area divergence.

Daily calculations for August 1975 of all the above types of area divergence appear in the Appendix. Two of the methods of deriving total area divergence (1a and 1b) are plotted together in the Appendix. As predicted by Gauss' divergence theorem, these two methods should be exact. Differences arise because of the centered finite difference scheme used to calculate divergence in method 1a. Errors arise because 24 of the 48 grid points are boundary points.

In method 1c, total area divergence is expressed without the use of an objective analysis scheme. The raw 5-minute wind data are processed by a simple line integral program which calculates inflow through the borders of

the mesonet network. This method is examined to test the possibility that only a set of wind stations along the perimeter of a particular mesoscale region can be used to predict the onset and amount of convective precipitation.

e. Radar-Derived Rainfall

The major consideration in choosing radar over rain gages was the fact that the areal coverage of the rain-gage network (598 km<sup>2</sup>) was considerably less than the areal coverage of the wind network (1440 km<sup>2</sup>). The reduction in wind network area necessary to match that of the rain gages was deemed undesirable. Radar data were obtained from the WSR-57 employed by the National Hurricane Center. The returned radar power from a scan every 5 minutes was digitized and written onto magnetic tape as described by Wiggert and Andrews (1974). The digitizer was operational from 0900 to 2100 EDT daily throughout the FACE 1975 experiment. FACE project personnel had no control over the operation of the radar. Therefore, there are occasionally times when instead of 5 minutes between digitized scans, there are 10 min, 20 min, and in some cases, hours between successive digitized scans. These data gaps had a number of causes, including the antenna rotation being stopped for operational observations, or the radar being inoperative because of malfunction or maintenance.

A considerable amount of time was expended in an effort to "clean up" the data as much as possible. These methods included examination of the noise levels and range bias of reflectivity, and checking for periods of anomalous propagation. Results of each of these studies appear below.

(1) Noise

Noise that was digitized and recorded can be attributed to a number of factors. Spurious returns from clear air were indeed a source of noise, but

the major contributions to noise came from the radar and digitizer electronics. A method suggested by Dr. Raul Lopez of NOAA was employed to determine the noise level. All odd hours from 0900 to 2100 EDT, inclusive, were examined to obtain a frequency distribution of the DVIP values. Noise was defined to be all DVIP values less than or equal to the mean plus two standard deviations. Once determined, the noise thresholds were placed in the rainfall analysis software to set to zero all those DVIP values assumed to be noise.

### (2) Range bias of reflectivity

Again, suggestions by Lopez were used to examine the variation of reflectivity with range. Weaker echoes at large distances were not detected, or fell into the noise level and were deleted; hence, only the strong echoes were detected and recorded. As a result, a plot of dBz versus range showed dBz increasing with increasing range. A correction was put into the software package to correct this bias. Basically, the minimum reflectivity detectable was determined at the far corner of the area of study. Any echoes whose reflectivity fell below this value in the remainder of the mesonet network were zeroed out.

### (3) Anomalous propagation

By far, one of the most serious problems was anomalous propagation (AP). At times when numerous heavy thunderstorms occurred over land, they resulted in cool moist air so located that large areas of strong "echoes" were observed and digitized. These echoes exhibited a tight gradient of intensity and sharply irregular boundaries not typical of weather echoes (Wiggert and Andrews, 1974). In order to avoid processing data with AP, reference was made to the radar log recorded during the FACE 1975 experiment in addition to viewing the National Hurricane Center 35 mm radar film. Portions of days

exhibiting moderate to strong AP in the mesonet network were not processed.

The radar data were recorded in polar coordinates. Even though the data were to be recorded in 2° intervals, in actual practice the azimuths ranged from 1.6° to 2.4° intervals. Because of this variability, data were not necessarily recorded at the same azimuth from one sweep to the next. This problem was remedied by converting the polar coordinates to Cartesian coordinates. The method used was the same scheme that has been used in the FACE program since 1974.

Using the Cartesian coordinate data, which are in the form of rain rates, a number of products were generated:

- (a) Rain volumes ( $m^3$ ) for the entire mesonet network for the time period between the previous and present scans.
- (b) Average rain depth for the same area and time period.
- (c) A cumulative rain depth for the mesonet network.

In addition, similar values were obtained for the buffer area. This area encloses the mesonet network by 15 nmi (27.8km) on each side so that showers moving into or out of the mesonet network can be examined. Daily plots of radar-derived mean rain depth for days in August 1975 with radar echoes in the FACE mesonet network are found in the Appendix.

#### f. Radar Rainfall Adjustment

The basic rainfall analysis procedure involves using both unadjusted and adjusted radar estimates of rainfall. A gage-to-radar rainfall ratio (G/R) is used for adjusting radar values. G is found by summing the gage rainfall in the FACE 1975 rain gage network and dividing the sum by the number of reporting gages. R is the sum of the radar rainfall values recorded in the

rain gage network divided by the area for the same time period as G. G/R is not applied on days when the  $G < 1$  mm. Adjusted radar rainfall is obtained by multiplying the unadjusted radar rainfall by G/R. A daily G/R is calculated using time periods when there is rainfall being recorded by the rain gages and radar data are available.

g. Visible Cloud Analysis

The relationship of visible cloud growth to surface convergence was examined by using August 1975 FACE mesonetwork data. The plots of surface divergence described previously were analyzed for the initiation times of specific cloud events in the divergence fields. These were related to the surface photographic data that were collected at the three Doppler radar sites and the upper air site (FOS). The visible cloud growth was also related to rain gage, radar, and other surface convergence measures during the evolution of a cloud system from initiation to complete dissipation. These relationships were qualitative in nature. However, they were sufficiently accurate in time to determine many important features of cloud system growth and evolution in the FACE mesonetwork.

Merger of radar echoes has been studied with FACE data. However, events shown by the accompanying fields of visible clouds and rain gages have not been considered. In order to analyze the visible cloud field accompanying radar echo merger, detailed photogrammetric techniques were developed for this specific situation. In particular, the goal was to map the cloud locations so that visible clouds could be plotted relative to the radar echo merger in the mesonetwork on August 19, 1975. Two cameras were pointing toward the subject clouds on this day; one camera was at the Clewiston Doppler radar site, and the other was at the Pahokee Doppler (Fig. 2).

Times were determined to the nearest minute for the two camera sites so

that mapping of the clouds could be accomplished by triangulation to the same cloud features. The horizontal azimuths from each camera to various features of ten clouds were made over a 20-min period when merger occurred on August 19. The azimuth of the highest point (HP) was found to each cloud from each camera at each time. This was actually the apparent highest point, that is, the highest part of the cloud visible from the camera site. The point may not have been the actual highest point, but it was apparently so from the camera's view. The azimuths to the left and right sides of each tower (LT, RT) were found from each camera when possible. The sides of the bubble-like tower rising during the growing stages of each cloud were defined by these azimuths. The azimuths to the left and right sides of the cloud body sides (LB, RB) also were found from each camera to the subject clouds. The sides of the cloud body include all significant portions of the total cloud, from top to base. When the cloud was mature, these azimuths included all of the area under which rain occurs, or where a radar return would be expected. When the side of the cloud tower or body was obscured, the azimuth to the right or left edge (RE, LE) was all that could be determined.

These cloud features were found at the desired clock times, and were used in a series of tracings and overlays that resulted in cloud maps. The first stage involved drawing the clouds, horizon, and surface landmarks on a large sheet of paper while the original 16mm film was shown by a stop-motion projector. Each drawing was made independently of any other time. Then comparisons were made of each cloud feature through time by plotting the change in azimuth for that cloud feature on graph paper. During the period of rapid cloud growth, it was sometimes difficult to be consistent in drawing the sides and tops of clouds.

Once the azimuths to cloud features were drawn consistently, their absolute values were found. In 1975, the angles to landmarks on the horizon (trees, bushes, posts, etc.) were surveyed by compass. Angles to cloud features were obtained by interpolation between azimuths to adjacent landmarks.

Directions to cloud tops, towers, and bodies were drawn on a mesonet network map from both cameras at each analysis time. Rectangles then enclosed each cloud top and body, with a cross denoting the top. The cloud shapes were then drawn to fill the rectangles in an orientation similar to the shape seen on the time-lapse photos, since at this stage use of the cloud pictures was preferable to total reliance on the drawings and tracings that had been produced. The result of this process was a map of visible cloud bodies and towers, and the location of the highest point, which was comparable in scale to the radar and rain gage maps. These comparisons were made for the August 19, 1975 merger case shown later in Section 5c.

### 3. INTERPRETATION OF DIVERGENCE-RAINFALL RELATIONSHIPS

#### a. Mean Conditions - August 1975

The divergence and rainfall data for August 1975 over the FACE mesonet network have been stratified into two regimes, wet and dry. Recall that this is a mesoscale region covering a  $1440 \text{ km}^2$  area just south of Lake Okeechobee. Days during August 1975 with area rainfall totaling 3 mm or more in the mesonet network were considered wet and those with less than 3 mm were labeled dry. Sixteen days were classified dry; only eleven days were wet. The remaining days were not used because of insufficient radar data to estimate precipitation amounts.

Fig. 3 illustrates the daily total area divergence versus time for 16 dry days. One standard deviation is plotted on either side of total area divergence. Notice that the divergence remains quite negative throughout the day with the maximum convergence occurring between 1400 and 1800 EDT. Burpee (1979) has shown for peninsula-scale convergence in south Florida that daily-averaged surface convergence is larger on sea-breeze days with little rainfall than on days with widespread rain. In this study, the scale is considerably smaller but still the dry days exhibit large amounts of convergence.

Fig. 4 shows the daily total area divergence versus time for the 11 days classed as wet. Area rainfall for the period is also depicted. The buildup of surface convergence reaches a maximum at approximately 1430 EDT followed by a maximum in area divergence several hours later associated with downdrafts and rainfall. The maximum in rainfall agrees quite well with the maximum of area divergence.

Fig. 5 presents the mean wet and dry soundings for August 1975. The wet sounding is somewhat more unstable in the lower layers (700-800 mb), becoming more stable between 500 and 400 mb. But the most important feature, which is

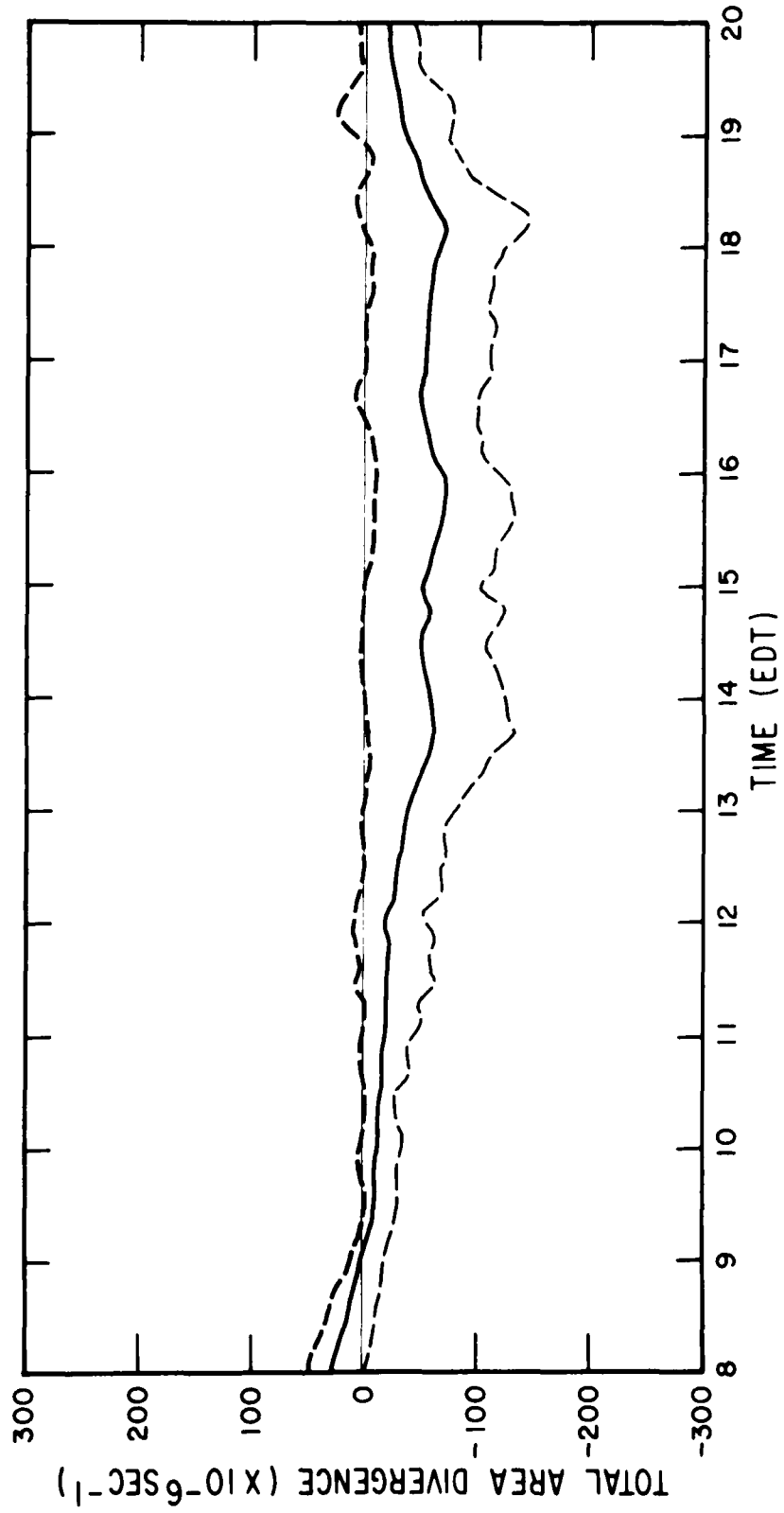


Figure 8. Total area divergence versus time for the 10 dry days ( $\leq 8$  mm) during August 1975 for the TREC mesonetwork. One standard deviation is also depicted.

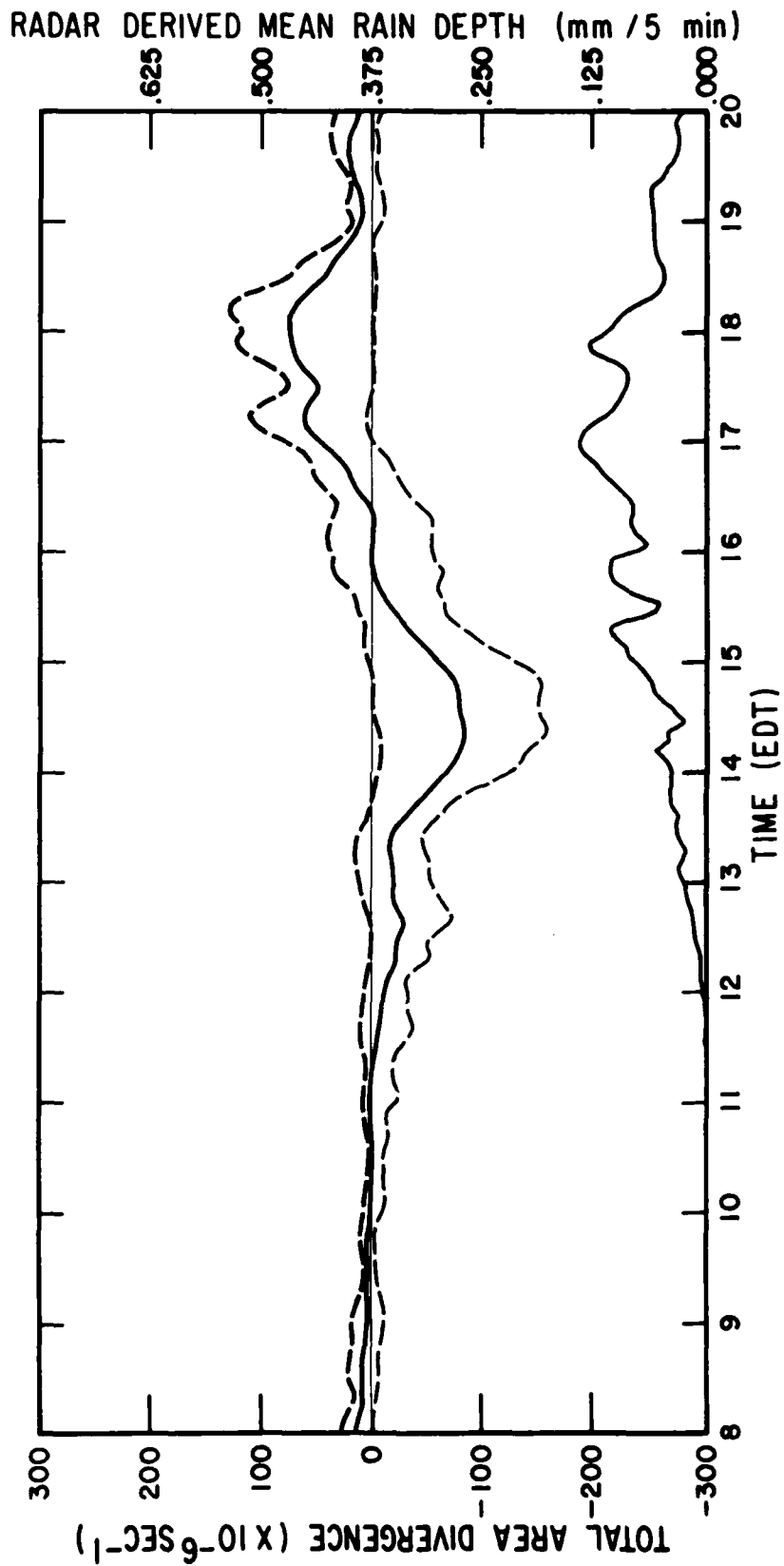


Figure 4. Total area divergence versus time for the 11 wet days (>3 mm) during August 1975 in the FACE mesonetwork. One standard deviation is shown. The mean radar-derived rain depth (mm/5 min) is presented for the same period.

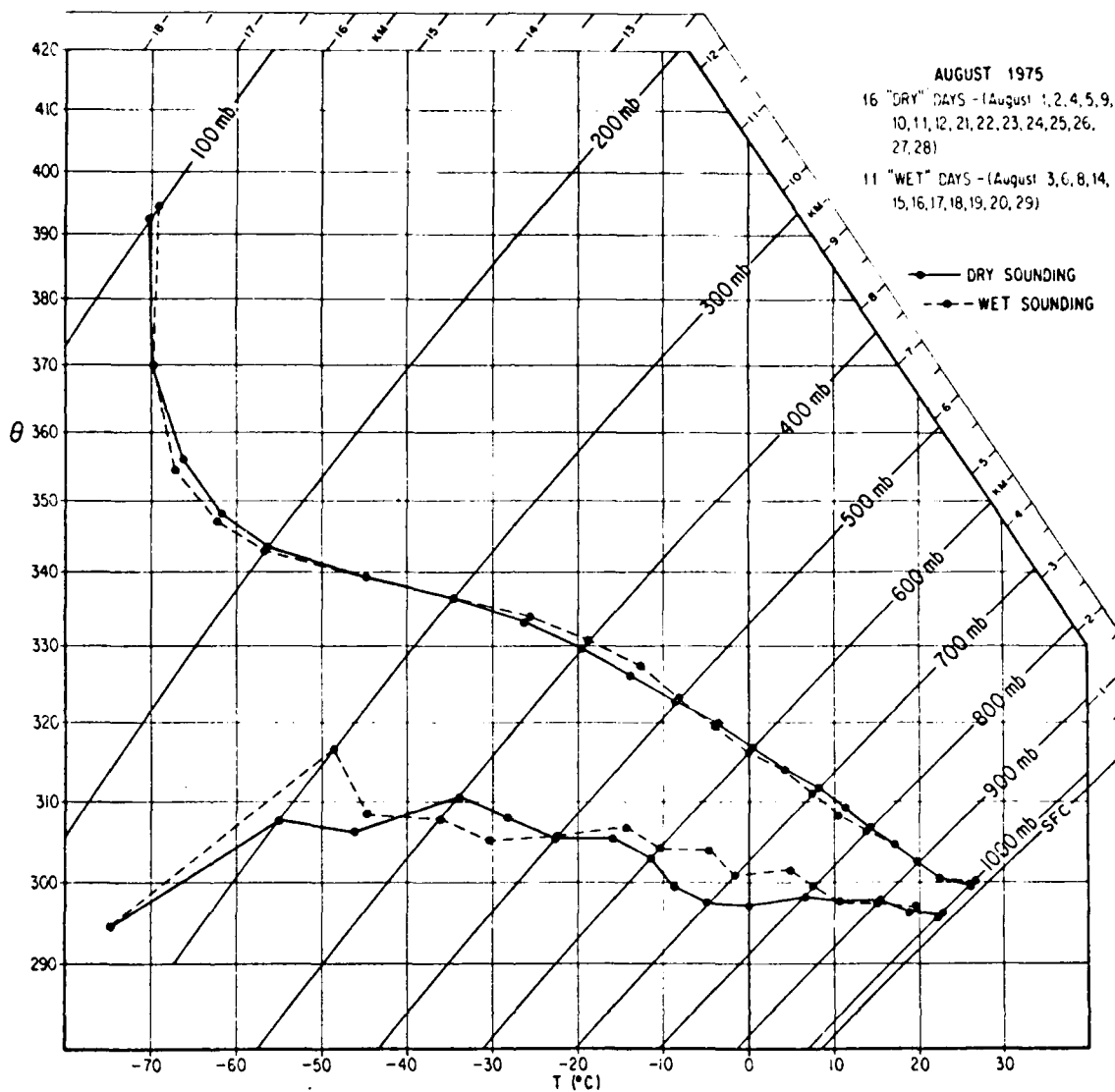


Figure 5. Averaged soundings for wet and dry days during August 1975 from 1200 UT Miami rawinsonde.

an underlying factor in the convergence-rainfall relationships, is the increase in mid-level moisture from 800 to 500 mb. As we show later, tapping this moisture improves the area precipitation efficiencies while also getting three times the amount of rainfall for approximately the same amount of area convergence.

The mesoscale surface area divergence reflects what is seen in the peninsula-scale divergence (Burpee, 1979); that is, larger amounts of convergence are seen on dry days and smaller amounts of convergence are recorded on wet days. The largest individual convergence values, however, occur on the wet days as strong inflow feeds the developing convective systems.

#### b. Background

The Thunderstorm Project found that deep convection was caused by convergence in the middle and lower troposphere (Byers and Braham, 1949). Ulanski and Garstang (1978) suggested that it is possible to nowcast the onset and intensity of convective precipitation through the use of surface convergence. Their relationships associated convective rainfall with individual cells of convergence. NOAA's research has concentrated on a somewhat larger scale. Statistical relationships between total area divergence and convective rainfall have been developed for a mesoscale region of about 1440 km<sup>2</sup>.

Several subsets of total area divergence are also investigated in this report. These include weighted convergence, weighted divergence, and the line integral divergence. Definitions for these quantities were presented in Section 2d. Weighted convergence and divergence require an inner grid where positive and negative divergence are calculated but the line integral of divergence needs only wind stations on the boundary. Weighted convergence filters out the gridpoints with positive divergence whereas the inverse is true for weighted divergence.

At the outset of this study, three factors that contribute to total area divergence were believed to be important in the forecasting of area rainfall:

- (1) The time covered by a convergence event from the beginning of the negative slope of total area divergence versus time to the changeover to a positive slope. For example, see daily plots of total area divergence versus time in the Appendix.
- (2) The minimum value of total area divergence that occurs during an event described in (1).
- (3) The maximum change in total area divergence for the time period in (1).

These three parameters were subjected to a multiple linear regression scheme to predict area rainfall. It was concluded that only the maximum change in total area divergence described in (3) was important when related to area rainfall.

The proper definition of an event must be made clear at this point. The definition of an event has been made in a fashion such that it describes an occurrence of significant convergence in the FACE mesonet network. Any time there is a sustained change in total area divergence less than  $-25 \times 10^{-6} \text{ s}^{-1}$  for more than 10 minutes is referred to as an event. To filter noise from the data, this definition was applied to a three-point running mean (15-minute average) of total area divergence. Some attempts were made to vary the definition of a convergence event, but it was found that smaller changes created many events that were considered to be noise, and larger changes missed rain events. This description of a convergence event is also used for weighted convergence.

The statistical relationships were segregated according to several parameters that may be important predictors of rainfall in south Florida. These

include mid-tropospheric relative humidity (850-500 mb), the mean vector wind from 1000 to 10,000 feet ( $\bar{V}_{1-10}$ ), and echo motion as described by radar. The K index was also examined for predictability. The K index is a representation of both instability between 850 and 500 mb and moisture at 850 and 700 mb. Mean soundings for August 1975 have shown that instability is not a factor; only moisture is important for heavier amounts of precipitation. Mid-level moisture, therefore, is included as the average mid-tropospheric relative humidity parameter.

All events are determined only by the total area divergence and weighted convergence time series. No distinction is made as to how cells (convective and convergent) are situated in the mesonet network. One day, 29 August 1975, was eliminated from the sample because it was impossible to relate convergence events to individual rainfall events (see Appendix for the time series of total area divergence and area rainfall). As shown in Section 4, this technique is highly area-dependent. The strength of total area divergence varies greatly with the size of the region. The convergence-rainfall statistics presented here are derived only for the FACE 1975 mesonet network, and are highly area dependent.

#### c. Total Area Divergence Versus Area Rainfall

In August 1975 there were 59 events of total area divergence of which 38 had rain. Table 2 summarizes the results of area divergence versus area rainfall for August 1975 in the FACE mesonet network. A convergence event is described by  $-25 \times 10^{-6} \text{ s}^{-1}$  or less except for one case. For the total ensemble, a correlation coefficient of  $-.6$  is found with a regression equation of

$$\text{RAIN} = -.044 (\text{dDIV} \times 10^6) - 1.422.$$

Only five rain events occurred without an associated convergence event for an

Table 2. Total area divergence versus area rainfall based upon FACE 1975 mesonetwork data.

$\Delta \text{DIV}$ ( $\times 10^{-6} \text{sec}^{-1}$ )	Other Criteria	No. of Cases	Rain Events	$\overline{\text{RAIN}}$ (mm)	$\overline{\Delta \text{DIV}}$ ( $\times 10^{-6} \text{sec}^{-1}$ )	r	Rain Misses	$\overline{\text{RAIN}}$ (mm) Misses
-25	-	59	38	1.72	-71	-.60	5	.18
-50	-	35	29	2.75	-94	-.52	14	.44
-25	$\overline{V}_{1-10} < 4\text{ms}^{-1}$	27	22	3.22	-89	-.60	1	.71
-25	$\overline{V}_{1-10} > 4\text{ms}^{-1}$	32	16	.45	-56	-.18	4	.05
-25	No Motion (echo)	21	14	2.98	-87	-.63	2	.37
-25	Motion (echo)	38	24	1.02	-62	-.46	3	.05
-25	RH > 52% (850-500 mb)	28	23	2.55	-75	-.76	3	.26
-25	RH < 52% (850-500 mb)	31	15	.96	-68	-.51	2	.06

average of 0.18 mm.

When the convergence event threshold is increased to  $-50 \times 10^{-6} \text{ s}^{-1}$  only the larger events are recorded. Twenty-nine out of 35 cases are rain events; however, 14 rain events are missed. A significant increase in the average maximum change in area divergence ( $-94 \times 10^{-6} \text{ s}^{-1}$ ) and average area rainfall (2.75 mm) is found when the convergence event threshold is larger.

The ensemble is now subdivided according to mean layer vector wind, echo motion, and mid-level moisture. Echo motion (only in vicinity of FACE mesonetwork) is determined by examining WSR-57 radar PPI film loops (Merceret et al., 1980) while the mean vector wind is found by averaging the 1200 and 0000 UT sounding data from the Miami rawinsonde between 1000 (.3 km) and 10,000 feet (3 km). Several days in August 1975 had large mean layer vector winds but no significant motion of the echoes in the region of the FACE mesonetwork. Mid-tropospheric moisture is found by determining the mean relative humidity between 850 and 500 mb. The value of 52% is used as the division between dry and moist conditions since it is the mean value for August 1975.

When the ensemble was divided according to a division of  $V_{1-10}$  above and below  $4 \text{ ms}^{-1}$  (Table 2), it was found that the weaker the wind the stronger the convergence event and the heavier the rainfall associated with each event. The correlation coefficient ( $r = .18$ ) for the strong wind regime is very low, showing the variability of this regime. Only 16 of the 32 convergence events had rain. The same effect is found when the ensemble is separated according to echo motion. Stationary echoes have stronger convergence and heavier rainfall than moving echoes.

The best correlation between area divergence and rainfall is found when the data are divided according to mid-level moisture. For approximately the

same amount of convergence per event,  $2\frac{1}{2}$  times more precipitation falls during high moisture conditions. For  $RH > 52\%$ , 23 out of 28 events had rainfall for a correlation of  $-.76$ , while only 15 out of 31 events had rainfall for  $RH < 52\%$ .

d. Weighted Convergence Versus Area Rainfall

Weighted convergence filters out any positive divergence occurring in the grid and amplifies the effect of convergence. There are only 54 cases meeting the criteria of  $25 \times 10^{-6} \text{ s}^{-1}$  maximum change in weighted convergence during August 1975 in the FACE mesonetwork. For the total ensemble, a correlation of  $.55$  is found with a regression equation of

$$\text{RAIN} = .0399 (\text{d W'CONV} \times 10^6) - 1.0063.$$

Table 3 summarizes weighted convergence and its relationship to convective rainfall. When the convergence event criterion is increased to  $50 \times 10^{-6} \text{ s}^{-1}$  only larger rain events are recorded. The number of rain events missed (14) increases while the correlation coefficient ( $.55$ ) suffers. Weighted convergence reflects what was seen in total area divergence relationships. Even when the ensemble is subdivided according to mean layer vector wind, echo motion, and mid-level moisture, the relationships are the same as for total area divergence. The weaker the wind or slower the echo motion, the stronger the convergence event and heavier the rainfall associated with each event. When mid-level moisture is high, two times more rainfall occurs for about the same amount of convergence.

Table 4 presents the time between convergence and rainfall milestones including beginning convergence and initial rain, beginning convergence and rain maximum, and end of convergence and rain maximum for both total area divergence

Table 3. Weighted convergence versus area rainfall based upon FACE 1975 mesonet network data.

$\Delta W'CONV$ ( $\times 10^{-6} \text{sec}^{-1}$ )	Other Criteria	No. of Cases	Rain Events	$\overline{RAIN}$ (mm)	$\overline{\Delta W'CONV}$ ( $\times 10^{-6} \text{sec}^{-1}$ )	r	Rain Misses	$\overline{RAIN}$ (mm) Misses
+25	-	54	38	1.86	72	.55	4	.09
50	-	31	28	3.10	99	.40	14	.33
25	$\bar{V}_{1-10} < 4\text{ms}^{-1}$	26	22	3.30	90	.53	1	.21
25	$\bar{V}_{1-10} > 4\text{ms}^{-1}$	28	16	0.52	55	.33	3	.05
25	No Motion (echo)	21	15	2.93	92	.58	2	.12
25	Motion (echo)	33	23	1.17	59	.39	2	.06
25	RH > 52% (850-500 mb)	28	23	2.52	70	.70	2	.12
25	RH < 52% (850-500 mb)	26	15	1.14	73	.46	2	.07

Table 4. Time in minutes between convergence and rain events based upon August 1977  
FACE mesonet network data. Standard deviations are in parentheses.

	Begin CONV and Initial Rain	TIME (min) End CONV Event and Rain Maximum	Begin CONV and Rain Maximum
Total Area Divergence	35 (35)	38 (35)	84 (44)
Weighted Convergence	39 (31)	32 (34)	89 (51)

and weighted convergence. Notice that the standard deviations are quite high because of the highly variable nature of the events involved.

e. Line Integral Divergence

The line integral method for calculating total area divergence is determined two ways. These methods are explained in Section 2d (methods 1b and 1c). The first and simplest method uses only the boundary wind sites, and divergence is found by integration around the border of the mesonet network. The second integration method uses the full grid of wind stations. An objective analysis is applied to the 5-minute data; then integration is performed on the gridpoint data along the boundaries. No convergence-rainfall statistics are developed for these methods of calculating total area divergence.

The second integration method uses the same objectively analyzed data as does the differential method (method 1a, Section 2d). According to Gauss's theorem, integration around the border is equal to the differential method. Slight discrepancies are noted that are due to the way divergence is calculated along the boundaries. The centered finite difference method is used at the interior gridpoints; it must be modified at the boundary. Of the 48 gridpoints (6 x 8 grid), 24 are on the borders.

The "boundary only" integral method shows much promise since only stations on the periphery may be used to determine total area divergence. A comparison is made with this integral method and total area divergence as found by the differential method using the full grid and an objective analysis scheme. A correlation coefficient of .85 is found for 29 days with 3654 cases. The basic trends are maintained on all days but because of different types of wind sensing equipment on the borders (see figure 2 and table 1) as found at

the inner stations, magnitudes are quite different. The average total area divergence for the integral method ("boundary only") is  $-43 \times 10^{-6} \text{ s}^{-1}$  compared with  $-26 \times 10^{-6} \text{ s}^{-1}$  for the differential method.

f. Convective Outflow Versus Area Rainfall

The Thunderstorm Project found that an area of heavy rain at the surface coincides with an area of strong divergence in the surface winds (Byers and Braham, 1949). When nine storms from Ohio and nine storms from Florida were analyzed, and divergence and rate of rainfall were related, correlation coefficients of .98 and .91, respectively, were found. It is understandable that there should be a better relationship between the outflow and rainfall than between inflow and rain since the precipitation causes the downdraft which in turn causes the horizontal outflow. The correlation between initial convergence and rain will be less since all the roots of the inflow may not be in the surface boundary layer. In this study, total area divergence and weighted divergence associated with the outflow are related to area rainfall. Total area divergence associated with the outdraft is defined as the maximum change in divergence, beginning at the minimum value, to the maximum value of area divergence. For weighted divergence, it is the maximum change that occurs during the positive slope. Major outflows may be seen in total area divergence and weighted divergence time series (Appendix) as large peaks. When the area rainfall versus time plots are compared with the divergence profiles, it is easily seen that the divergence peaks are associated with rainfall maxima.

Only events with precipitation were examined. There were 38 rainfall events in the August 1975 ensemble used in the convergence-rainfall relationships. Tables 5 and 6 present the total area divergence and weighted divergence

Table 5. Area divergence associated with convective outflow as related to area rainfall based upon FACE 1975 mesonet network data.

Criteria	No. of Cases	r	RAIN (mm)	$\overline{\Delta \text{DIV}}$ ( $\times 10^{-6} \text{ sec}^{-1}$ )
All	38	.76	2.64	131
$\overline{V}_{1-10} < 4\text{ms}^{-1}$	20	.76	4.31	172
$\overline{V}_{1-10} > 4\text{ms}^{-1}$	18	.33	0.80	85
No Motion (echo)	14	.77	4.40	199
Motion (echo)	24	.64	1.62	91
RH > 52% (850-500 mb)	24	.83	2.95	128
RH < 52% (850-500 mb)	14	.63	2.11	135

Table 6. Weighted divergence associated with convective outflow as related to area rainfall based upon FACE 1975 mesonet network data

Criteria	No. of cases	r	RAIN (mm)	$\overline{\Delta W \text{DIV}}$ ( $\times 10^{-6} \text{ s}^{-1}$ )
All	38	.77	2.64	84
$\overline{V}_{1-10} < 4\text{m s}^{-1}$	19	.73	4.53	118
$\overline{V}_{1-10} > 4\text{m s}^{-1}$	19	.62	0.76	51
No motion (echo)	13	.70	4.74	133
Motion (echo)	25	.76	1.55	59
RH > 52% (850-500 mb)	25	.77	2.84	87
RH < 52% (850-500 mb)	13	.79	2.27	79

statistics associating rain and outflow. The improvement of correlation coefficients are considerable in all categories. The presence or absence of mid-level moisture plays little or no role in the strength of outflow divergence and associated rainfall. For approximately the same amount of weighted divergence and total area divergence, the average rain per event is about equal for high and low mid-level moisture. However, mean layer wind and echo motion criteria still play an important role but in the logical sense; that is, when the divergence is greatest, larger amounts of rain occur. When the average time between maximum outflow and rain maximum (MAX divergence - rain MAX) is determined, total area divergence averages 17 minutes, and weighted divergence averages 14 minutes after the rain maximum.

g. Forecasting Test

The regression equations for determining convective rainfall with the use of total area divergence and weighted convergence were found by using August 1975 FACE data. Seven days in July were selected for the forecasting test. Selections were based on light, medium, and heavy rain occurrences in the FACE mesonetwork. Several other July days were included since they were being processed for cloud seeding operations. In the seven July days, five had echo motion, three had mean layer winds above  $4 \text{ ms}^{-1}$ , and three had mid-level relative humidity greater than 52%. There were 21 total area divergence events and 18 weighted convergence events with two missed events.

It was found that the best correlation coefficients occurred when the ensemble was divided according to mid-level moisture conditions. Only those predictions are presented here. Fig. 6 shows the regression lines developed from August data for the prediction of convective rain. They are based upon both total area divergence and weighted convergence for high (> 52%) and low (< 52%) mid-level relative humidity (850-500 mb). Notice the steep slopes for

high moisture conditions in this relation that could result in very heavy rain events. The July convergence events are plotted on each figure showing the actual convergence and rainfall associated with each event. Two events that occurred on a dry day are almost an order of magnitude from the regression lines. These two events happened on 24 July 1975. When the Miami WSR-57 radar data were examined, it was discovered that the convective systems that occurred in the FACE mesonetwork were the only major convective systems in south Florida on this day. The large amount of rainfall on 24 July in the FACE mesonetwork was not representative of the rest of the south Florida peninsula.

Table 7 presents the average predicted rainfall for each event, average actual rain, and the percent difference between the two. Two events were not predicted by weighted convergence and were missed. The data are also separated according to mid-level relative humidity. The percent difference range is large, from 2 to 112%. When 24 July is included in the low moisture ensemble, both area divergence and weighted convergence show over 100% difference between forecast and actual rainfall. But when 24 July is removed from the set, the percent difference drops to approximately 30%. The best forecast tool appears to be weighted convergence when mid-level moisture conditions are high.

#### h. Area Precipitation/Moisture Flux Ratios

This section is devoted to quantifying the efficiency of convective systems that grew in the FACE mesonetwork during August 1975. The rainfall efficiency is considered an area rainfall efficiency. It is not the purpose here to define cloud boundaries and relate inflow to water-vapor flux through cloud base. The inflow is therefore equated to a water-vapor upward flux for the entire mesoscale region.

*Table 7. Percent difference between predicted and actual rainfall for each day in July 1975*

	Predicted	Actual	%Difference
Total area divergence	2.79	2.61	6
Total area divergence(RH > 52%)	3.17	1.84	42
Total area divergence(RH < 52%)	2.00	4.14	107
Weighted convergence	2.08	2.91	40
Weighted convergence(RH > 52%)	2.17	2.13	2
Weighted convergence(RH < 52%)	1.95	4.14	112
Total area divergence(RH < 52%) (without 24 July 75)	1.99	1.37	31
Weighted convergence(RH < 52%) (without 24 July 75)	1.94	1.37	29

The procedure for determining area precipitation efficiency is basically the following. The area moisture flux for any given 5-minute period is calculated by integrating the moisture flux into the FACE mesonetwork. The boundary layer depth is held constant at 900 m. Johnson (1977) has shown that the mixed layer over south Florida in 1975 was 100-120 mb deep. Because of poor temperature and moisture instrumentation in the field, a constant mixing ratio of  $18 \text{ g kg}^{-1}$  is used. It is believed that a better estimator of the boundary layer wind is the surface wind multiplied by a constant factor of 1.5 (Brown and Hansen, 1978). The moisture flux is then integrated in time for the period when there is area convergence. The beginning time for integration is approximately 1030-1100 EDT and is continued until a major outflow occurs and the total area divergence versus time curve crosses the 0.0 divergence value.

The area rainfall is a total depth as estimated from the WSR-57 National Weather Service radar in Miami for a particular day as adjusted by the rain collected by the FACE rain-gage network. The area precipitation efficiency is defined as area rainfall  $\div$  water-vapor flux through the top of the boundary layer of the mesonetwork.

Table 8 presents times of convergence, area convergence sums, adjusted radar rainfall, area precipitation efficiency, echo motion, and mid-level relative humidity for most of August 1975. Efficiencies show a wide range of values from 0.03% to 85%. Individual time plots of area divergence and rainfall for each day can be seen in the Appendix. Here again, it is clear that much more convergence occurs on dry days than on wet days.

Table 9 divides the days into several categories based on echo motion and mid-level moisture. On 23 days in August the radar was used to estimate

Table 8. Area precipitation efficiency for the FACE 1975 mesonet network.

Date August	TIMES (EDT)	$\Sigma$ Total Area DIV ( $\times 10^{-6} \text{ sec}^{-1}$ )	Adjusted Rain (mm)	Area Precipitation Efficiency (%)	Echo Motion	850-500 mb Mean RH
1	-	-	0.0	-	Yes	78
2	1415-1910	1713	1.5	12	No	60
3	1300-1630	3125	9.4	41	No	72
4	1300-1900	3803	0.01	.03	No	51
5	-	-	0.0	-	No	42
6	1100-1650	4734	1.8	5	No	32
7	No Radar	-	-	-	No	45
8	1325-1630	1307	8.1	85	Yes	85
9	1100-1900	3338	0.2	.9	Yes	35
10	-	-	0.0	-	Yes	37
11	1155-1935	5556	0.03	.07	No	30
12	1550-1845	2677	2.4	12	No	37
13	No Radar	-	-	-	No	60
14	1210-1515	2550	6.8	37	No	71
15	1155-1630	2830	10.5	51	Yes	70
16	1130-1240	842	5.2	84	No	45
17	1330-1455	2665	9.6	49	No	48
18	1155-1525	1542	3.6	32	No	46
19	1345-1555	4075	17.4	59	No	54
20	1415-1730	4174	13.8	45	Yes	68
21	1100-1730	5320	2.3	6	Yes	64
22	1200-1555	5490	0.8	2	Yes	50
23	1210-1900	7559	0.9	2	Yes	46
24	1030-1800	-	0.0	-	(Yes)*	33
25	1115-1800	8021	0.6	1	Yes	35
26	1030-1940	7724	1.3	2	Yes	57
27	1030-1800	7513	0.4	1	Yes	60
28	1030-1415	3299	0.2	1	Yes	58
29	1030-1455	2586	8.5	45	No	53
30	No Radar	-	-	-	-	-
31	No SFC Wind Data	-	-	-	-	-

\*Determined from upper air data.  
(no radar film)

Table 9. Area precipitation efficiencies categorized by echo motion and mid-level relative humidity.

Type	Number of Days in Sample	Area Precipitation Efficiency (%)
All	23	16
Motion	11	9
No Motion	12	25
RH > 52%	12	24
RH < 52%	11	7

rainfall. These days were subdivided by echo movement. On days when the radar echoes move, the efficiency drops to 9%; on days that show very little echo movement the efficiency is much higher (25%). It is believed that convergence occurring outside the network and rainfall occurring inside the network or vice-versa do not contribute to more or less rainfall. However, rainfall occurring on an echo-motion day is highly variable as compared with no-motion days. As shown previously, it is possible to get 2.5 times more precipitation on a high mid-level moisture day as opposed to low moisture for about the same amount of convergence change attributed to a single event. When mid-level moisture was available, the storms were also more efficient.

The procedure in determining area precipitation efficiencies is a radical departure from previous calculations of precipitation-moisture flux ratios. However, the results appear to be encouraging especially when subdivided into echo motion and available moisture categories. The importance of the mid-level moisture cannot be taken lightly. The lower relative humidities would favor greater evaporation of precipitation, and entrainment of dry air at the mid levels into the convective cells would lead to greater evaporation of water already condensed in the updraft. This study, also, verifies what Woodley et al. (1977)

found on seed and control days during the FACE I experiment, 1970-1975; that is, days with light winds tend to be wetter than days on which the winds are stronger.

i. Summary

In summary, when total area divergence is used to predict convective precipitation within a small convective region, promising results have been found. It was further documented that, when the ensemble was divided according to low-level mean layer wind speed and mid-level moisture, some improvement of correlation coefficients has occurred. It was also found that the weaker the wind speed, the stronger the convergence and heavier the rainfall. For approximately the same amount of convergence per event,  $2\frac{1}{2}$  times more precipitation fell during times of high mid-level relative humidities with the best correlation of .76. The same results were found when area precipitation efficiencies were examined. When mid-level moisture was available and echo motion was small, the convective systems within the mesonet network were more efficient. Somewhat satisfactory results were found when several July 1975 days were used to test the regression equations developed from August 1975 data.

#### 4. EFFECT OF INCREASED STATION SEPARATION AND VARIABLE NETWORK SIZE ON MESOSCALE WINDS AND DIVERGENCE ANALYSIS

##### a. Introduction

The objectives of this section are twofold. First, the goal is to determine if the 6.4-km grid spacing for the surface wind sites of the FACE 1975 mesoscale experiment can be degraded to 12.9 km and 19.3 km without losing important features that describe circulations beneath convective systems found over the south Florida peninsula during the summer. Secondly, since this study deals with area divergence and its relationship to area rainfall, the question arises as to the optimum size of a region that best describes the convective activity within the region. For area divergence to be of importance, the mesoscale region must be sufficiently small so that there can be a mass imbalance within that region. The convective activity must be fed from outside the region. If the region is too large, the convective system's dipoles (inflow and outflow) may cancel, and a scale much larger than a convective cluster would be measured. For example, if total area divergence were measured in an area the size of south Florida, only peninsula scale divergence would be recorded and individual convergence and divergence associated with a small or even a large convective cluster would be lost. Several network sizes which are subsets of the FACE 1975 mesonetwork are examined.

For both studies, five case days are investigated, each having their own individual characteristics. Table 10 reviews the weather conditions experienced on these case days. The days were selected mainly by amount of rainfall and variety of convective activity.

*Table 10. Case study days for examination of variable grid and station separation*

Date	Weather
12 August 1975	Moderate rain, strong gust front triggering secondary convection.
16 August 1975	Moderate rain, several examples of secondary development triggered by outflows.
19 August 1975	Heaviest rain of August 1975.
25 August 1975	Light rain, moderate surface winds.
26 August 1975	Light rain, moderate surface winds, small individualized convective cells.

b. Variable Station Separation

The rationale for this investigation is to determine, for future network designs, the largest surface station separation possible that will still give an accurate representation of the actual meso- $\beta$  fields. It may be possible to double or triple the distance between sites and still obtain credible results.

It has been shown by Ulanski and Garstang (1978) that grid spacings of about 6.5 km were adequate for describing circulations applicable to convective systems in south Florida. For the present study the FACE 1975 mesonet network on a 6.4 km (4 st mi) grid was used as the base analysis. The network was degraded from the 6.4 km grid by removing individual wind sites to obtain grid spacings of 12.9 km (8 st mi) and 19.3 km (12 st mi).

Table 11 lists the sites selected for the 12.9 and 19.3-km analyses. The locations of these sites can be found in Fig. 2. On any given case-study day, an average of only 33 wind sites is operational out of 46. For the degraded networks, all sites are considered operational. An average of 15 sites is used for the 12.9-km grid while an average of 9 stations is analyzed for the 19.3-km grid. The objective analysis used is the Cressman scheme described in Section

Table 11. Wind sites used in variable grid analysis

12.9-km station separation

<u>Date</u>	<u>Sites</u>
12 August 1975	A-6, A-13, C-1, C-4, C-8, C-12, E-13, G-2, G-8, G-10, H-1, H-8, I-2, I-10, I-13
16 August 1975	A-6, A-13, C-1, C-4, C-8, C-12, E-13, G-2, G-6, G-10, H-1, H-8, I-2, I-10, I-13
19 August 1975	A-6, A-13, C-1, C-4, C-8, C-12, E-13, G-2, G-6, G-10, H-1, H-13, I-2, I-10, I-13
25 August 1975	A-2, A-10, A-13, C-1, C-4, C-8, C-12, E-12, G-2, G-6, G-10, H-2, H-8, H-12, I-2, I-10
26 August 1975	A-6, A-13, C-1, C-4, C-12, E-13, G-2, G-6, G-10, H-1, H-8, I-2, I-10, I-13

19.3-km station separation

<u>Date</u>	<u>Sites</u>
12 August 1975	A-2, A-8, A-13, E-1, E-10, E-13, I-2, I-10, I-13
16 August 1975	A-2, A-8, A-13, E-1, E-10, E-13, I-2, I-10, I-13
19 August 1975	A-2, A-8, A-13, E-1, E-10, E-13, I-2, I-10, I-13
25 August 1975	A-2, A-8, A-13, E-1, E-10, E-12, I-2, I-10, I-13
26 August 1975	A-2, A-10, A-13, E-1, E-10, E-13, I-2, I-10, I-13

2c. So that the objective analysis was not a factor in the analysis, all input variables such as the radius of influence remain constant. A 6 x 8 grid mesh is used for all scales with a grid point separation of 6.4 km.

Two examples showing the sensitivity of the variable grid are presented. Both examples have unique circulations, but they are not unusual compared with other days in August 1975. One day is dominated by small-scale flow patterns and convective scale interactions while the other is influenced by a scale larger than the mesonetwork.

(1) 16 August 1975

August 16, 1975 is of very great interest because the cells remain reasonably small for some time before merging into a large complex. As the cells mature, their outflows appear to create new confluence zones which in turn, initiate new convection. This process cycled through four generations of convection before merging into a large system. This day is also presented because of the inability of total area divergence to predict area rainfall.

Figs. 7 and 8 present the streamline/isotach-radar and divergence patterns in 5-minute increments from 1300 to 1630 EDT for 16 August 1975. These analyses contain all the available FACE 1975 mesonetwork wind data located on a 6.4 km grid. Radar information is overlaid on the streamline/isotach analyses in 10 dBz increments beginning with 20 dBz. It is assumed here that the 6.4 km grid analyses are the "ground truth" for comparison with the larger grid scale presentations. The main interest for the variable station separation lies in the time period of 1430 to 1530 EDT. Other time periods are presented for the variable grid study in the latter part of this section. The chronology of events as shown for 16 August 1975 is as follows.

At 1400 EDT, outflow from a small precipitating cell is seen near the southwest corner of the mesonetwork (see Fig. 7). A convergent singular point is noted in the west central part of the region (see Fig. 8) with a confluent zone extending northeastward toward the northern border. Strongest divergence is found in the southwest corner while a V-shape convergence zone is shown in the northwest quarter of the network. Gradually the confluent zone becomes more east-west (1415 EDT) but is accompanied by only weak convergence. At 1430 EDT, the echo in the southwest corner intensifies as it moves over a more favorable

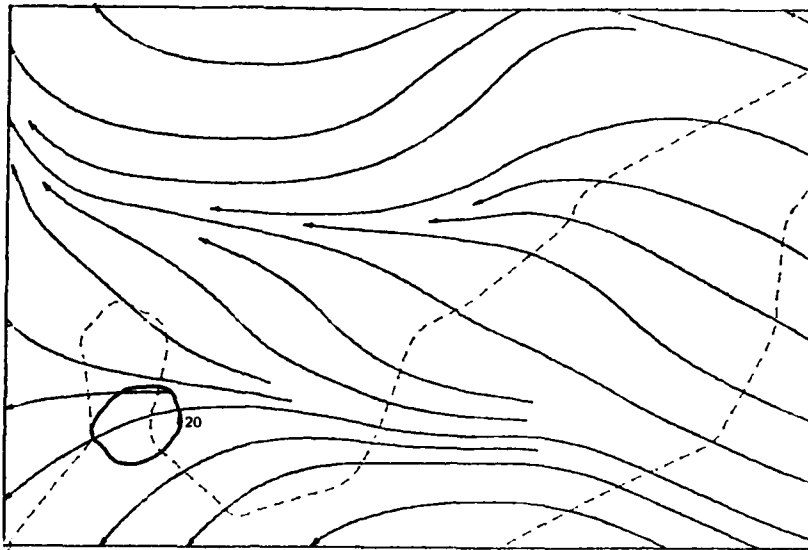
*Figure 7. Streamline/isotach and radar patterns on 16 August 1975 for each 5 minute period between 1300 and 1640 EDT on a 6.4 km station grid. Radar echoes are superimposed in dBz.*

F A C E 7 5 .

DATE... 0165

STREAMLINES

TIME... 1300



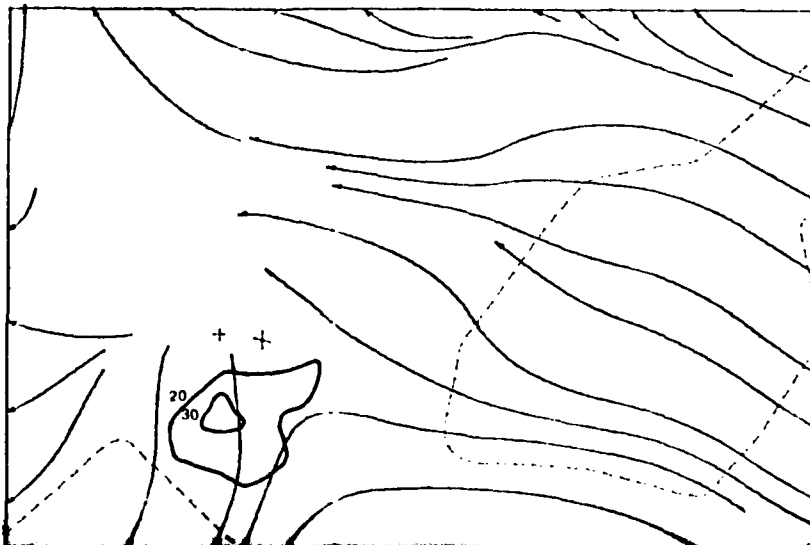
STREAMLINES

TIME... 1305



STREAMLINES

TIME... 1310

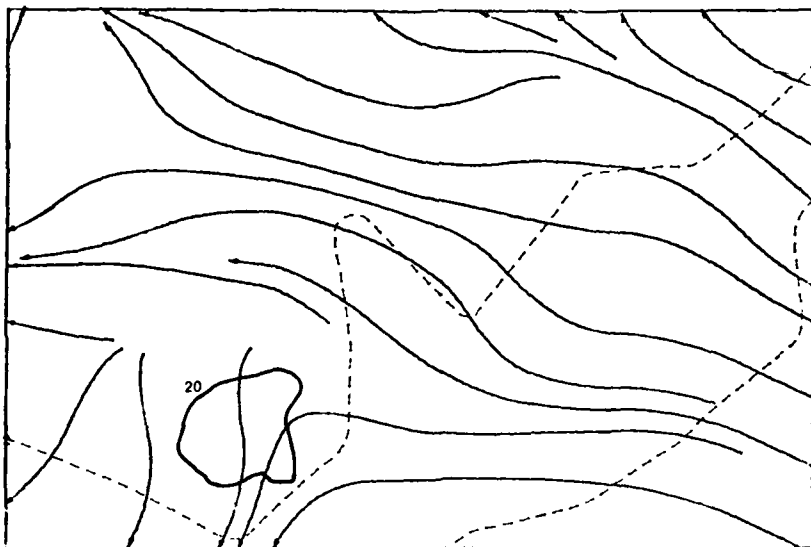


F A C E 7 5.

DATE... 0105

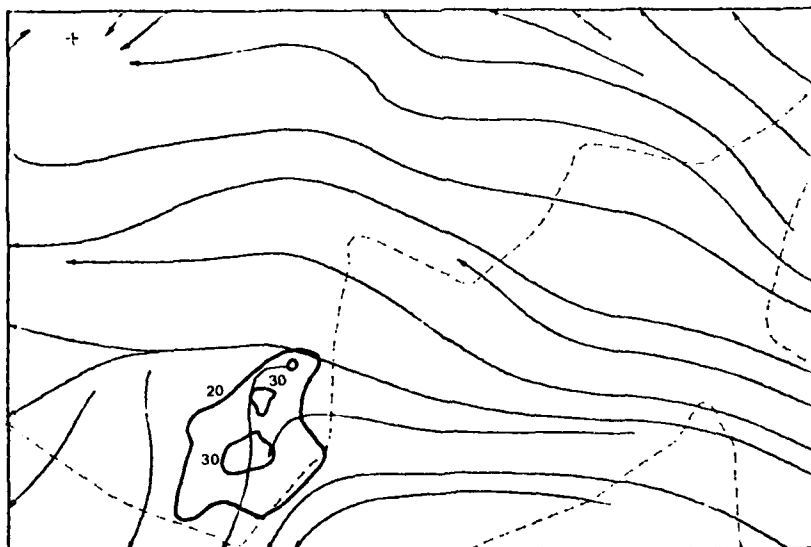
STREAMLINES

TIME... 1315



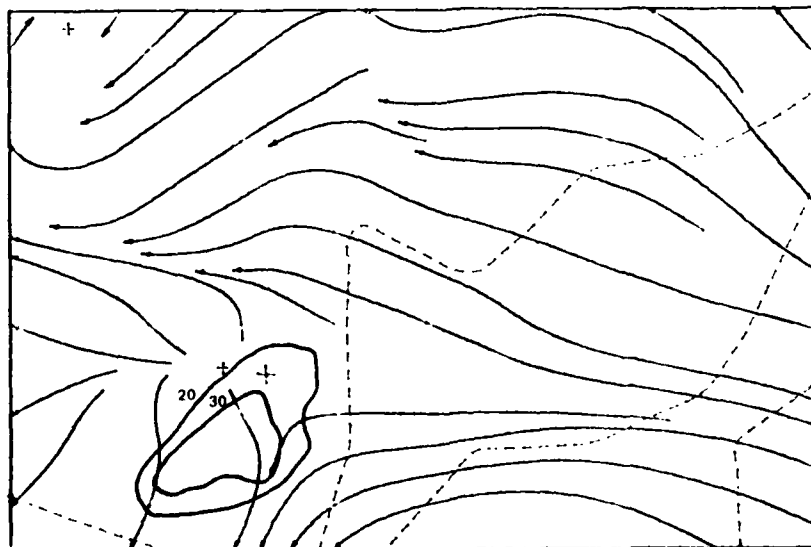
STREAMLINES

TIME... 1320



STREAMLINES

TIME... 1325

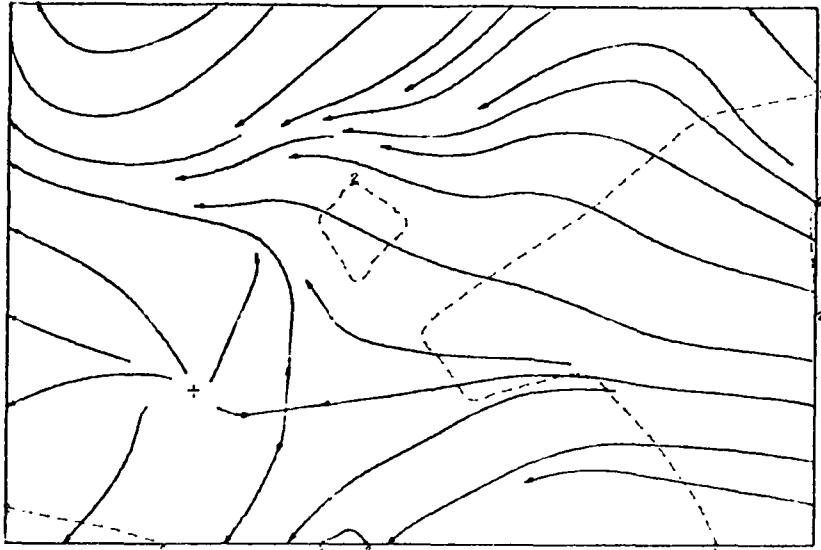


F A C E 7 5.

D A T E . . . 0165

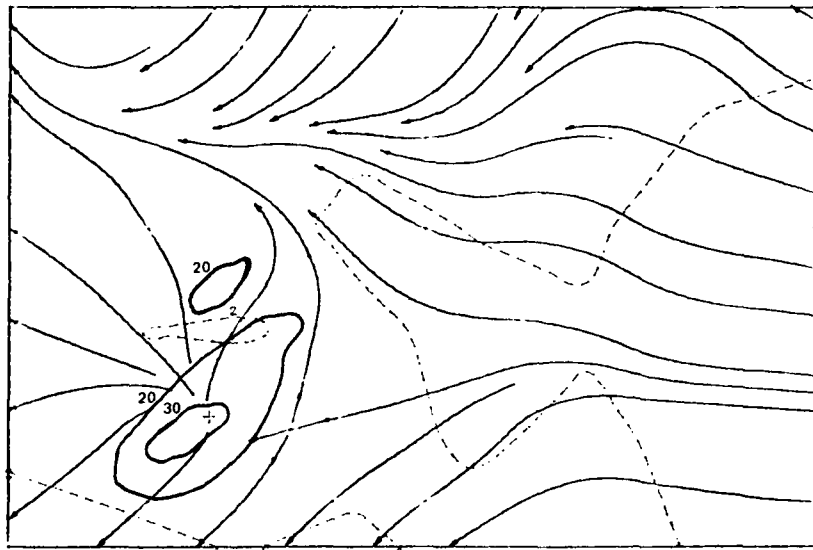
S T R E A M L I N E S

T I M E . . . 1330



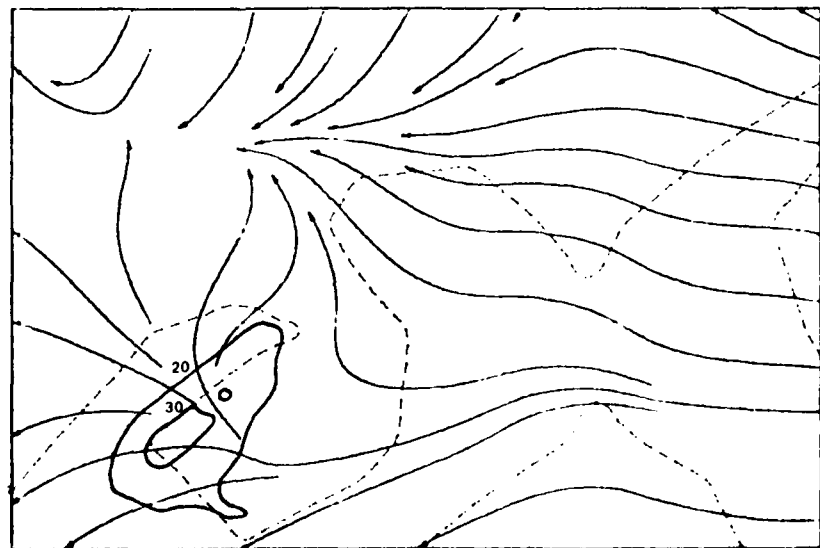
S T R E A M L I N E S

T I M E . . . 1335



S T R E A M L I N E S

T I M E . . . 1340

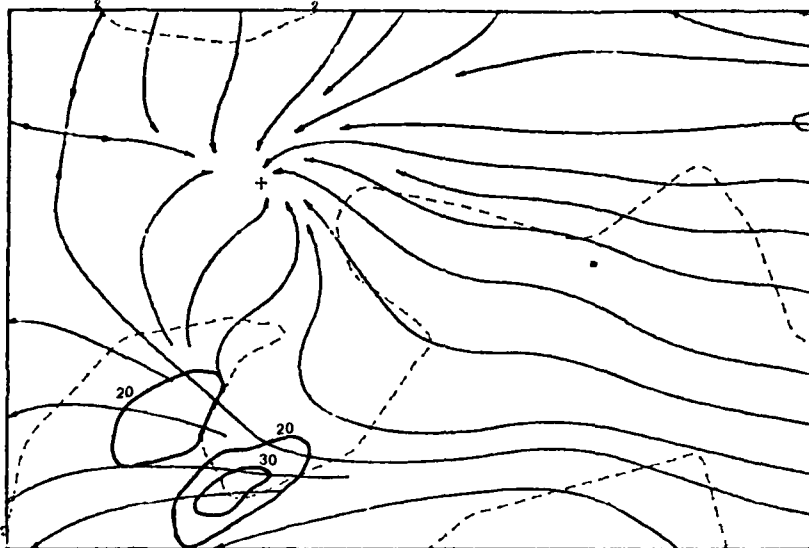


FACE 75.

DATE... 0165

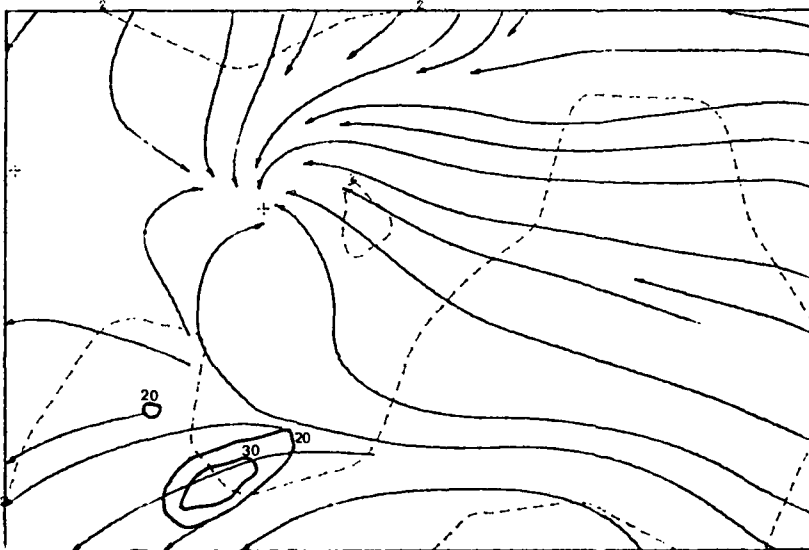
STREAMLINES

TIME... 1345



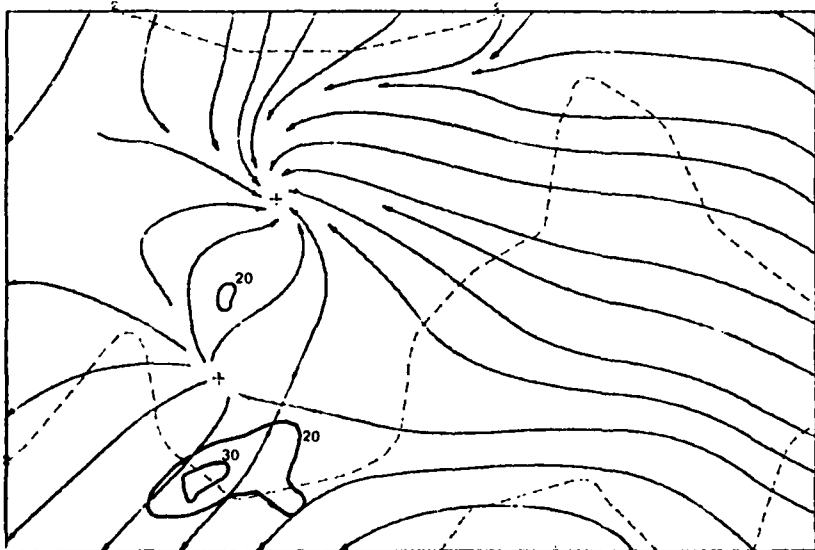
STREAMLINES

TIME... 1350



STREAMLINES

TIME... 1355

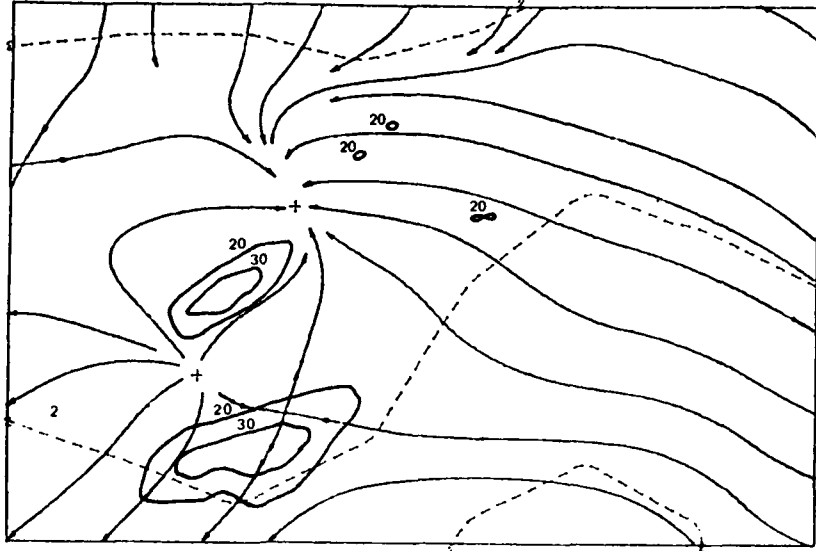


F A C E 7 5.

DATE... 0165

STREAMLINES

TIME... 1400



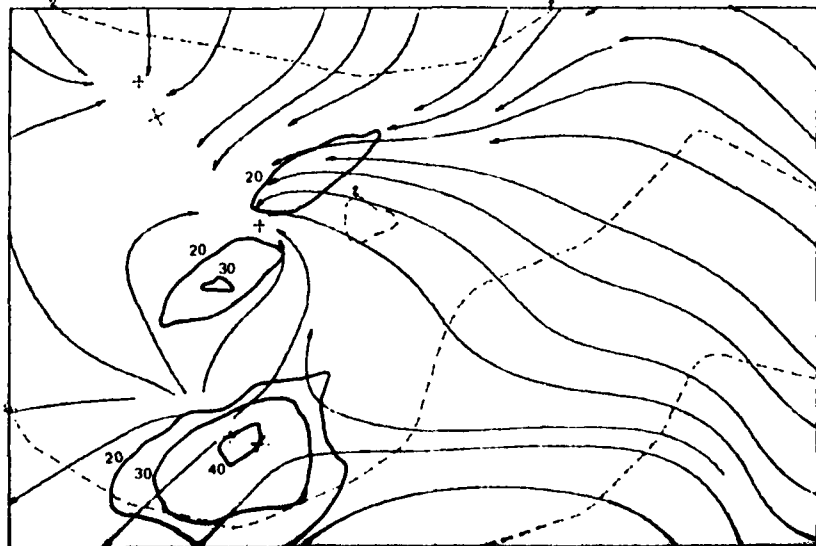
STREAMLINES

TIME... 1405



STREAMLINES

TIME... 1410

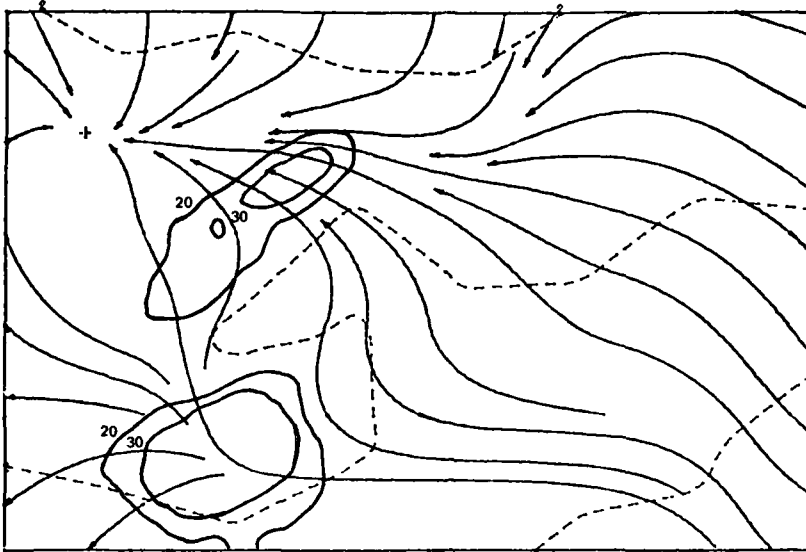


F A C E 7 5 .

DATE... 8165

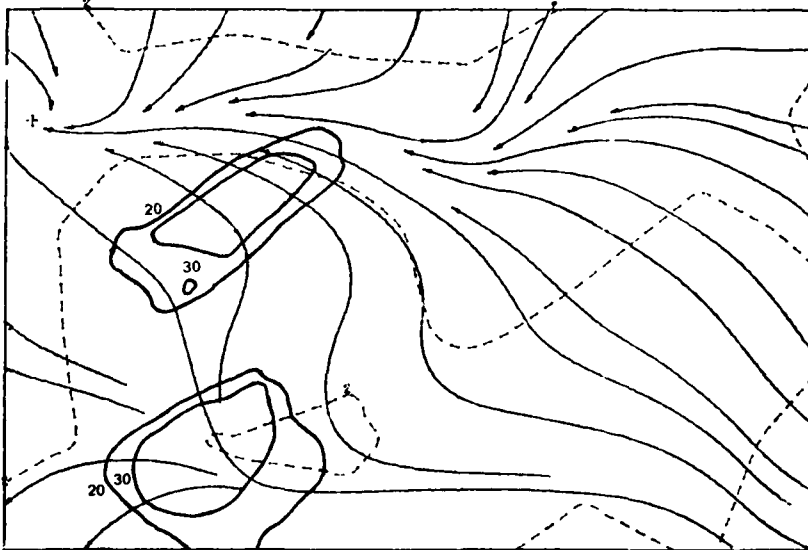
STREAMLINES

TIME... 1415



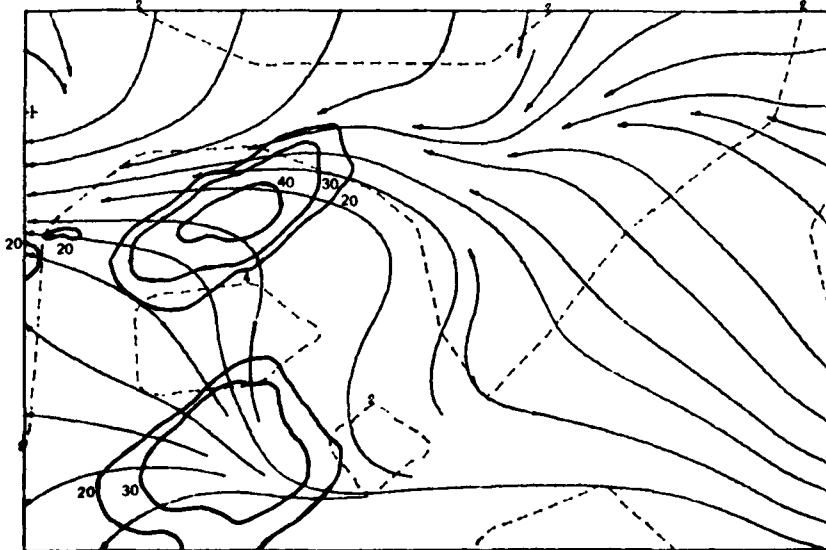
STREAMLINES

TIME... 1420



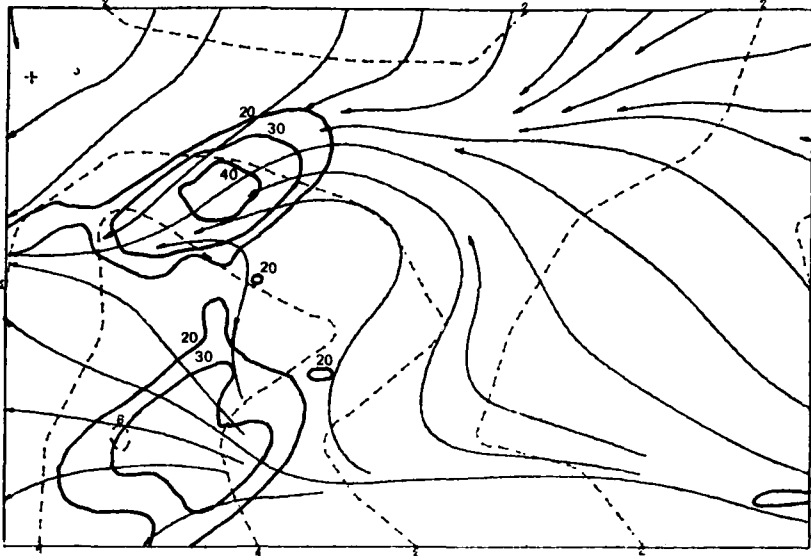
STREAMLINES

TIME... 1425



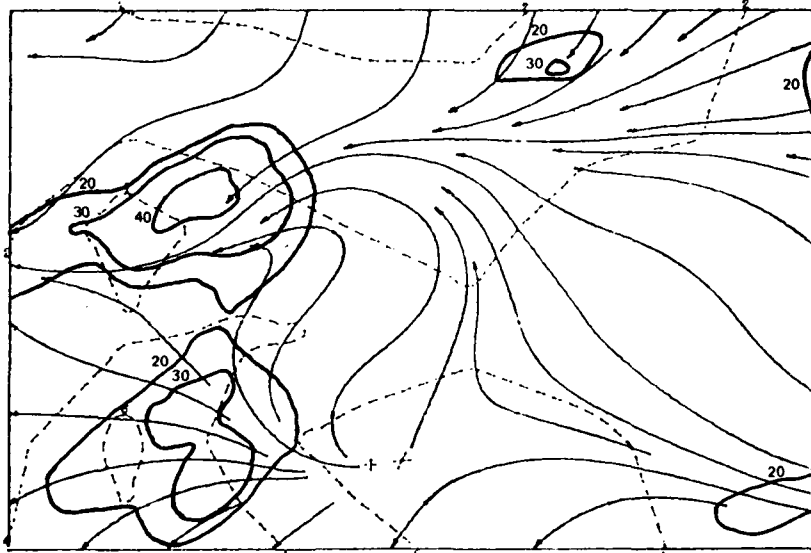
STREAMLINES

TIME... 1430



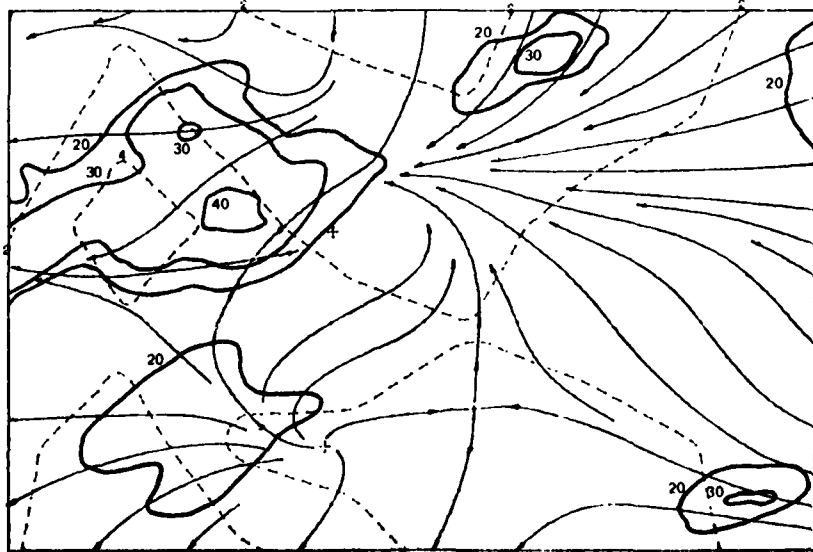
STREAMLINES

TIME... 1435



STREAMLINES

TIME... 1440

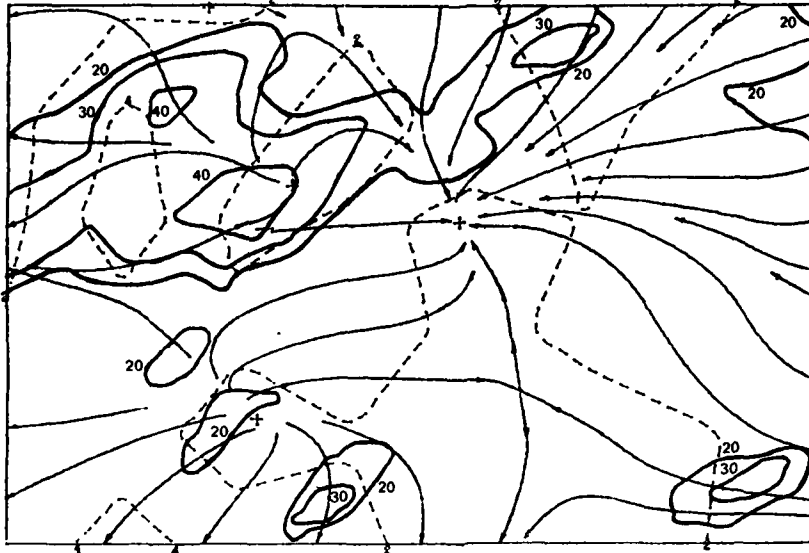


PAGE 75.

DATE... 0165

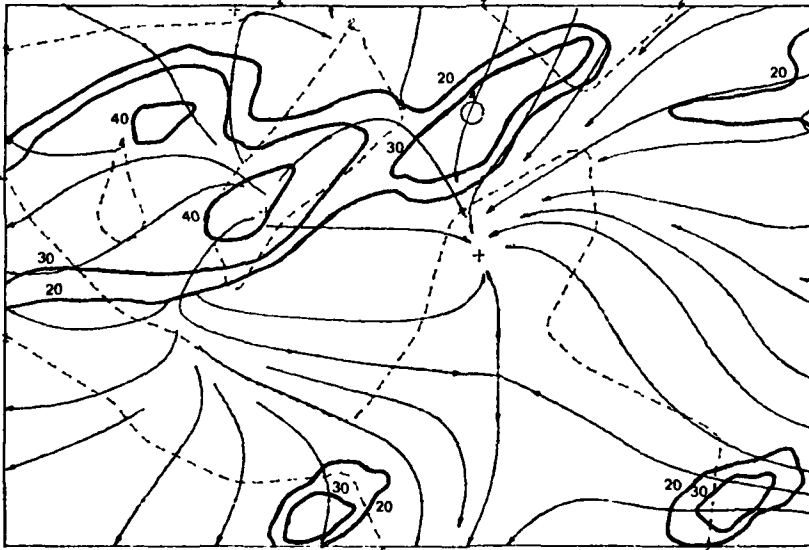
STREAMLINES

TIME... 1445



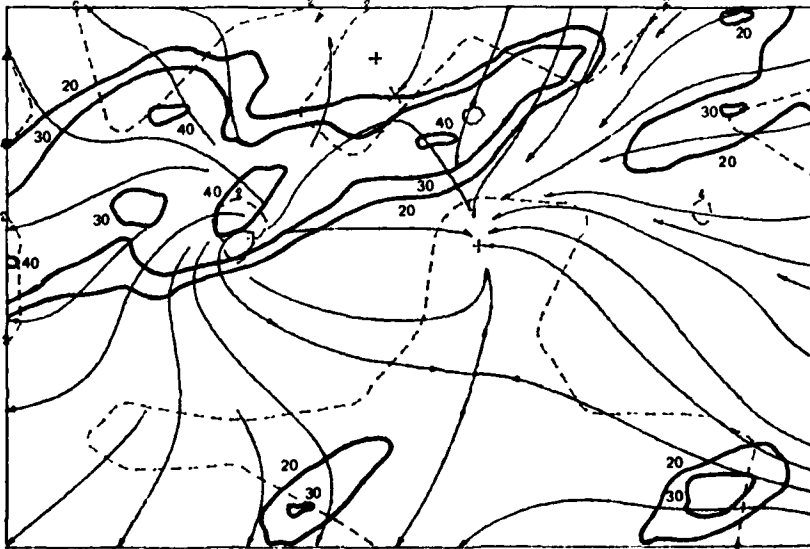
STREAMLINES

TIME... 1450



STREAMLINES

TIME... 1455

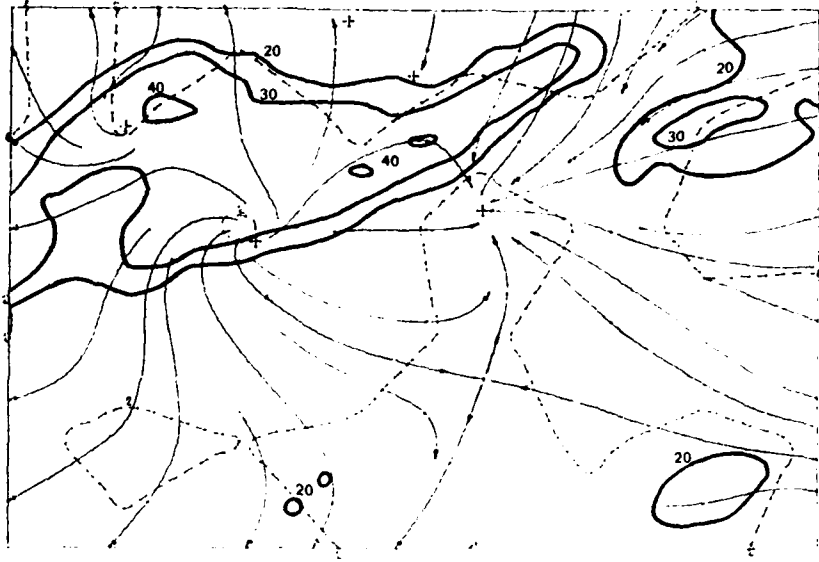


PAGE 73

TIME 1500

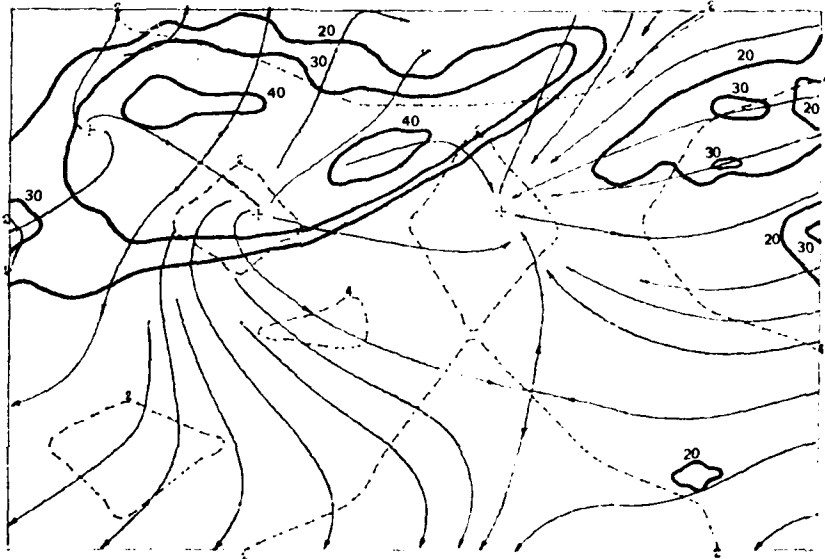
STREAMLINES

TIME 1500



STREAMLINES

TIME 1510



STREAMLINES

TIME 1510

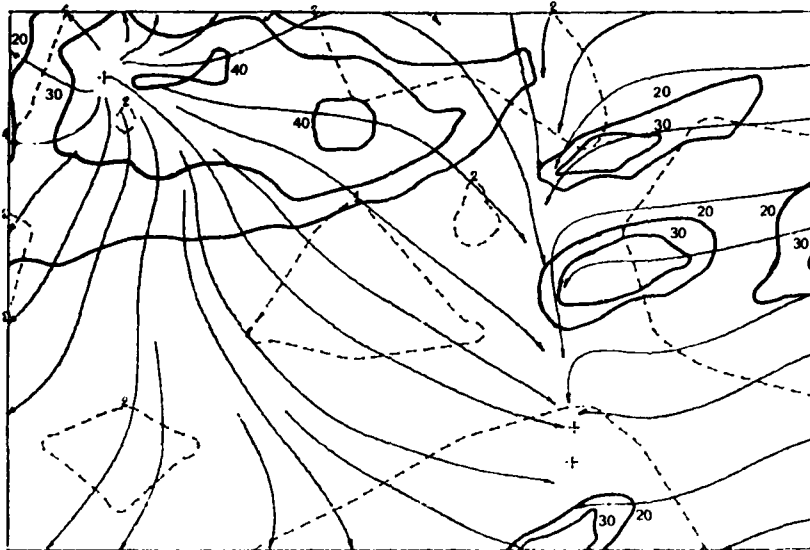


FACE 75.

DATE... 0165

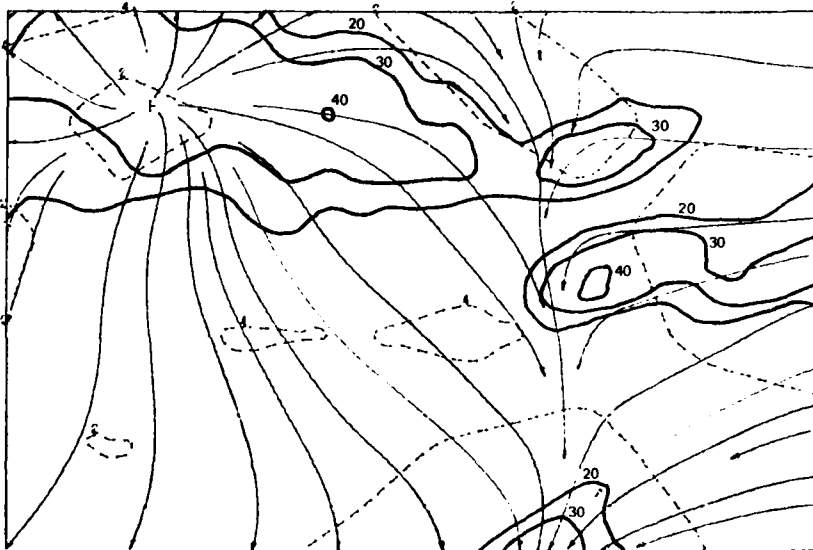
STREAMLINES

TIME... 1515



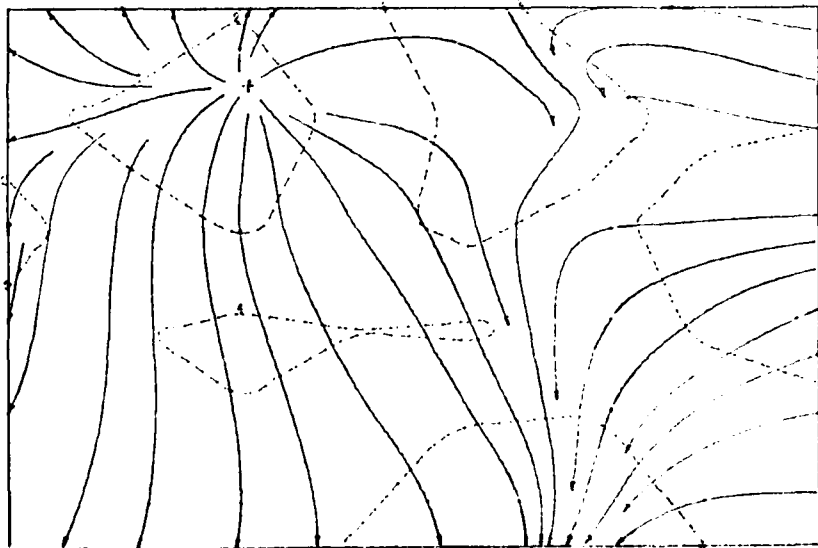
STREAMLINES

TIME... 1520



STREAMLINES

TIME... 1525

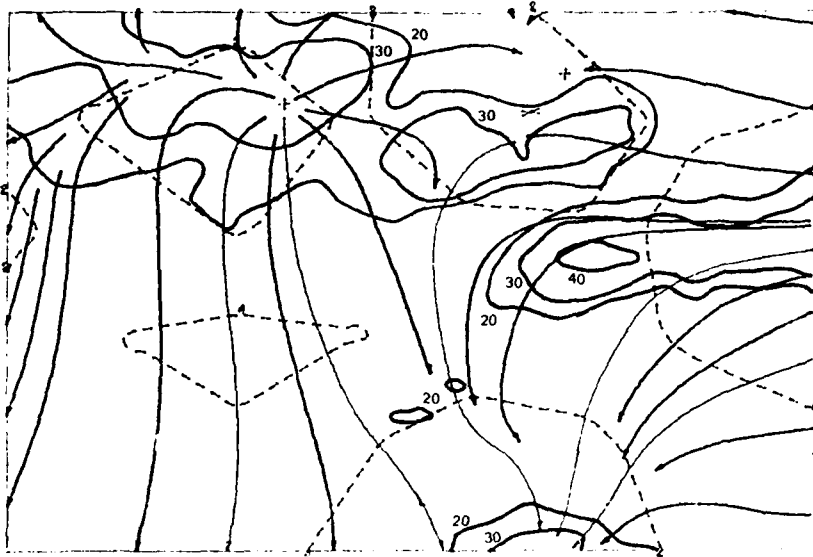


PAGE 7

DATE 2041

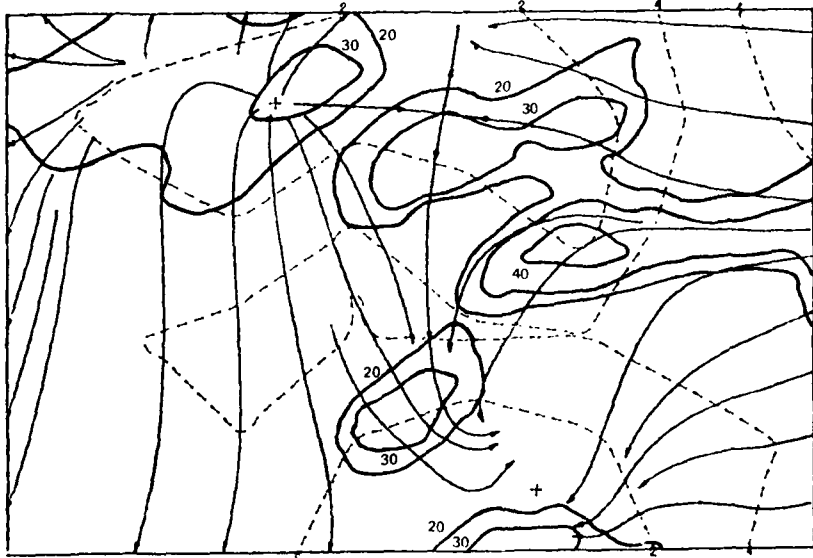
STREAMLINES

TIME 1510



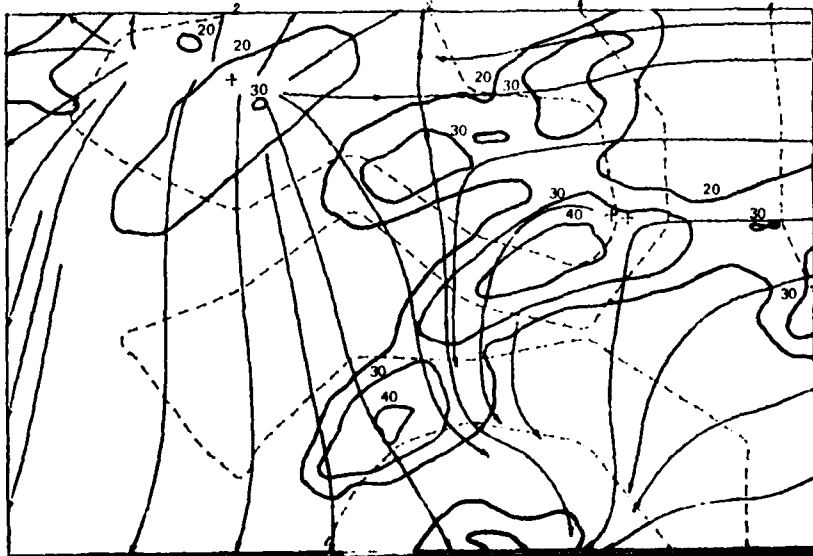
STREAMLINES

TIME 1535



STREAMLINES

TIME 1540



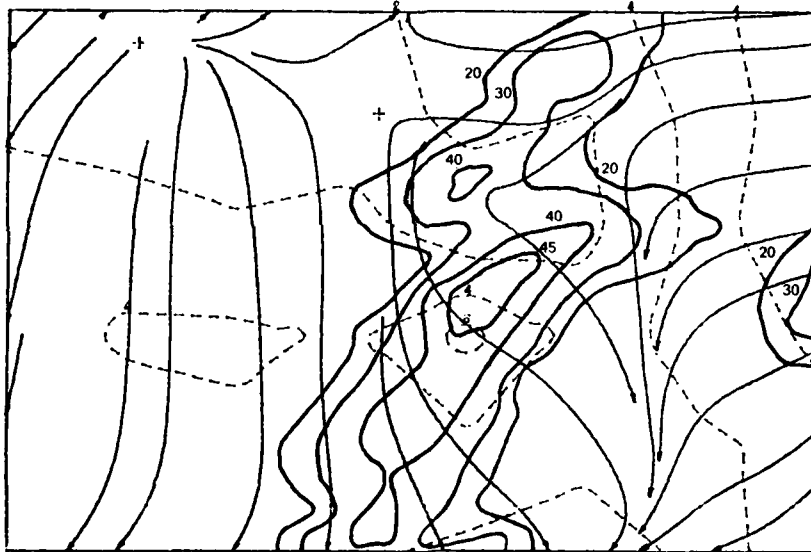
STREAMLINES

TIME... 1545



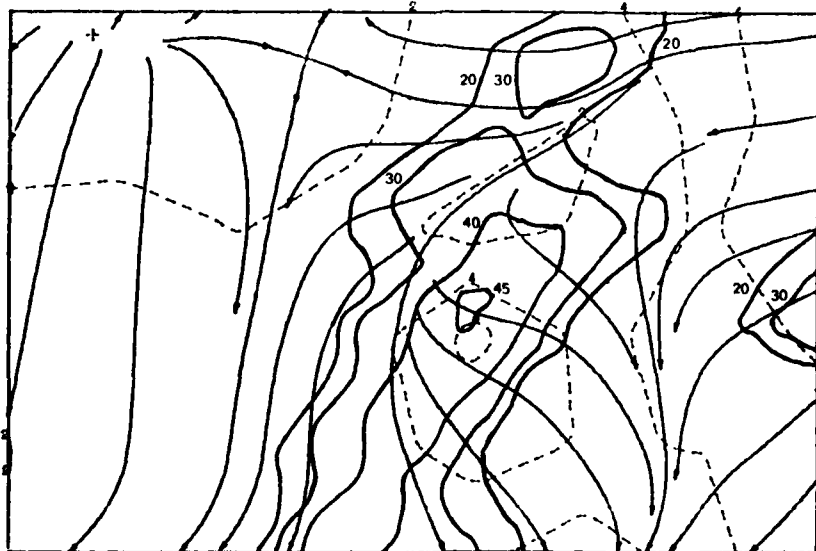
STREAMLINES

TIME... 1550



STREAMLINES

TIME... 1555

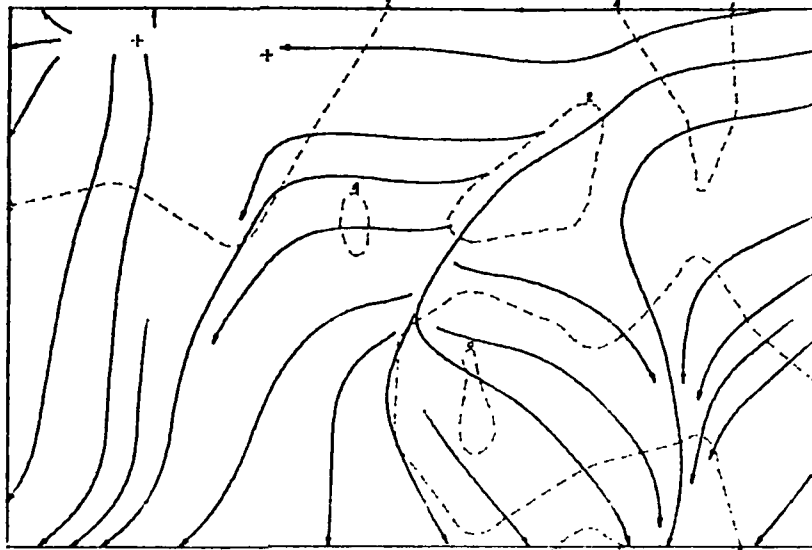


F A C E 1 5.

DATE... 0165

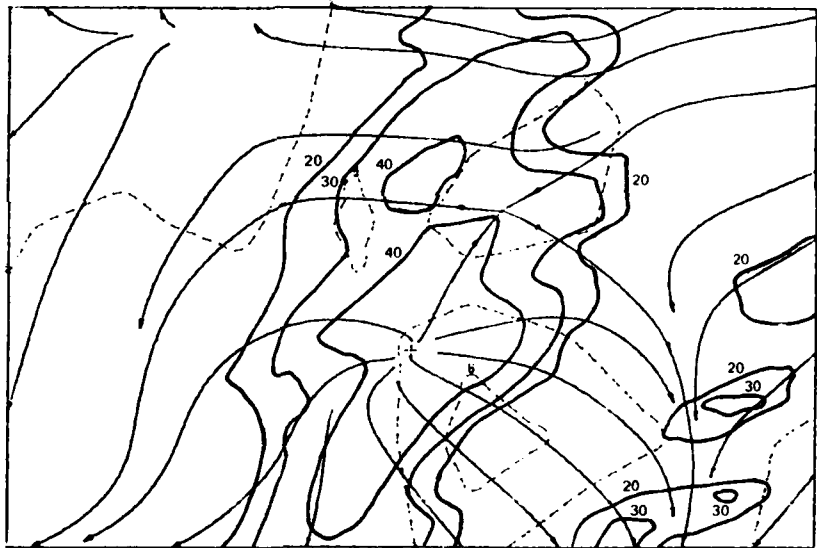
STREAMLINES

TIME... '600



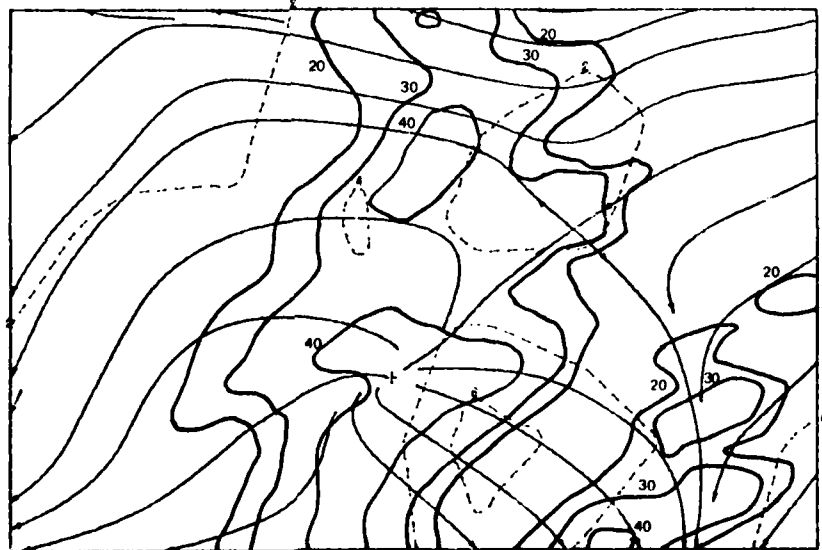
STREAMLINES

TIME... '605



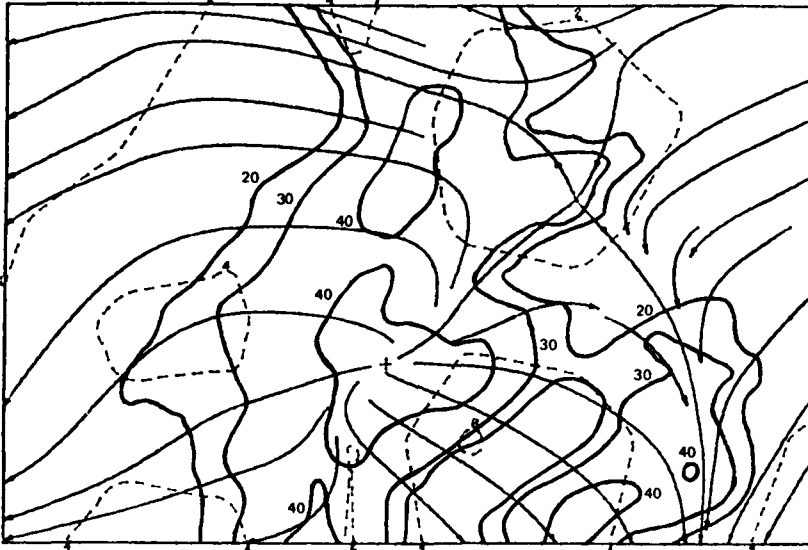
STREAMLINES

TIME... '610



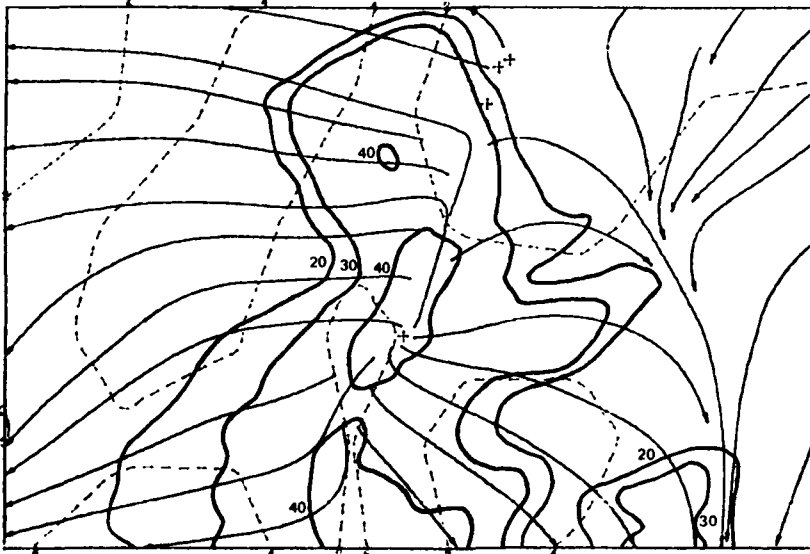
STREAMLINES

TIME... 1615



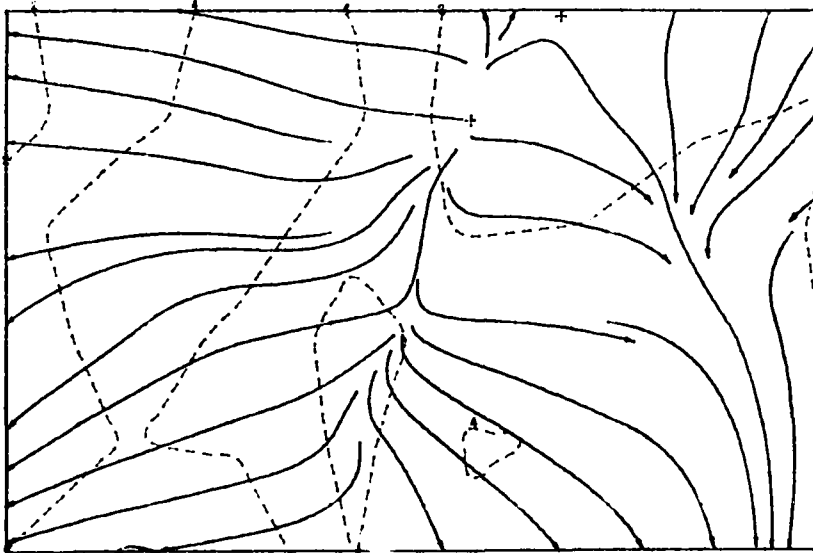
STREAMLINES

TIME.. 1620



STREAMLINES

TIME.. 1625

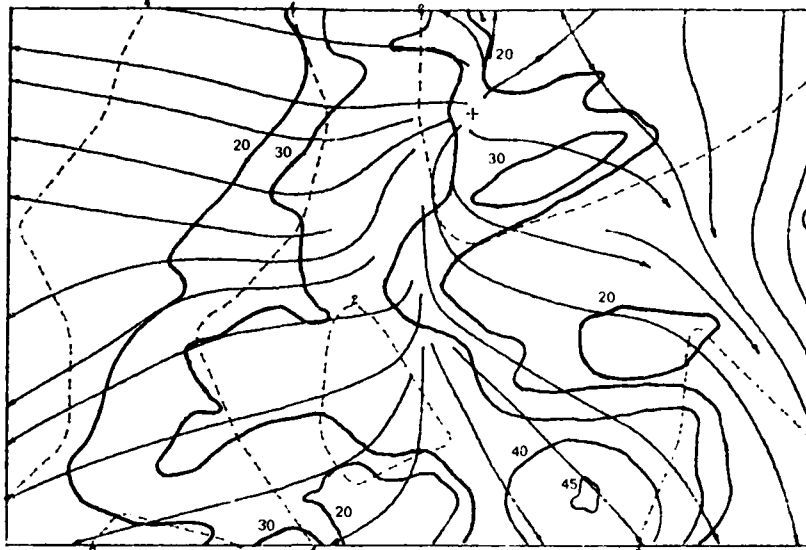


P. H. C. E. / 5.

DATE... 0165

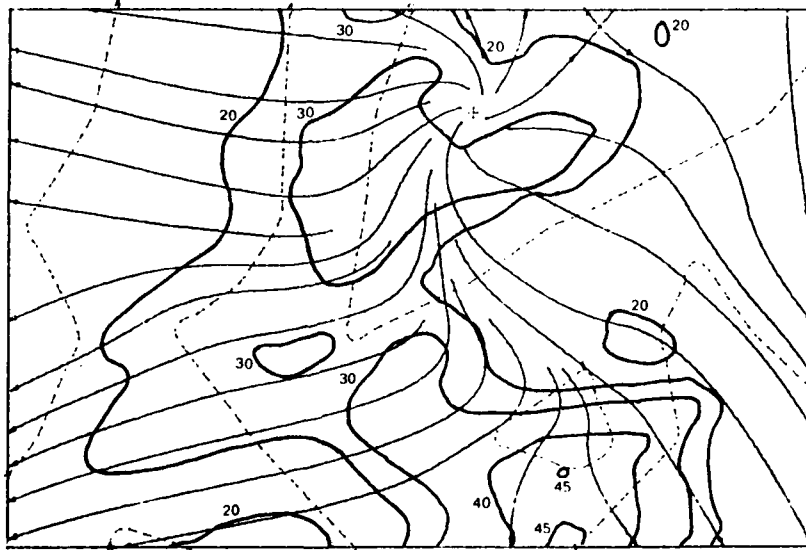
STREAMLINES

TIME... 1630



STREAMLINES

TIME... 1635



STREAMLINES

TIME... 1640

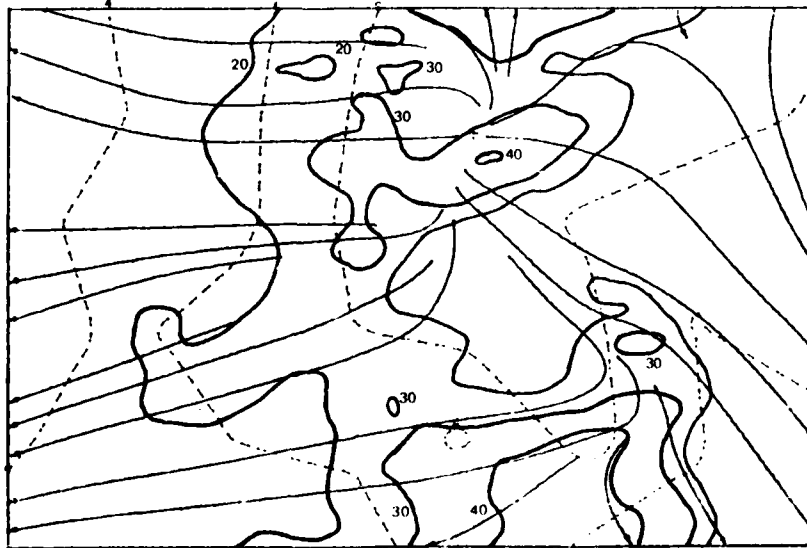


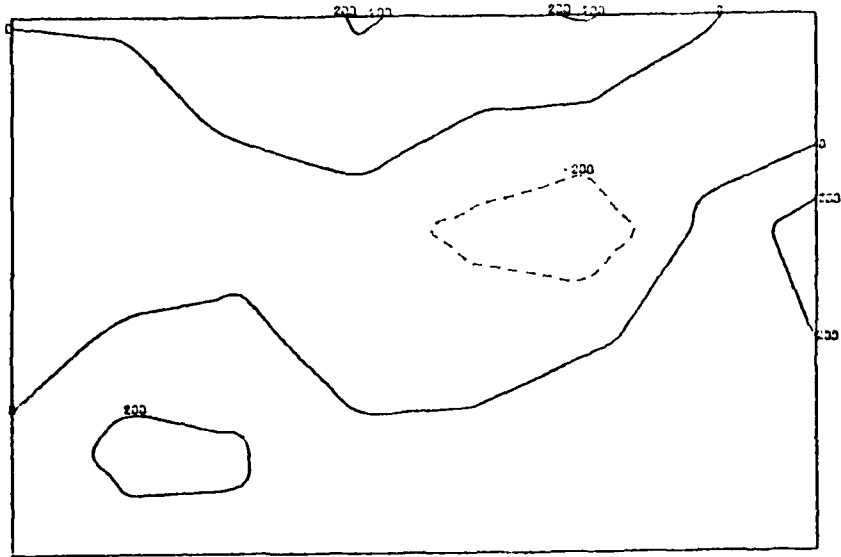
*Figure 8. Divergence patterns on 16 August 1975 for each 5 minute period between 1300 and 1640 EDT on a 6.4 km station grid.*

FACE 75.

DATE... 0165

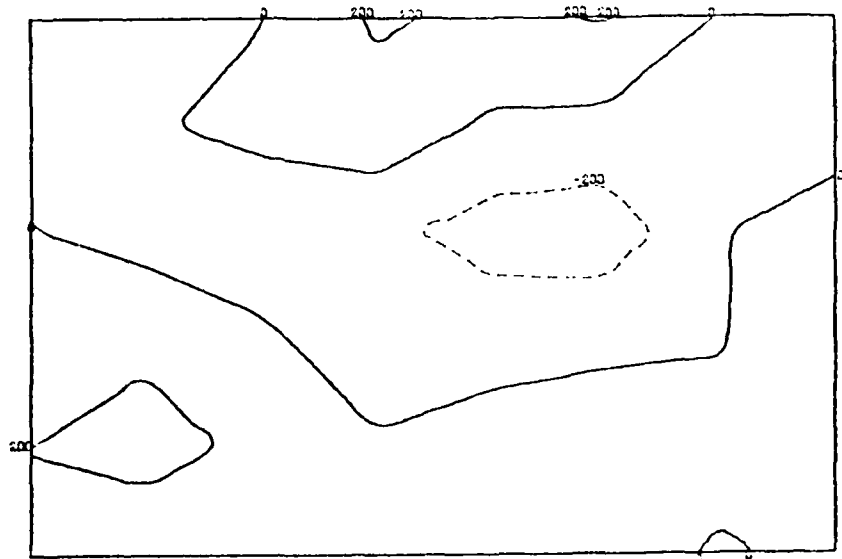
DIVERGENCE

TIME... 1300



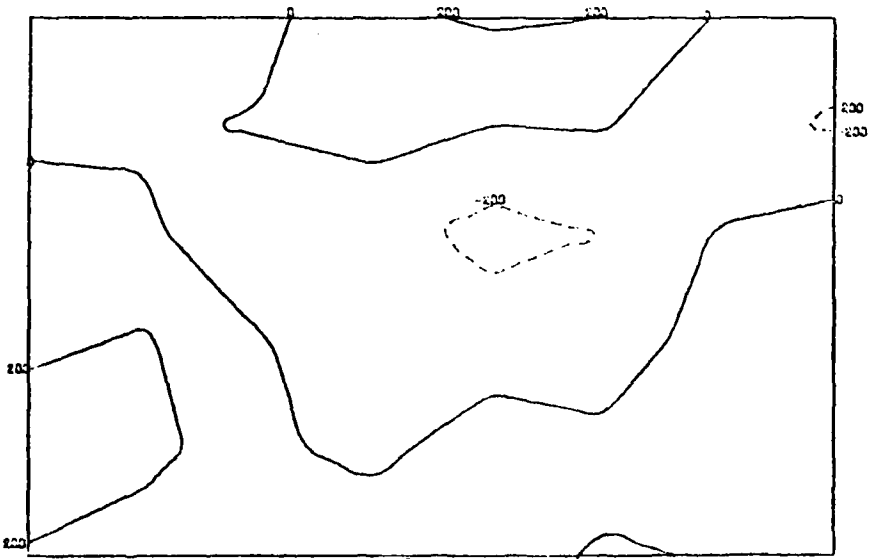
DIVERGENCE

TIME... 1305



DIVERGENCE

TIME... 1310

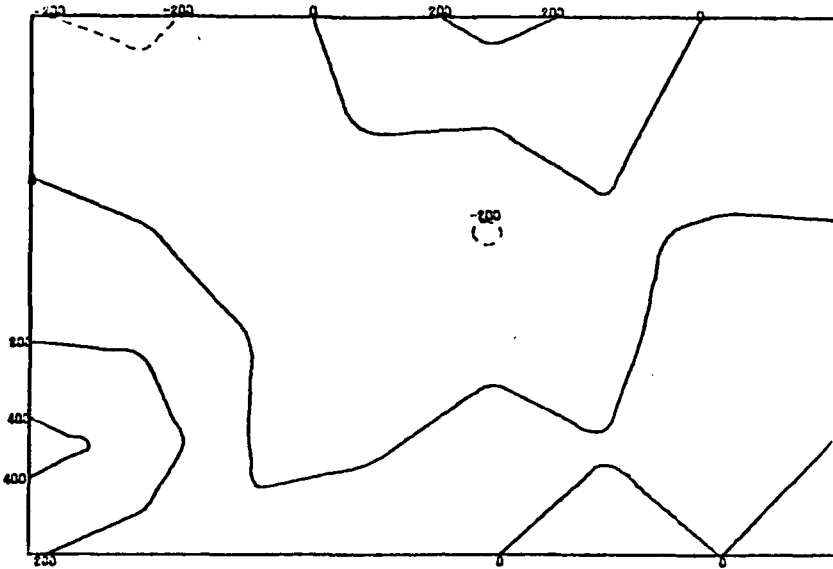


FACE 75.

DATE... 8165

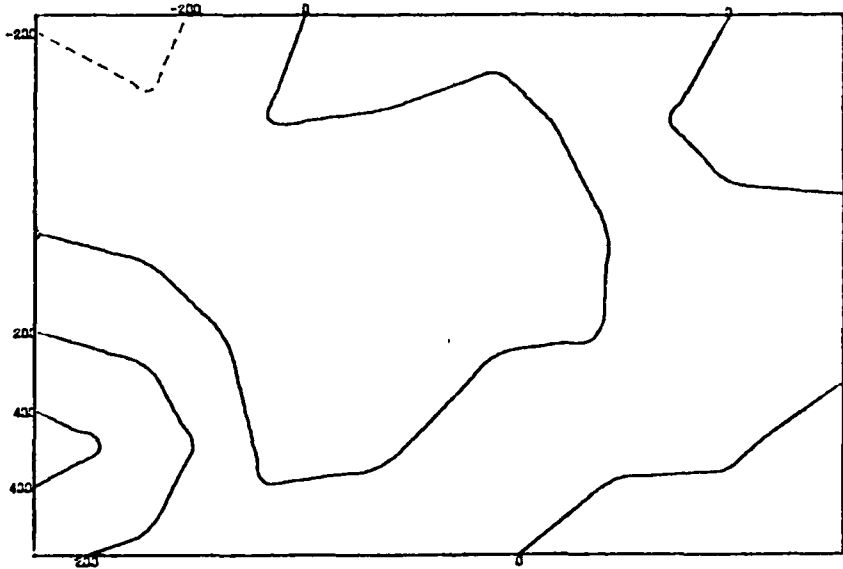
DIVERGENCE

TIME... 1315



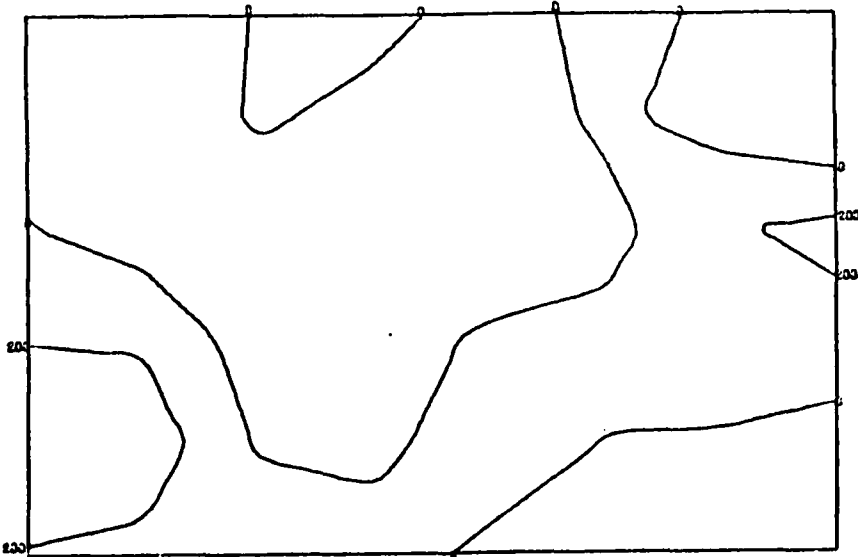
DIVERGENCE

TIME... 1320



DIVERGENCE

TIME... 1325

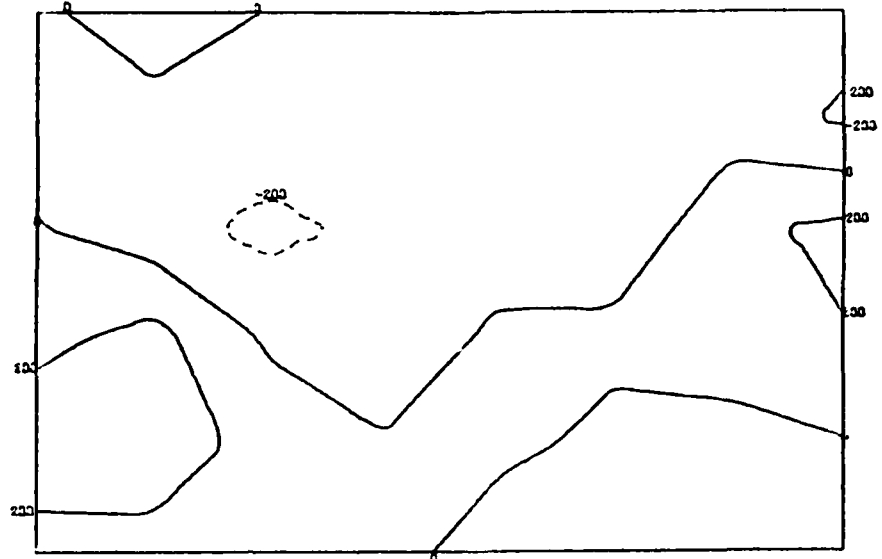


P H C E / S.

DATE... 0100

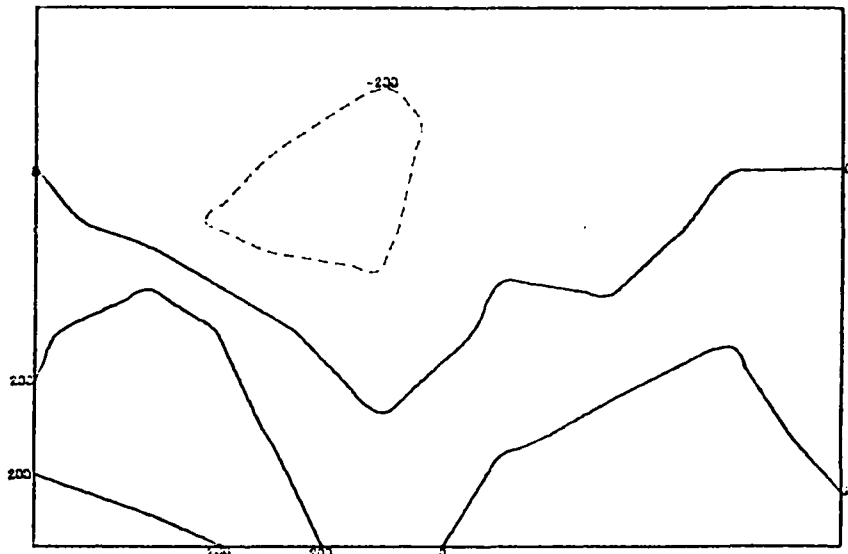
DIVERGENCE

TIME... 1330



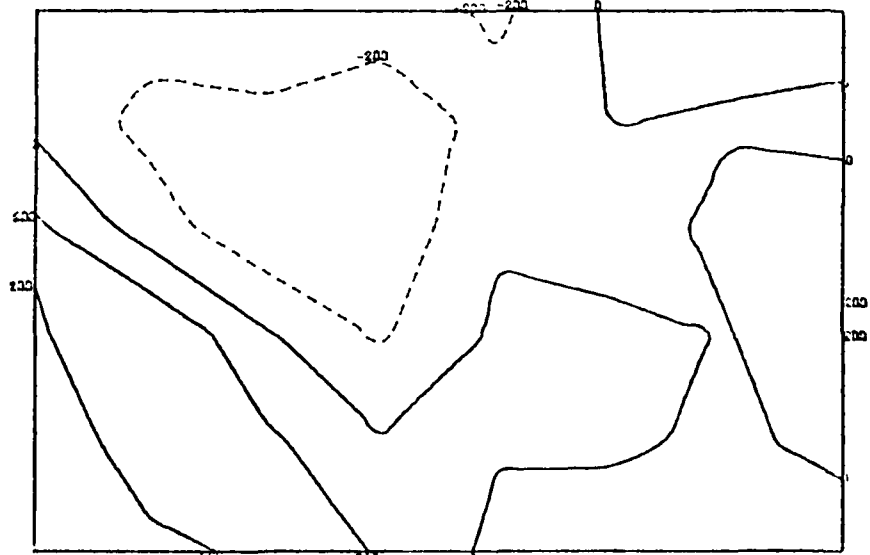
DIVERGENCE

TIME... 1335



DIVERGENCE

TIME... 1340

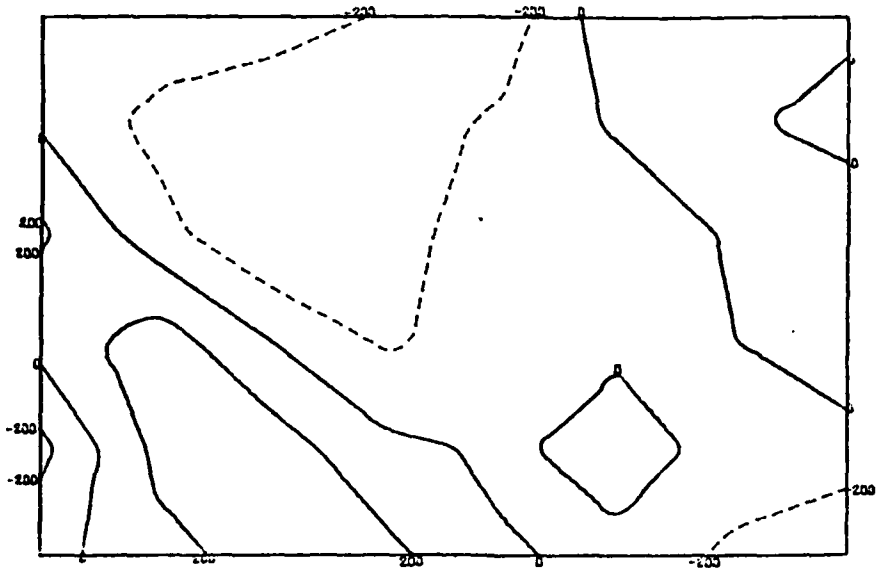


FACE 75.

DATE... 0165

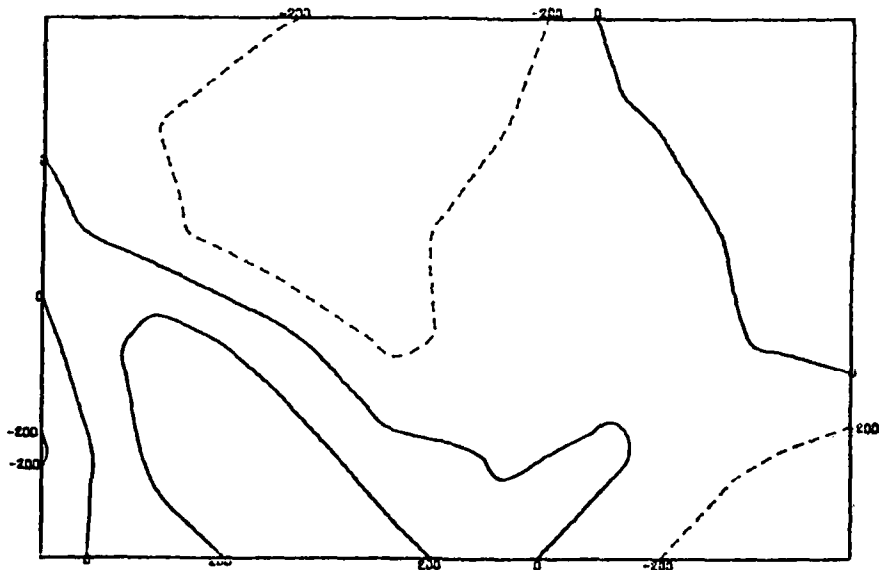
DIVERGENCE

TIME... 1345



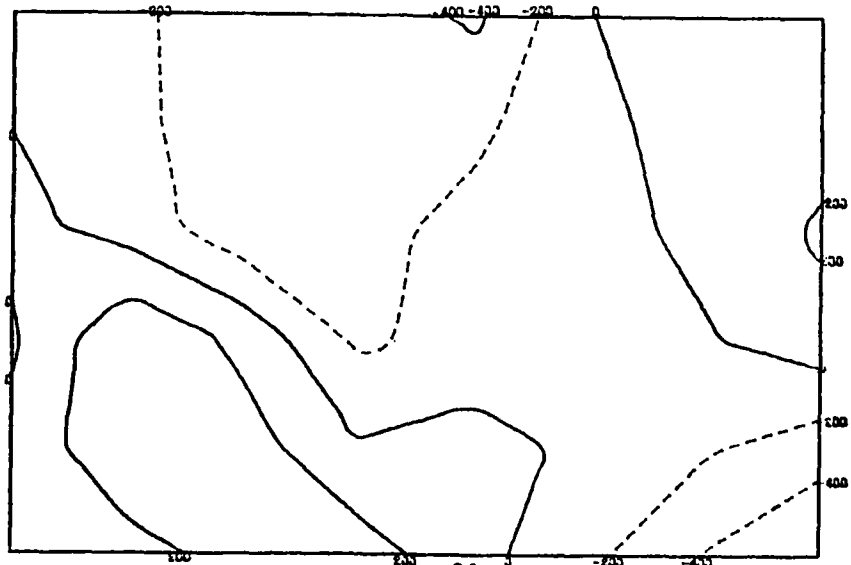
DIVERGENCE

TIME... 1350



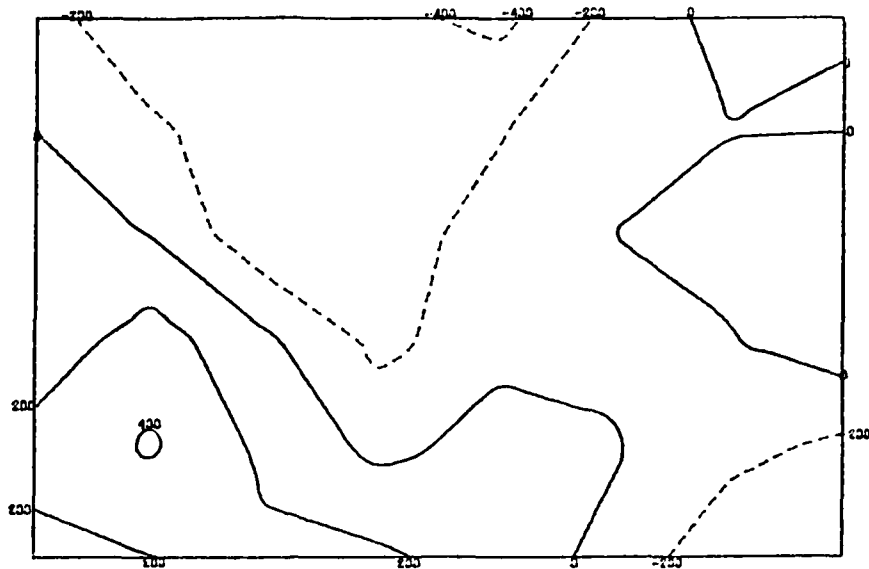
DIVERGENCE

TIME... 1355



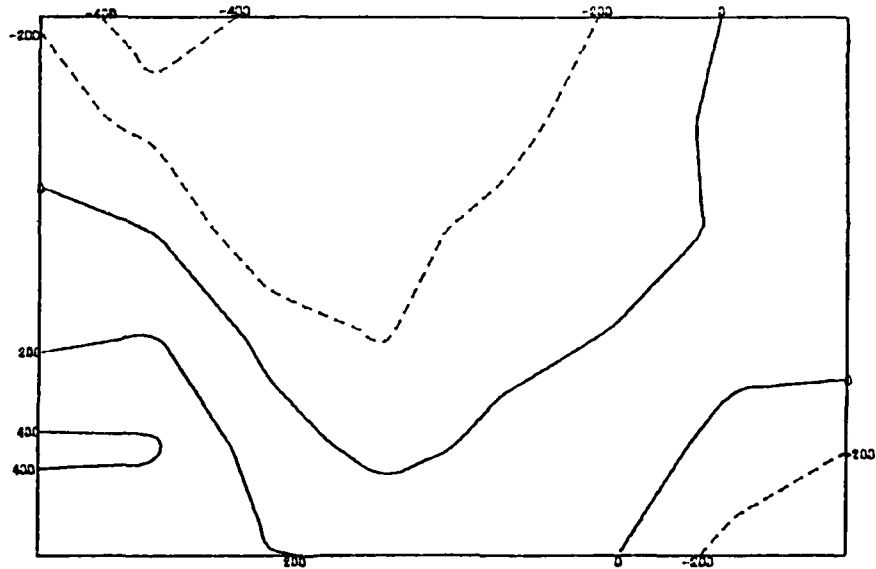
D I V E R G E N C E

T I M E . . . 1 4 0 0



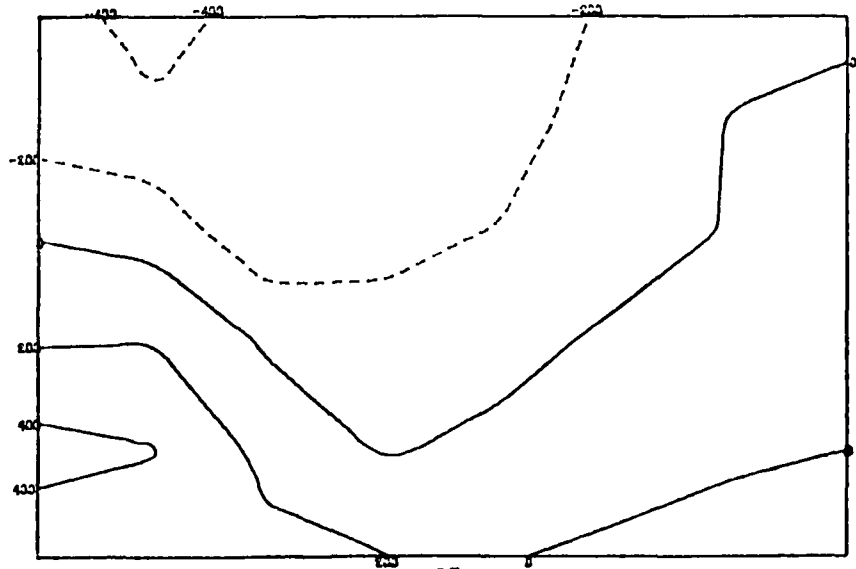
D I V E R G E N C E

T I M E . . . 1 4 0 5



D I V E R G E N C E

T I M E . . . 1 4 1 0

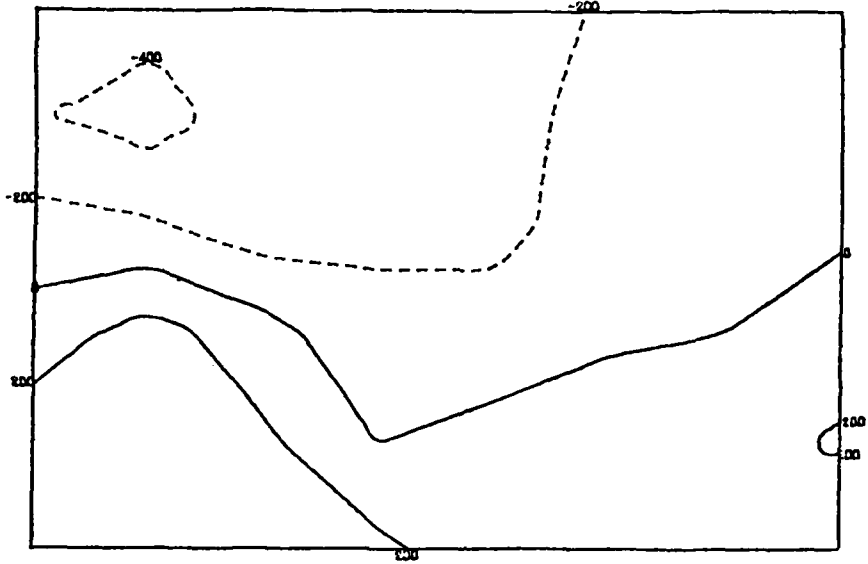


FACE 75.

DATE... 8165

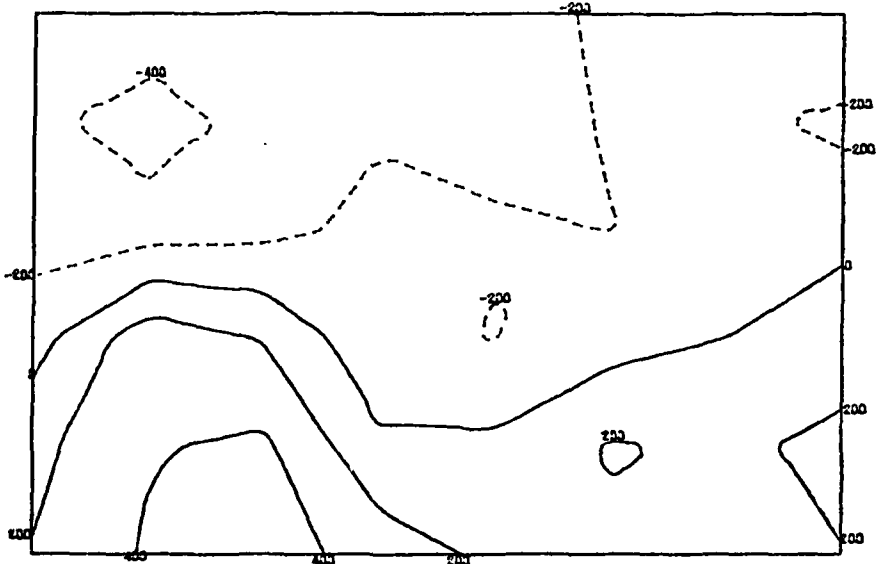
DIVERGENCE

TIME... 1415



DIVERGENCE

TIME... 1420



DIVERGENCE

TIME... 1425

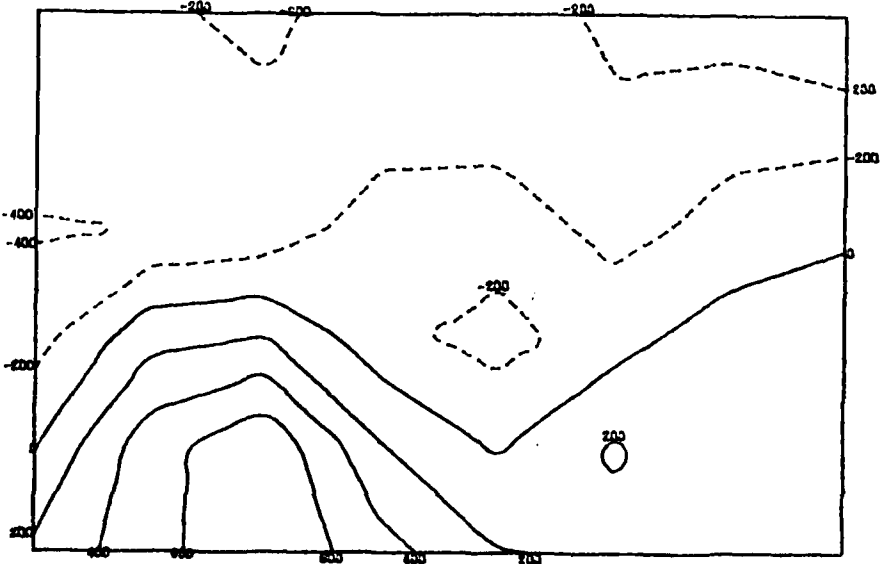
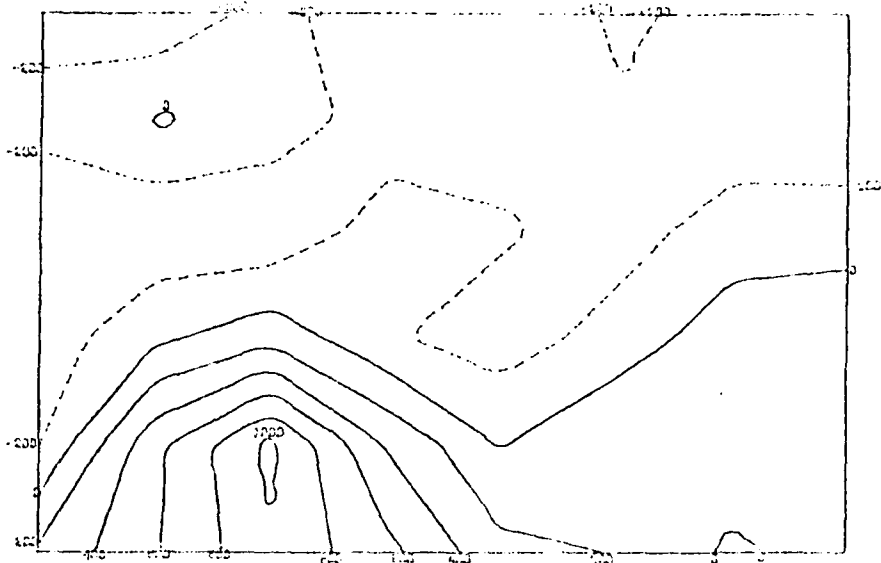


FIGURE 1

DATE: 07/13

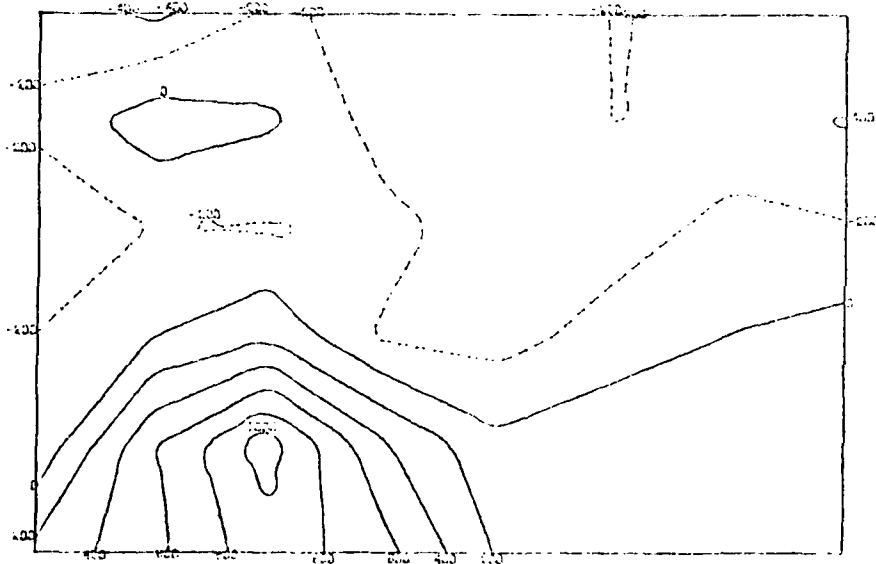
DIVERGENCE

TIME: 1430



DIVERGENCE

TIME: 1435



DIVERGENCE

TIME: 1440

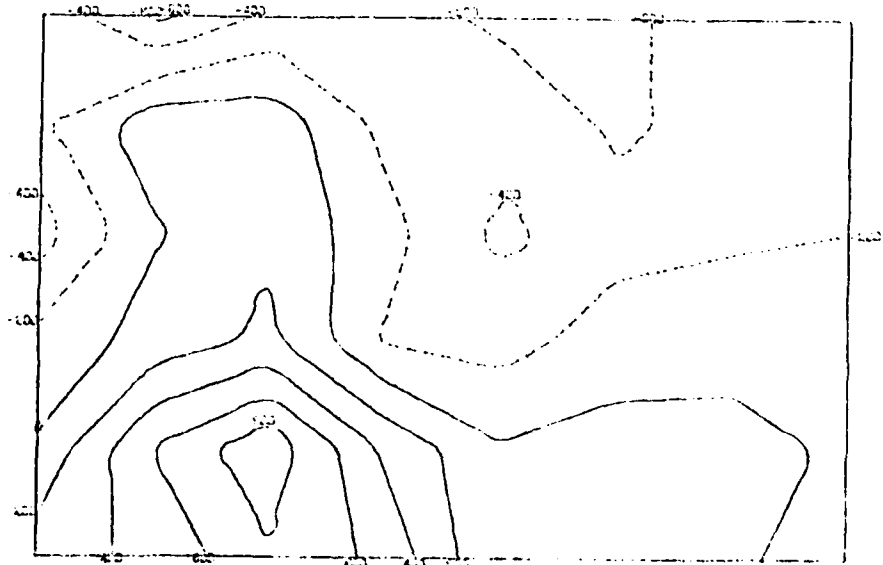
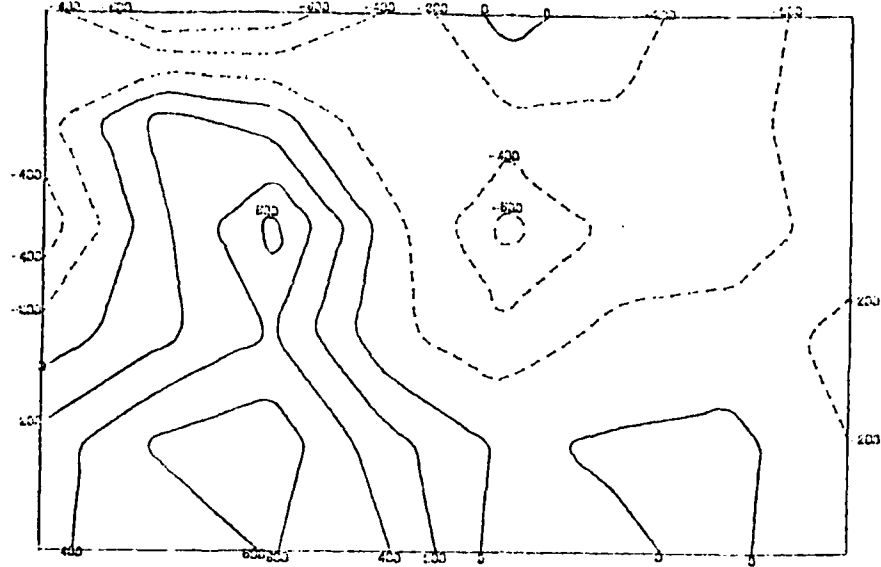


FIGURE 5.

DATE... 0105

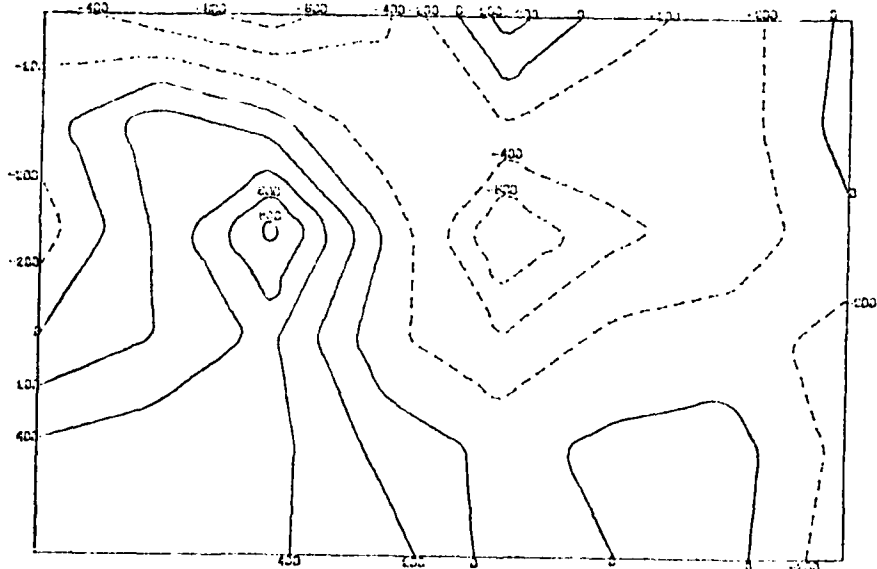
DIVERGENCE

TIME... 1445



DIVERGENCE

TIME... 1450



DIVERGENCE

TIME... 1455

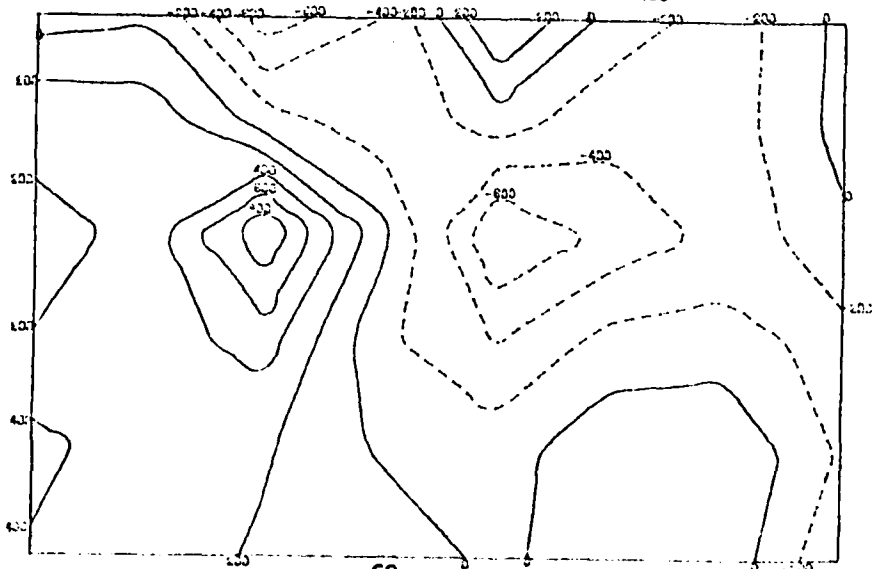


FIG. 10

DIVERGENCE

LINE 1510



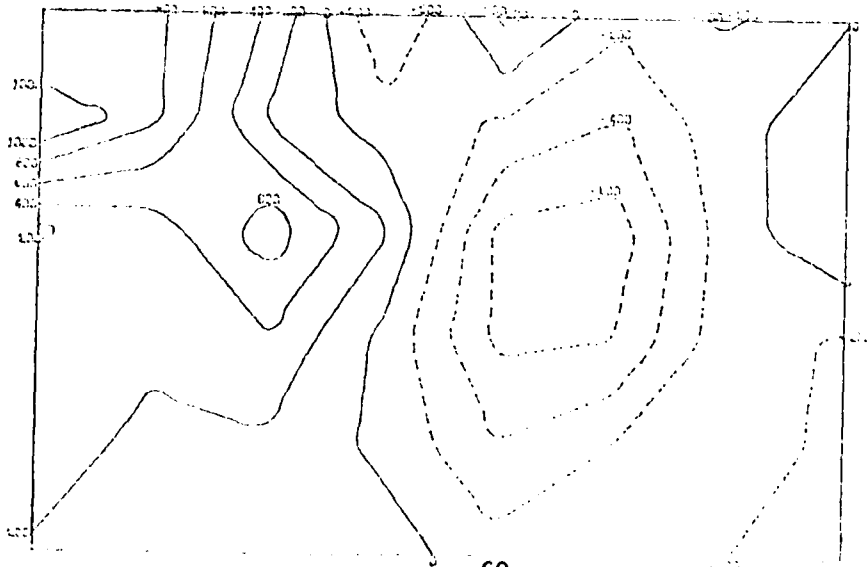
DIVERGENCE

LINE 1510



DIVERGENCE

LINE 1510

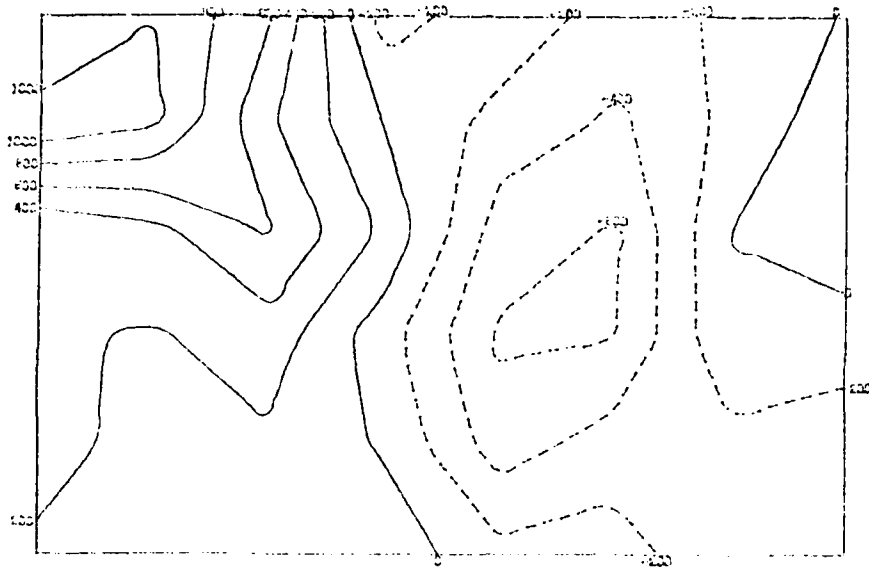


FACE 7 S.

DATE... 0765

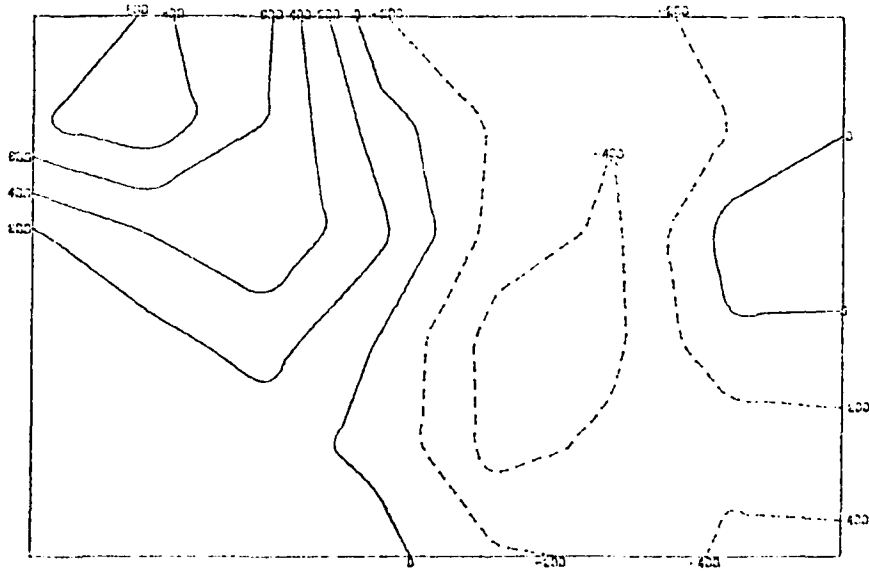
DIVERGENCE

TIME... 1515



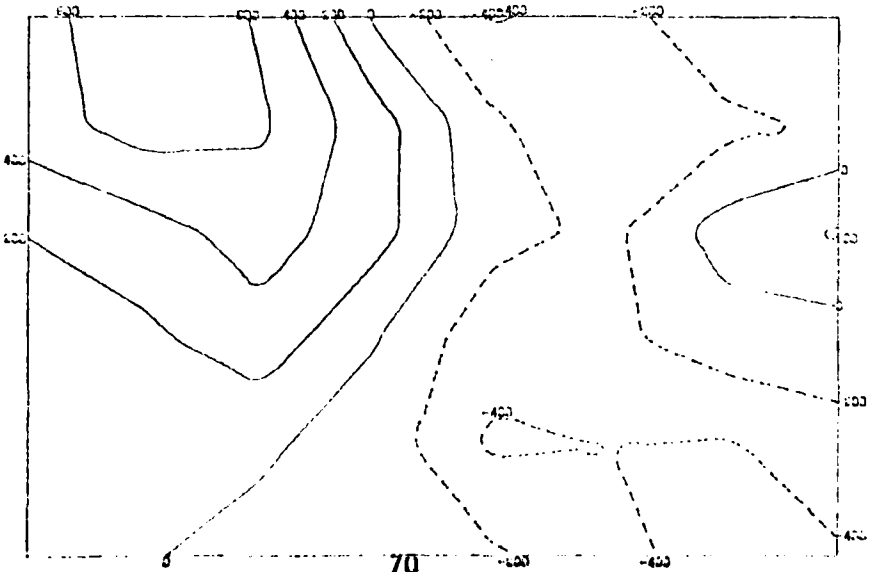
DIVERGENCE

TIME... 1620

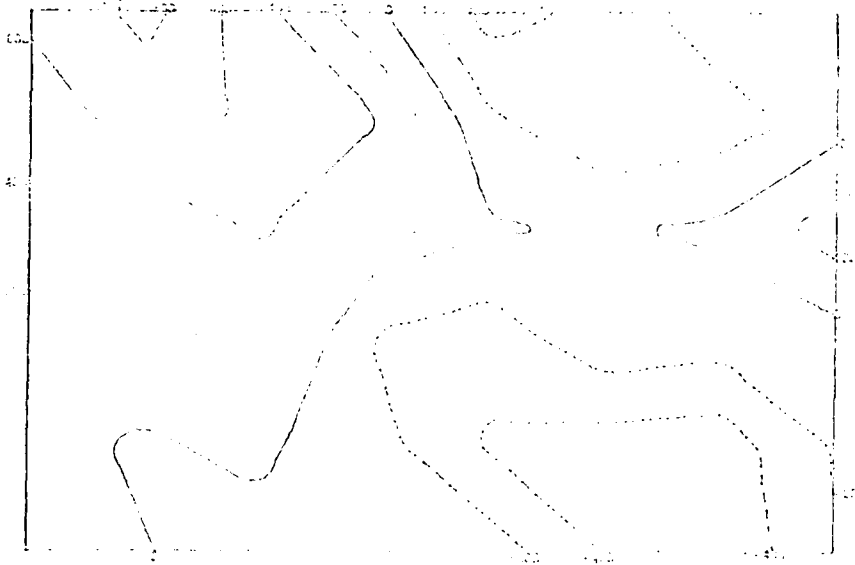


DIVERGENCE

TIME... 1800

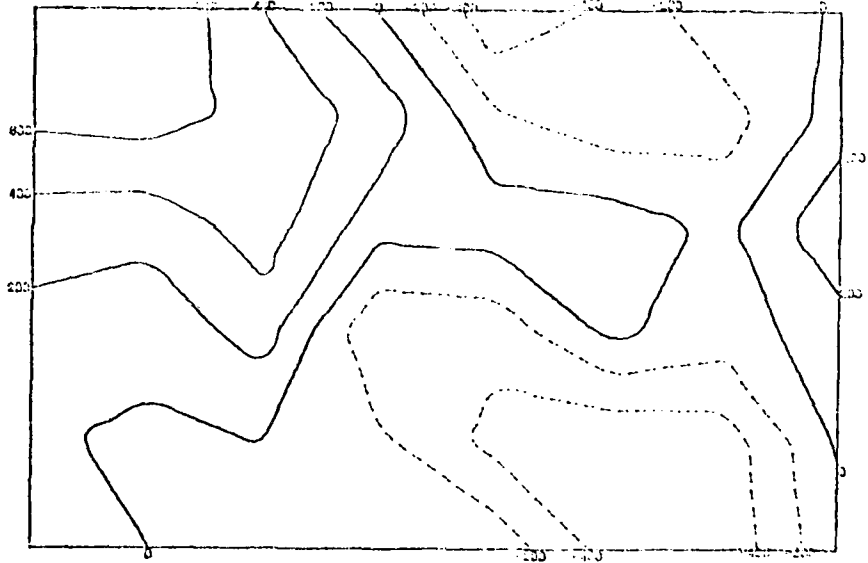


DEVELOPMENT



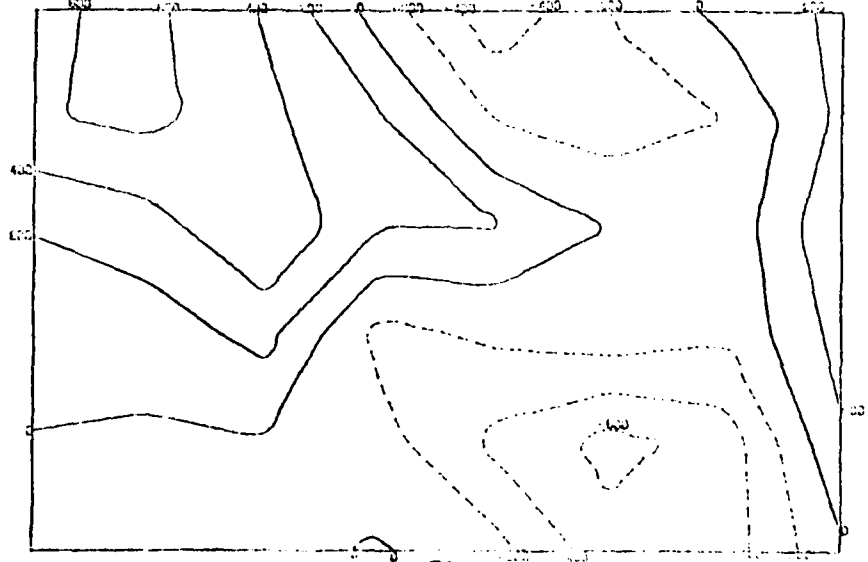
DIVERGENCE

TIME 1530



DIVERGENCE

TIME 1540

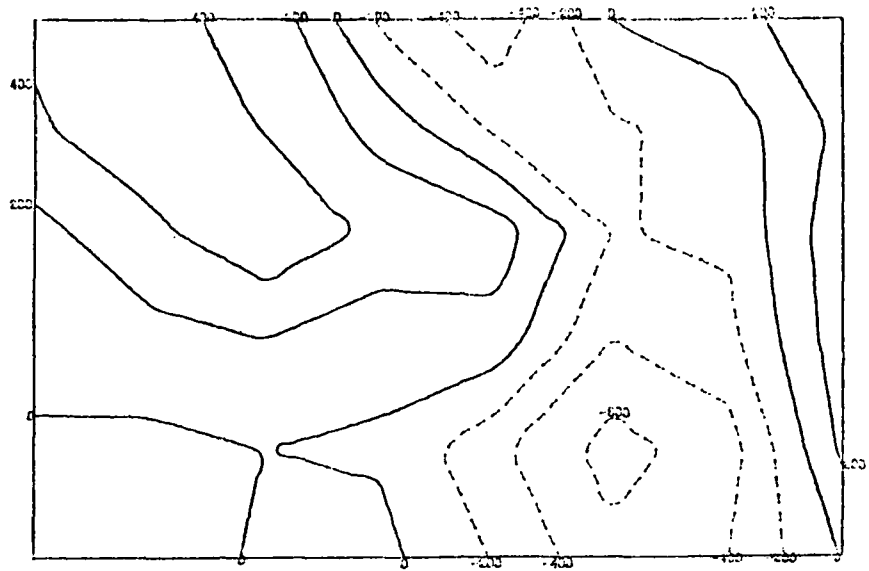


F A C E 7 S.

D A T E . . . 0 1 6 5

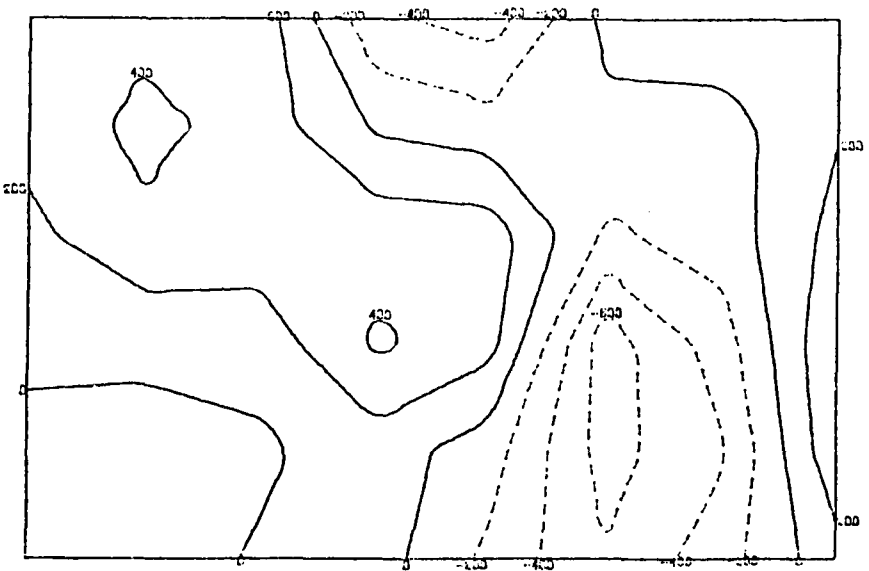
D I V E R G E N C E

T I M E . . . 1 5 4 5



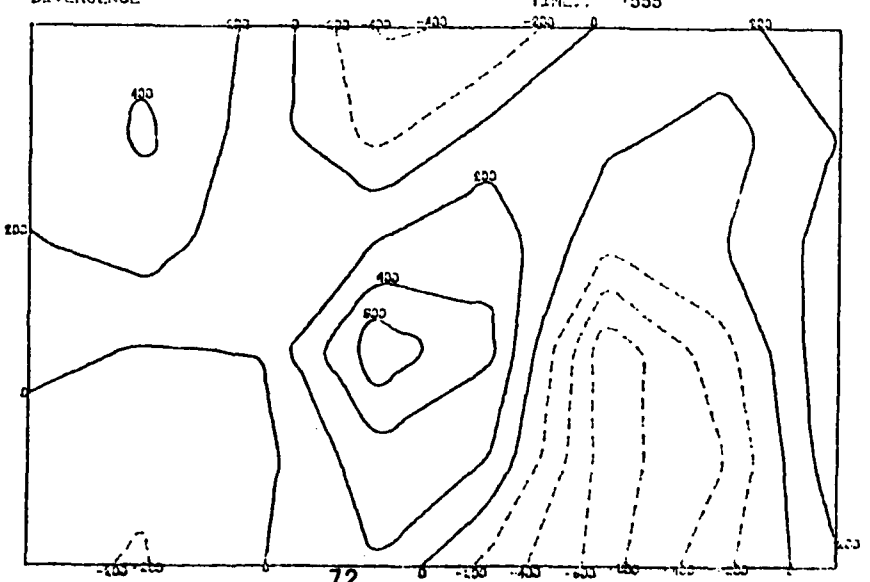
D I V E R G E N C E

T I M E . . . 1 5 5 0



D I V E R G E N C E

T I M E . . . 1 5 5 5

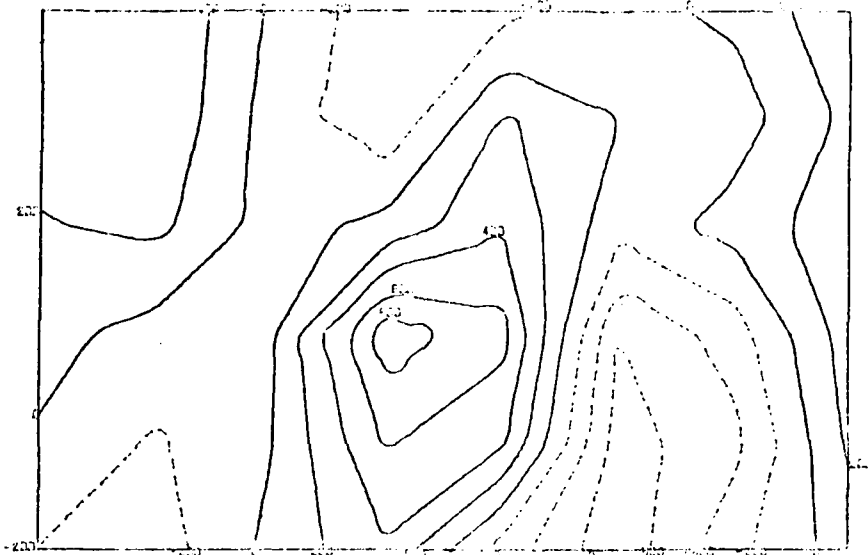


F R C E Y S

DATE: 11-10

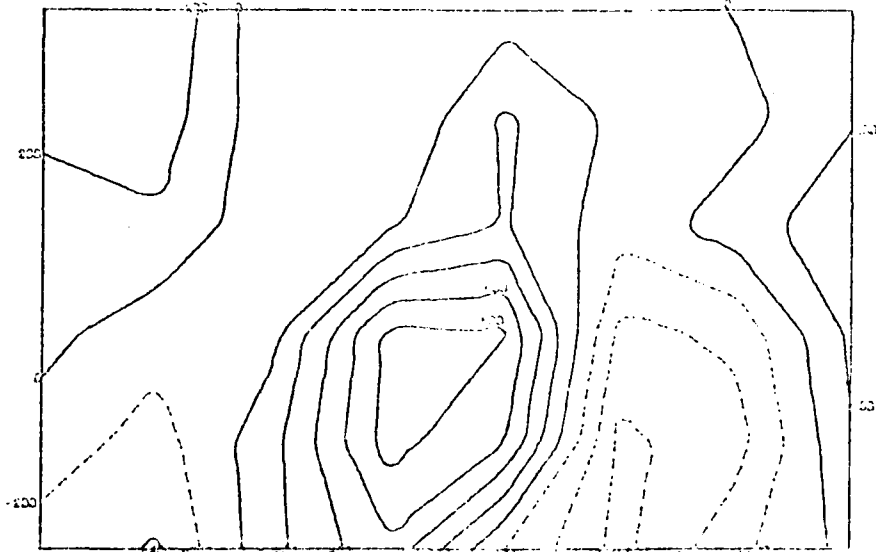
DIVERGENCE

TIME: 1600



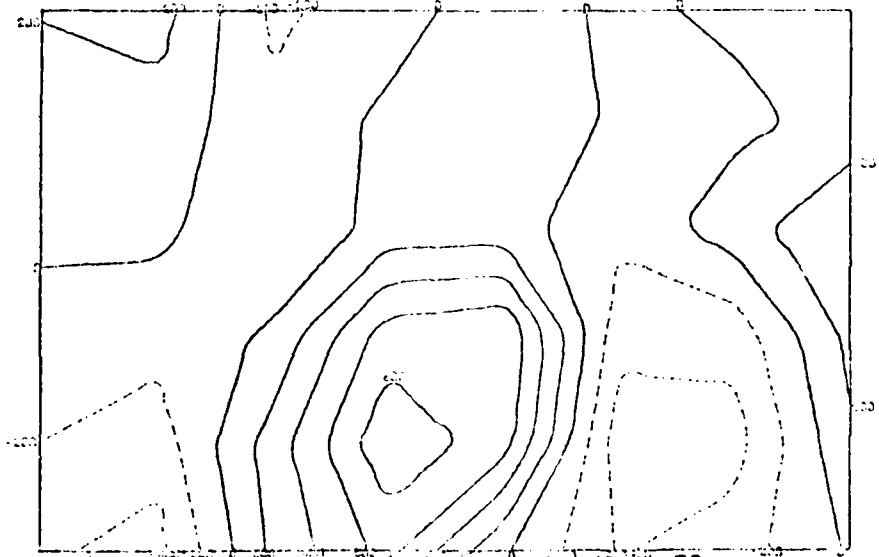
DIVERGENCE

TIME: 1605



DIVERGENCE

TIME: 1610

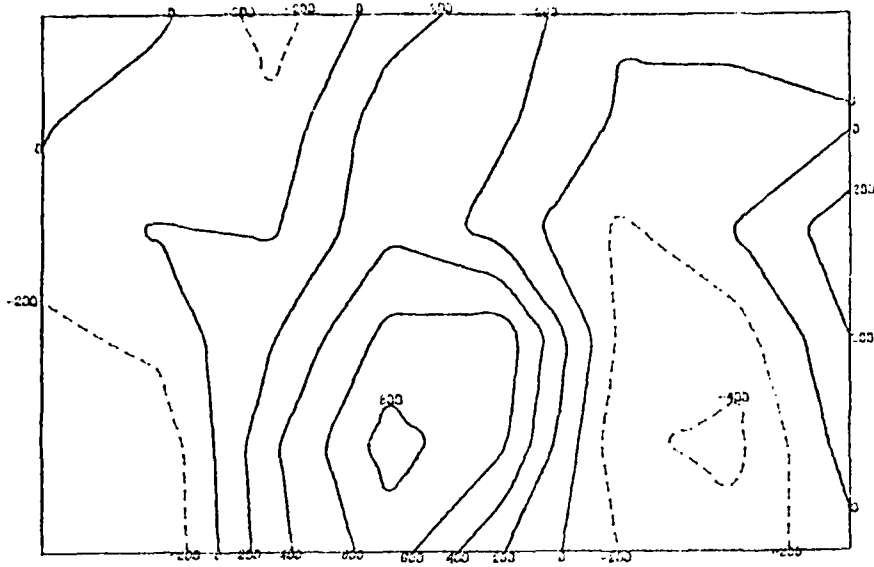


F A C E 7 5 .

D A T E . . . 8 1 0 3

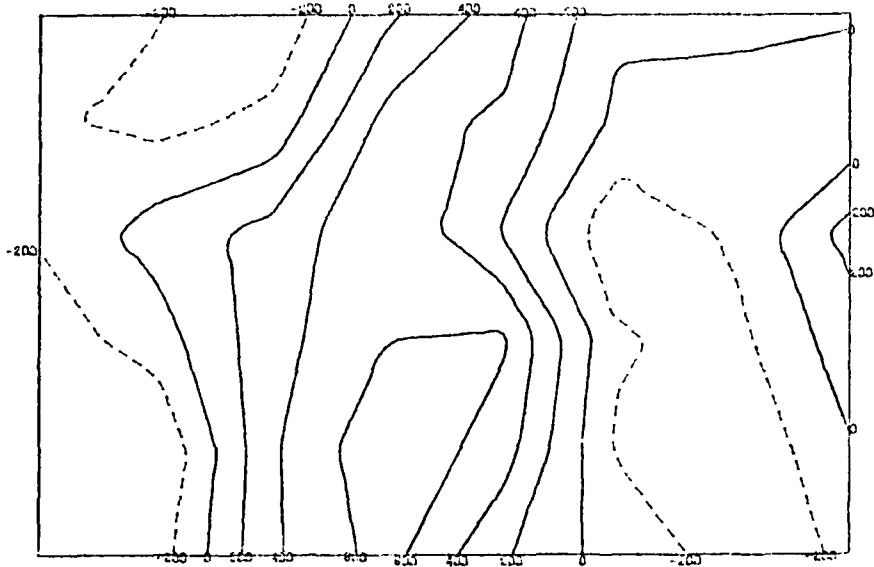
D I V E R G E N C E

T I M E . . . 1 6 1 5



D I V E R G E N C E

T I M E . . . 1 6 2 0



D I V E R G E N C E

T I M E . . . 1 6 2 5

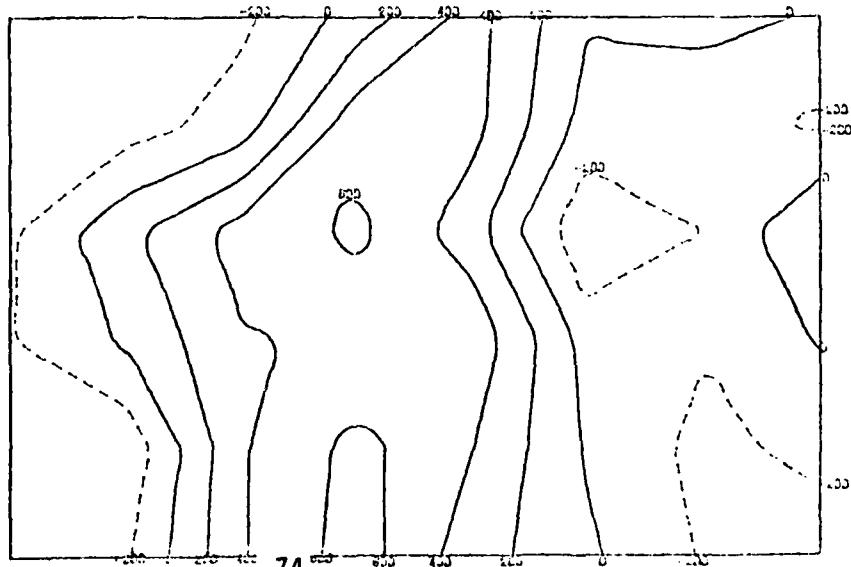
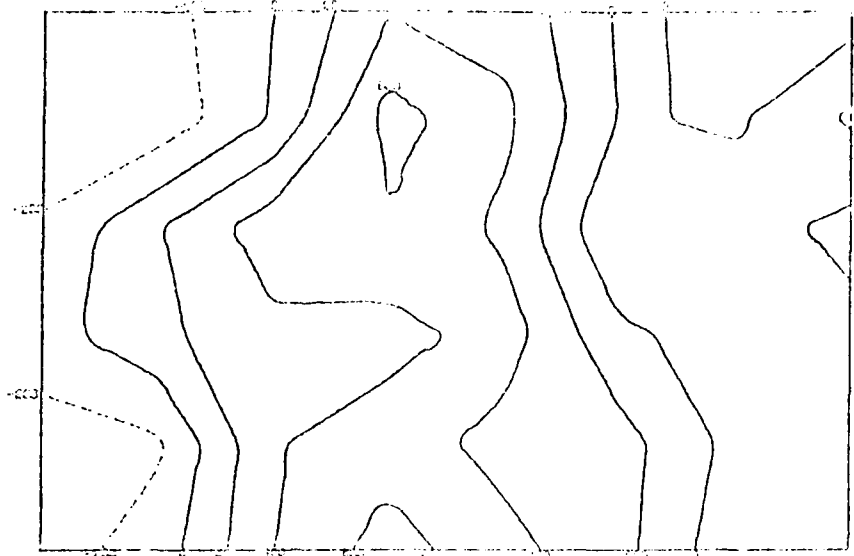


FIG. 5.1.4

DATE: 1963

DIVERGENCE

TIME: 1600



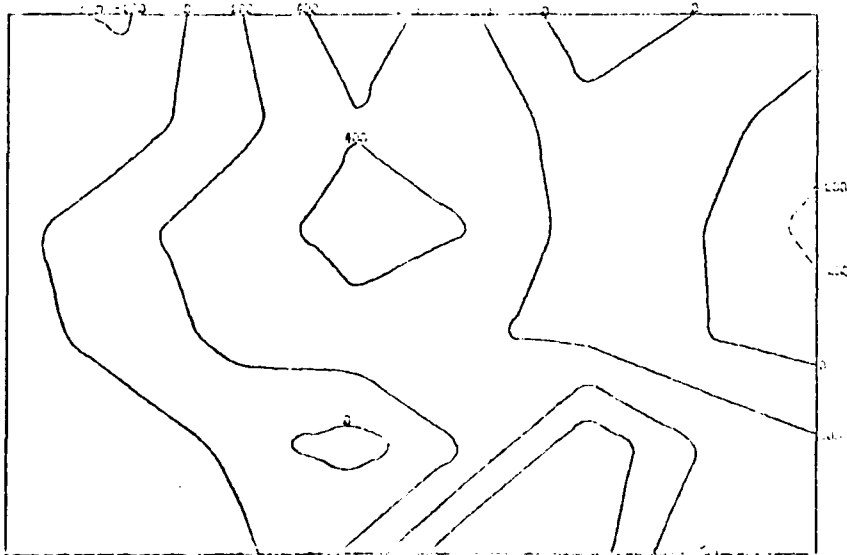
DIVERGENCE

TIME: 1600



DIVERGENCE

TIME: 1600

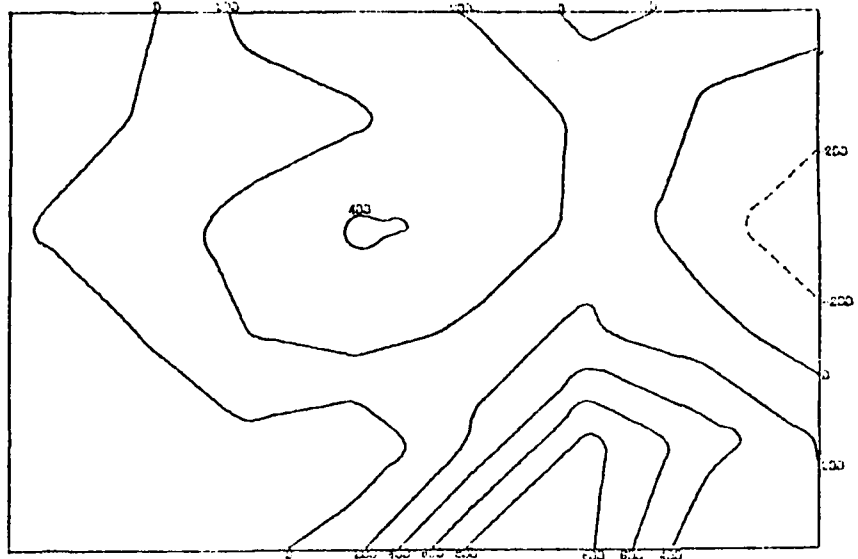


F R C E 7 S.

DATE... 0185

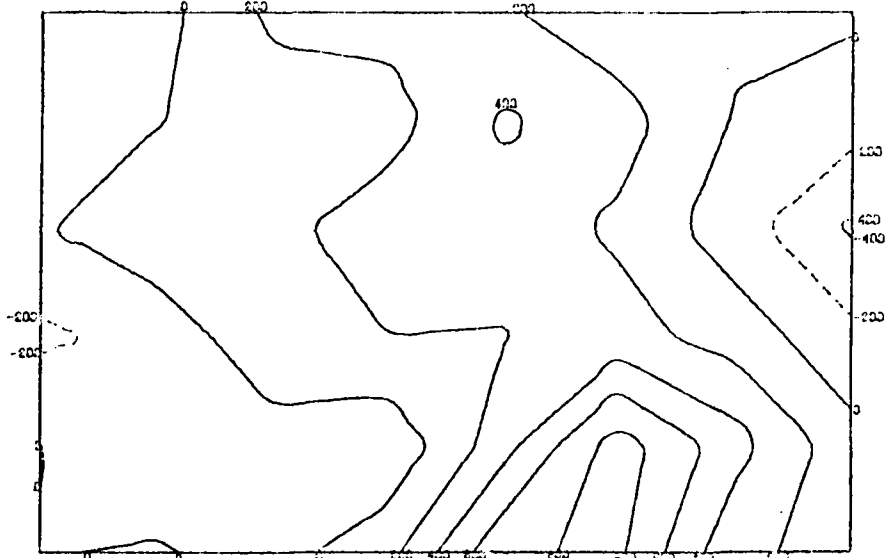
DIVERGENCE

TIME... 1645



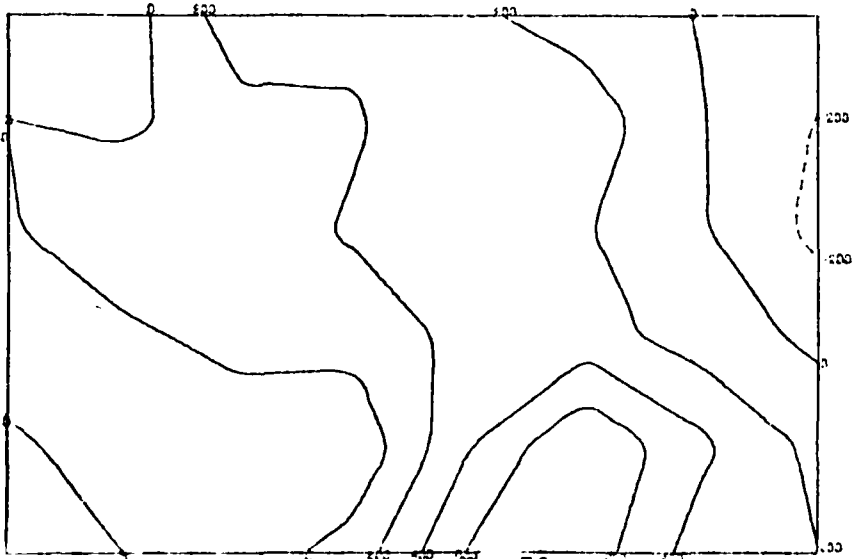
DIVERGENCE

TIME... 1650



DIVERGENCE

TIME... 1655



convergence zone. By 1445 EDT, the northern cell is precipitating. Outflow from this cell coupled with the dissipating cell in the southwest corner reorientates the confluence zone in a more north-south configuration. Divergence has pushed northward from the southwest corner. Strong convergence accompanies the inflow pattern in the north-central part of the network. Radar shows that the southwest cell is all but dissipated while the cell near the western border is spreading eastward along the old east-west confluence zone.

By 1450 EDT, the northernmost cell has the dominant outdraft. At 1500 EDT, a second outflow becomes visible near the northwest corner of the grid. By 1510 EDT, the outdraft near the northwest corner becomes the major cell. Many of the outdrafts in the western half of the network feed the north-south convergence zone in the eastern third of the region. The north-south convergence zone is at its maximum at this time. At 1540 EDT, a north-south line of echoes appears just west of the convergence zone. The outflow from this new line of showers appears to push the convergence zone to the east where, at 1610 EDT, a new line of echoes forms in the southeast corner. After 1630 EDT, the two complexes combine and begin to dissipate with mainly divergence occurring over the entire mesonet network.

When the radar pattern is compared with the streamline/isotach pattern, it becomes apparent that the 6.4-km grid gives a very accurate estimation of what should be occurring in the mesoscale, beneath the given echoes. Comparison now turns toward the 12.9 and 19.3-km grids. Figs. 9 and 10 show a 1-hour comparison, in 5-minute increments, of the three grids beginning at 1430 EDT for 16 August 1975. Fig. 9 is the streamline/isotach pattern; Fig. 10 presents the divergence patterns. The top panel is the 6.4-km grid, the middle panel is

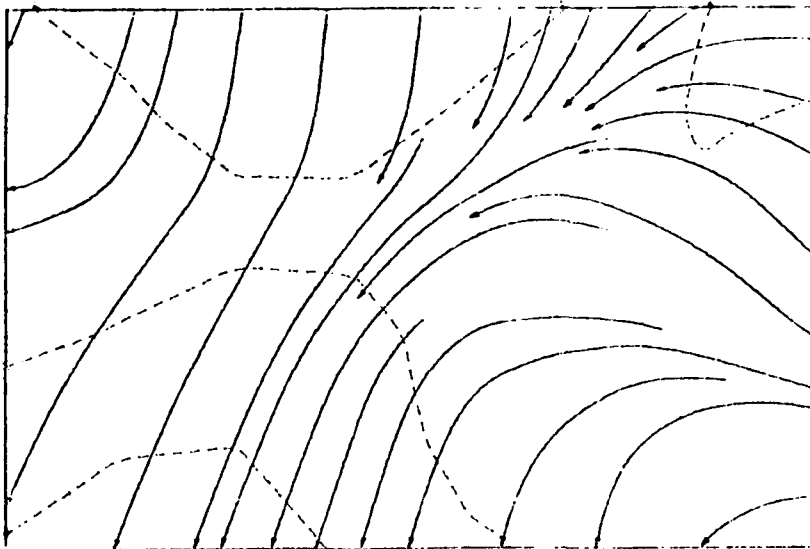
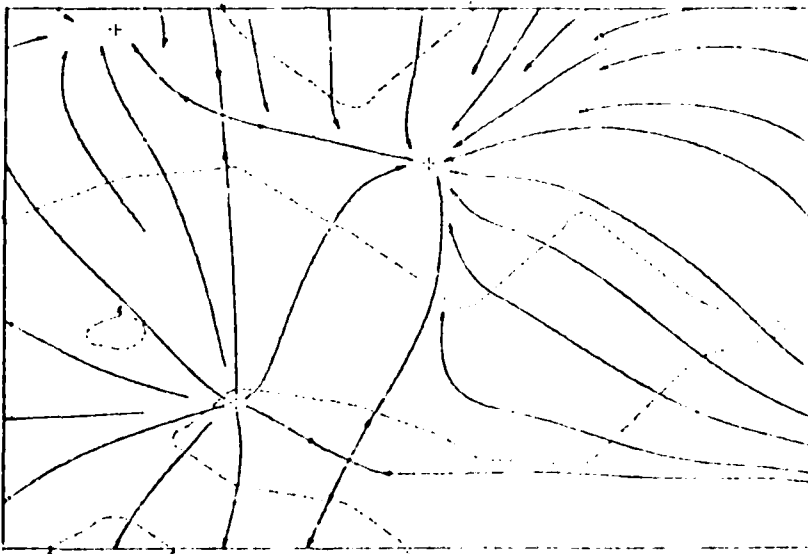
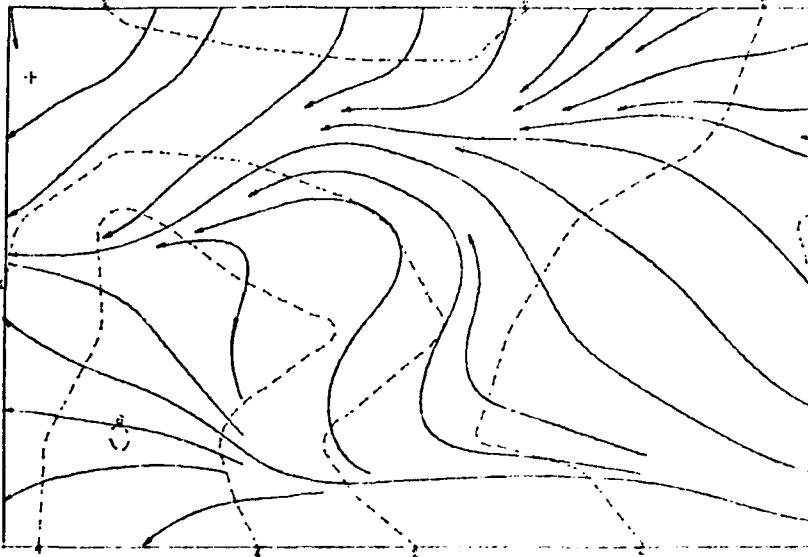
*Figure 9. Streamline and isotach patterns on 16 August 1975 for each 5 minute period between 1430 and 1530 EDT. For each time period, the top panel refers to the 6.4 km station grid, the middle panel corresponds to a 12.9 km site separation, while the bottom panel refers to the 19.3 km station grid.*

FACE 75

DATE 1965

STREAMLINES

TIME 1400



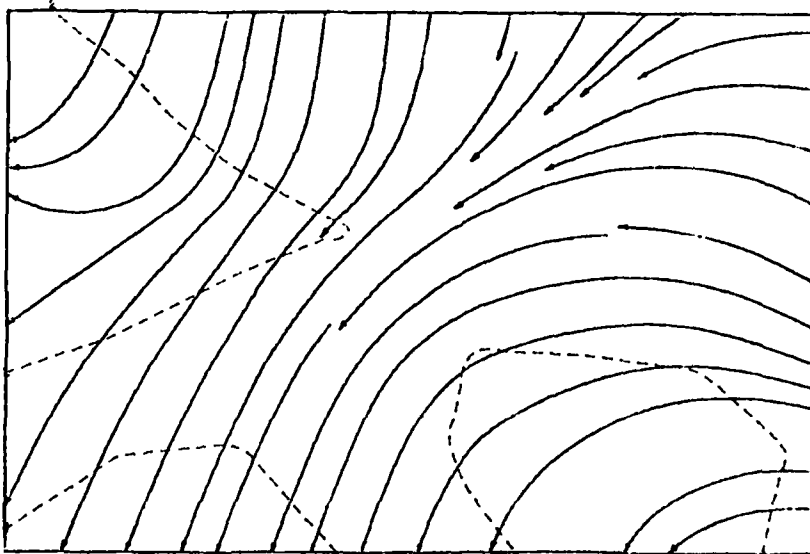
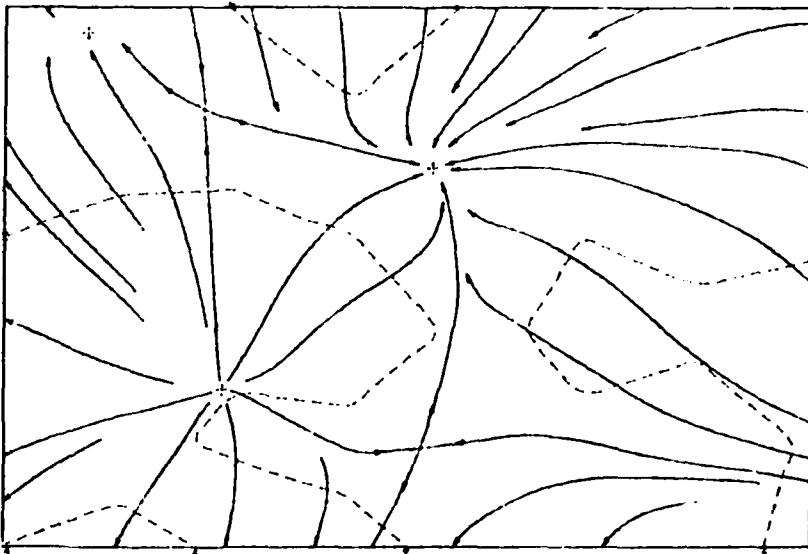
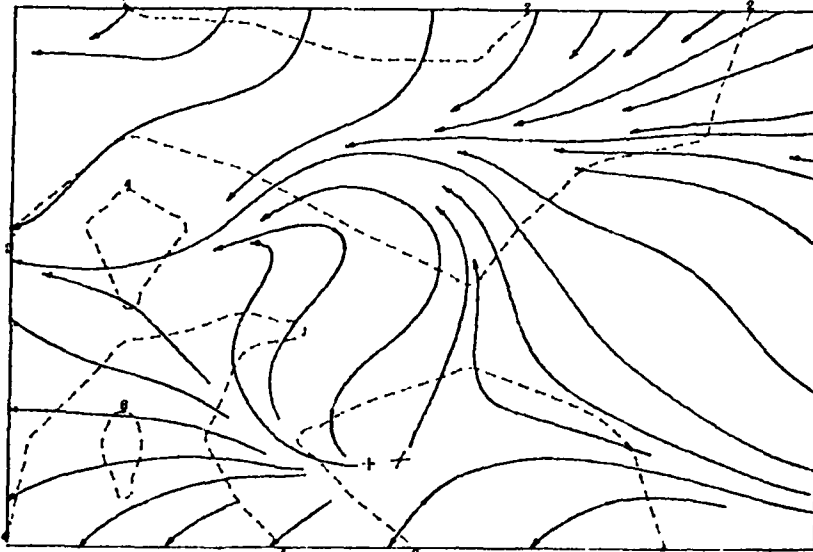
FACE 75.

STREAMLINES

LEVEL... SURFACE

DATE... 0165

TIME... 1405



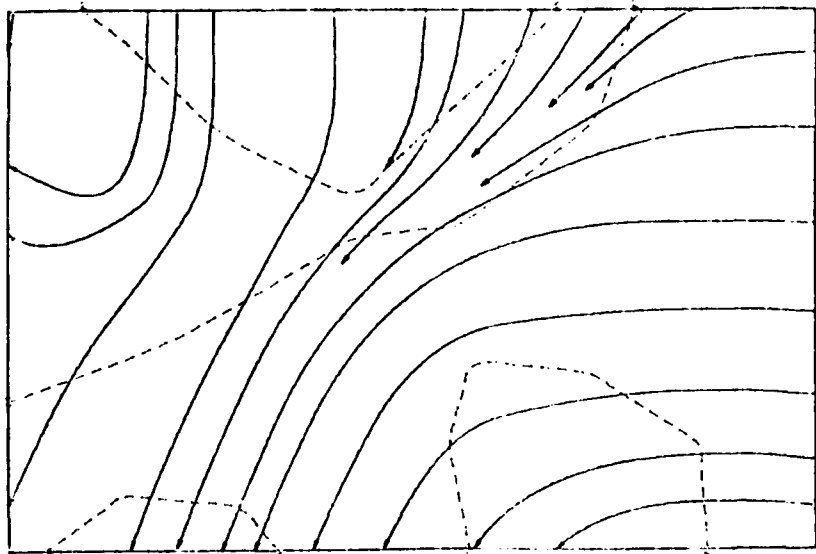
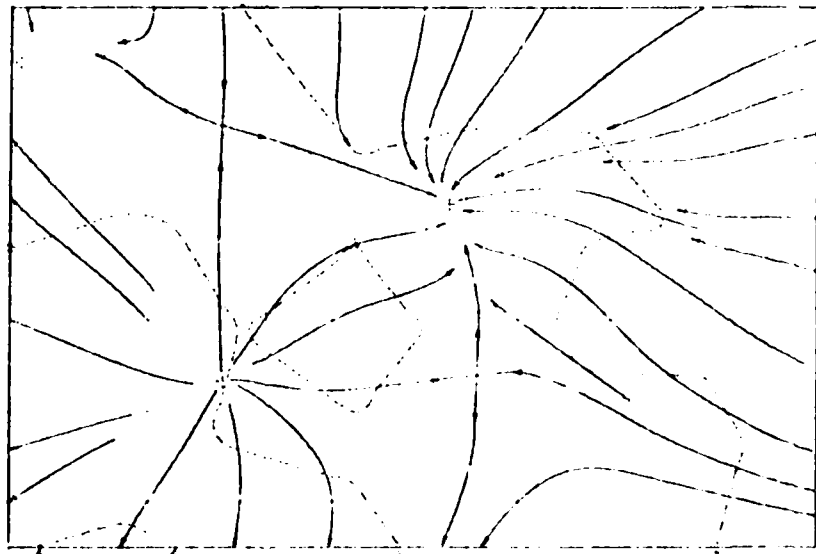
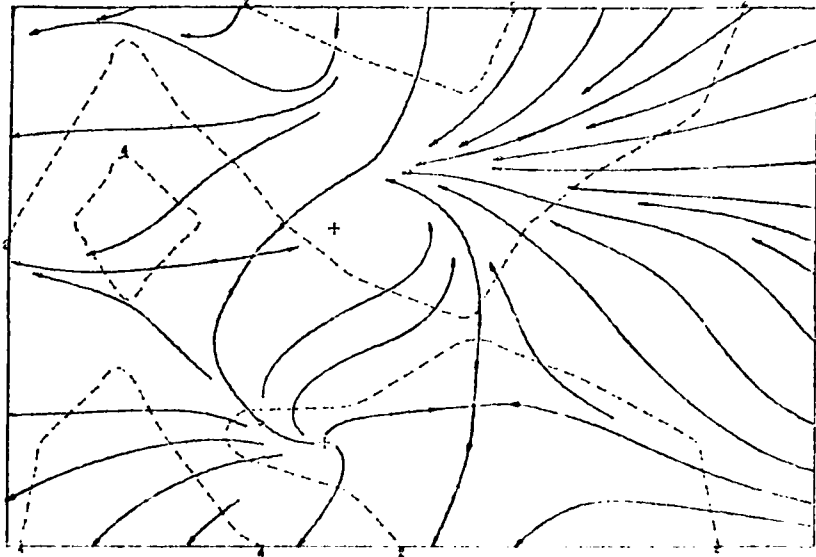
LEVEL... SURFACE

F A C E 7 5.

DATE... 0165

STREAMLINES

TIME... 1440



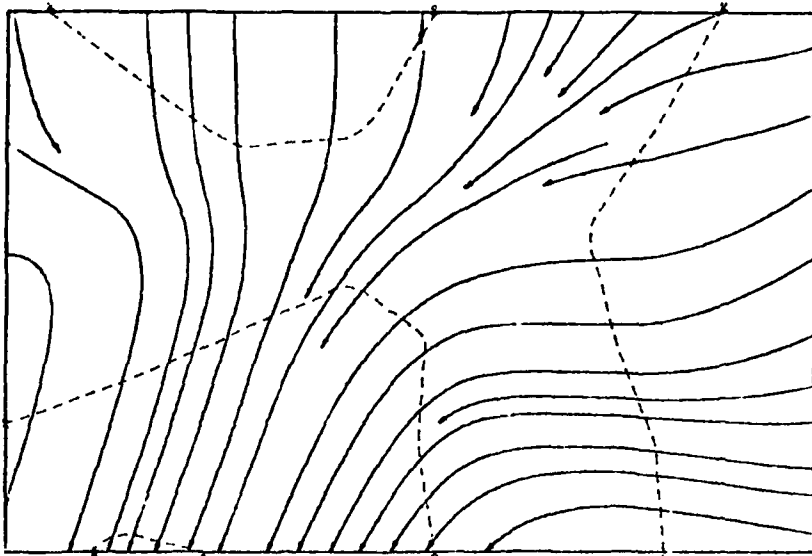
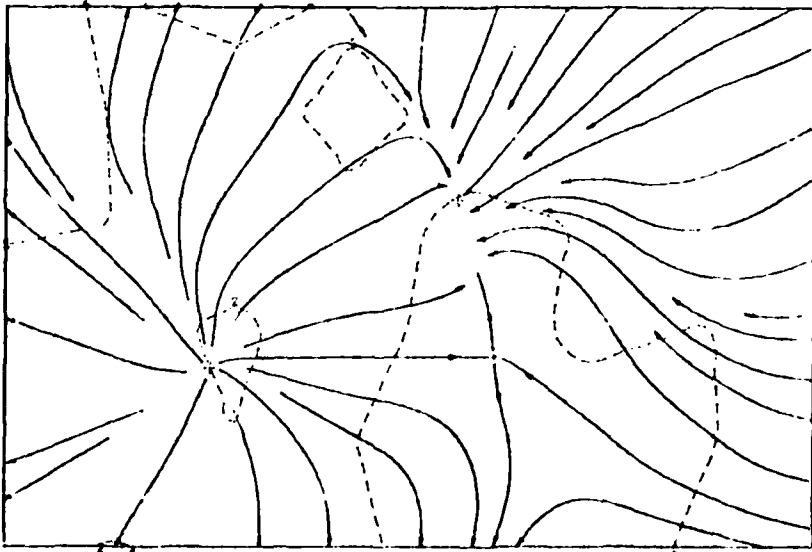
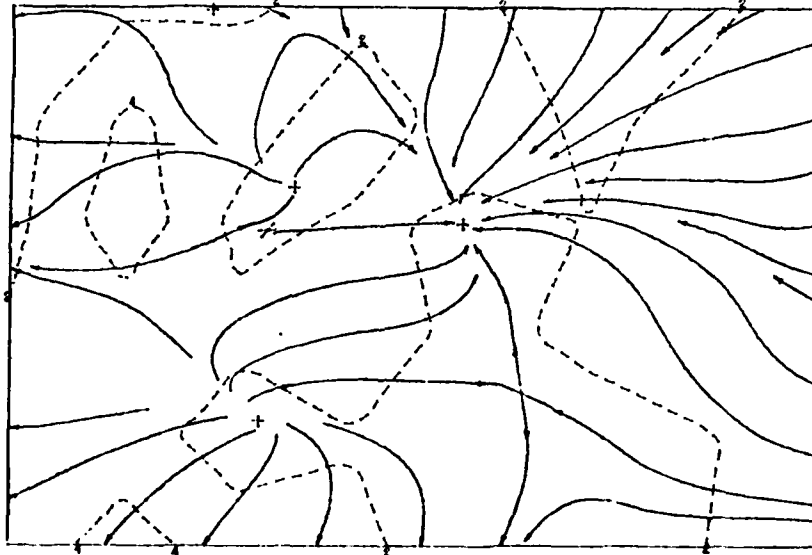
F A C E 7 5.

STREAMLINES

LEVEL... SURFACE

DATE... 0165

TIME... 1445



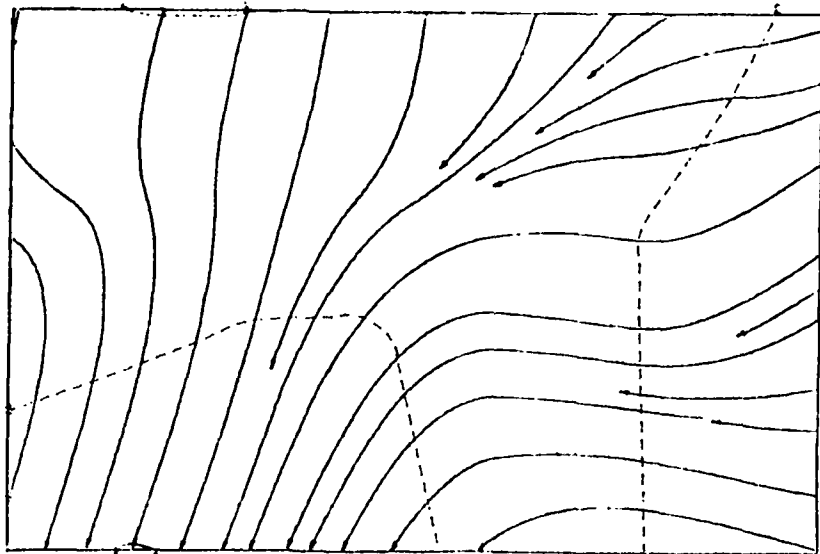
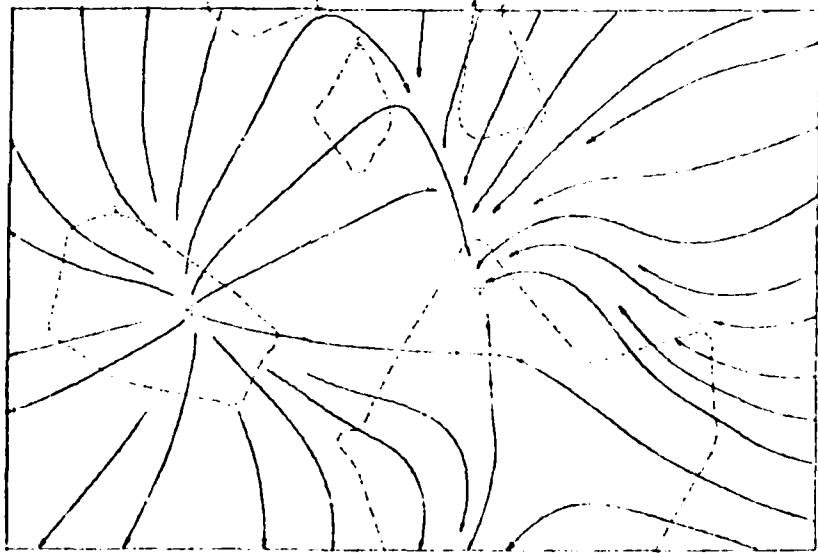
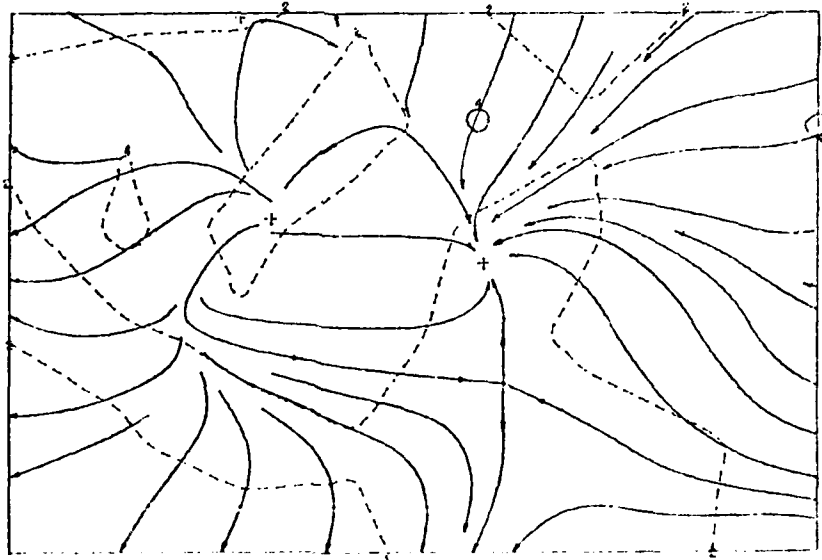
F A C E 7 5.

STREAMLINES

LEVEL... SURFACE

DATE... 6105

TIME... 1430



LEVEL... SURFACE

F A C E 7 5.

DATE... 0365

STREAMLINES

TIME... 1455

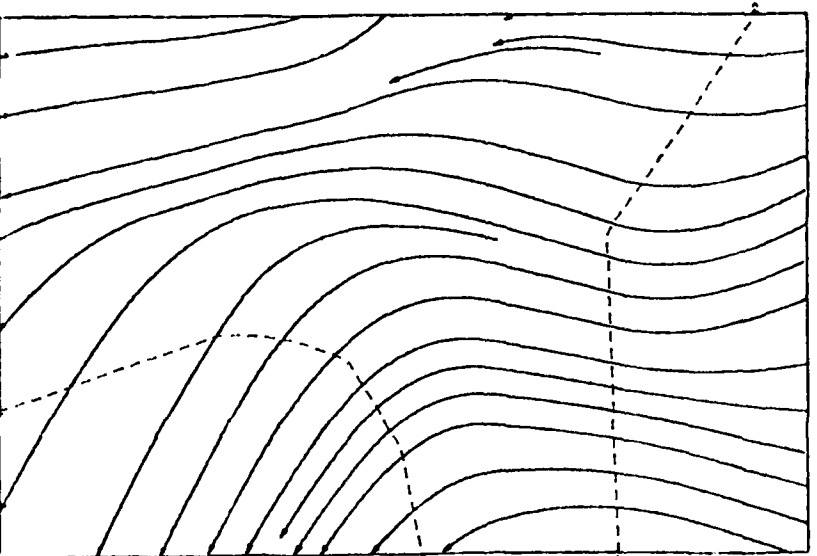
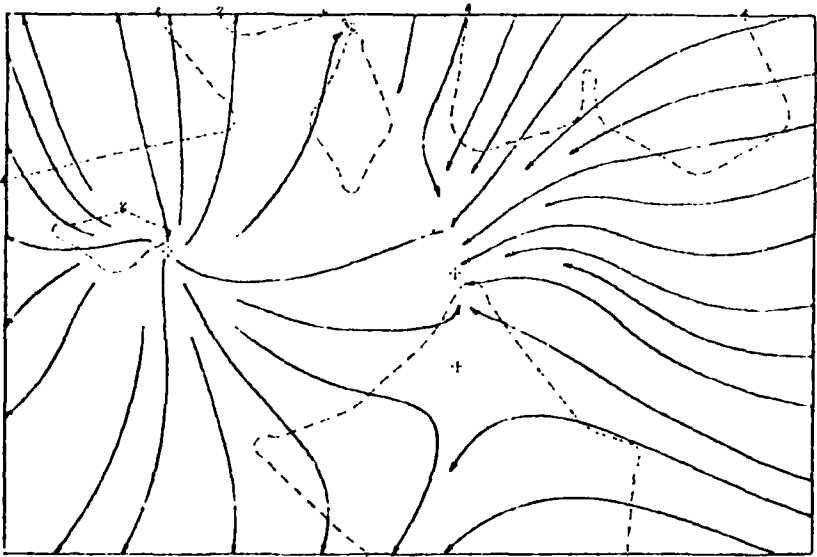
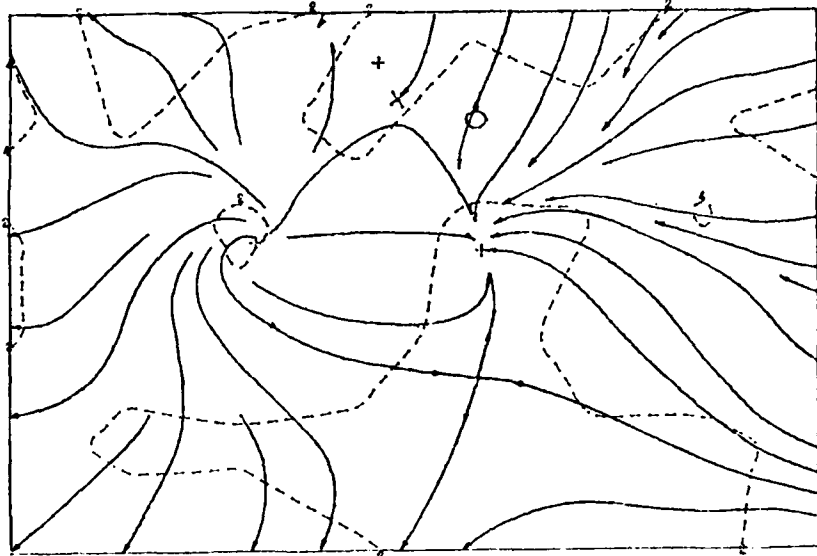
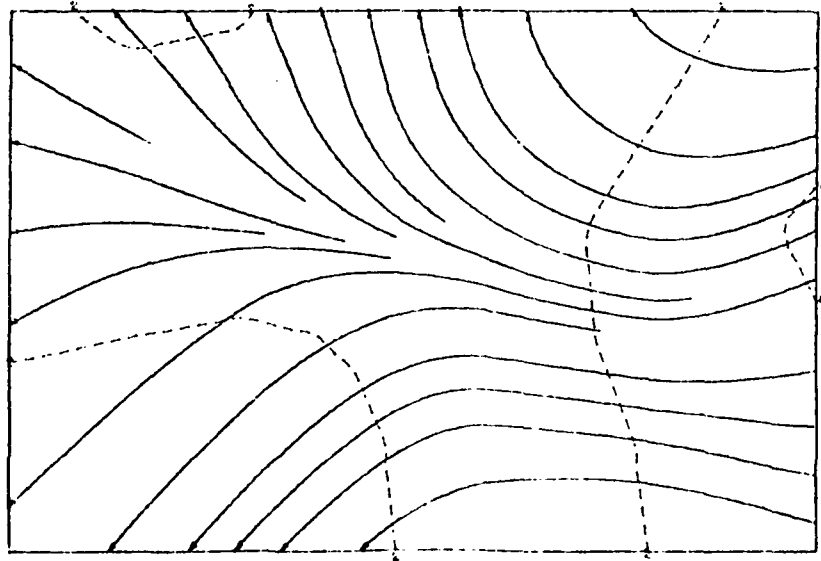
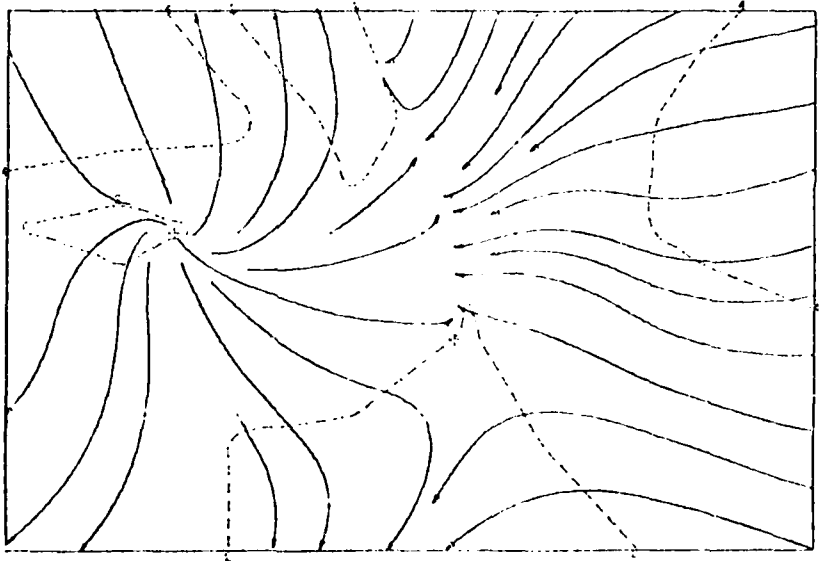
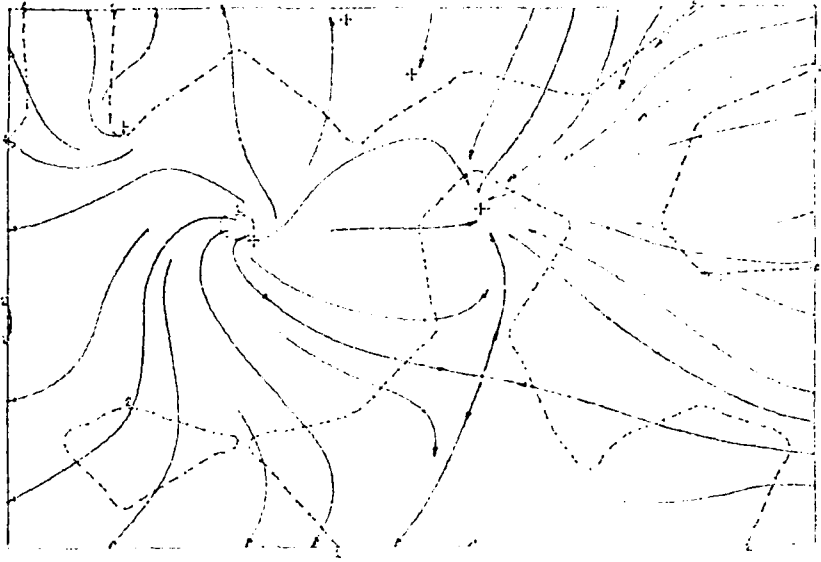


FIGURE 1  
STREPLINES

DATE: 1950  
INSTRUMENT



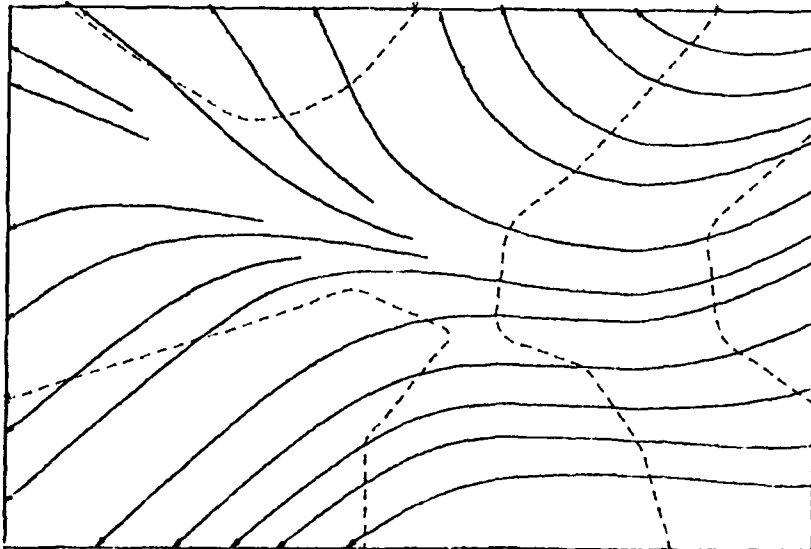
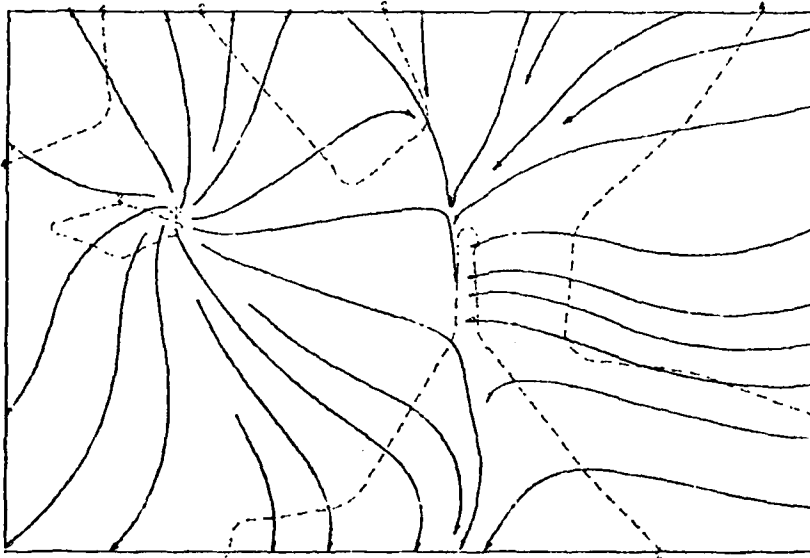
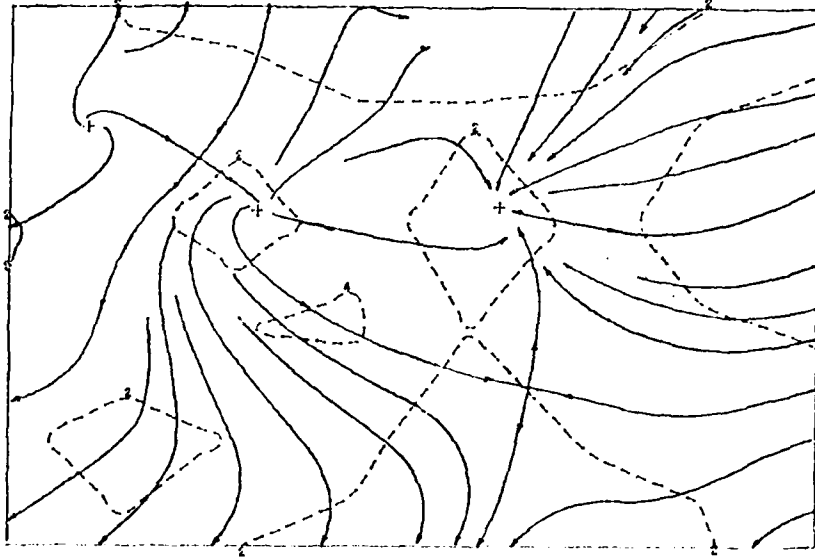
F A C E 7 5.

STREAM LINES

LEVEL.. SURFACE

DATE.. 0165

TIME.. 1505



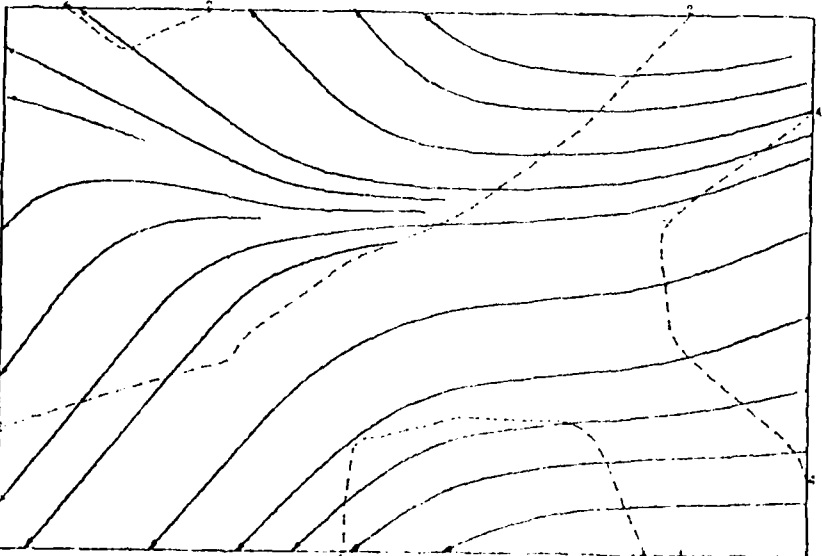
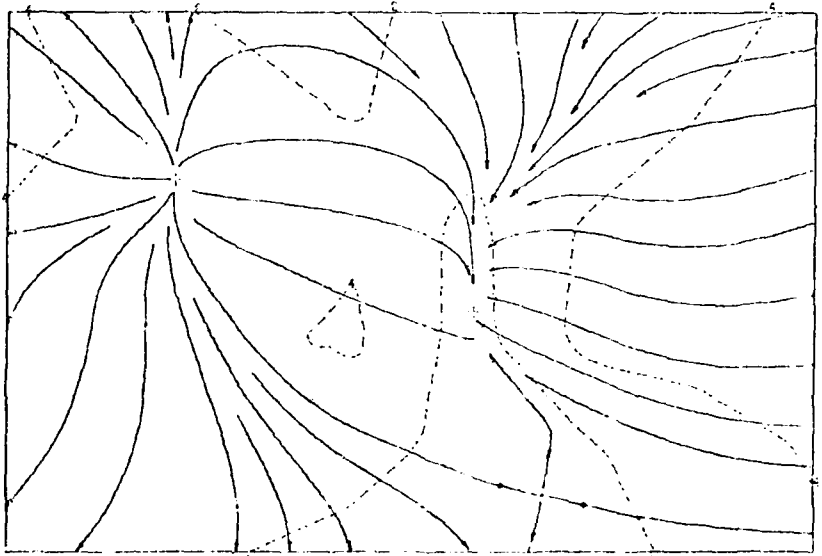
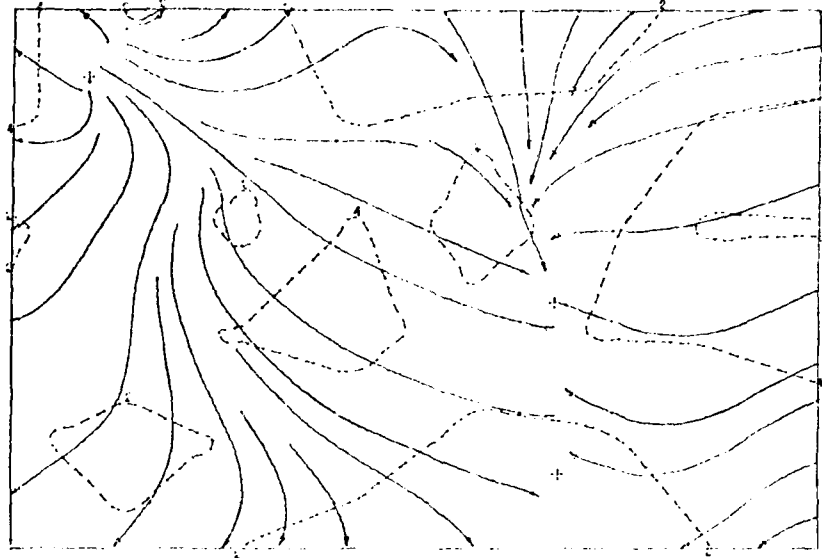
F R O E Y S.

STREAMELINES

0-100 0-100

STREAMLINES

TIME 1910



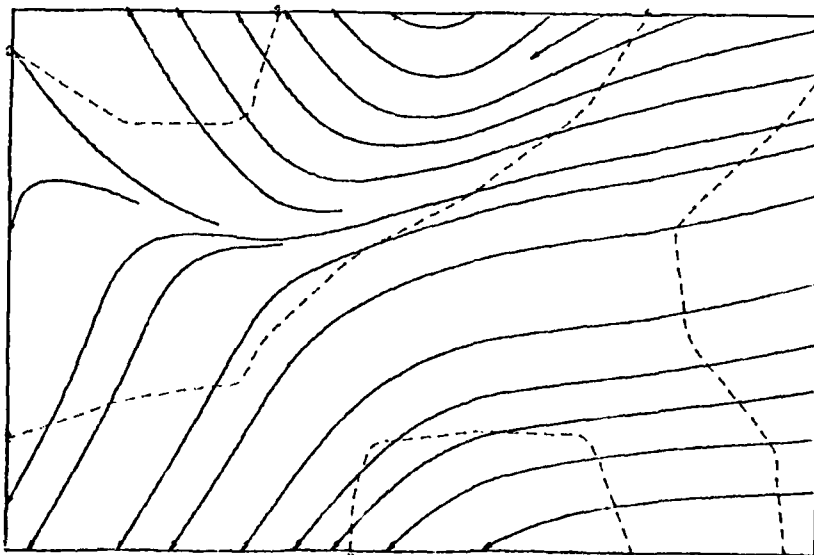
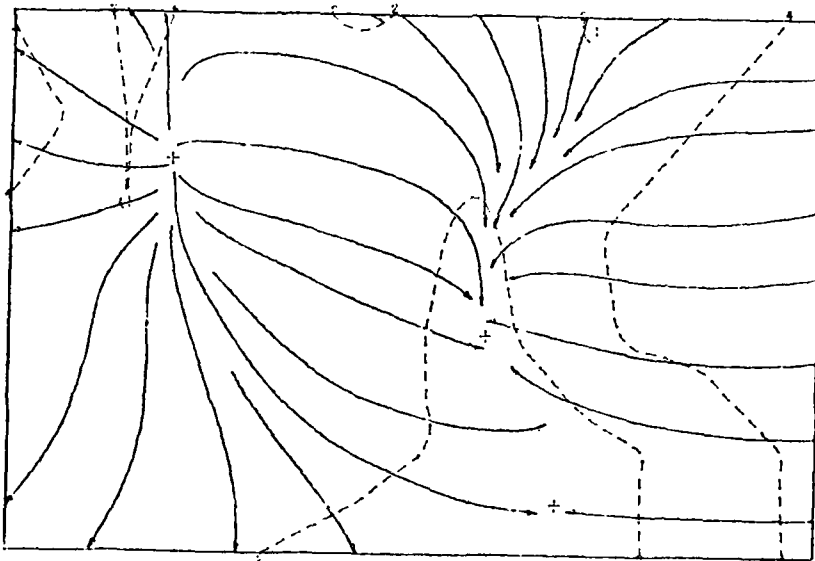
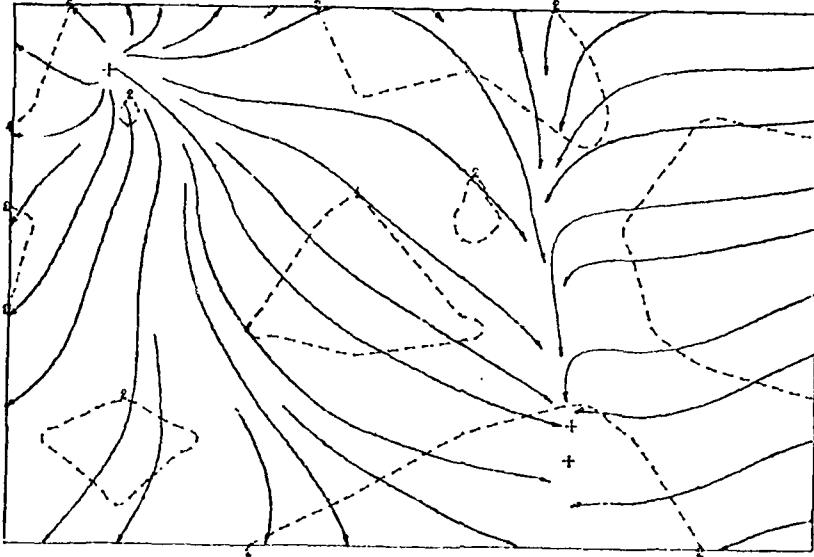
FACE 75.

STREAMLINES

LEVEL... SURFACE

DATE... 0165

TIME... 1515



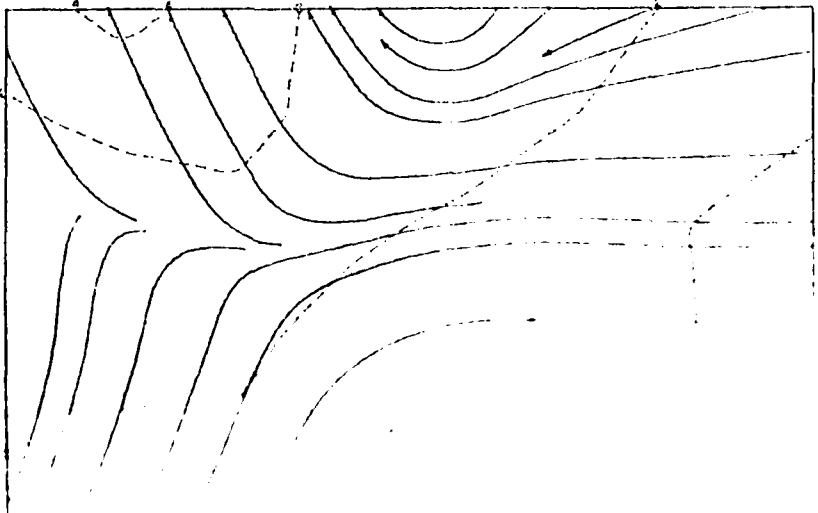
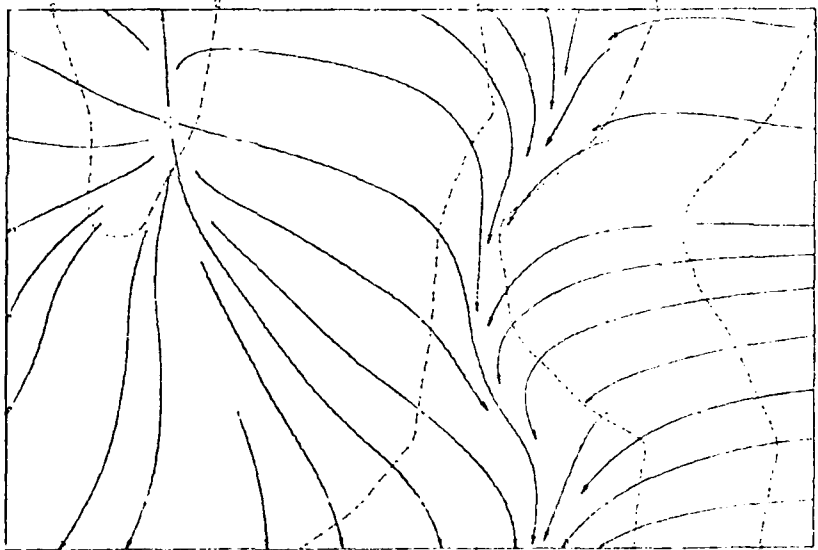
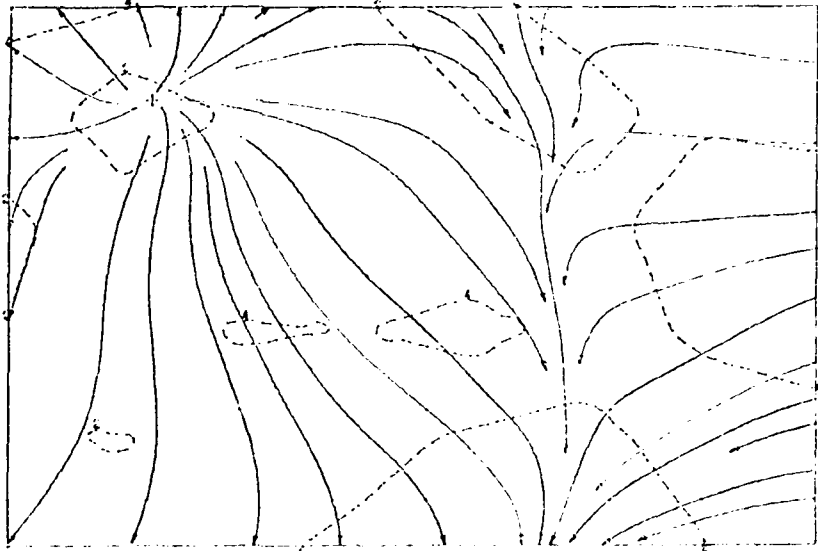
IN ALL... 1920

FACE 75.

DR. E. L. 5165

STREAMLINES

TIME... 1920



Handwritten notes on the left margin, possibly indicating a scale or reference.

AD-A097 553

ILLINOIS STATE WATER SURVEY URBANA

F/G 4/2

LOW-LEVEL CONVERGENCE AND THE PREDICTION OF CONVECTIVE PRECIPIT--ETC(U)

FEB 81 A I WATSON; R L HOLLE; J B CUNNING

NSF-ATM78-08865

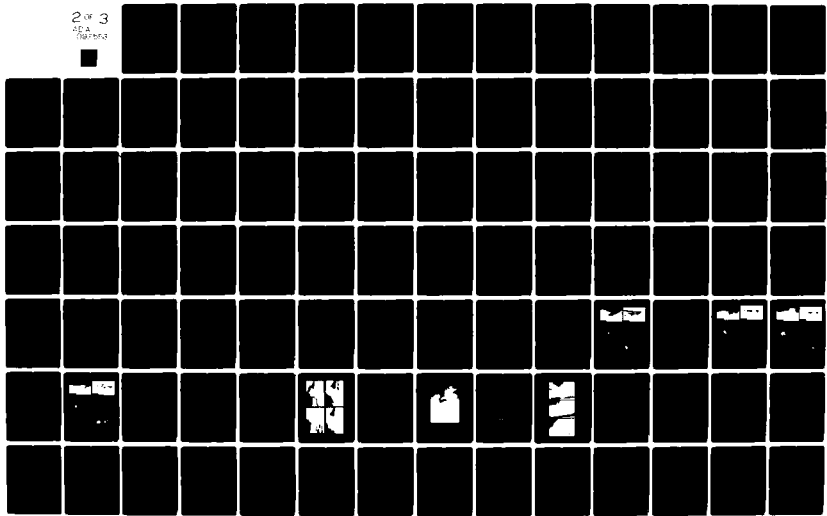
UNCLASSIFIED

TR-4

ARO-15529.6-65

NL

2 of 3  
of a  
frames



LEVEL... SURFACE

F A C E 7 5.

DATE... 0165

STREAMLINES

TIME... 1525

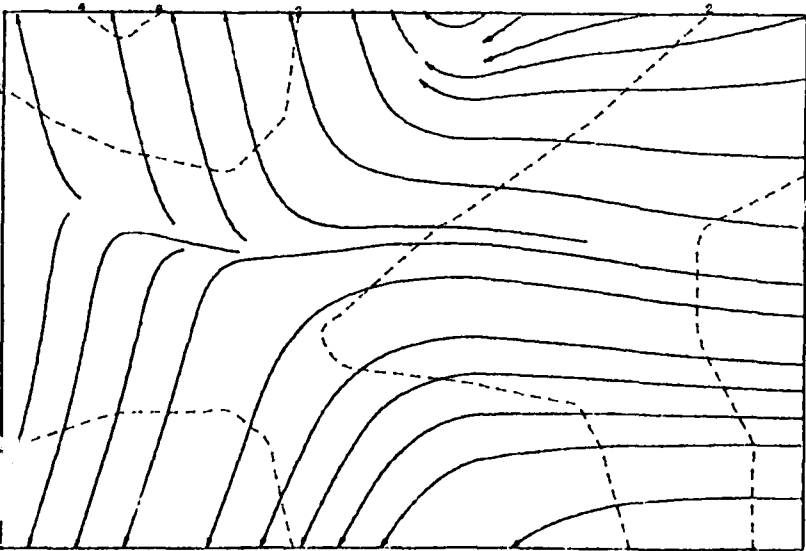
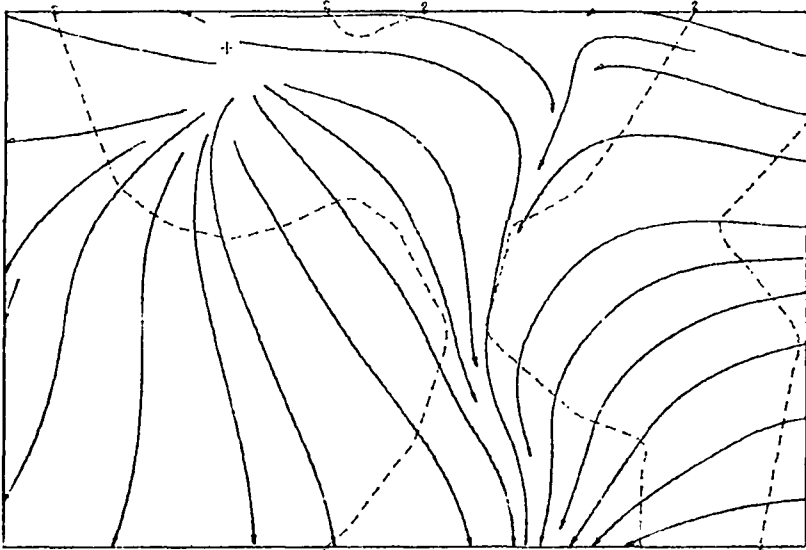
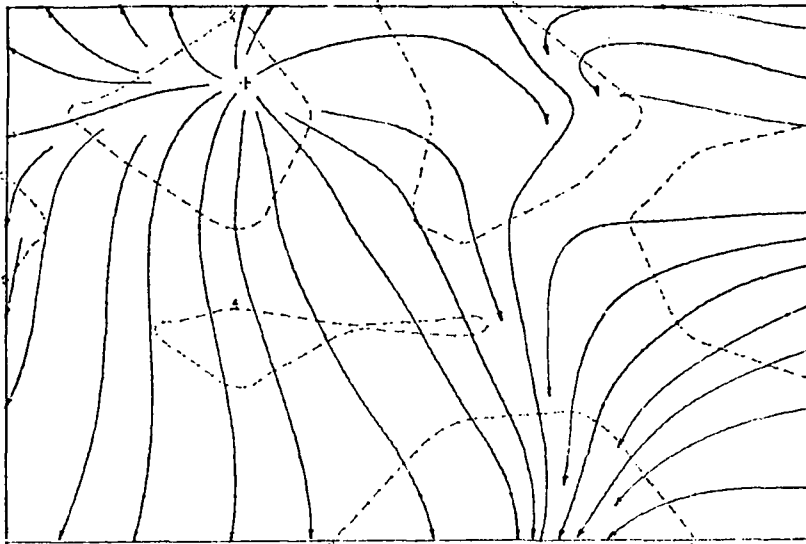
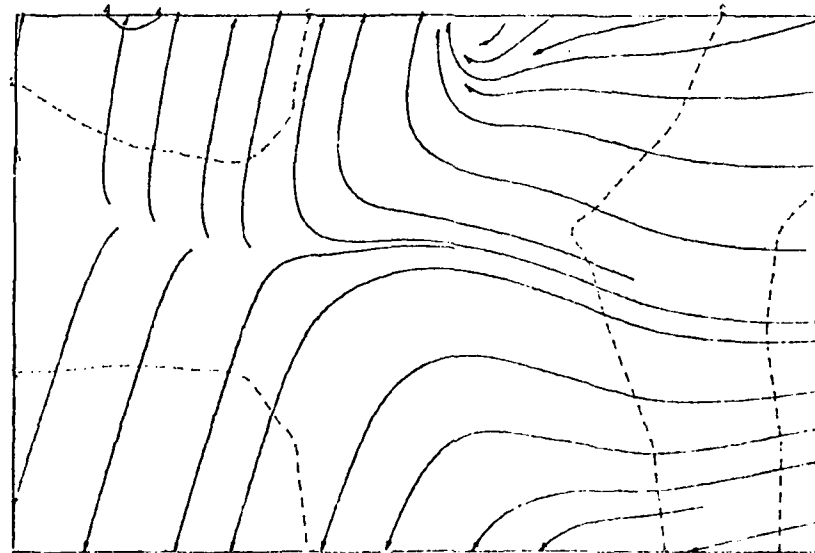
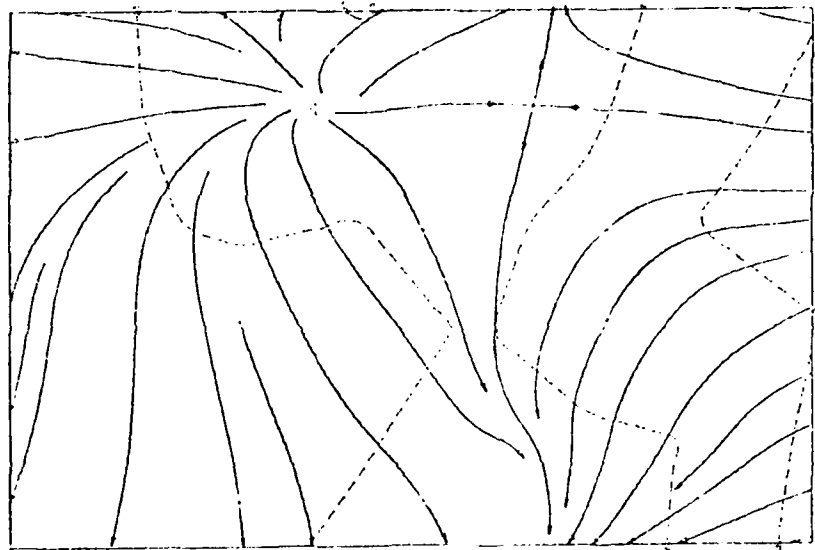
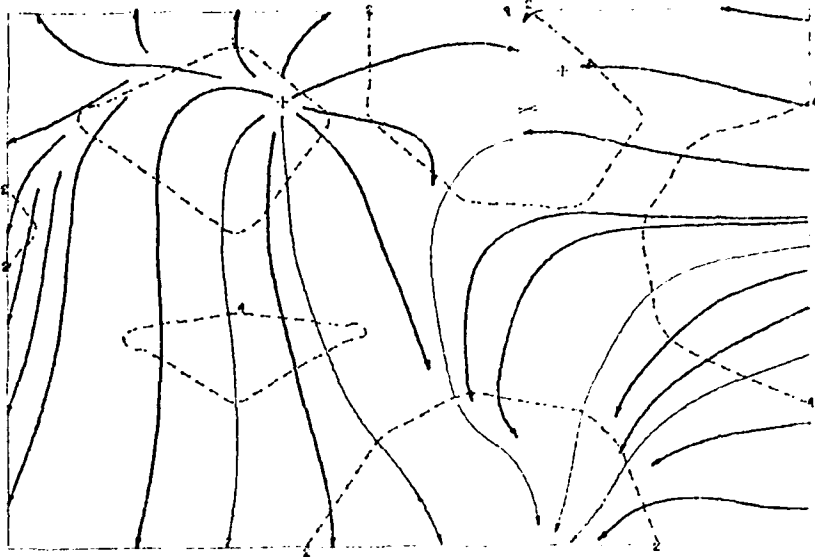


PLATE 79

CONTOUR LINES



*Figure 10. Divergence patterns for 16 August 1975 for each 5 minute period between 1430 and 1530 EDT. For each time period, the top panel refers to the 6.4 km station grid, the middle panel corresponds to a 12.9 km site separation, while the bottom panel refers to the 19.3 km station grid.*

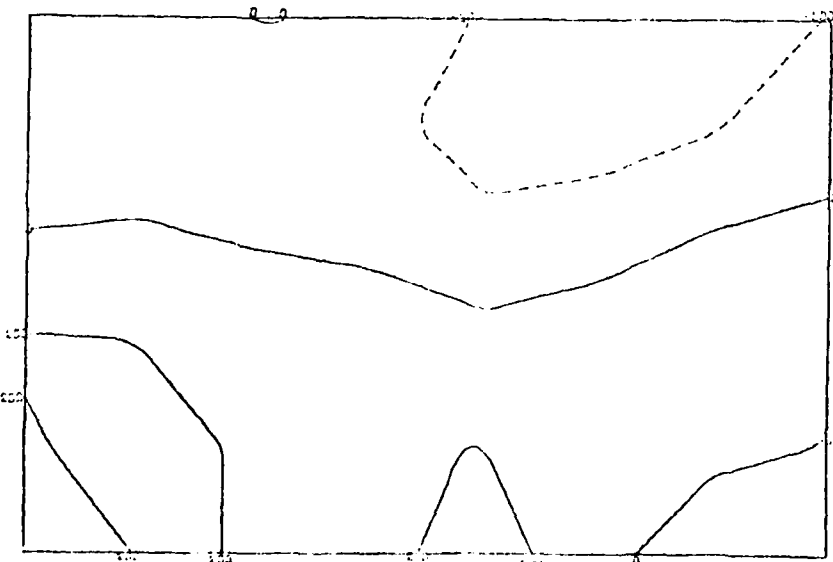
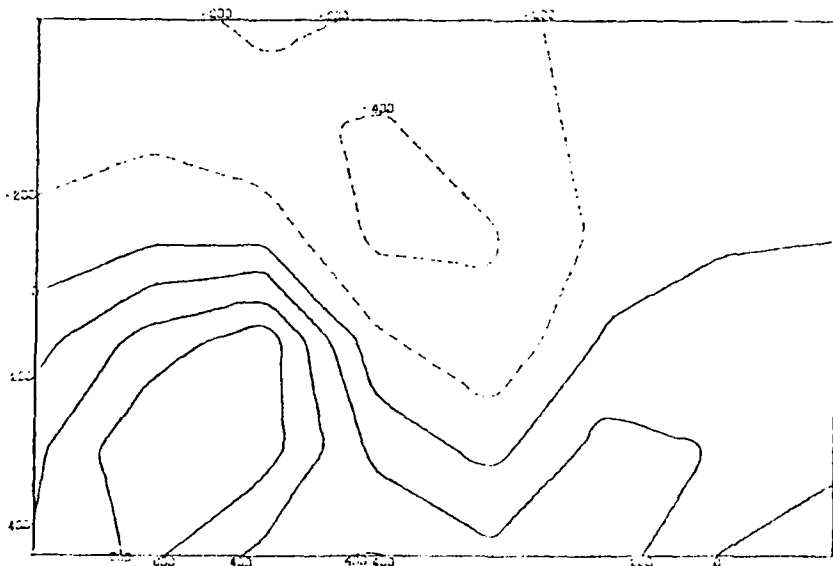
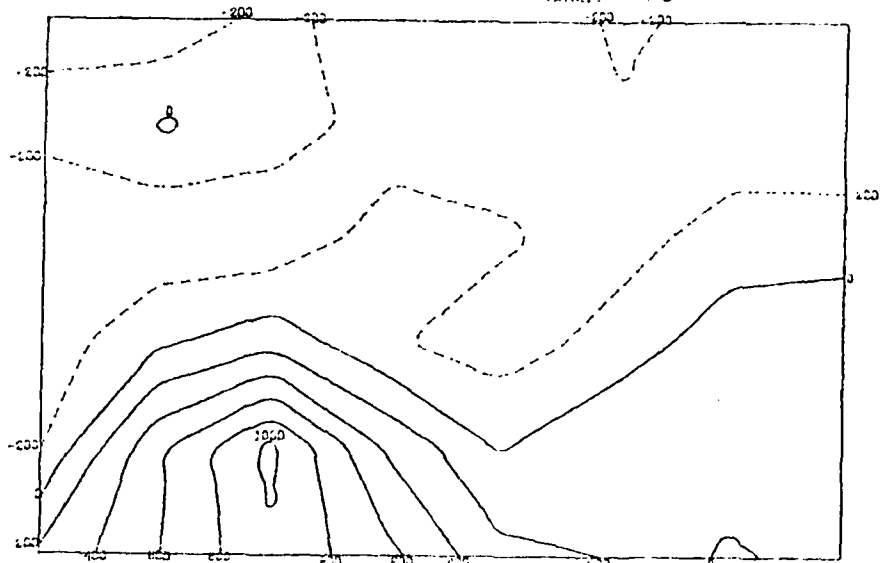
F A C E 7 5 .

D I V E R G E N C E

LEVEL... 5056 PCE

DATE... 6165

TIME... 14:0



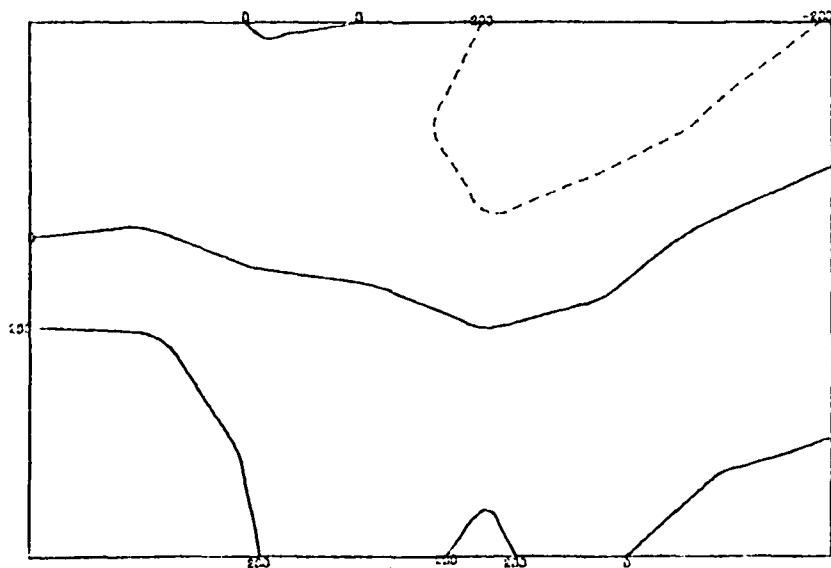
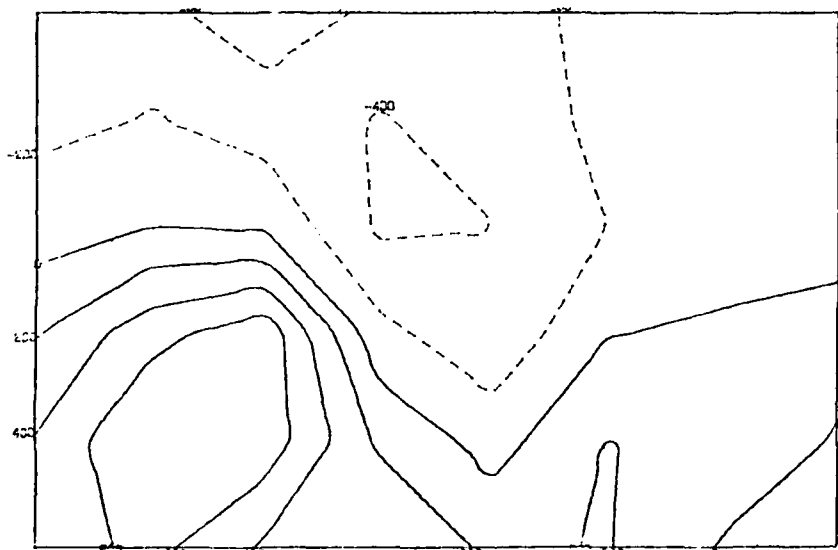
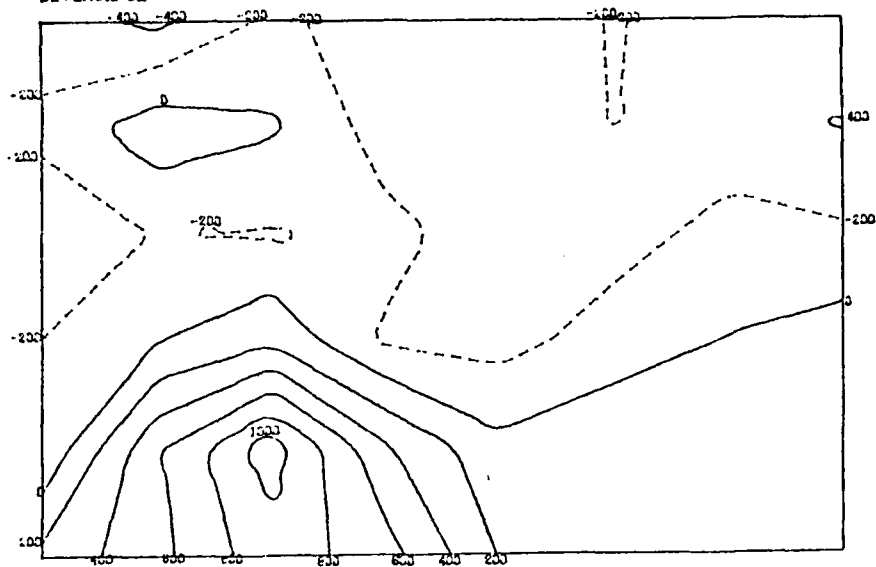
LEVEL... SURFACE

FACE 75.

DATE... 0165

DIVERGENCE

TIME... 1435

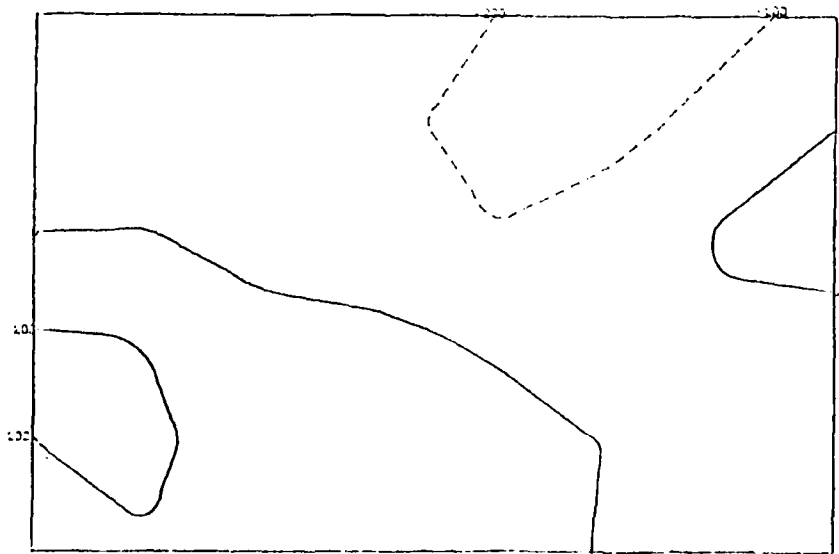
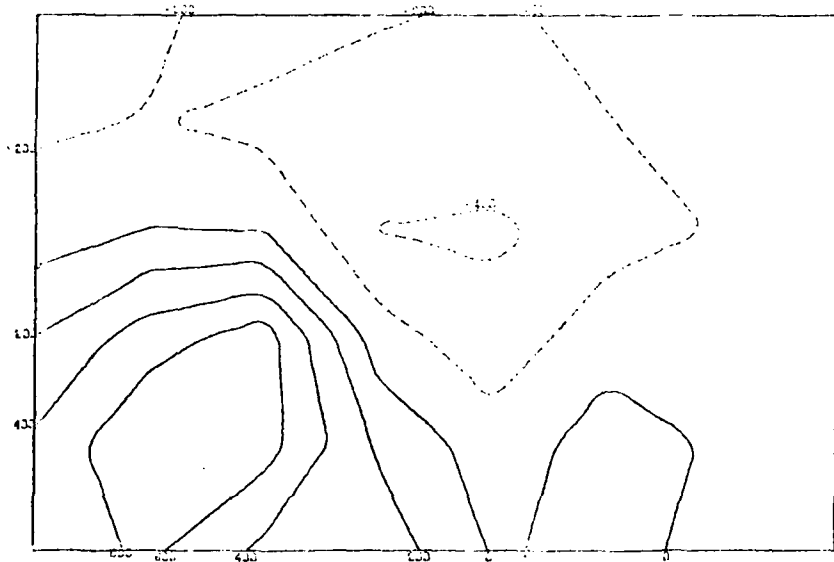
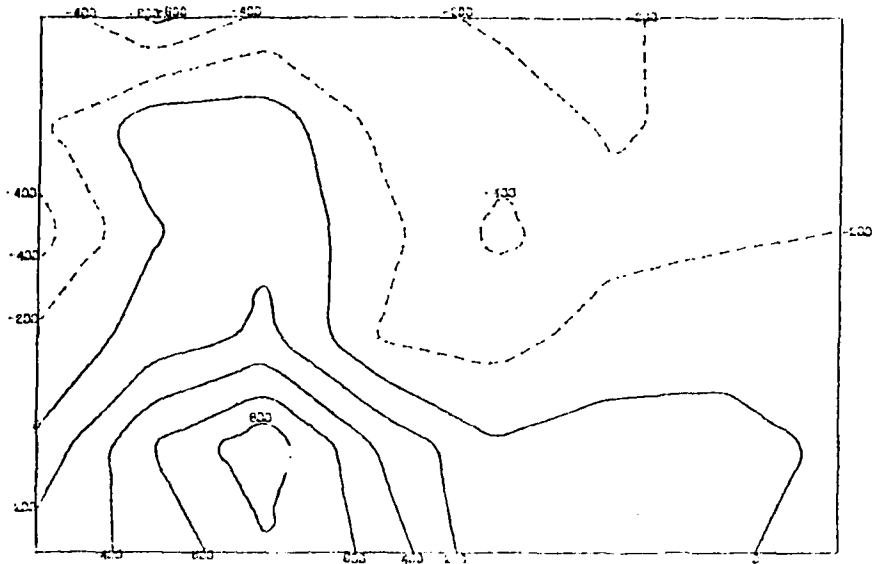


FACE 7 S.

DATE... 0160

DIVERGENCE

TIME... 1440



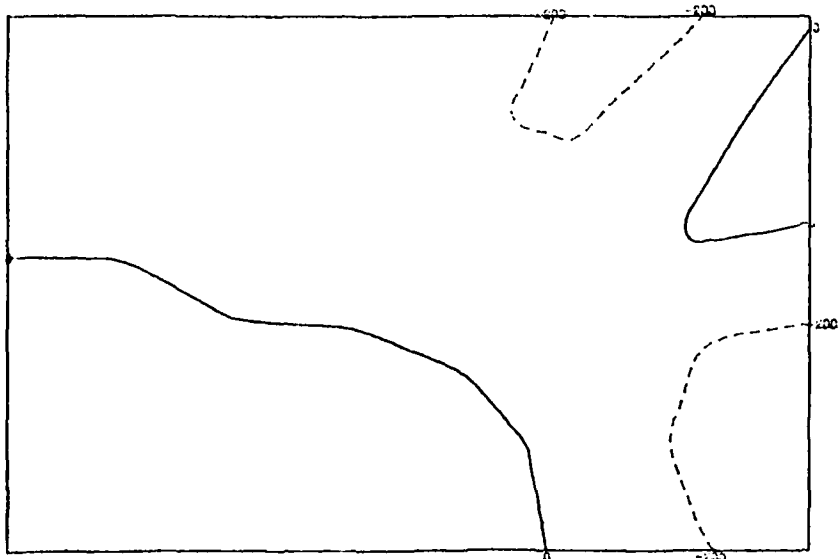
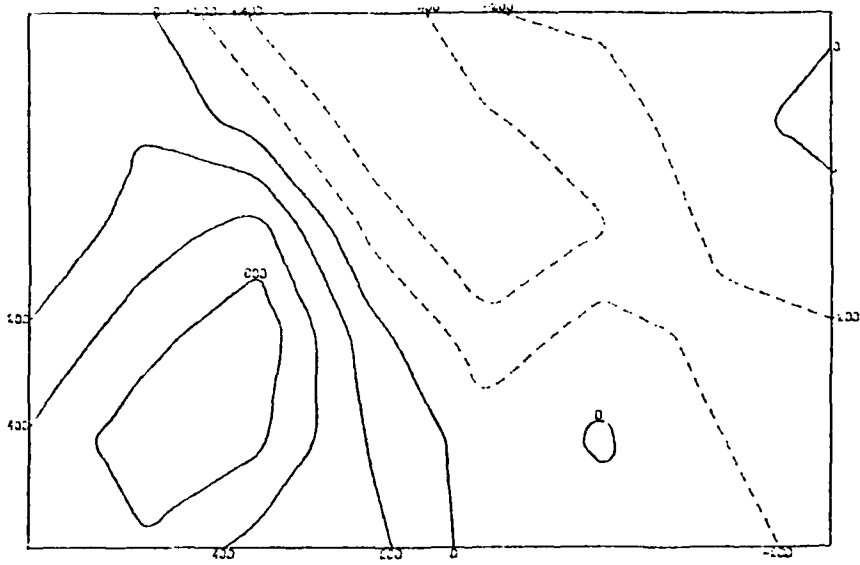
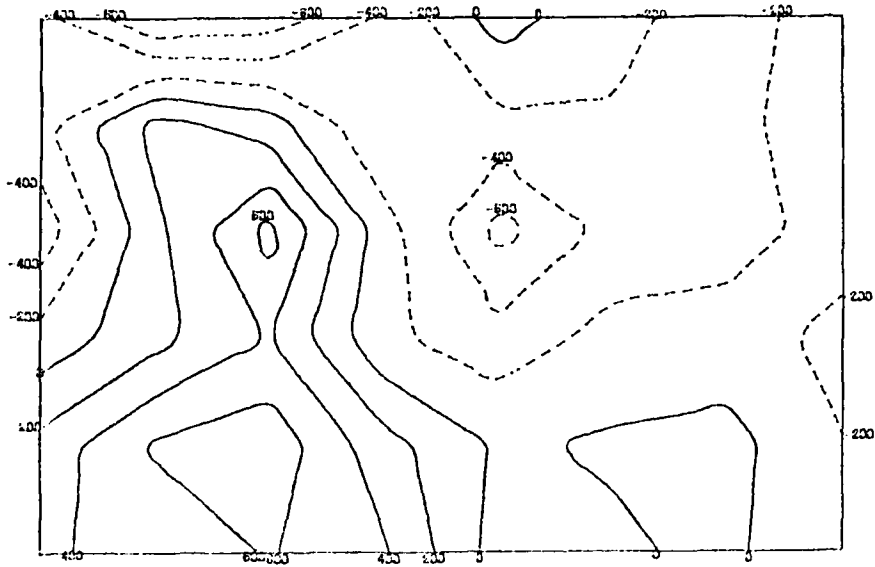
LEVEL... SURFACE

F A C E 7 5.

DATE... 0165

DIVERGENCE

TIME... 1445

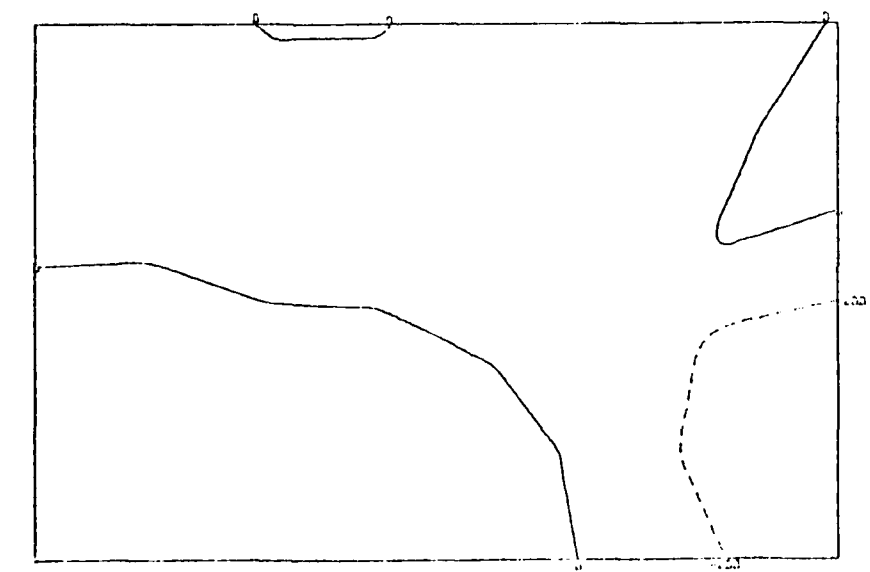
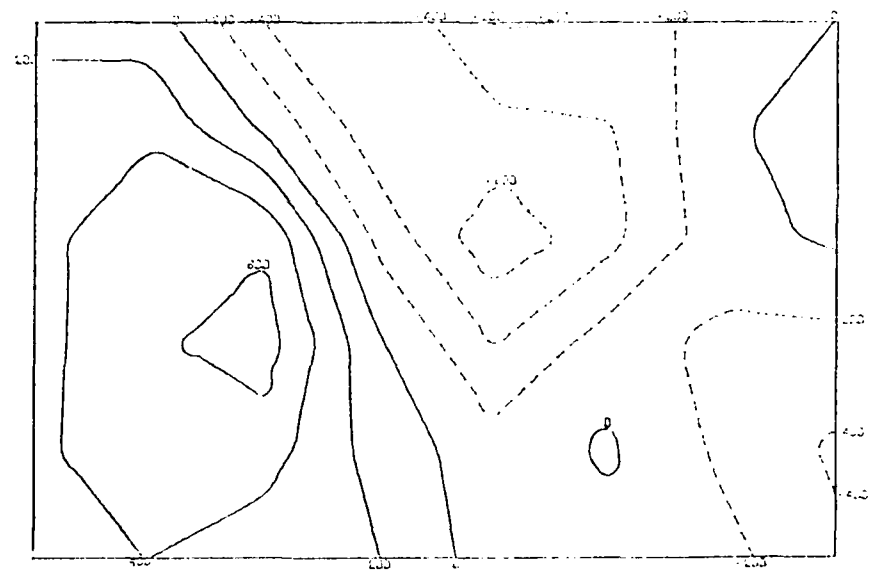
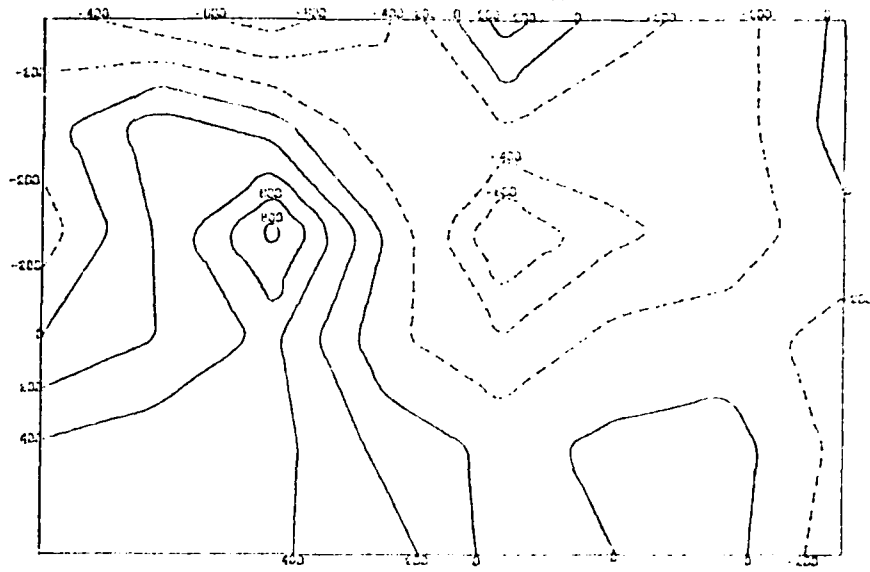


PAGE 5.

DATE: 0105

DIVERGENCE

TIME: 1400



LEVEL... SURFACE

FACE 75.

DATE... 0165

DIVERGENCE

TIME... 1455

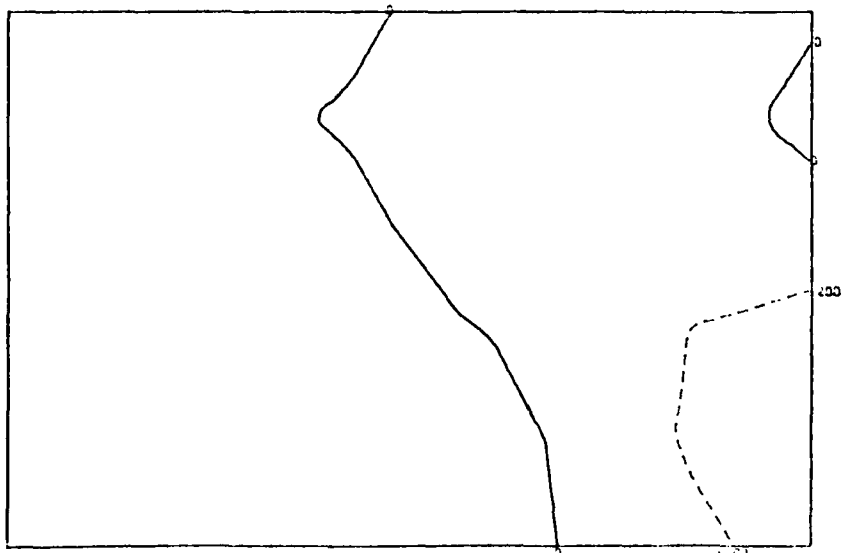
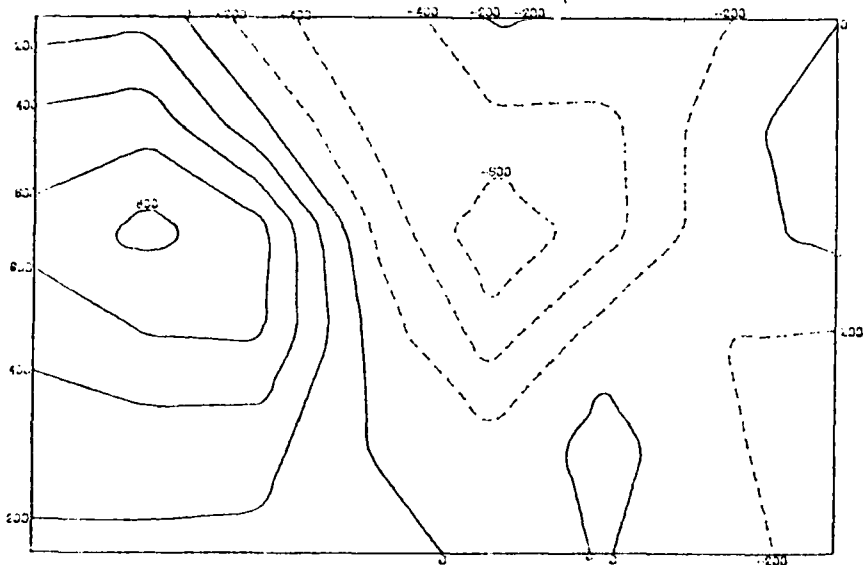
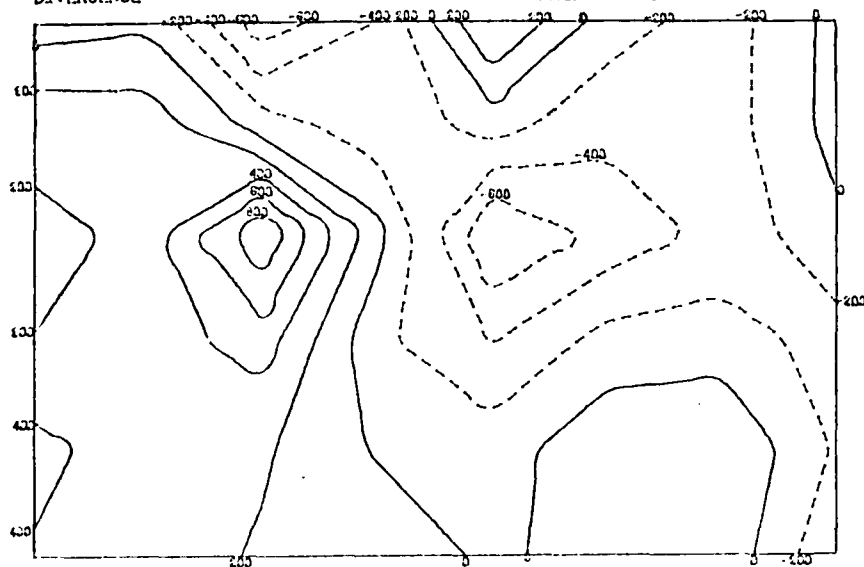
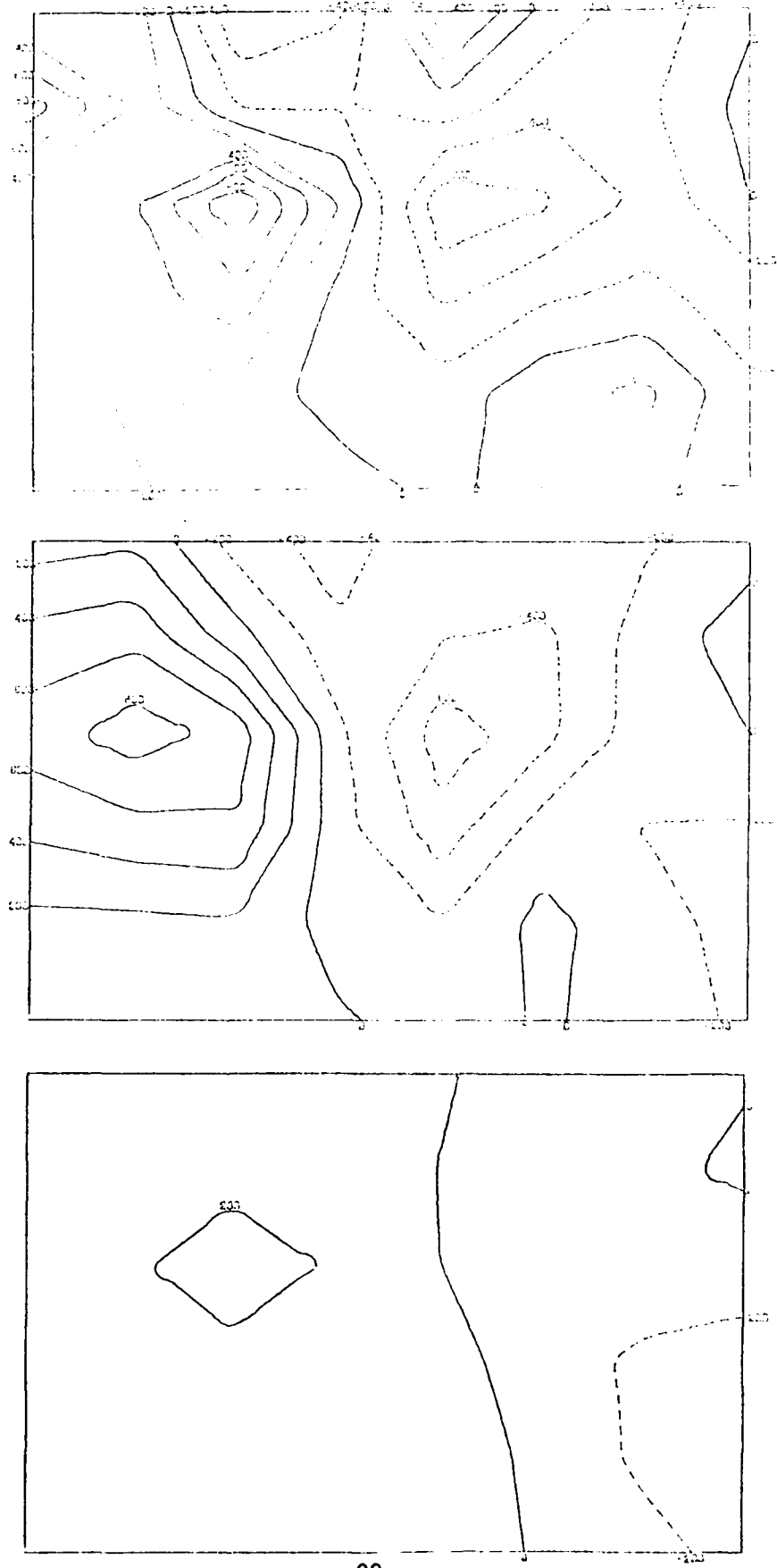


FIGURE 5.  
DIVERGENCE.

LINE 1500



FACE 75.

DATE... 0103

TIME... 1505

DIVERGENCE

LINE... 1505

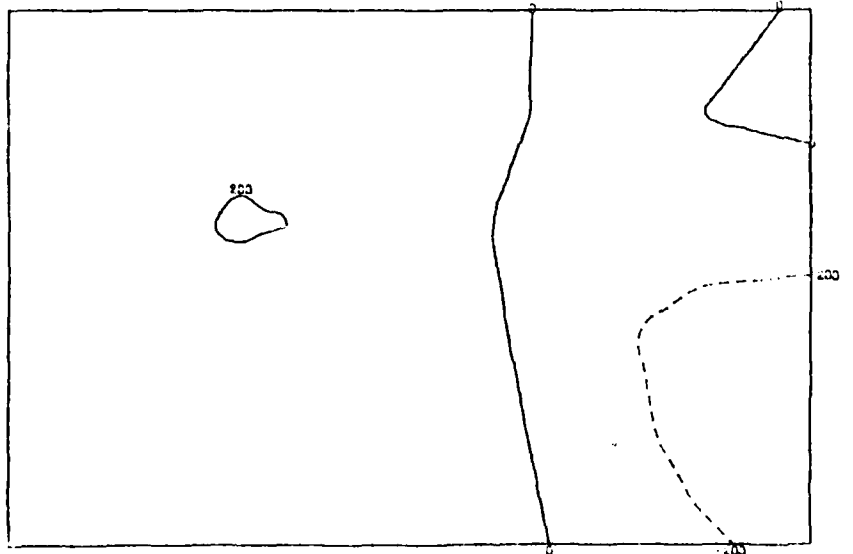
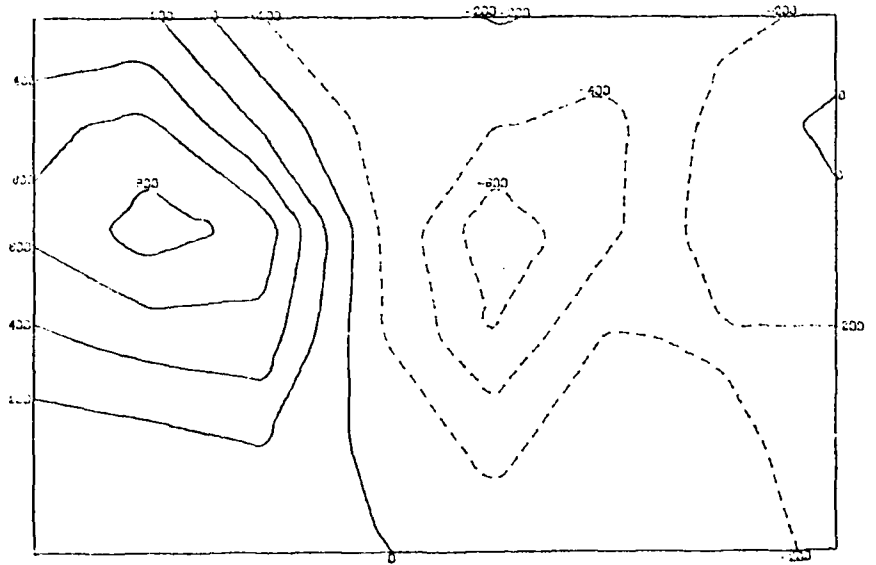
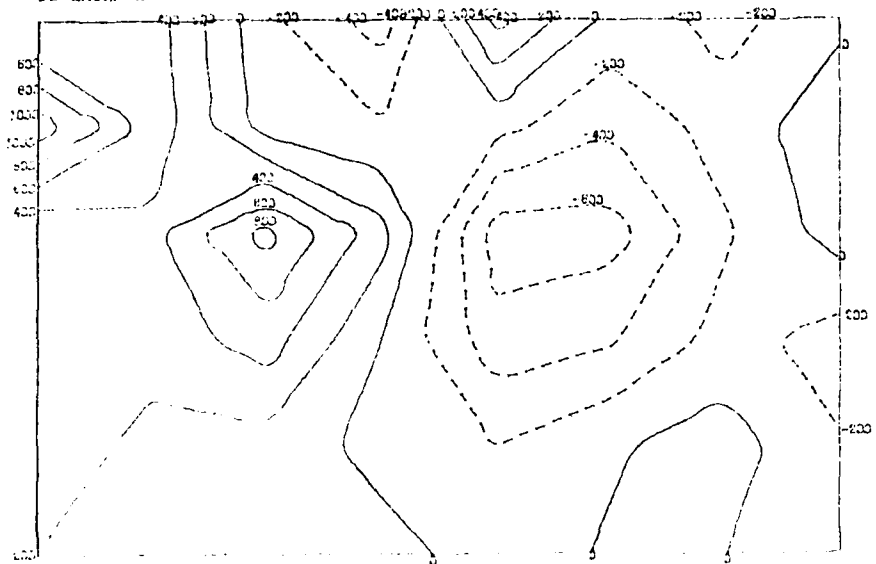
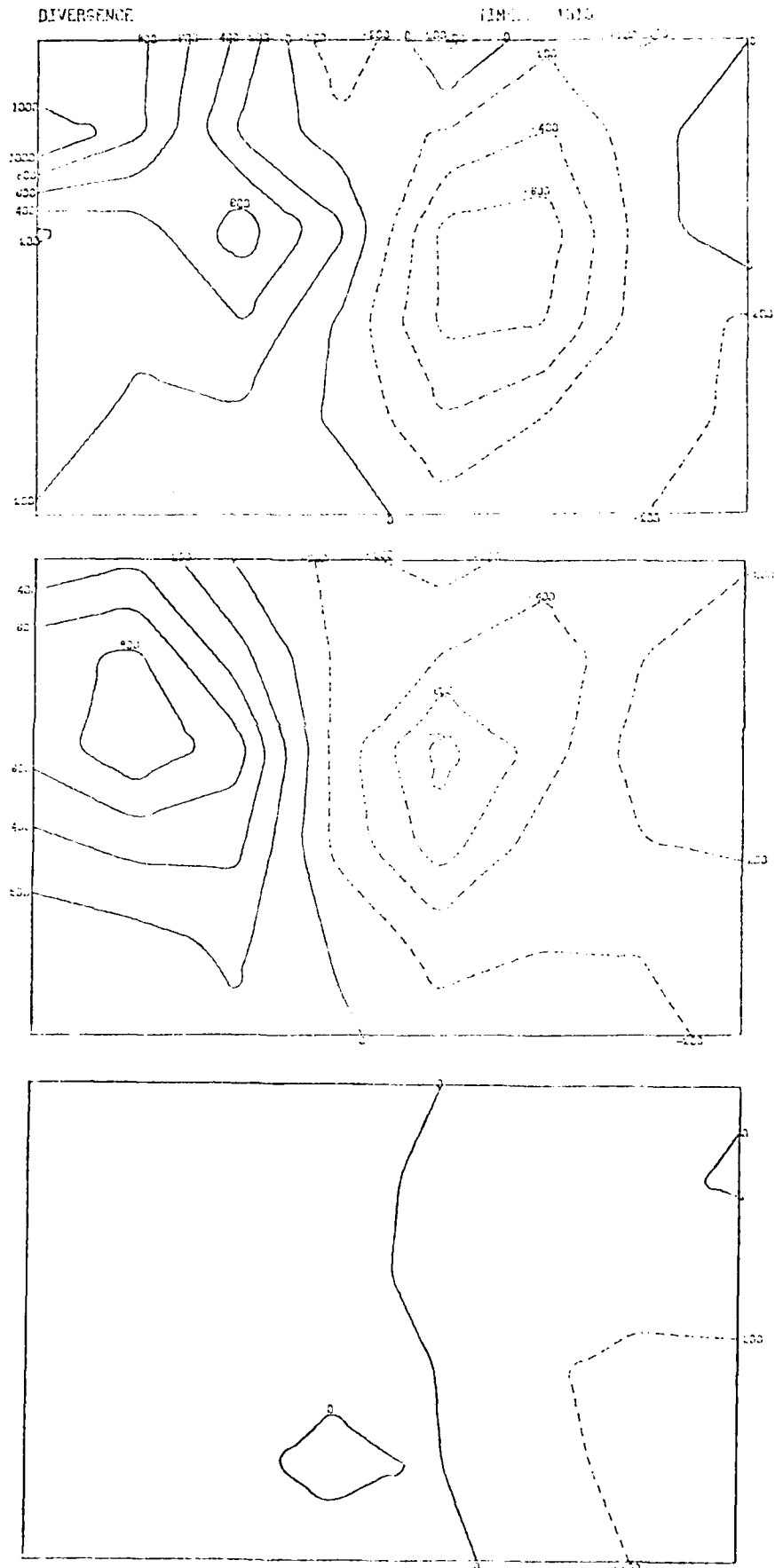


FIGURE 5.

DATE: 6/10/61  
TIME: 1510



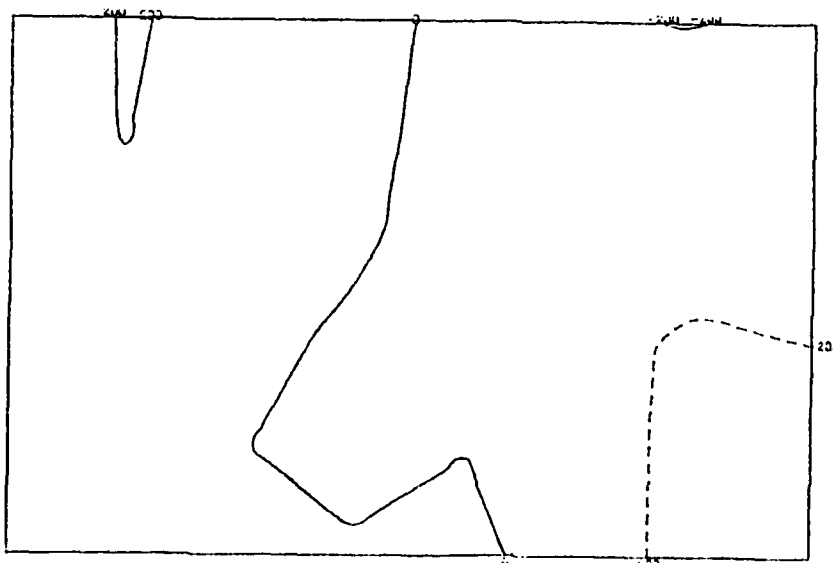
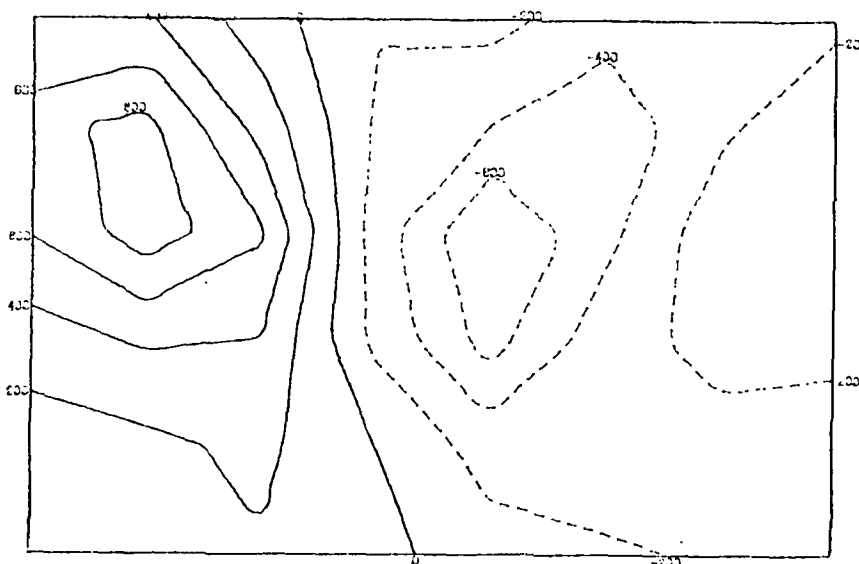
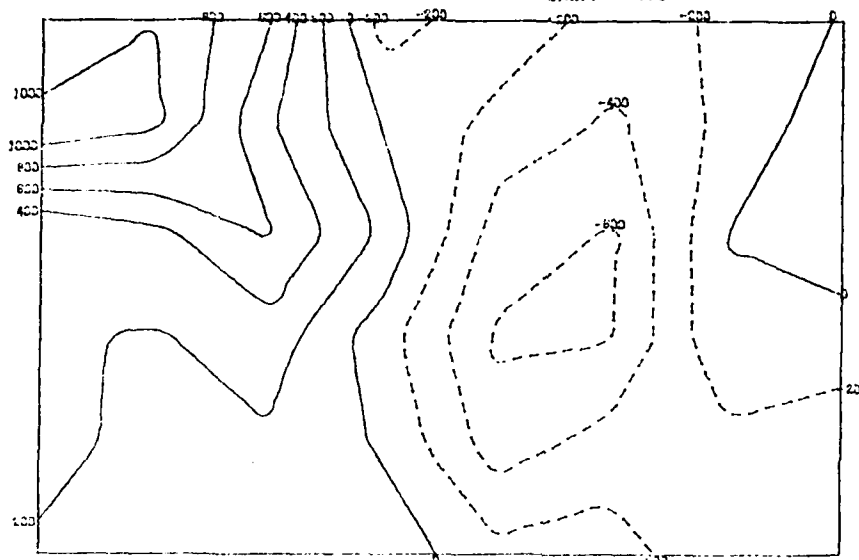
F A C E 7 S.

LEVEL ... SURFACE

D A T E ... 0165

D I V E R G E N C E

T I M E ... 1515



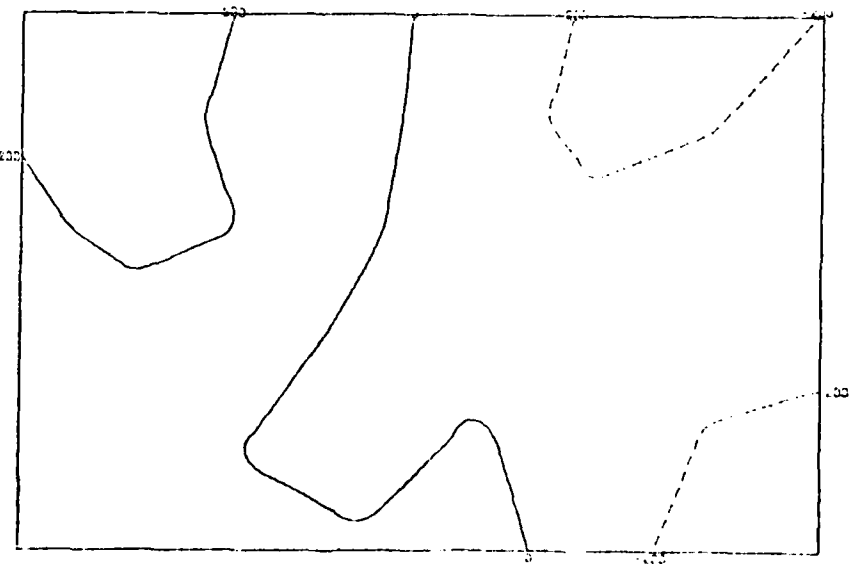
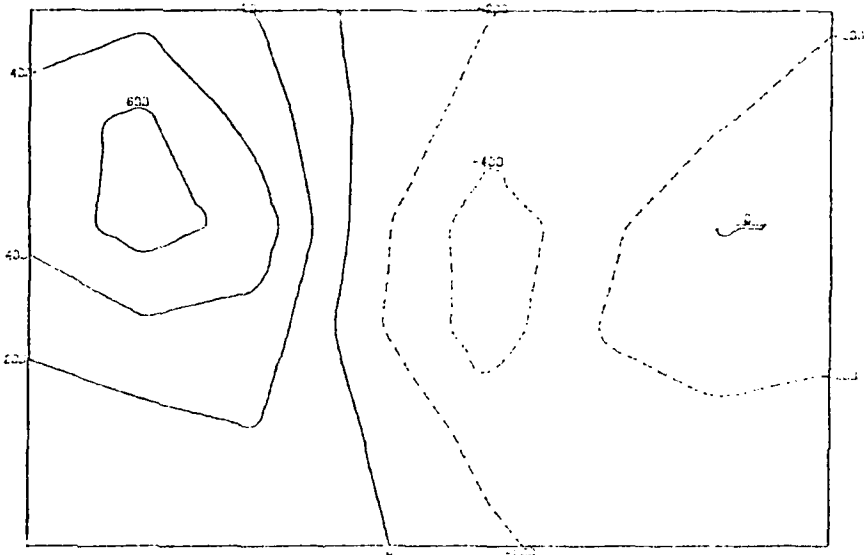
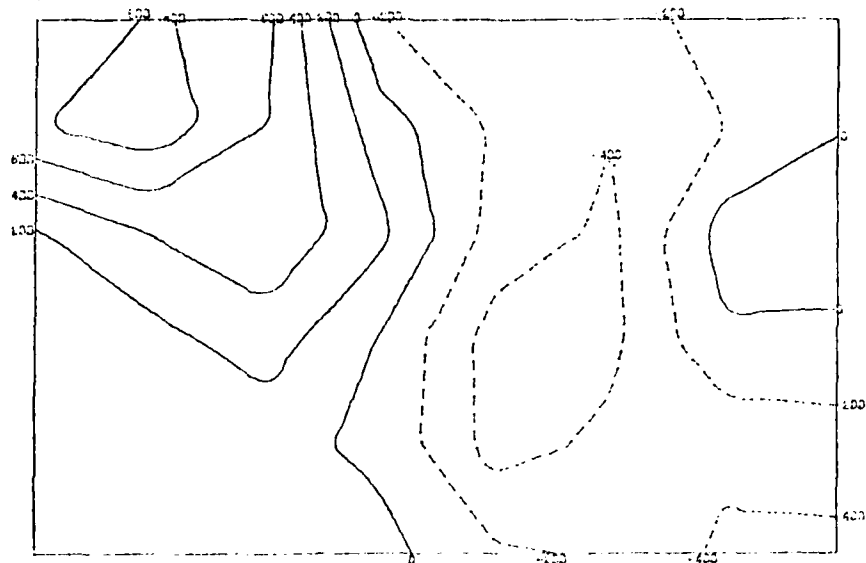
F R C E 7 S.

DIVERGENCE

LEVEL... 500 HGT

DATE... 0105

TIME... 1500



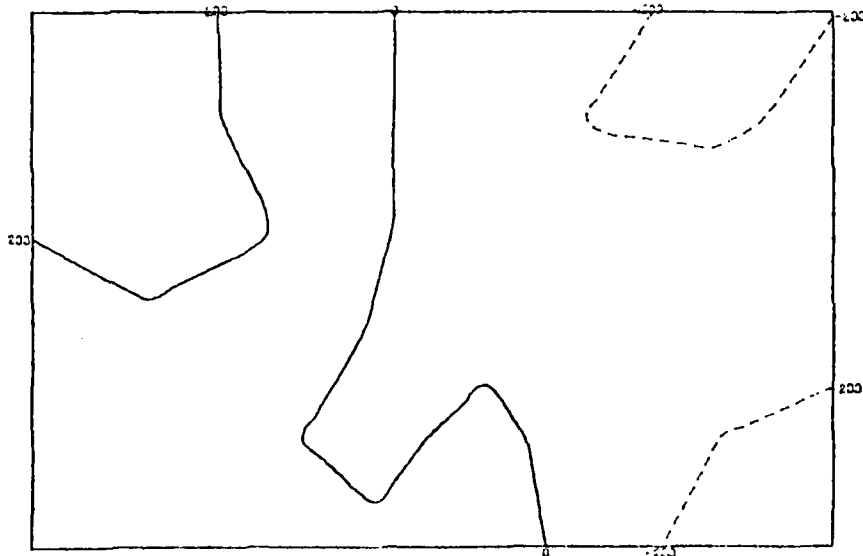
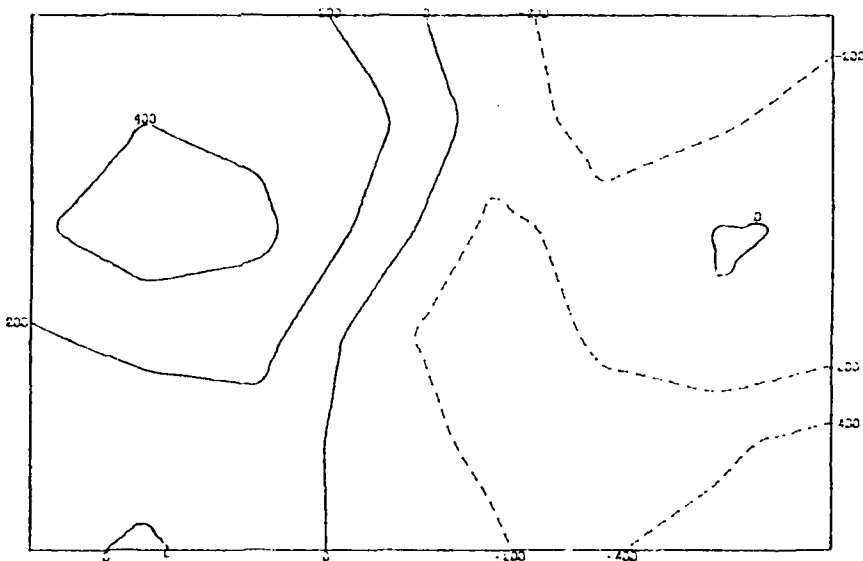
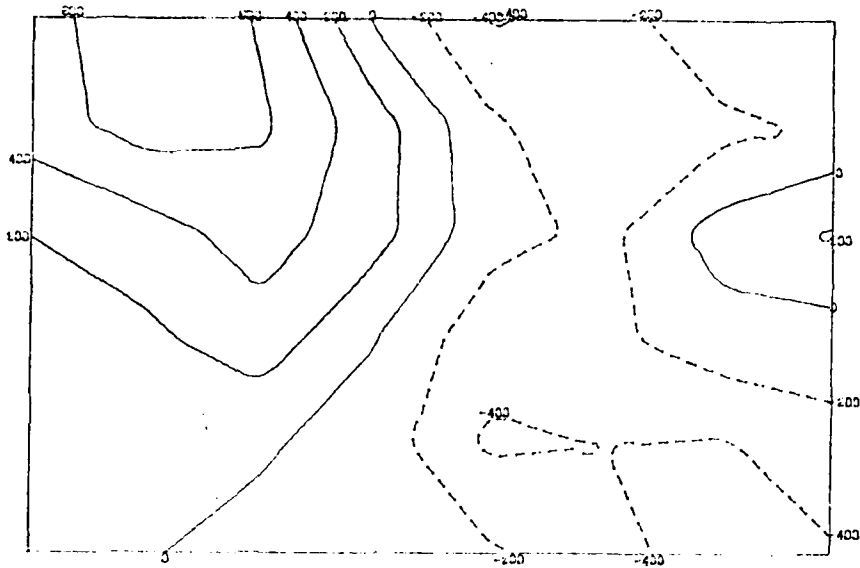
LEVEL... 1000 FT

FIG. 7.5.

DATE... 8/10/51

DIVERGENCE

TIME... 1520



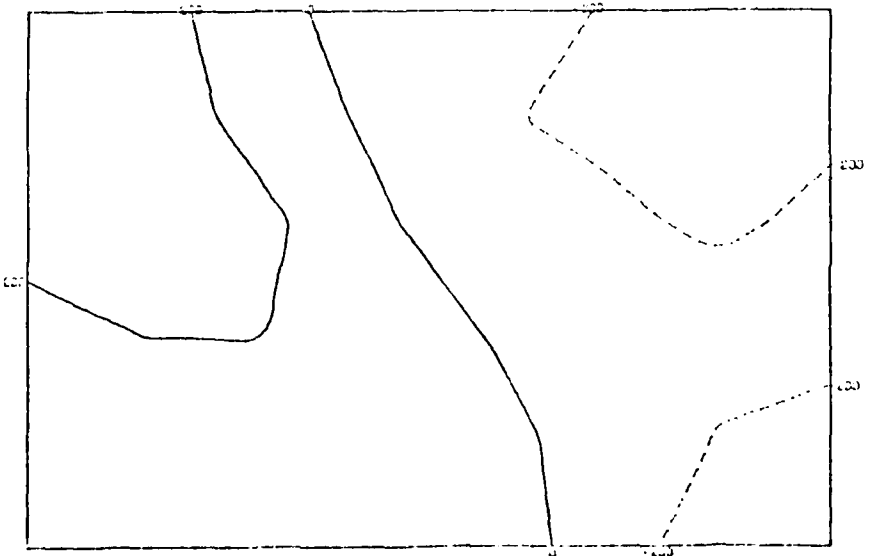
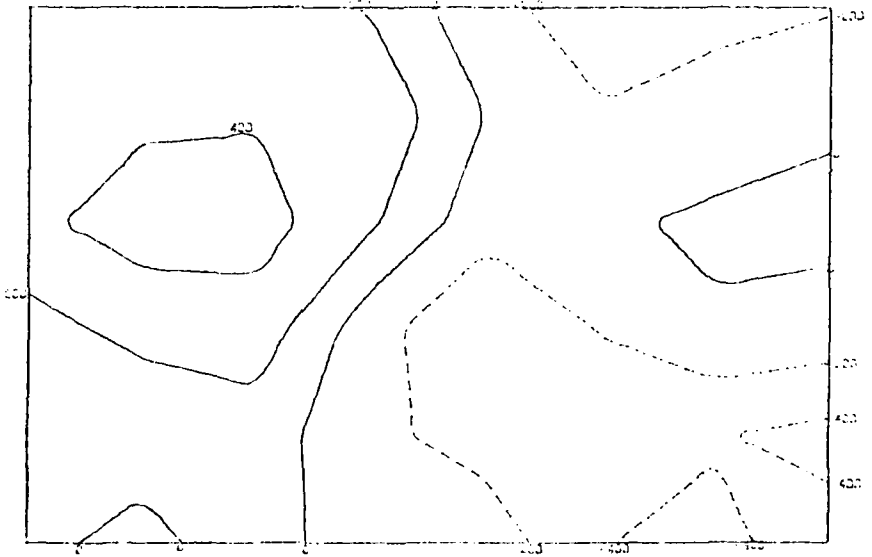
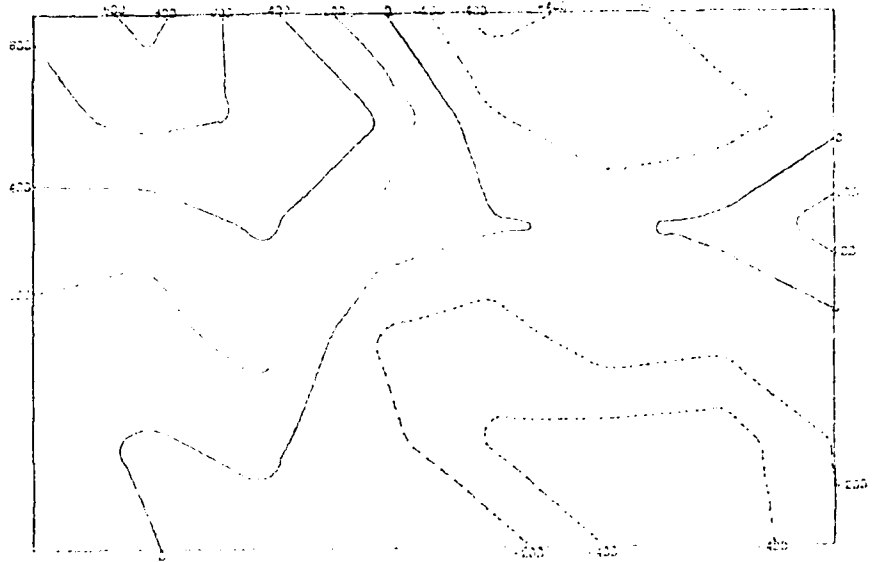
FACETS

DATE: 11/19/67

DRY: 616

DIVERGENCE

TIME: 1800



the 12.9-km grid analysis, and the bottom panel shows the 19.3-km grid. The 12.9-km grid compares very favorably with the 6.4-km output. One exception is the confluence zone in the western part of the network from 1430-1440 EDT. It is shifted toward the northern border in the 12.9-km grid analysis. The 19.3-km pattern is a different story. The smaller-scale features are lost in the coarse grid. The divergence panels are also vague; only the general positive divergence values (western half) and negative divergence (eastern half) can be observed. The magnitudes are quite different, too. It appears that the increase in station spacing from 6.4 to 12.9 km has had relatively little effect but from 12.9 to 19.3 km, many of the smaller-scale features are lost.

(2) 25 August 1975

This day is characteristic of many summer days in south Florida. Low-level flow is moderate with a subsidence inversion trapping much of the moisture below 3 km. South of Lake Okeechobee, in the mesonet network, the lake breeze penetrates southward interacting with the moderate easterly flow to cause a confluence zone to be established during maximum heating in the afternoon. The Doppler radar study, in Section 5, investigates a seeded cumulonimbus cloud on this particular day.

Figs. 11 and 12 present the streamline/isotach, radar, and divergence patterns for the time period 1430-1515 EDT for all three grid analyses. The radar is overlaid on the 6.4-km streamline/isotach pattern. The basic northeast-southwest confluence zone is shown in all three analysis grids. The effect of the rain shower after 1500 EDT on the surface flow appears to be lost in the 19.3-km grid analysis. The 6.4- and 12.9-km divergence panels show good agreement. The northeast-southwest convergence zone correlates remarkably well, and the divergence cell in the western portion of the network also shows good agreement. The northeast-southwest confluence zone in the 19.3-km grid does compare favorably with the smaller grid. But its orientation becomes confused

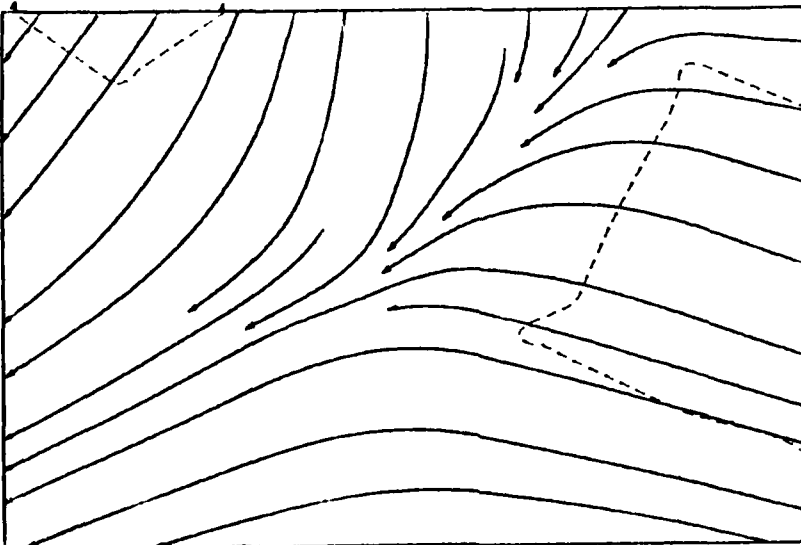
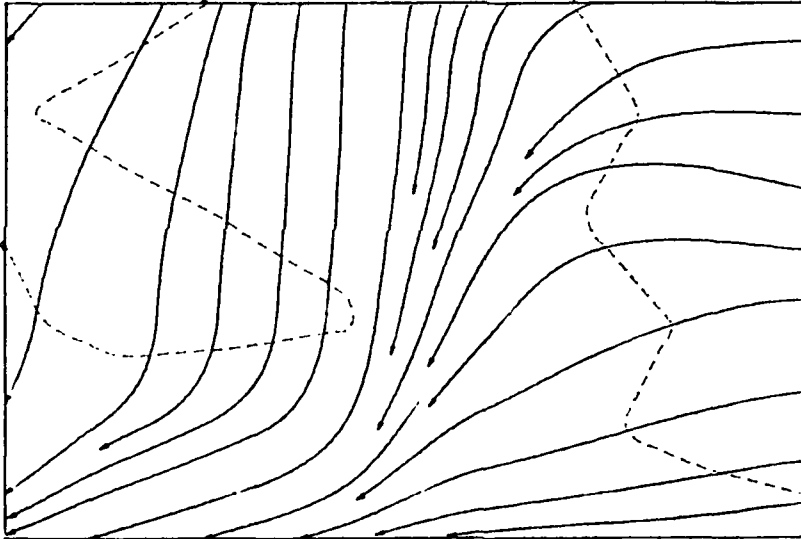
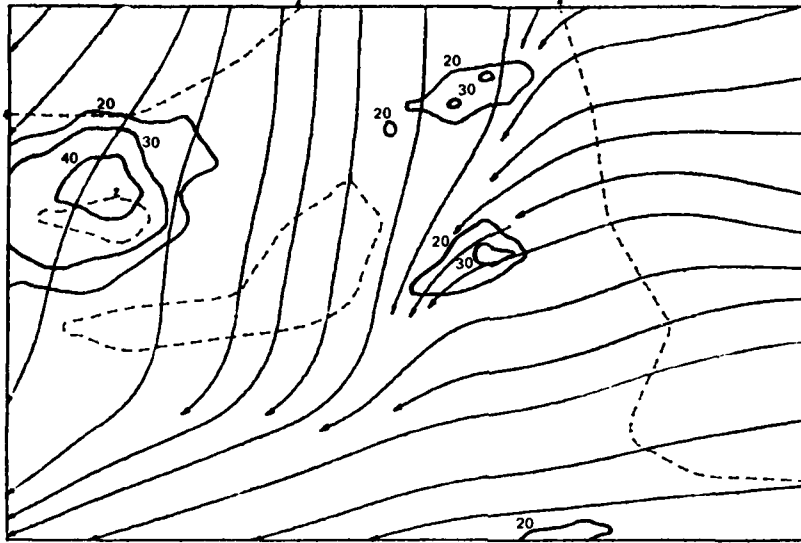
*Figure 11. Streamline/isotach patterns on 25 August 1975 for each 5 minute period between 1430 and 1515 EDT. For each time period, the top panel is the 6.4 km grid with radar echoes (dBz), the middle panel is a 12.9 km site separation, while the bottom panel is the 19.3 km grid.*

FACE 75.

DATE... 8255

STREAMLINES

TIME... 1430

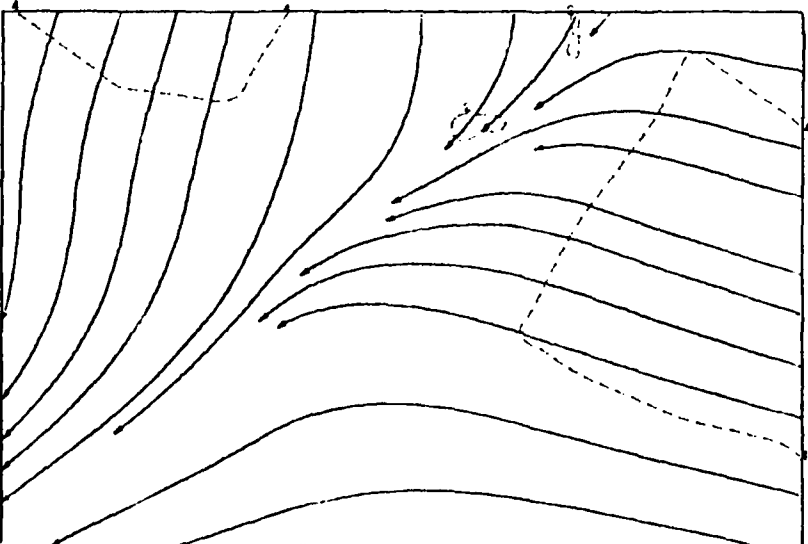
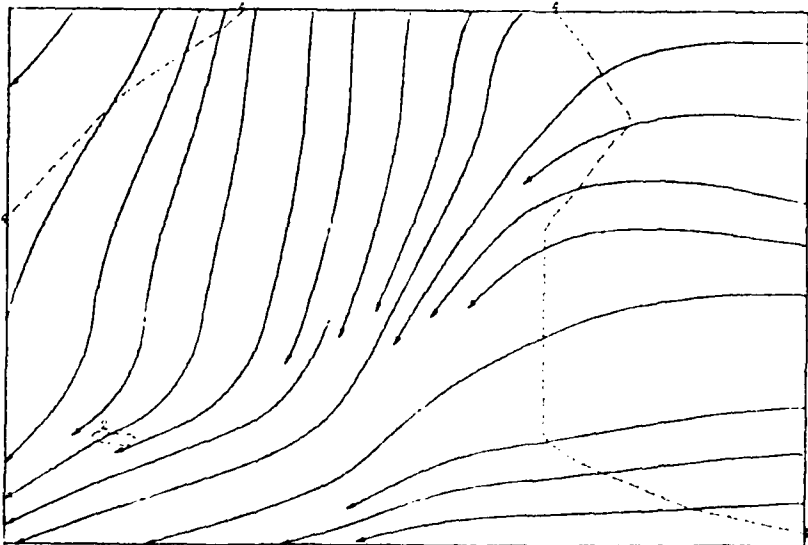
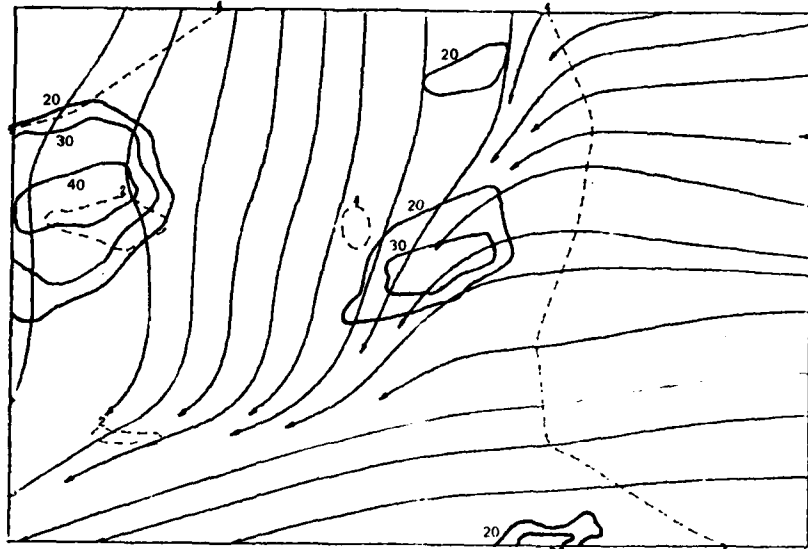


F A C E 7 5 .

D A T E . . . 8 2 5 5

S T R E A M L I N E S

T I M E . . . 1 4 3 5

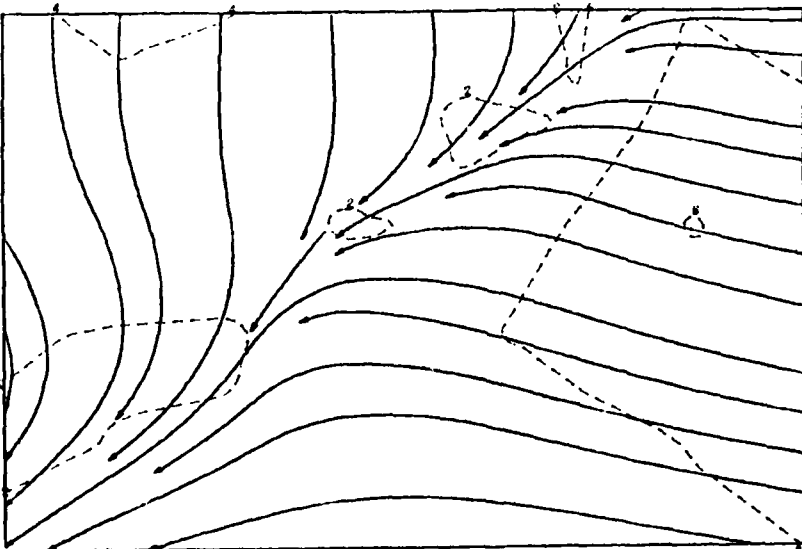
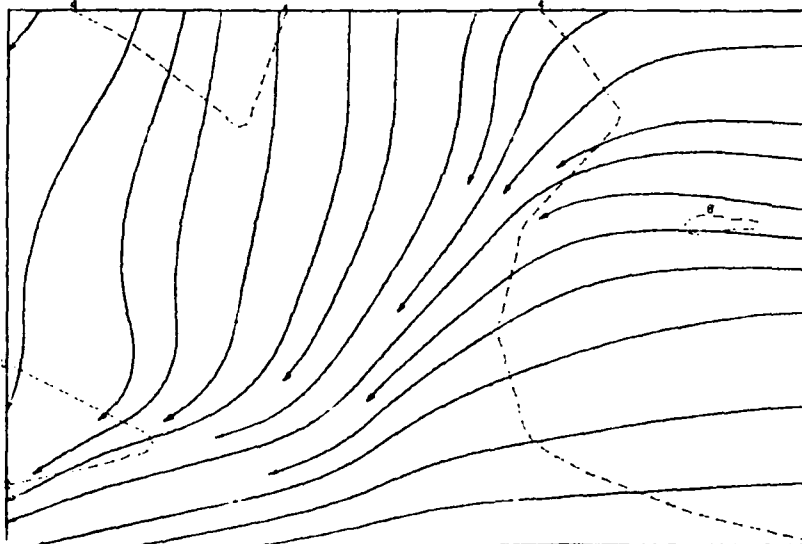
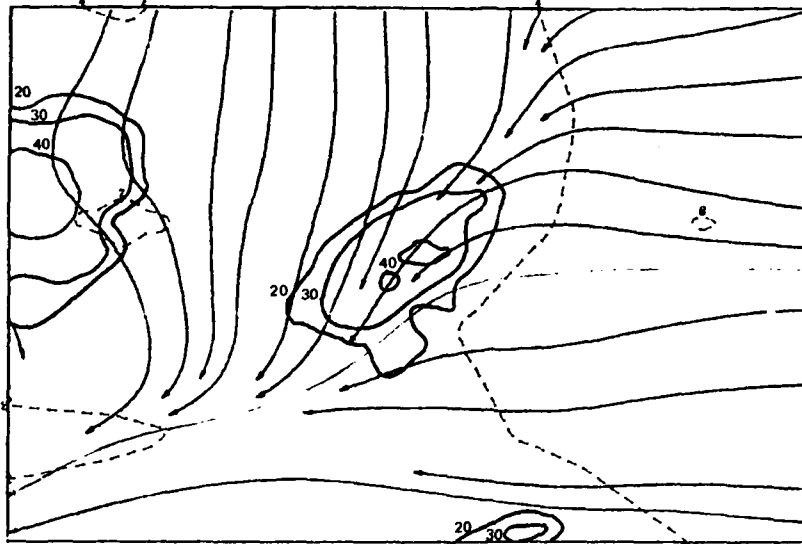


FACE 75.

DATE... 0255

STREAMLINES

TIME... 1440

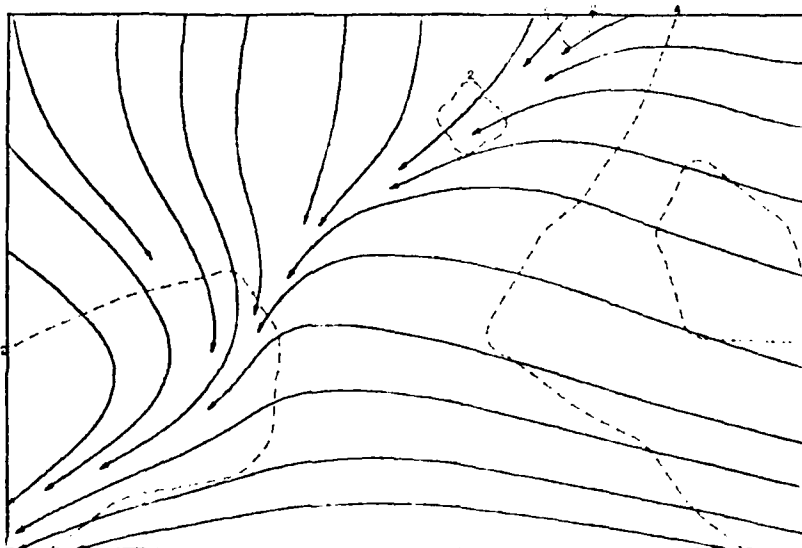
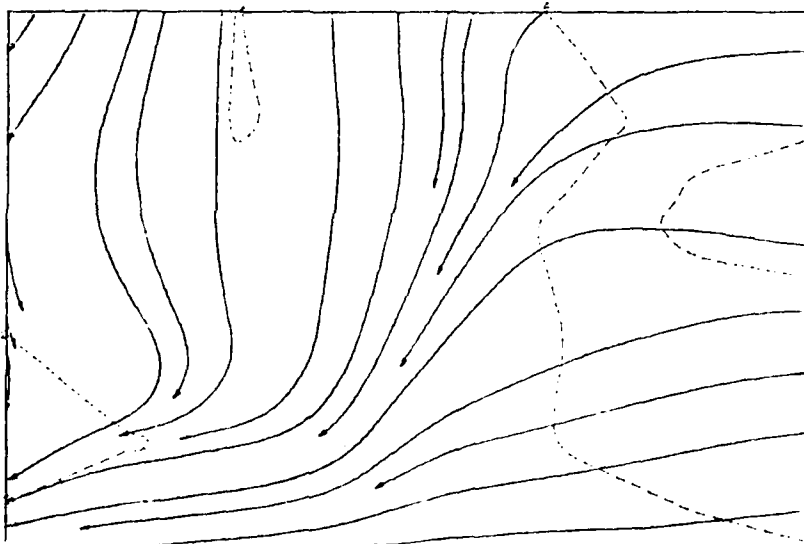
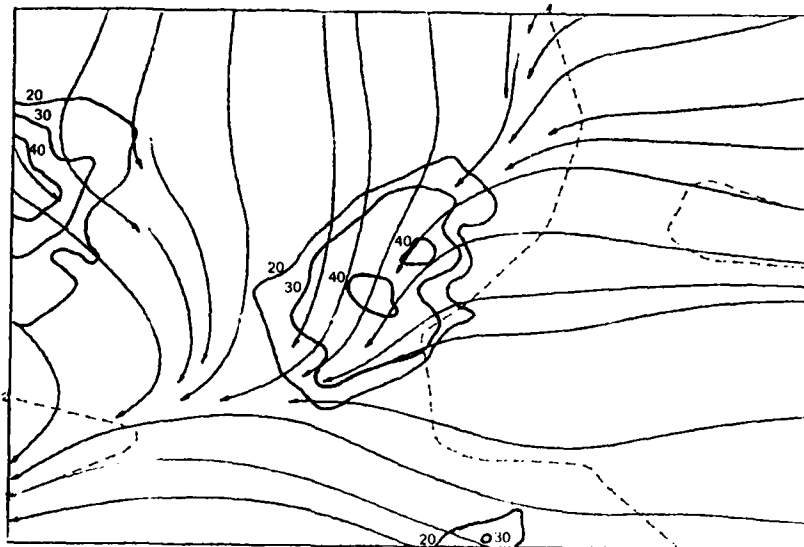


FACE 75.

DATE... 0255

STREAMLINES

TIME... 1445

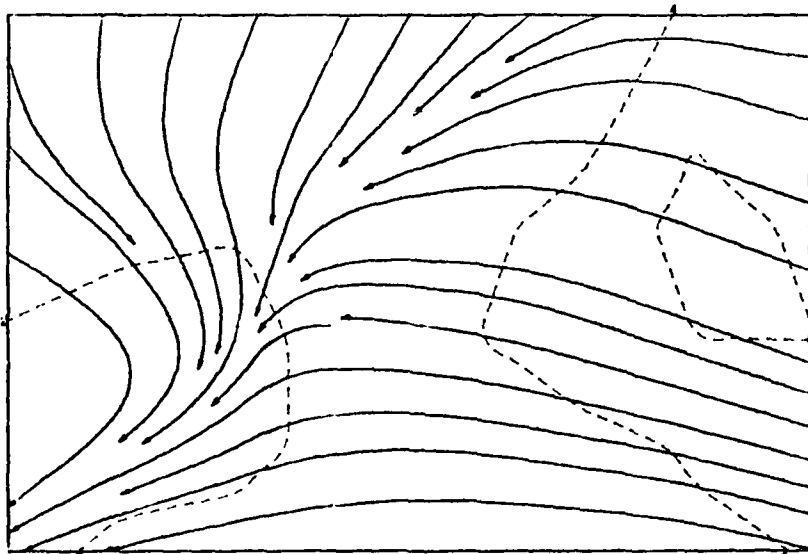
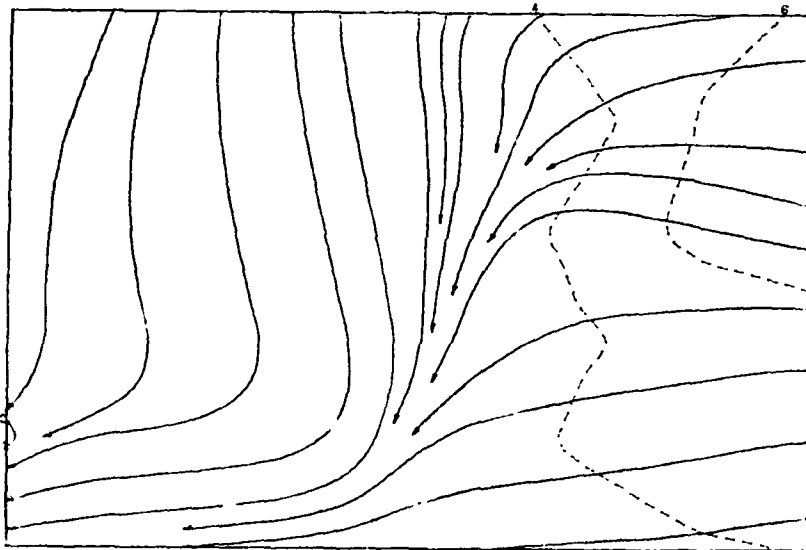
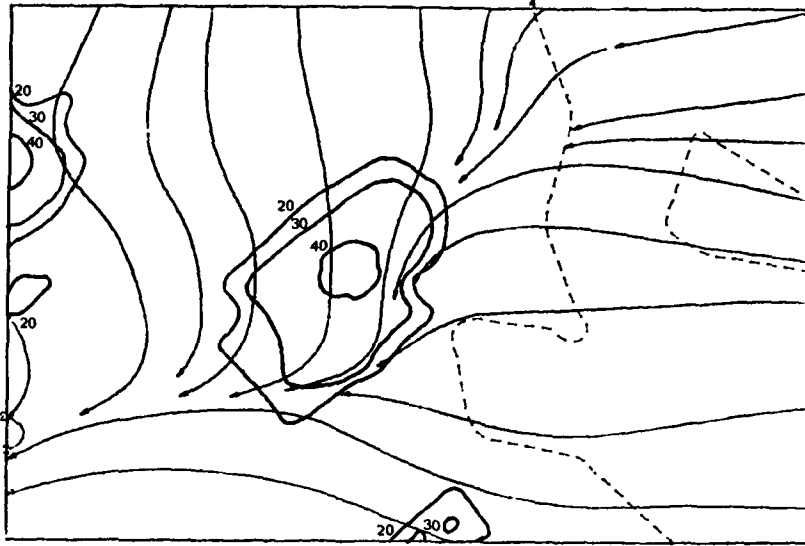


F A C E 7 5.

DATE... 0255

STREAMLINES

TIME... 1450

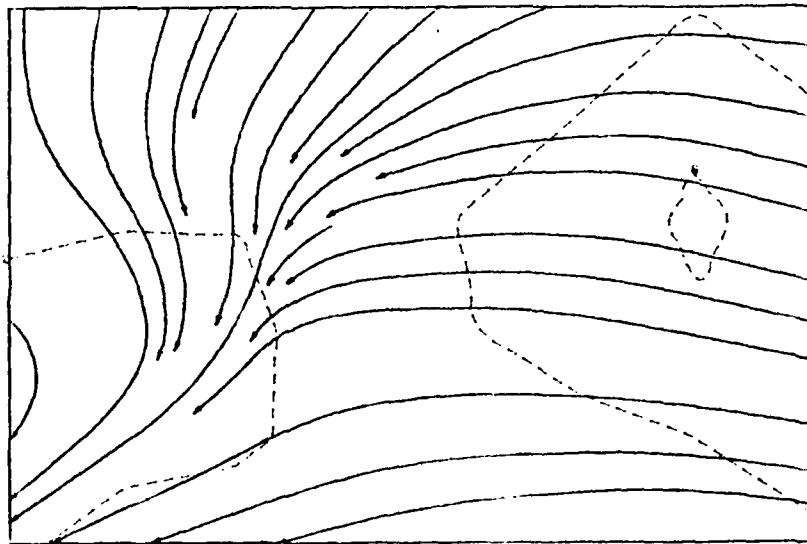
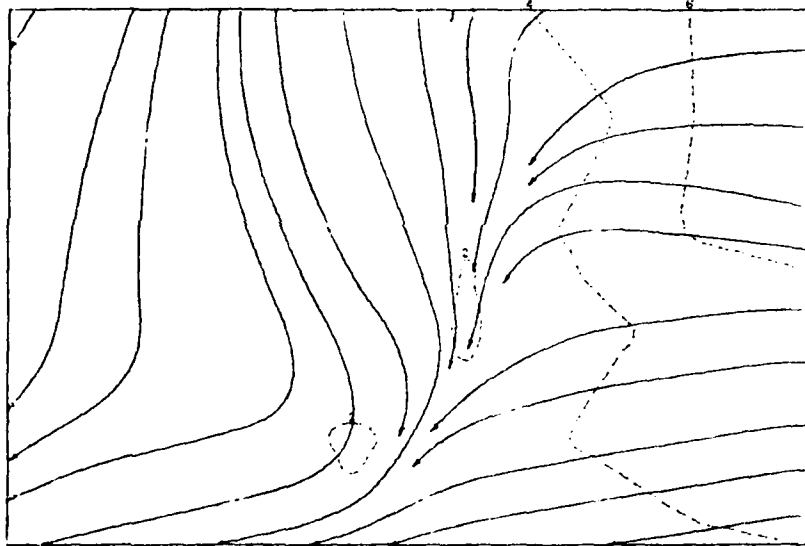
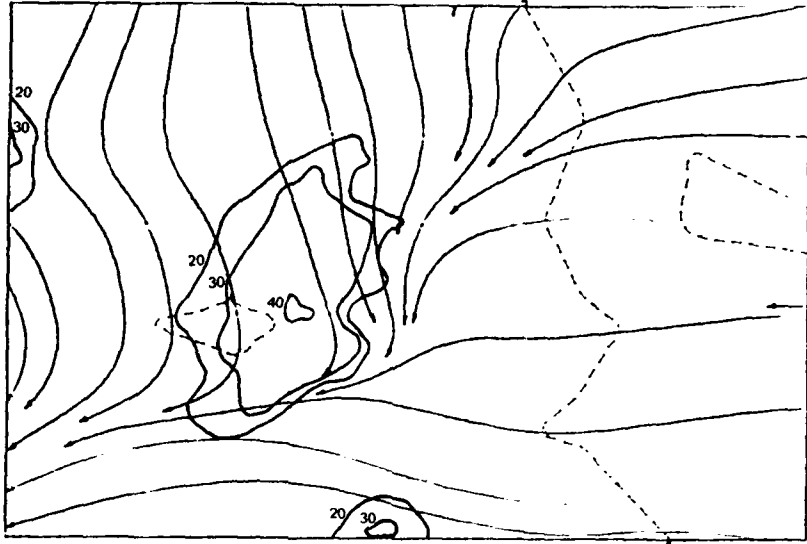


PAGE 75.

DATE... 8255

STREAMLINES

TIME... 1455

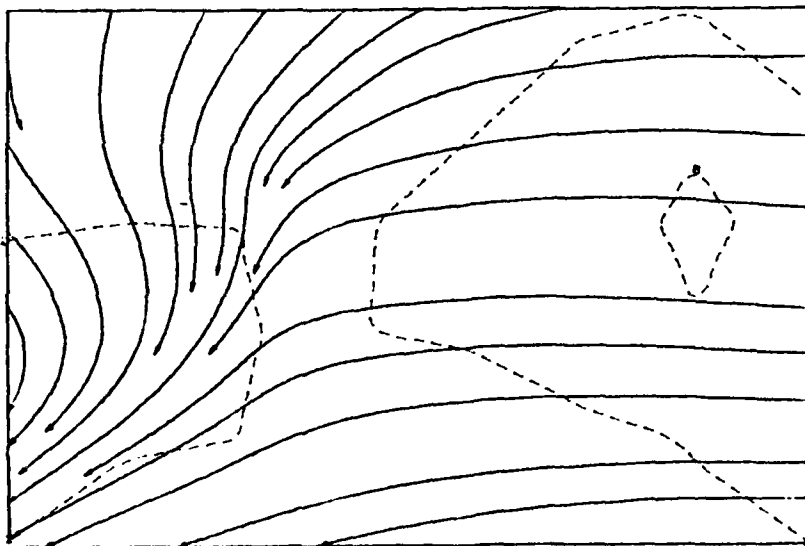
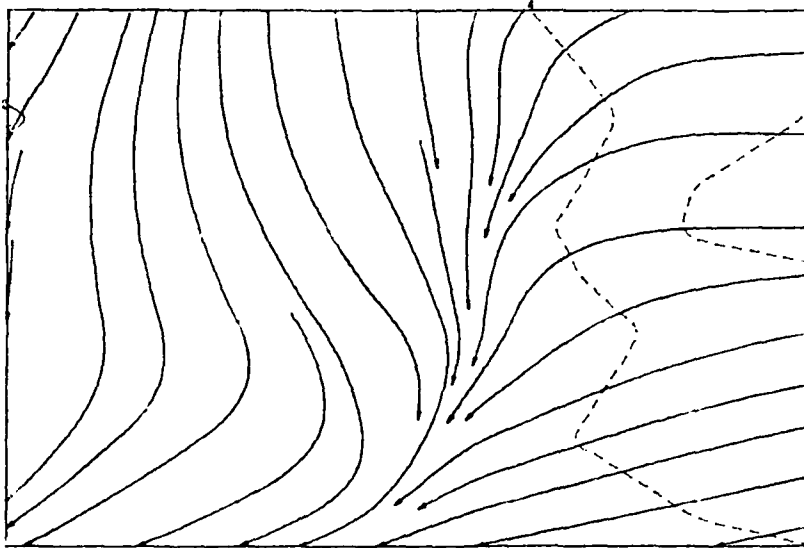


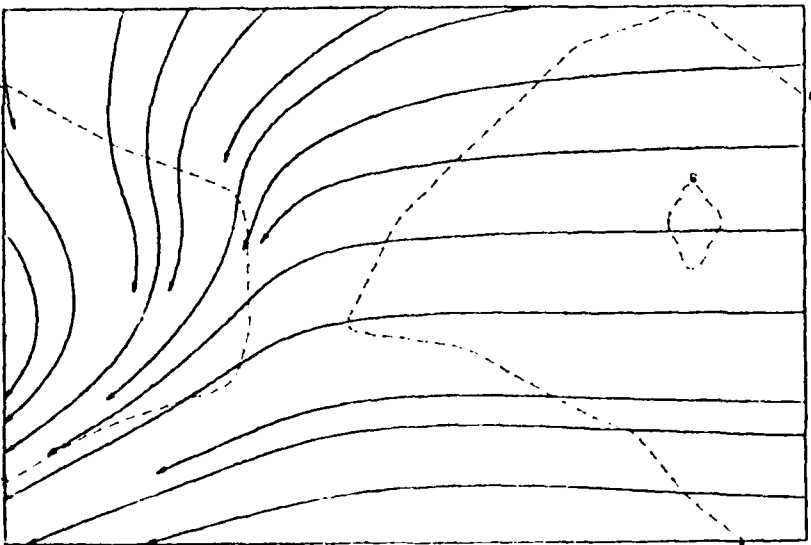
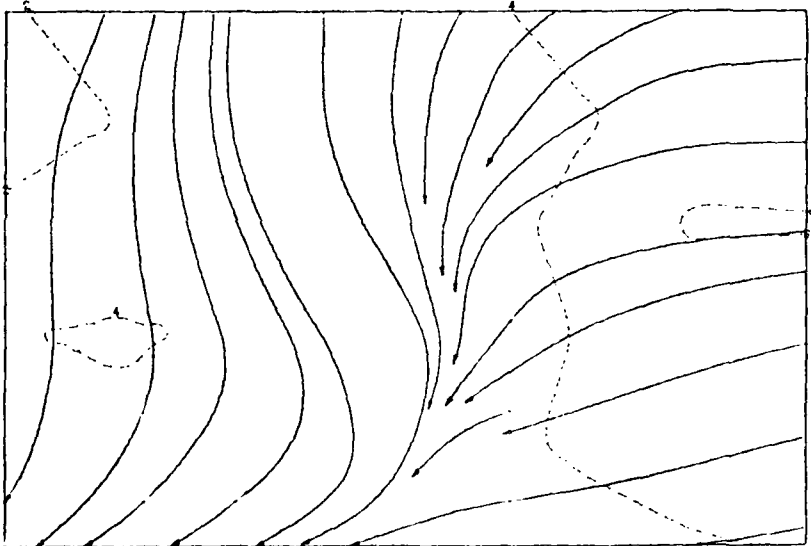
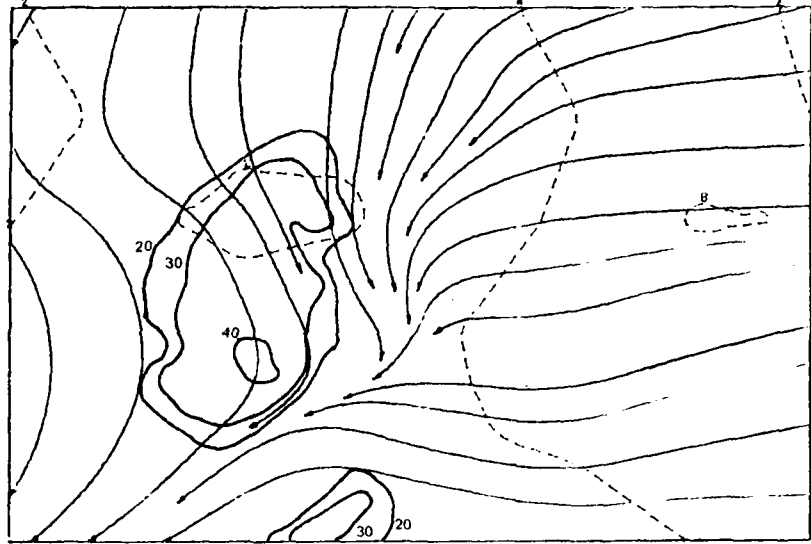
F A C E 7 5 .

DATE . . . 0255

STREAMLINES

TIME . . . 1500



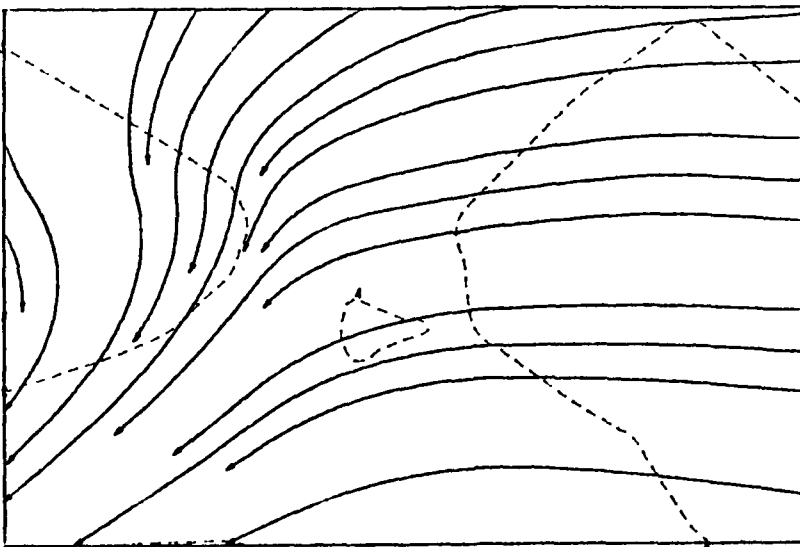
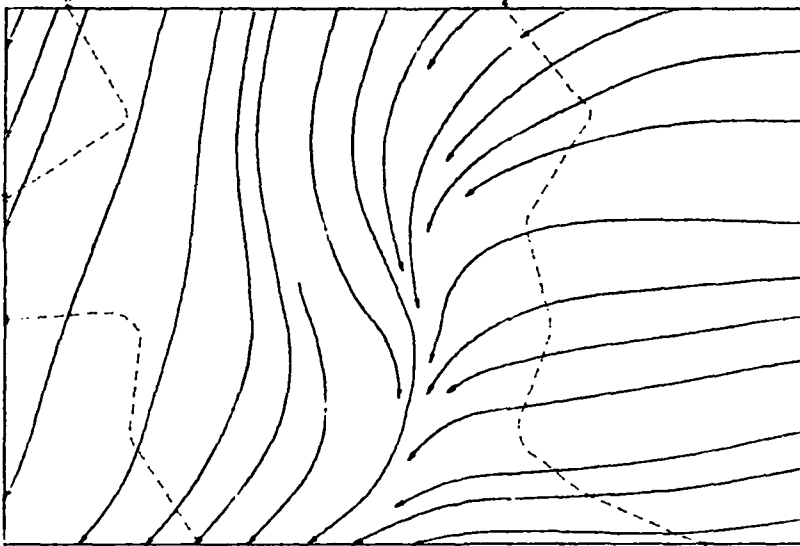
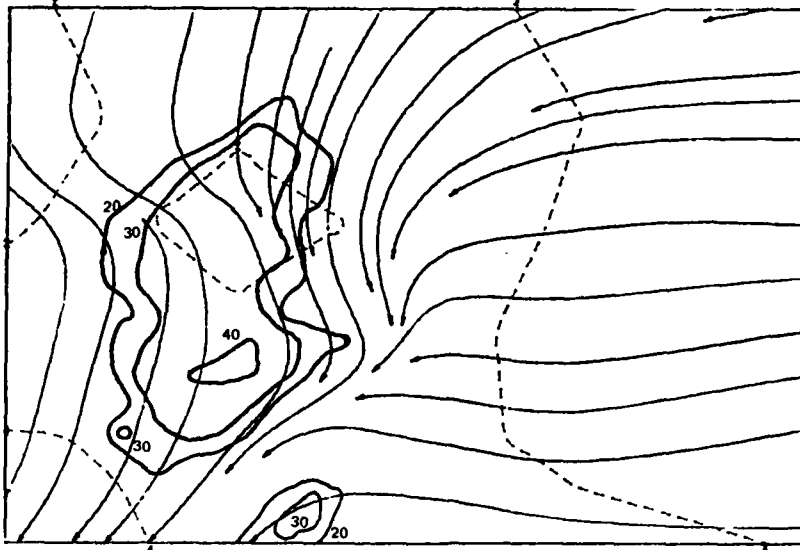


F A C E 7 5 .

D A T E . . . 0 2 5 5

S T R E A M L I N E S

T I M E . . . 1 5 1 0



F A C E 7 5 .

D A T E . . . 0 2 5 5

S T R E A M L I N E S

T I M E . . . 1 5 1 5

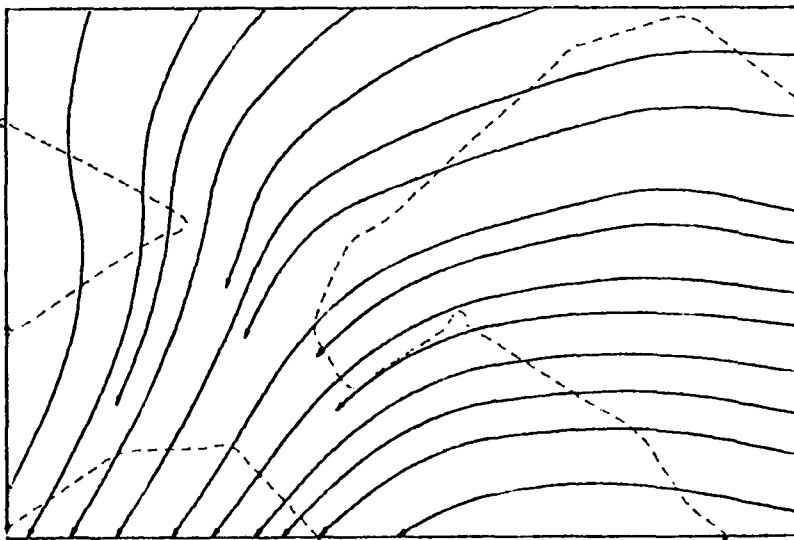
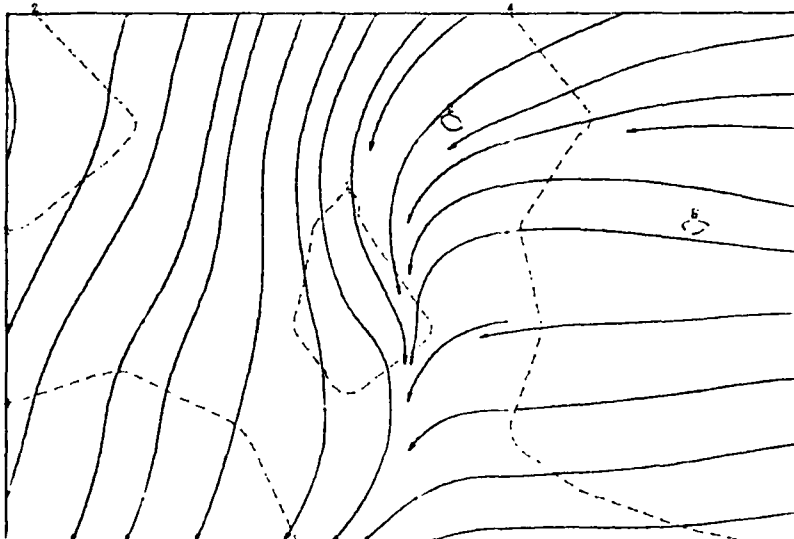
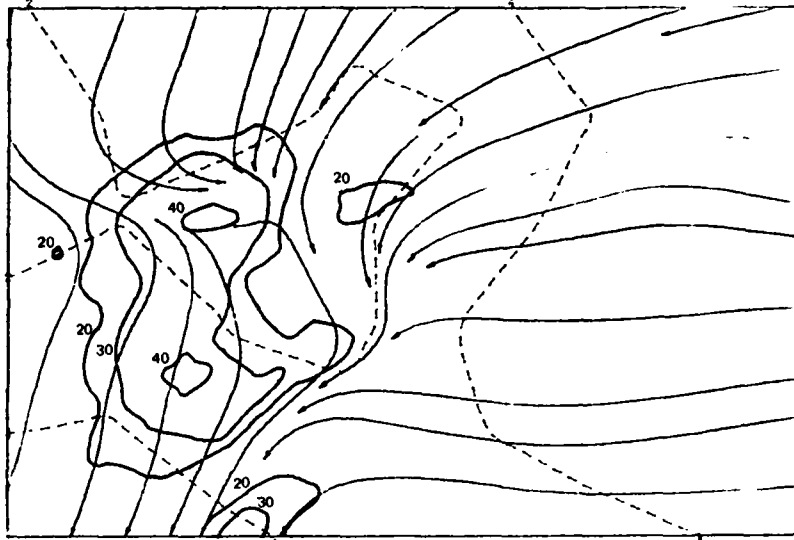


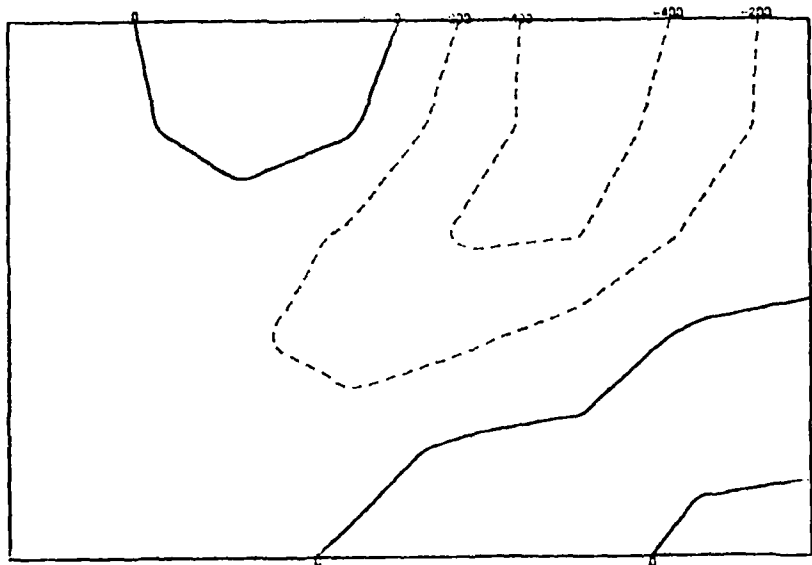
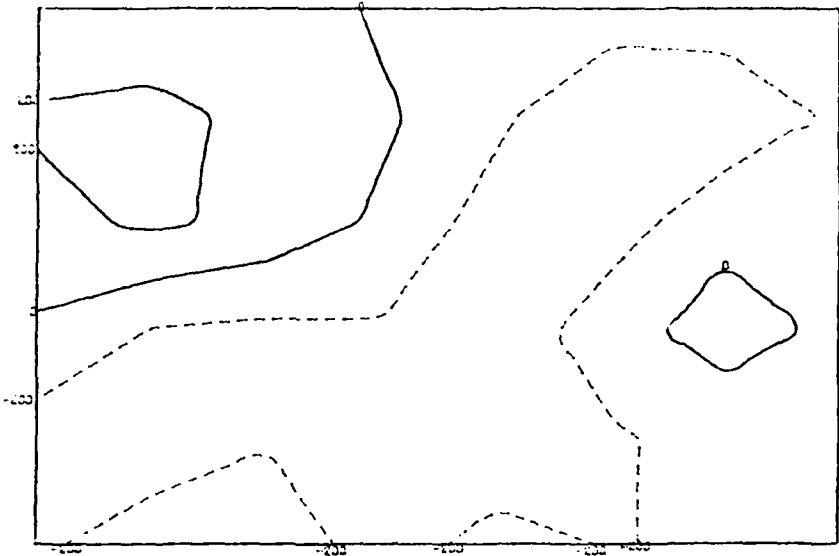
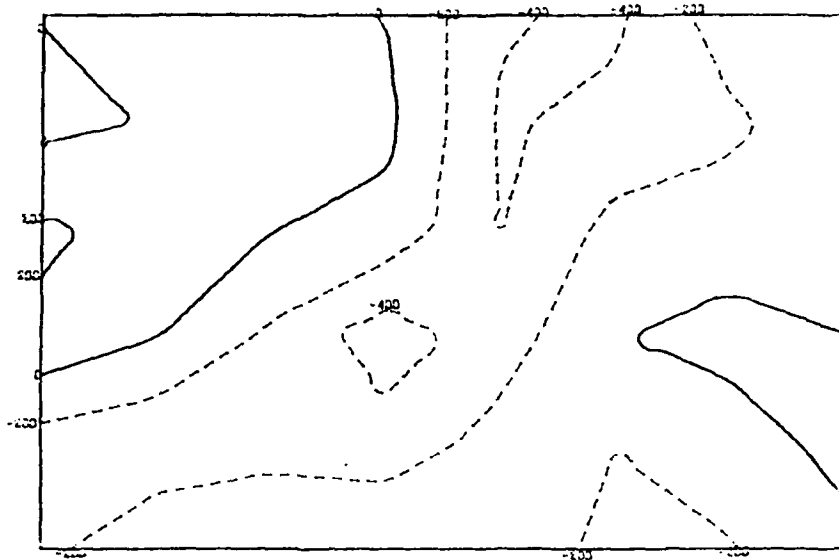
*Figure 12. Divergence patterns on 25 August 1975 for each 5 minute period between 1430 and 1515 EDT. Top panel is the 6.4 km grid, the middle panel is the 12.9 km grid, while the bottom panel is the 19.3 km station grid.*

FACE 75.

DATE... 0255

DIVERGENCE

TIME... 1430

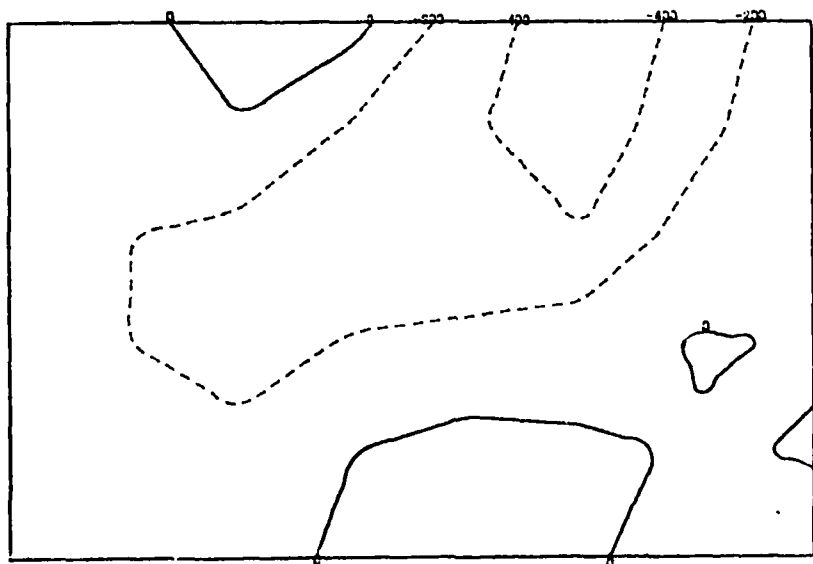
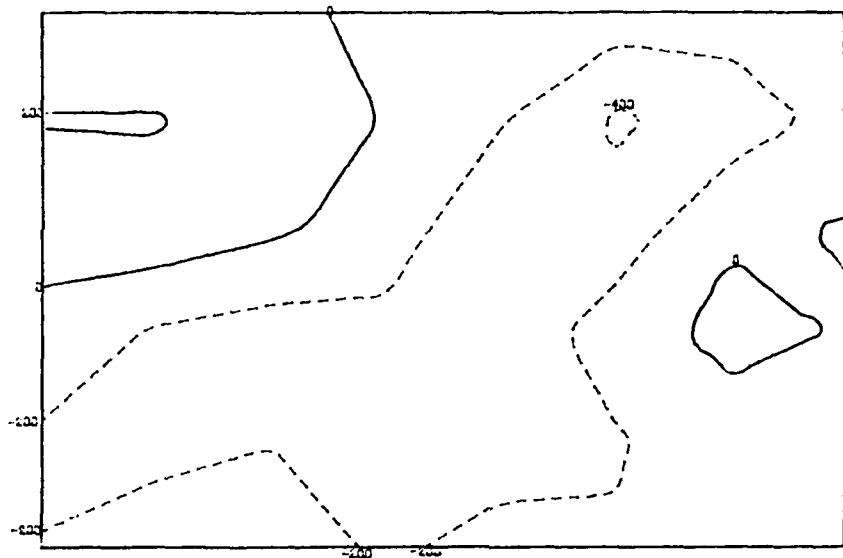
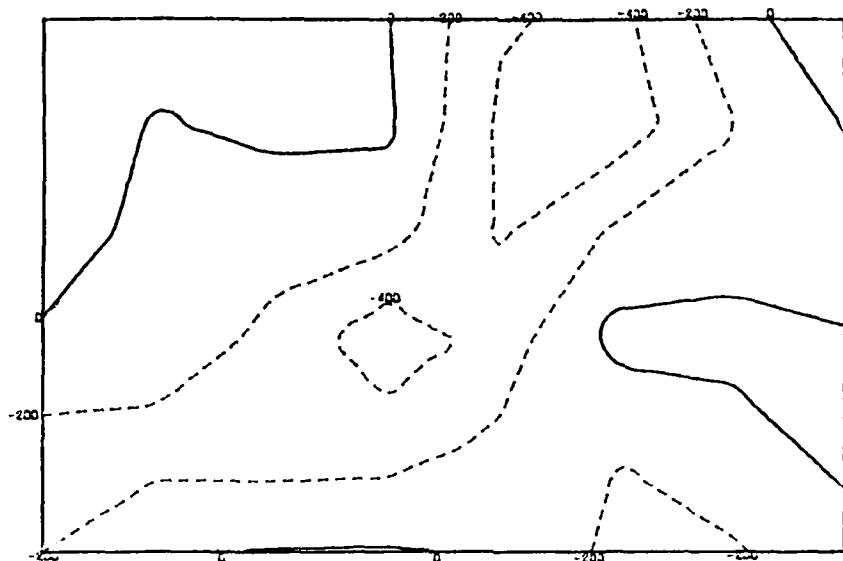


PAGE 75.

DATE... 0255

DIVERGENCE

TIME... 1405

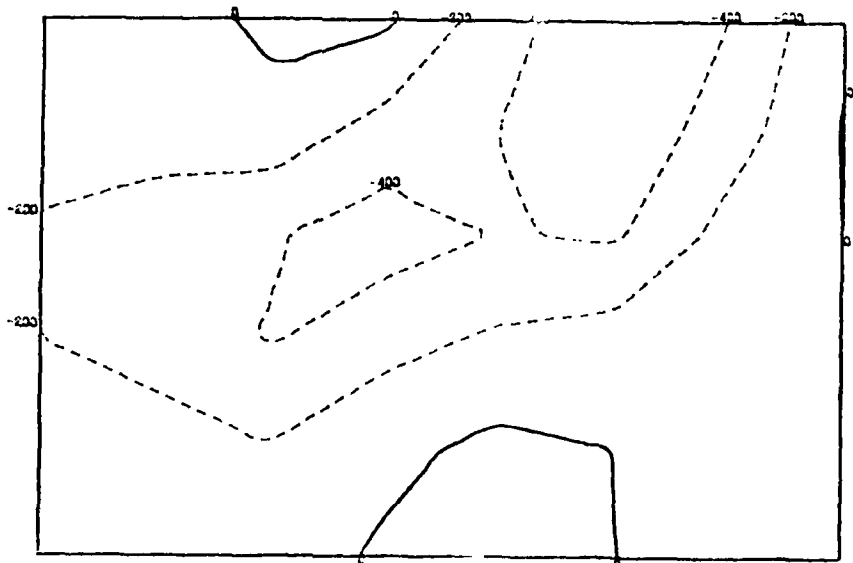
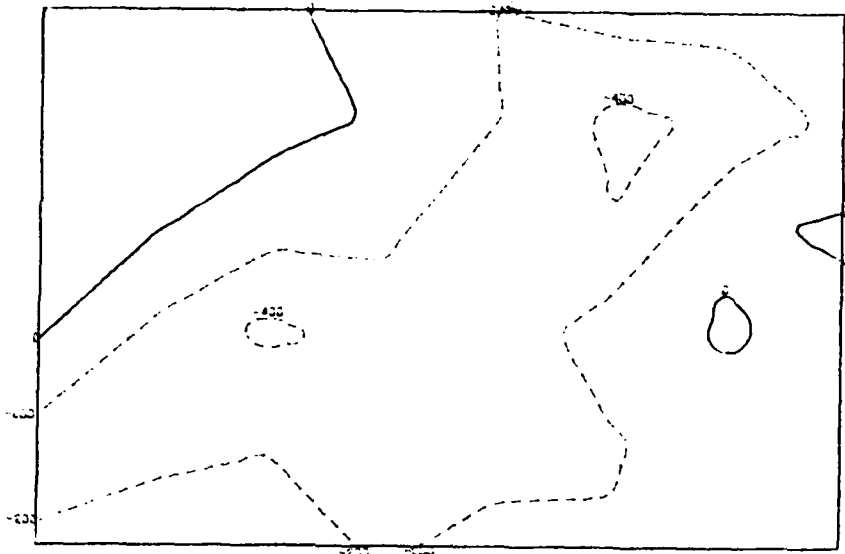
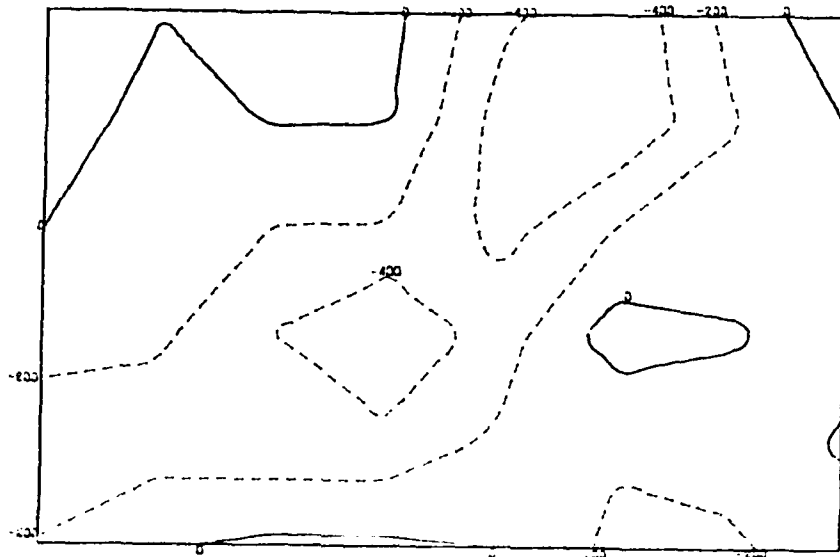


F A C E 7 5.

DRIF... 0255

DIVERGENCE

TIME... 1440

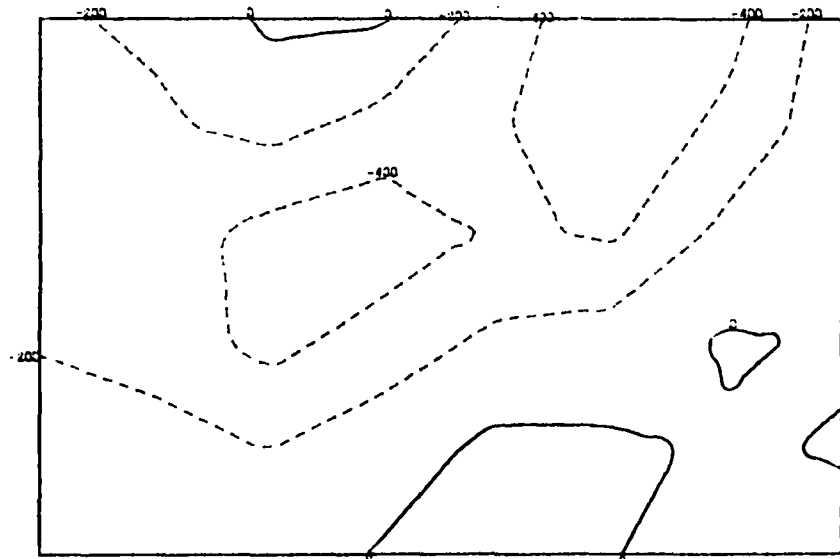
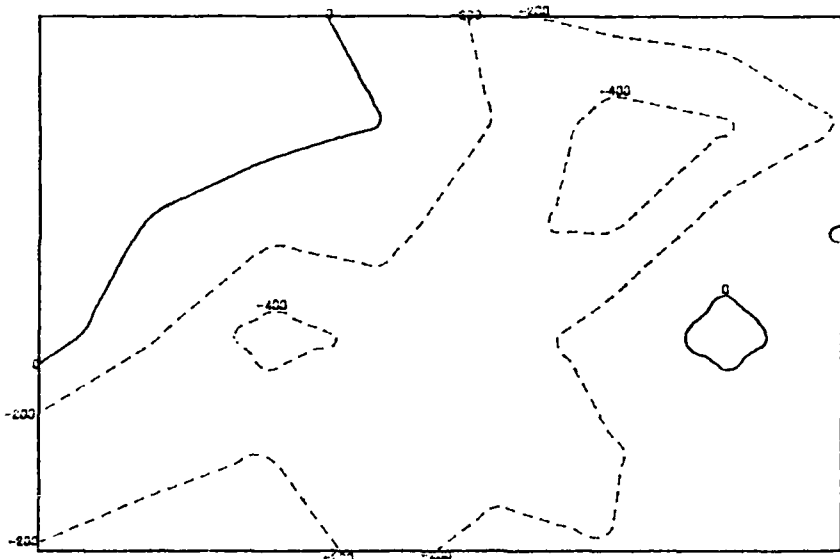
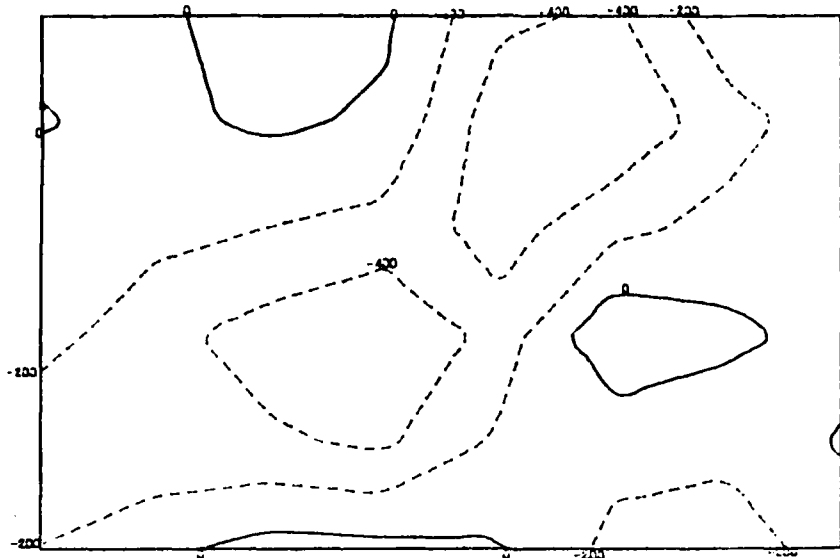


F A C E 7 5.

D A T E . . . 0 2 5 5

D I V E R G E N C E

T I M E . . . 1 4 4 5

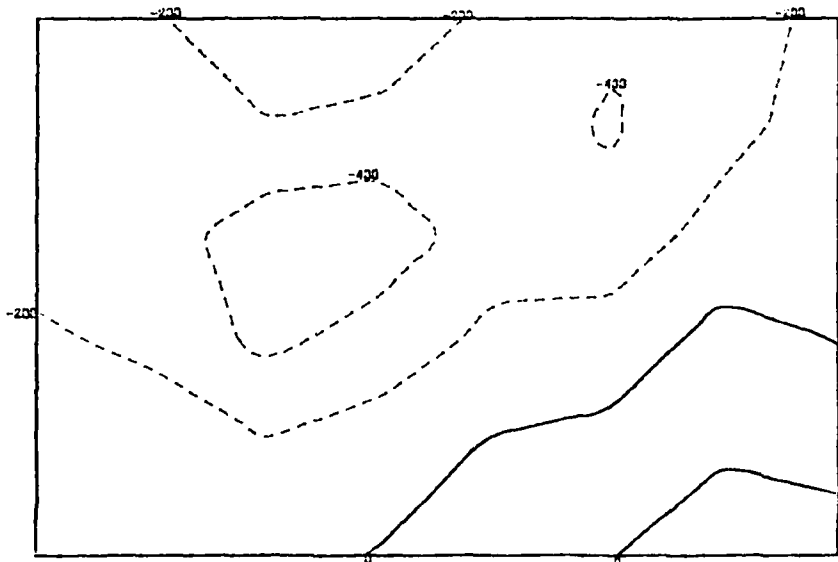
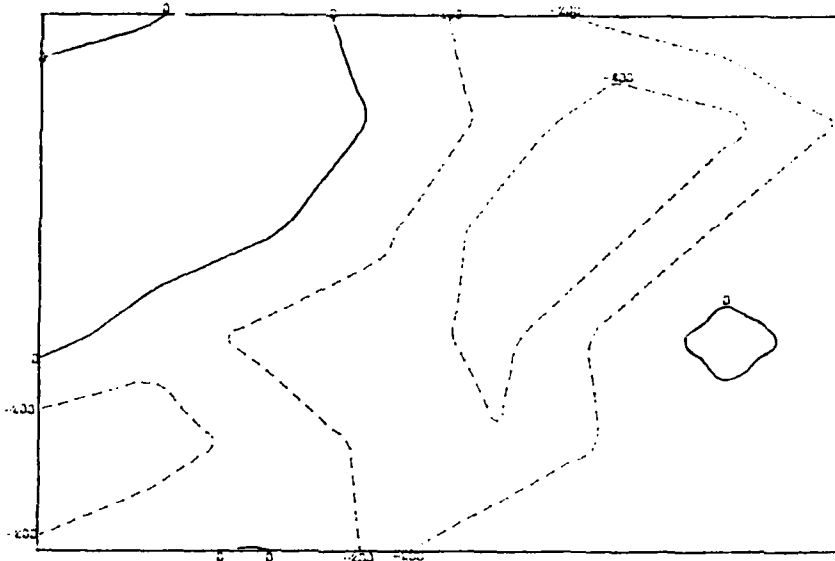
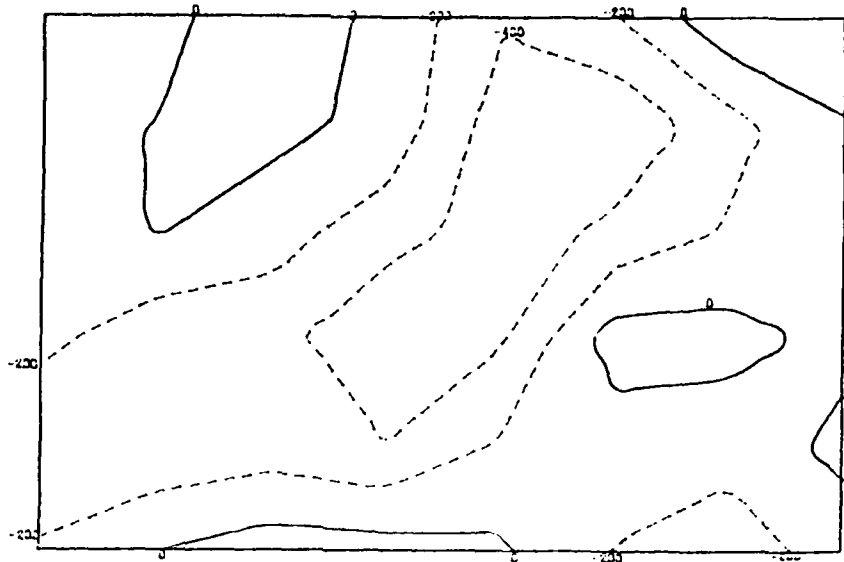


F A C E 7 5 .

D A T E . . . 0 2 5 5

D I V E R G E N C E

T I M E . . . 1 4 5 0

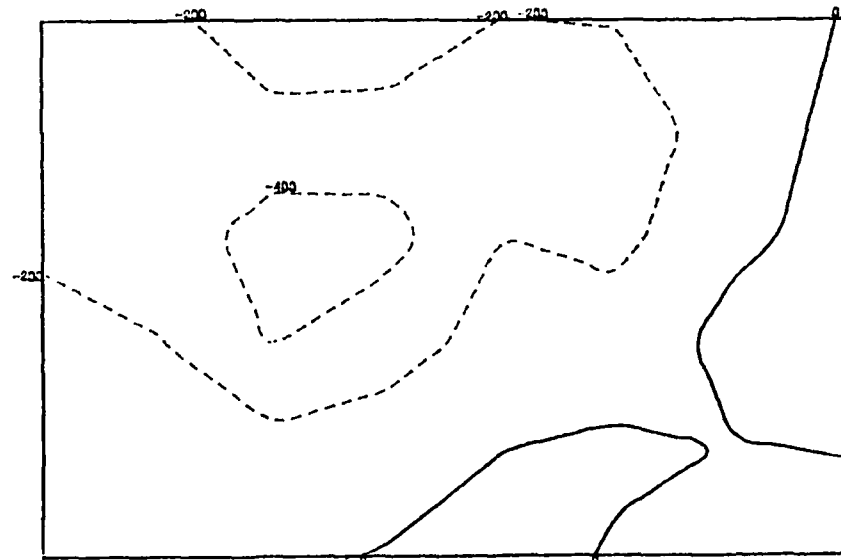
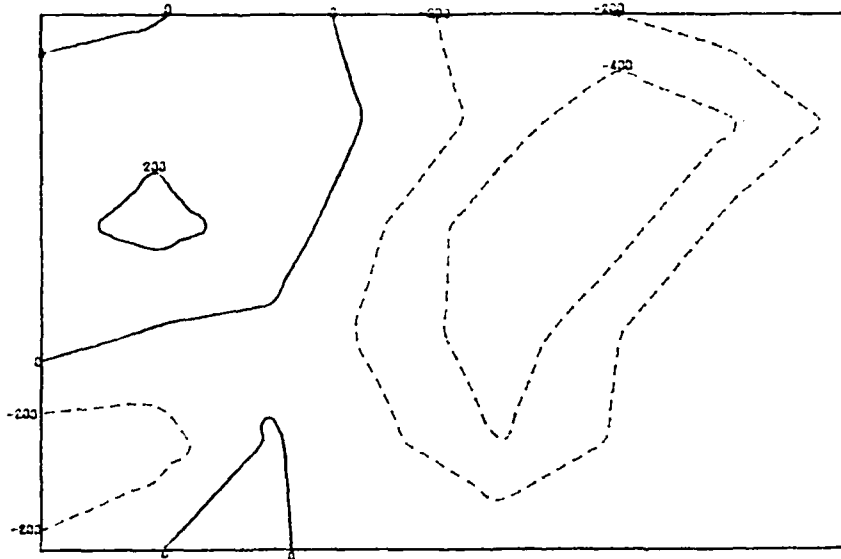
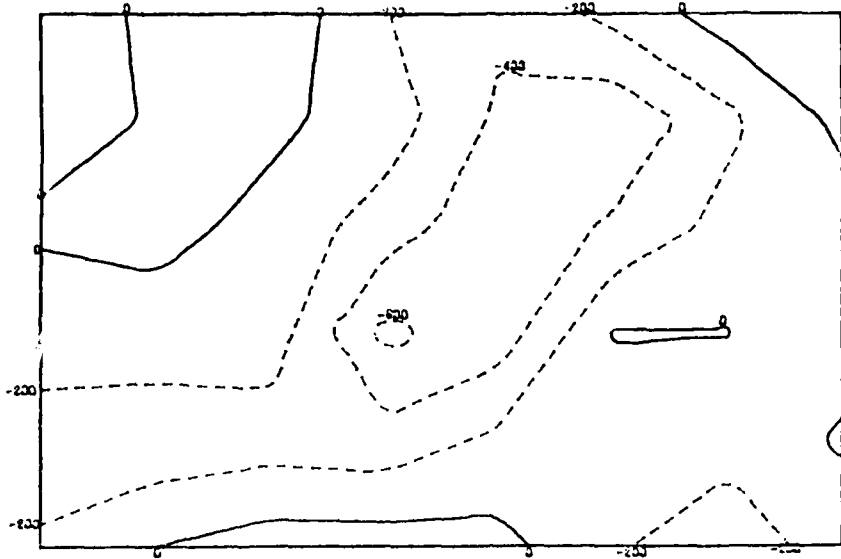


F A C E 7 5.

DATE... 0255

DIVERGENCE

TIME... 1455

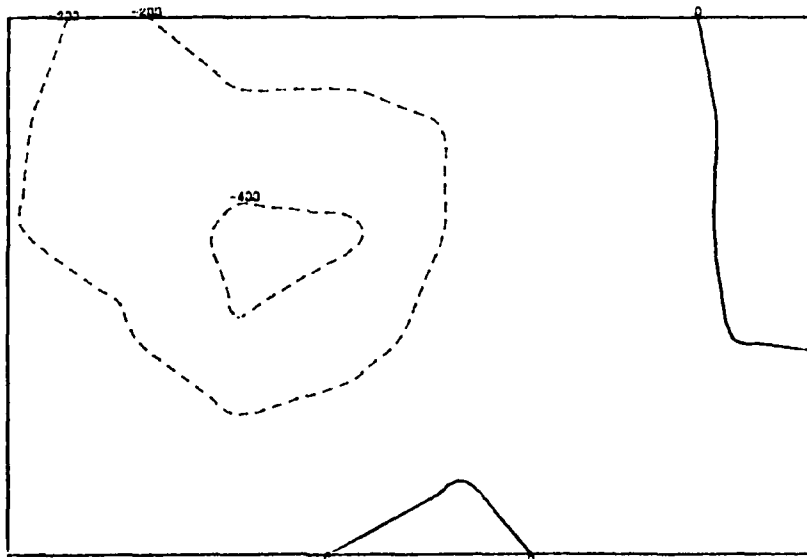
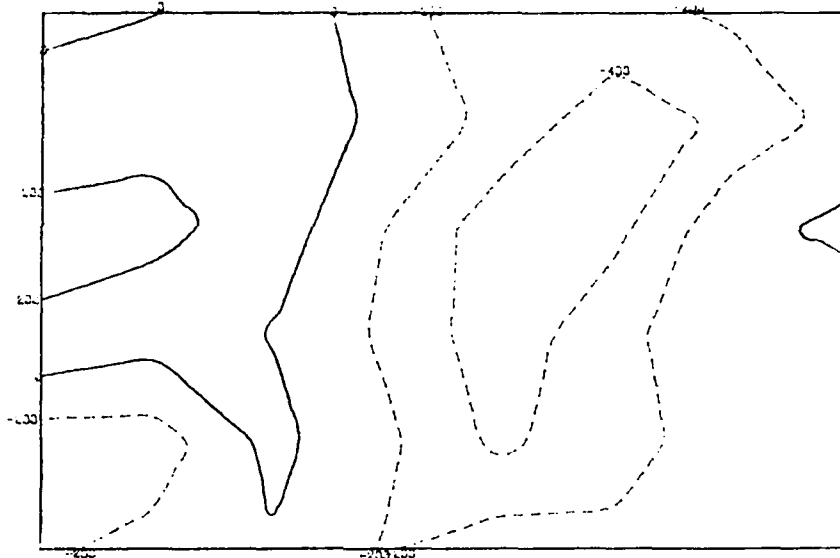
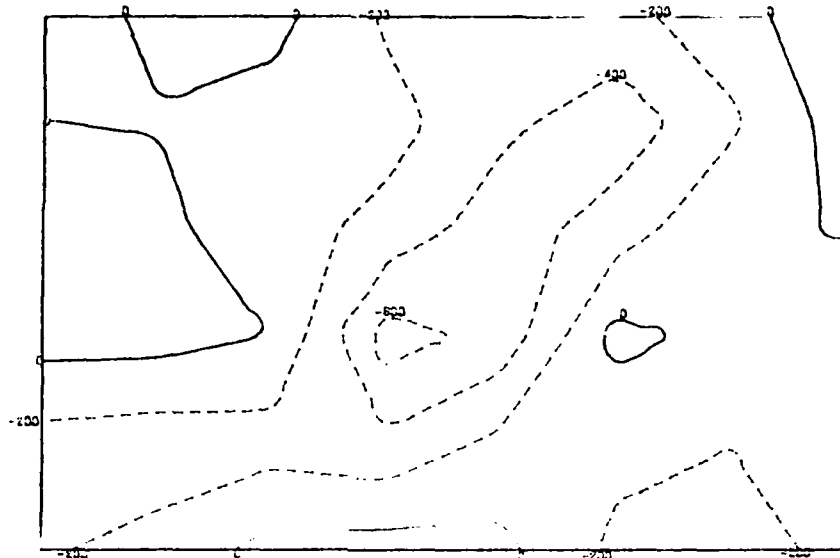


F A C E 7 5 .

DATE . . . 0255

DIVERGENCE

TIME . . . 1500

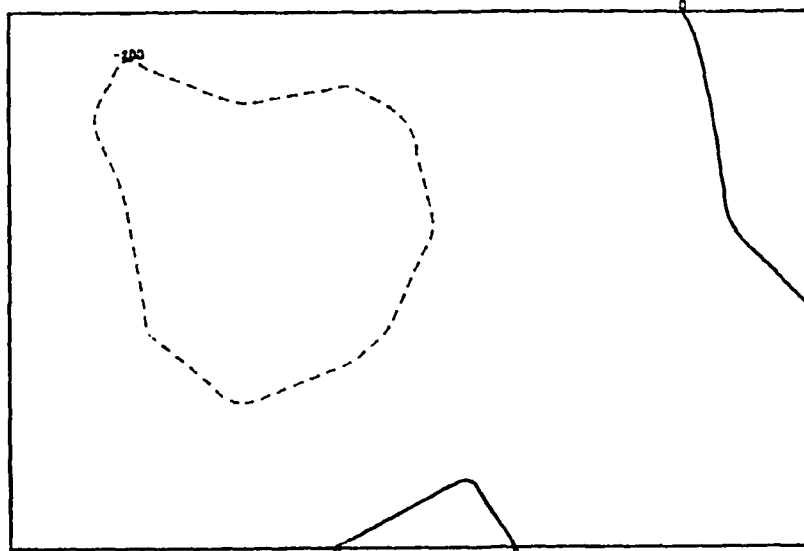
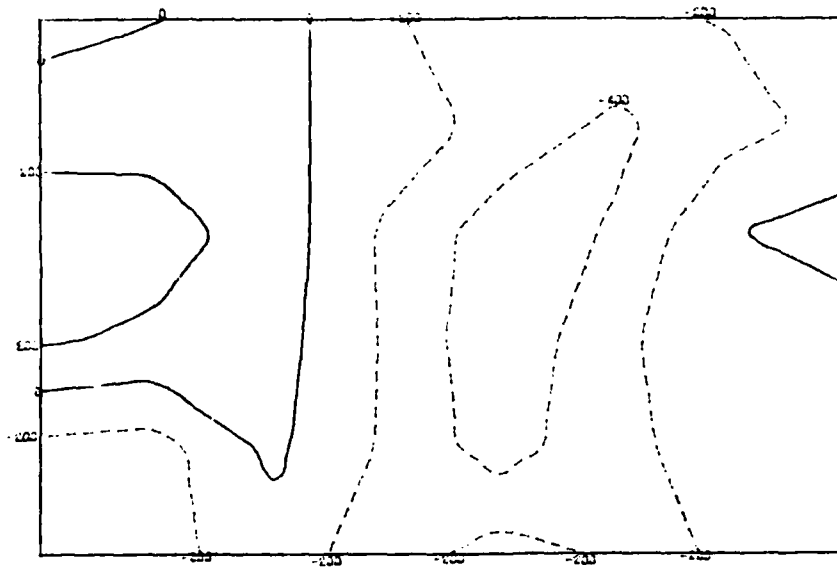
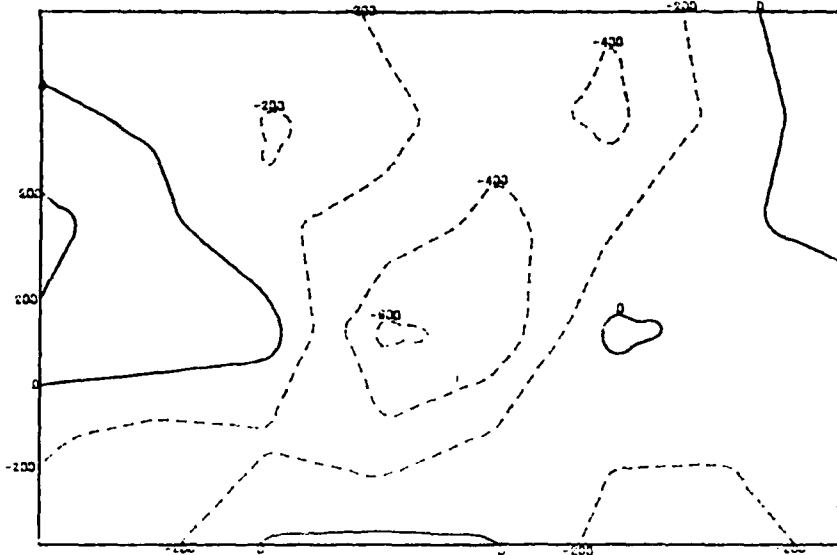


F A C E 7 5.

DATE... 0255

DIVERGENCE

TIME... 1505

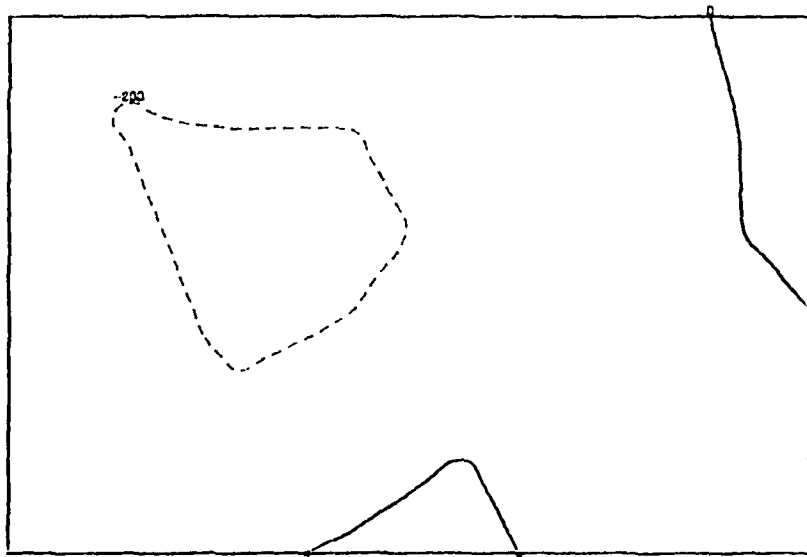
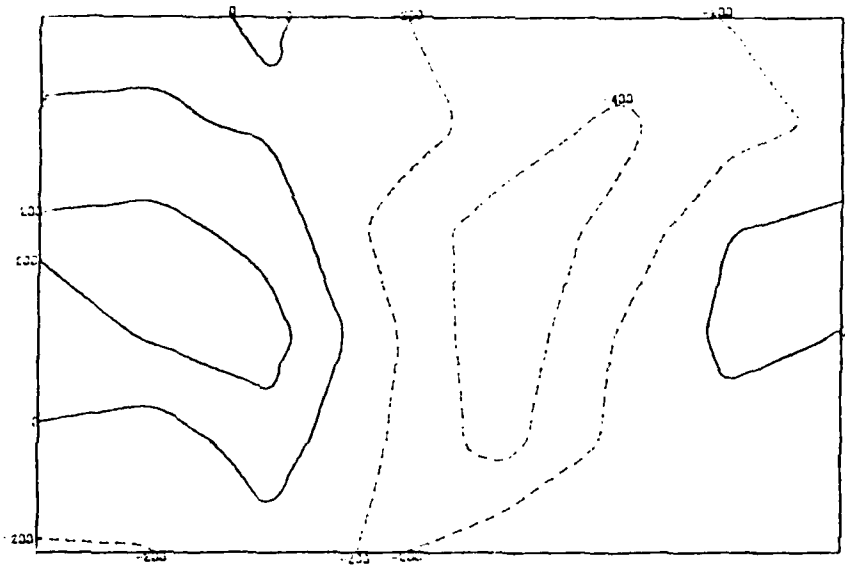
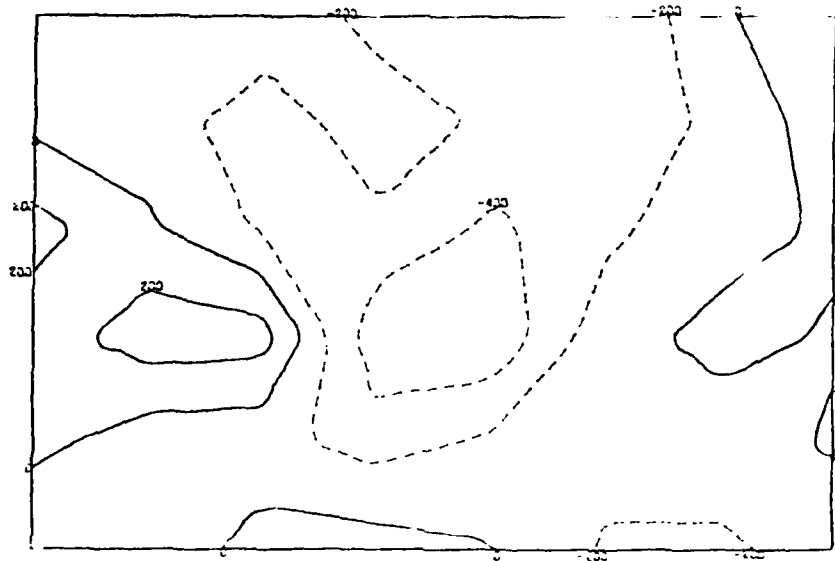


F A C E 7 5 .

D A T E . . 8 2 5 5

D I V E R G E N C E

T I M E . . 1 5 1 0

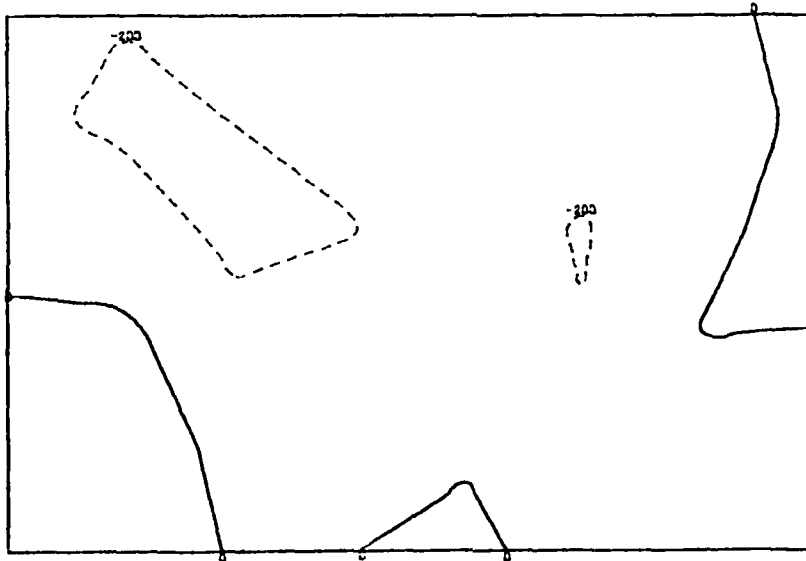
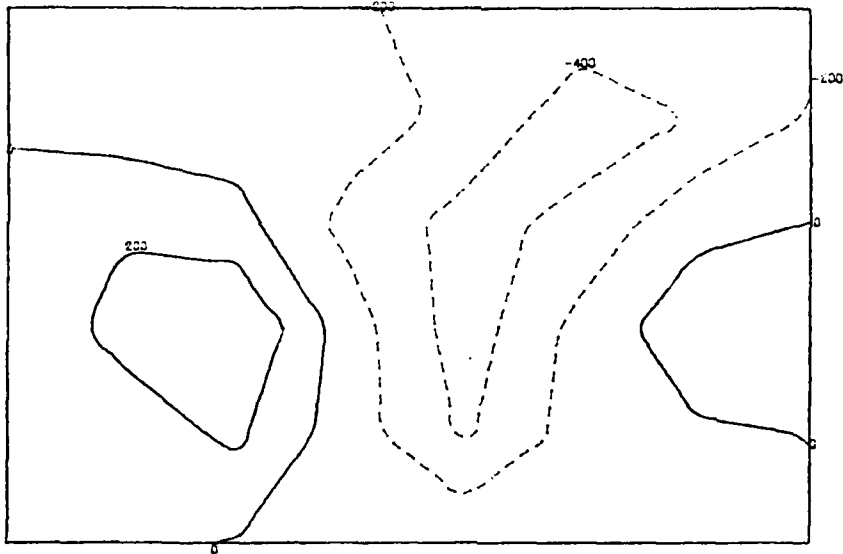
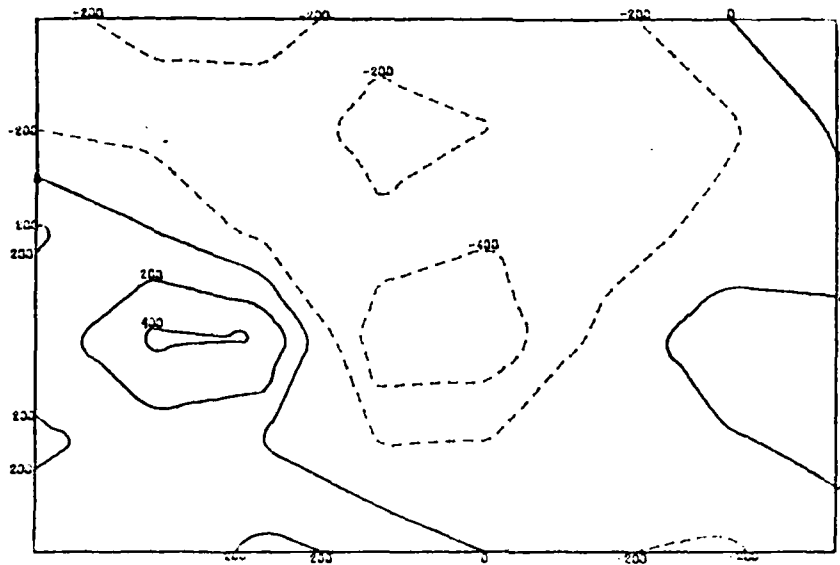


F R C E 7 5.

DATE... 0255

DIVERGENCE

TIME... 1515



after 1500 EDT, hiding the more acceptable divergence zone in the western half of the network revealed by the smaller-scale analyses.

### (3) Discussion

Both case study days presented in detail have shown that the coarser the grid the less the smaller-scale features can be described. This is quite understandable since there are data from only 9 stations to describe features that data from 33 stations described in the 6.4-km grid network.

Table 12 includes the mean quantities, u-component and v-component, and standard deviation for each grid point throughout a 12-hour period (0800-2000 EDT) for all three grid scales on five case-study days. When the different scales are compared, the values for the averaged quantities for each day are quite close. The coarser the grid, the smaller the standard deviation because the objective analysis scheme does much more averaging when there are fewer data. Table 13 shows the average divergence and the mean divergence deviation. The mean divergence deviation is the difference between the "ground truth" divergence at 6.4 km and one of the larger grid scales at each grid point. Little difference is noted between the grid scales. But the standard deviation for the average divergence deviation shows the large variability between the 6.4-km and 19.3-km grids.

Table 14 presents the correlations between the wind components at 6.4 km with each of the larger grid scales. The poorest correlation is found between 6.4-km and 19.3-km grids. This decrease in correlation is shown for each of the individual days.

Since total area divergence is the underlying quantity used to predict area rainfall in this study, total area divergence is examined as determined by the

Table 12. Averaged u-component and v-component velocities for each 5-min grid value for the five case-study days. Standard deviations are in parentheses

Date	Cases	$\bar{u}(6.4 \text{ km})$	$\bar{u}(12.9 \text{ km})$	$\bar{u}(19.3 \text{ km})$	$\bar{v}(6.4 \text{ km})$	$\bar{v}(12.9 \text{ km})$	$\bar{v}(19.3 \text{ km})$
12 August	6912	0.29 (1.24)	0.20 (1.19)	0.72 (1.08)	-0.52 (2.18)	-0.50 (2.09)	-0.57 (1.87)
16 August	6912	-1.52 (1.34)	-1.51 (1.32)	-1.42 (1.02)	-0.24 (1.22)	-0.26 (1.20)	-0.20 (1.11)
19 August	6912	0.18 (1.50)	0.11 (1.47)	0.16 (1.22)	0.03 (1.35)	0.06 (1.32)	-0.03 (1.30)
25 August	6912	-2.68 (1.61)	-2.72 (1.65)	-2.65 (1.48)	-0.84 (1.02)	-0.97 (1.00)	-0.82 (1.05)
26 August	6912	-3.59 (1.73)	-3.46 (1.61)	-3.35 (1.74)	-0.62 (1.05)	-0.67 (1.06)	-0.63 (1.06)

Table 13. Average divergence and average divergence deviation for various grid comparisons for each of the five case-study days, with the standard deviations for each quantity

Date	Averaged divergence( $\times 10^{-6} \text{ s}^{-1}$ )			Cases	Averaged divergence deviation( $\times 10^{-6} \text{ s}^{-1}$ )	
	6.4 km ( $\sigma$ )	12.9 km ( $\sigma$ )	19.3 km ( $\sigma$ )		6.4 vs. 12.9 km ( $\sigma$ )	6.4 vs. 19.3 km ( $\sigma$ )
12 August	-1 (65)	-10 (52)	-2 (63)	6912	8 (117)	1 (140)
16 August	9 (38)	17 (42)	9 (47)	6912	-8 (115)	0 (156)
19 August	-4 (80)	5 (80)	-2 (81)	6912	-9 (127)	-3 (159)
25 August	-66 (52)	-62 (51)	-60 (51)	6912	-4 (104)	-6 (113)
26 August	-57 (38)	-30 (37)	-47 (42)	6912	-27 (128)	-10 (146)
All days	-24 (65)	-16 (61)	-20 (65)	34560		

Table 14. Correlation between wind components at 6.4 km with larger grid scales for five case-study days.

	u-, v-component 6.4 vs. 12.9 km	u-, v-component 6.4 vs. 19.3 km	Cases
12 August 1975	0.92	0.84	13824
16 August 1975	0.90	0.75	13824
19 August 1975	0.86	0.74	13824
25 August 1975	0.94	0.88	13824
26 August 1975	0.93	0.91	13824
All days	0.93	0.88	69120

three grid layouts. Figs. 13 and 14 are the time series of total area divergence for the 6.4-, 12.9- and 19.3-km grids for the two days previously examined in detail, 16 and 25 August 1975. The three examples for 16 August 1975 (Fig. 13) show a remarkable resemblance to each other. Even the smaller features are recorded in the larger grid scales. The striking resemblance between the grids holds true for 25 August 1975 (Fig. 14) also. The spike observed on the 6.4-km and 19.3-km scales between 1430 and 1500 EDT is severely damped on the 12.9-km grid. This is probably due to station selection in the 12.9-km grid.

Table 15 correlates total area divergence for each 5-minute period for each of the case-study days. The best correlation for area divergence is found between the 6.4- and 19.3-km grids. For 720 5-minute periods (all five case days), there is an increase of only 0.03 correlation coefficient for the 6.4-/19.3-km grids over the 6.4-/12.9-km grids. However, the wind component correlations were reversed. Since stronger signals of area convergence lead to heavier convective rainfall, large negative values ( $< -50 \times 10^{-6} \text{ s}^{-1}$ ) of area divergence on the 6.4-km grid scale are correlated with corresponding values of area divergence on the coarser grids in Table 15. Again the correlation between the 6.4- and 19.3-km grid scales yields better results than the smaller-scale data, probably because of station selection.

In summarizing the variable grid study, it has been shown that the smaller the station separation, the better the field describes the actual mesoscale circulations. Little detail is lost in the 12.9-km grid, compared with the 6.4-km grid. The 19.3-km grid yields few or none of the small-scale features. Comparison of wind components of the 6.4-km grid and the larger grids reveals that the correlations drop off considerably between 6.4 and 19.3 km. The mean

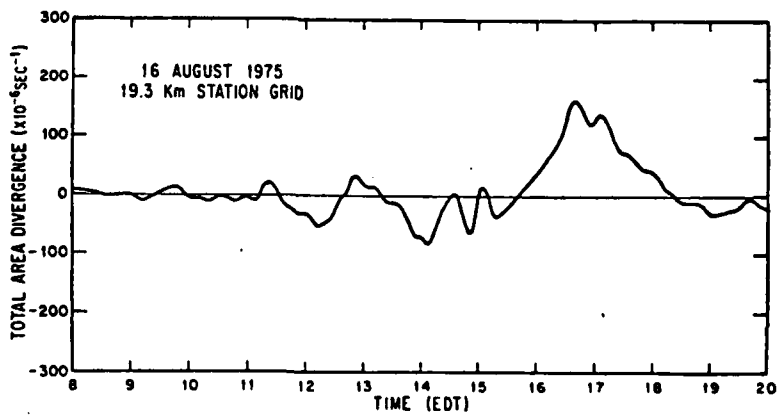
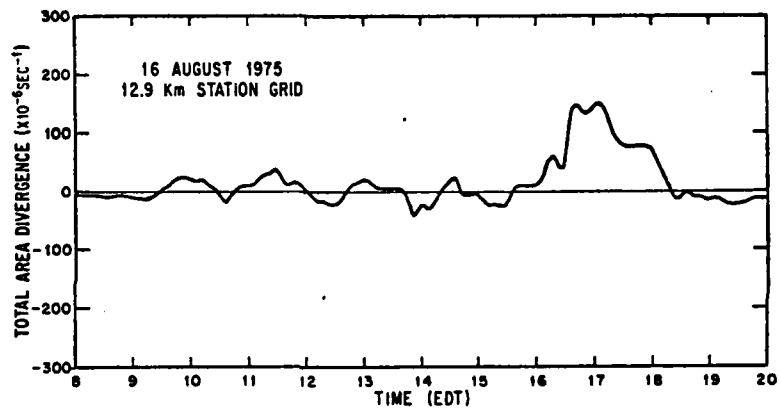
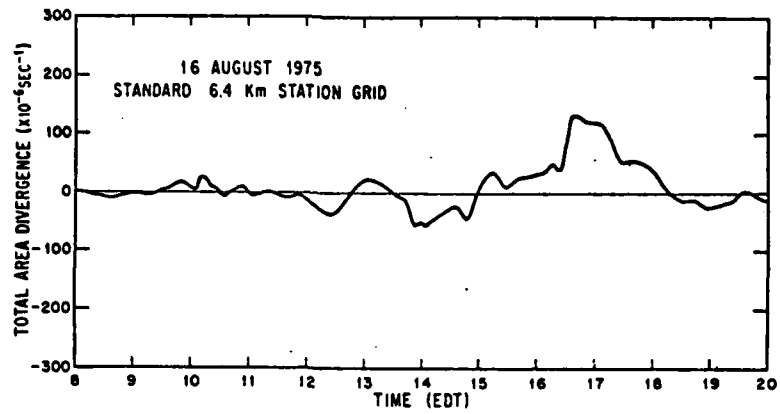


Figure 13. Total area divergence versus time for 16 August 1975  
 a) Standard 6.4 km station grid  
 b) 12.9 km station grid  
 c) 19.3 km station grid

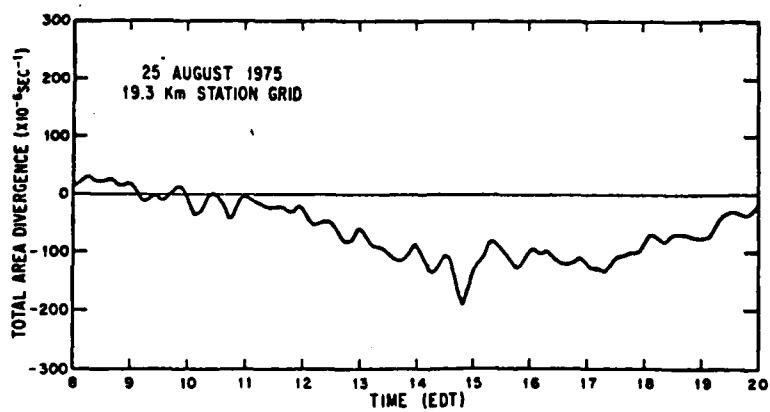
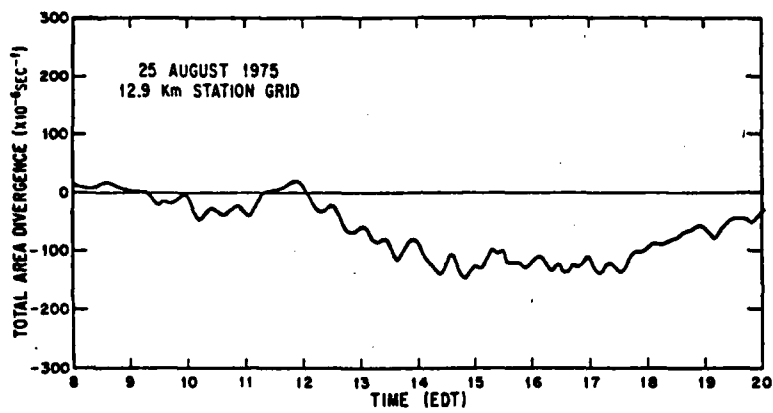
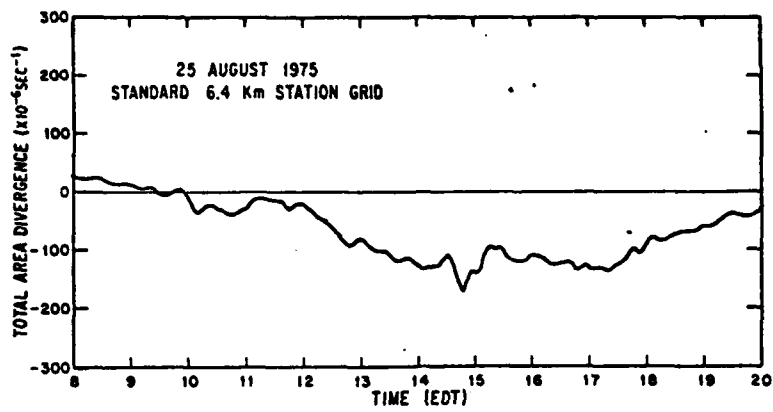


Figure 14. Same as Figure 13, except for 25 August 1975.

Table 15. Correlation of total area divergence at  $6.4$  km versus larger grid scales and correlation of large values of area convergence (less than  $-50 \times 10^{-6} \text{ s}^{-1}$ ) at  $6.4$  km with coarser grid scales

	Cases	Total area divergence 6.4 vs. 12.9 km	Total area divergence 6.4 vs. 19.3 km	Total area divergence $< -50 \times 10^{-6} \text{ s}^{-1}$ 6.4 vs. 12.9 km	Total area divergence $< -50 \times 10^{-6} \text{ s}^{-1}$ 6.4 vs. 19.3 km	Cases
12 August 1975	144	0.92	0.97	0.95	0.95	17
16 August 1975	144	0.89	0.93	0.98	-0.54	3
19 August 1975	144	0.97	0.98	0.86	0.91	27
25 August 1975	144	0.96	0.98	0.87	0.92	82
26 August 1975	144	0.88	0.96	0.82	0.87	85
All days	720	0.94	0.97	0.87	0.95	214

divergence deviation between 6.4 and 19.3 km shows the large variability between the two grid patterns. Finally, the correlations of area divergence between the 6.4-km grid and the coarser grid patterns do not drop off significantly. The correlation signal remains high even at station spacings of 19.3 km.

c. Variable Network Size

Because of the nature of total area divergence or its equivalent, the line integral of divergence, only the flow perpendicular to the boundaries of the mesonetwork is important to the computation of these quantities. There must be a mass imbalance of flow in or out of the network for total area divergence to be effective. If the mesonetwork is composed of several interconnected convergence and divergence centers, then the resulting area divergence may be canceled. If by chance, there is a major convergence zone covering a large portion of the network, then the area divergence would reflect a large negative value. During the decay stage of a convective storm, much of the network is affected by outflow, thereby creating large positive values of total area divergence. It should be possible, when the network is on a scale equal to or smaller than the divergence/convergence zone, to forecast area precipitation solely on the basis of total area divergence.

In the following discussion, examples will be presented to show how focusing on a convective event by decreasing the network size can improve the chance of total area divergence to predict rainfall. 16 and 25 August 1975, which were examined exhaustively in the previous section, will again be presented.

(1) 16 August 1975

A problem with total area divergence is its dependence on the size of the mesonetwork and the convective system being investigated. On 16 August 1975 it

is apparent that the FACE mesonet network is much too large for early growth of convection to be detected. As stated previously, cells remained reasonably small on this day as their outflows initiated new convection through several generations of cloud growth. From 1200 EDT until 1600 EDT, when a major outflow occurred, total area divergence for the entire mesonet network was quite vague in the detection of convergent inflow. The streamline/isotach, radar, and divergence analyses for each 5-minute period between 1300 and 1630 EDT appear in Figs. 7 and 8.

Fig. 15a presents the total area divergence versus time for four variations of network sizes. The variable grids are all subsets of the FACE 1975 mesonet network which is laid out on a 6x8 grid with 6.4-km grid separation. The other grids examined are 4x6, 4x4, and 3x4. The locations of the variable grids relative to the full size 6x8 grid are also found in Fig. 15a. The 3x4 grid has been selected to focus on one particular convective system.

While Fig. 15a shows the time series of total area divergence for the variable network sizes, Fig. 15b is the time series of area rainfall for each grid scale as estimated by the WSR-57 in Miami. It is easily seen that the different scales measure varying amounts of divergence and rainfall. Each scale tells a different story. Very little convergence or divergence is recorded during 1400-1600 EDT in the full 6x8 grid. Even the next smaller scale (4x6) has a confused pattern during that period. But the two smallest scales have very large and distinct convergence/divergence patterns.

The 3x4 grid centers on the east-west line of showers that forms after 1410 EDT (see Figs. 7 and 8) and spreads eastward after 1440 EDT. The strong decrease in area convergence after 1330 EDT (Fig. 15a, 3x4 grid) can be seen in the 5-minute divergence panels (Fig. 8) as a convergence cell beginning to

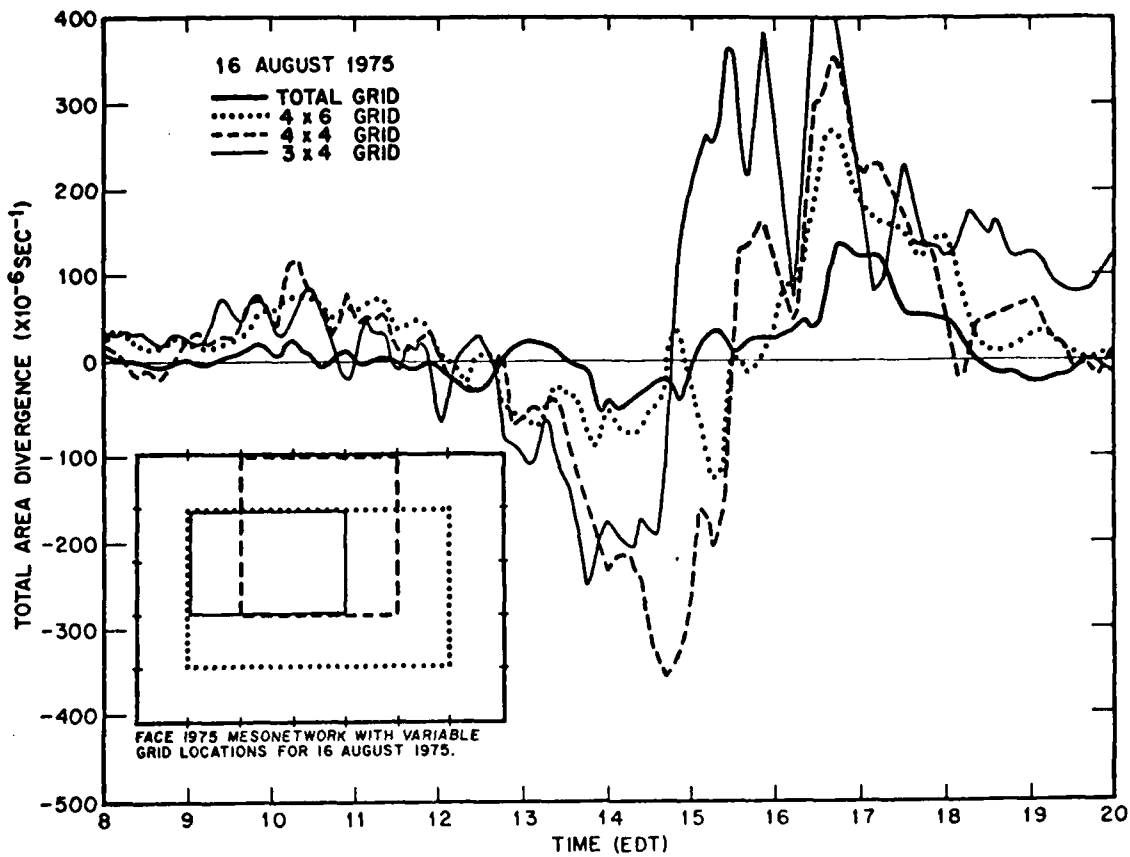


Figure 15. a) Total area divergence versus time for 16 August 1975 at 4 grid sizes. Variable grid locations are found in the lower left corner of graph.

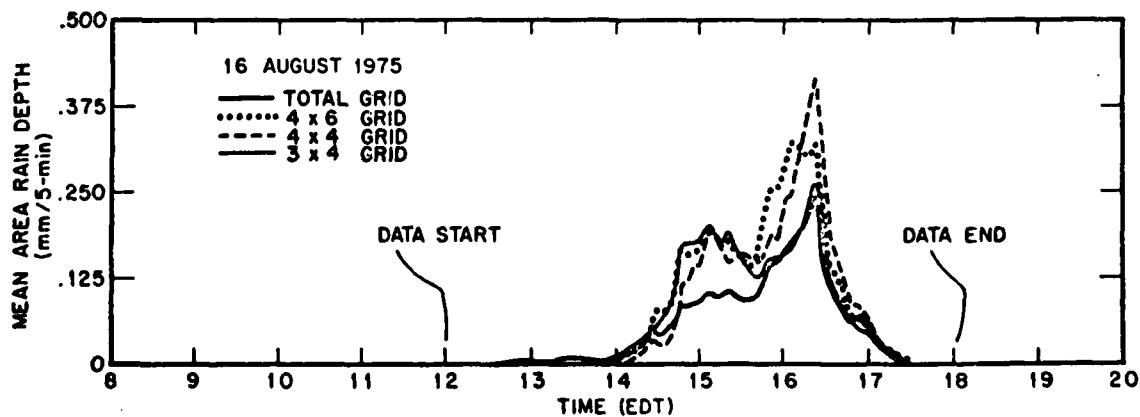


Figure 15. b) Mean area rain depth as derived from radar for the 4 grid sizes on 16 August 1975.

increase in intensity. This convergence cell decreases in intensity after 1345 EDT as a divergent outflow begins to affect the southern fringes of the 3x4 grid. The 3x4 grid also shows an early outflow in the area divergence time series (Fig. 15a) compared with the other scales. The 5-minute panels of divergence (Fig. 8) show an outflow in the region where the 3x4 grid is located as the southwesternmost divergence center reorientates itself to the north after 1440 EDT. In the more east-west orientated grids (6x8 and 4x6), a divergence dipole is set up which cancels any effect and creates a total area divergence near zero. The 4x4 grid records the effect of the convergence cell (seen in panels after 1440 EDT) much longer because it is centered closer to the convergence cell than any of the other grids. By 1520 EDT, the outflow shows a much greater influence in the 4x4 grid, and by 1530 EDT the divergence zone has squeezed out an east-west pattern from the major diffluence zone in the western portion of the network. The radar-estimated rainfall for the four scales (Fig. 15b) shows that the 4x4 grid focuses on the echoes best but that the 4x6 grid is a close second with very little area convergence. The 3x4 scale that records the best early convergence ( $\approx$  1330 EDT) yields the largest amount of early rainfall. It is interesting to note the V-shaped pattern appearing in the 4x6 grid area divergence time series from 1445-1530 EDT. The 5-minute divergence panels (Fig. 8) reveal the weakening divergence cell in the western half of the mesonet network after 1455 EDT while the convergence cell increases and reaches a maximum at 1510 EDT, the same time as the divergence minimum in the time series. The gradual weakening of the convergence cell and the spreading eastward of the western divergence zone is the reason for the large positive area divergence values that occur on all time-series plots after 1600 EDT.

(2) 25 August 1975

25 August 1975 is characterized by two individual cells that are formed in the lake breeze confluent zone and, after initial growth, move westward out of the network. Three of the grid scales examined in the 16 August 1975 study are the same for 25 August 1975, that is, the 6x8, 4x6, and 4x4 grid scales. A new 3x3 grid scale focuses on one of the convective cells during its initial growth stage.

Individual 5-minute panels of divergence, streamline/isotach, and radar analyses are shown in Figs. 11 and 12. Only the period 1430 to 1515 EDT is presented. Fig. 16a is the total area divergence time series for 25 August 1975 for all four grid scales. The relative locations of the grids are found in the lower left-hand corner of Fig. 16a.

All grid scales show the strong mesoscale convergence zone due to the interaction of northerly flow from Lake Okeechobee and the prevailing easterly flow. This zone is shown quite well in the divergence and wind panels (Figs. 11 and 12, top panels). The area divergence time series (Fig. 16a) has the confluent zone beginning at approximately 1300 EDT and continuing very strong until after 1730 EDT.

Attention is centered on the period when the second convective cell begins to develop after 1430 EDT. Radar shows that the first small echo return occurs at 1420 EDT. By 1440 EDT (Fig. 11, top panel), 40 dBz returns are recorded, and at 1545 EDT the cell exits the western side of the FACE mesonet. The time series of area divergence reveals that the 3x3 grid, centered where the echo initially forms, records the largest decrease in divergence. All grid scales reflect the large increase in convergence but the 3x3 scale views it the best. This day is also of interest since this cloud is seeded between

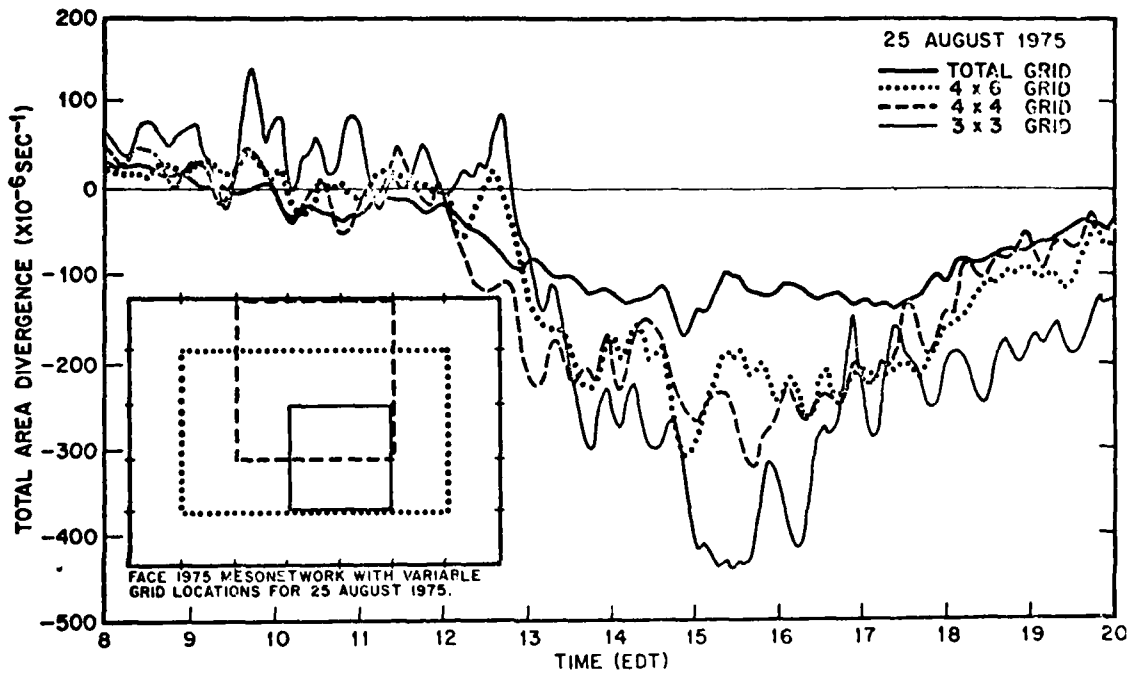


Figure 16. a) Same as Figure 15 a), except for 25 August 1975.

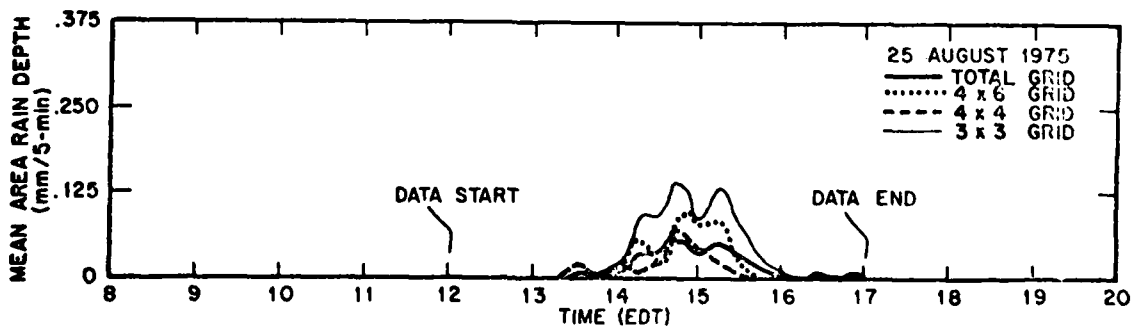


Figure 16. b) Same as Figure 15 b), except for 25 August 1975.

1434 and 1440 EDT (17 flares), and what may be viewed here is the seeding signal that is transferred to the boundary layer as the seeding effect increases the buoyancy of the cloud.

The associated radar estimation of rainfall for each grid scale is shown in Fig. 16b. Again the smallest grid that focuses on the developing cloud records the largest amount of rainfall.

d. Summary

The size of the mesonetwork plays a major role when area divergence is used as a tool for forecasting convective rainfall. The smaller the convective system, the smaller the network required to describe the system. The smaller systems will be lost in a large mesonetwork. If by chance it is possible with a large network of wind sets to focus in on certain regions of convergence, it will be possible to make a convective rainfall forecast for several areas at the same time. However, the forecasting technique is highly area dependent and the strength of total area divergence varies greatly with the size of the region.

## 5. ADDITIONAL RESEARCH BASED ON BOUNDARY LAYER FORCING MECHANISMS AND CUMULUS DEVELOPMENT

### a. Visible Cloud Growth Related to Convergence

The manner in which convection responds to convergence has been shown with the use of radar data in preceding portions of this report. Here, visible cloud growth before radar echoes form will be investigated with time-lapse photographs taken during August 1975, plus the June 15, 1973 case that had been analyzed earlier.

Nine cases were found that were sufficiently well-defined with photographic, radar, and wind data to be intensively analyzed. The first step in finding these cases was to locate periods when a significant but isolated radar echo grew and matured completely within the mesonet network of wind stations. Next, the time-lapse film was searched for the clouds corresponding to the radar echoes. Time-lapse pictures were taken from as many as four locations in the FACE mesonet network on 16-mm color film with Bolex cameras during the late morning and afternoon on many August 1975 days. Nevertheless, in most situations, it was found that the cameras were not directed toward the exact location where the isolated echo was detected, other clouds obscured the view, or the cameras were not operating. In nine cases, however, clouds formed and grew over the wind network in view of a camera, and had a distinct radar echo.

Three events were determined for these cases: time of first convergence (event A), time of first visible cloud response to the convergence (event B), and time of maximum visible cloud growth (event C). First convergence was found to the nearest 5 min from several of the tools available for the studies of convergence and rainfall described earlier in this report. The daily time

profile of area convergence was consulted first at the time near the visible cloud and radar echo growth. In only a few cases was this a sufficient indicator of convergence initiation for the subject cloud, because the cloud's convergence signal was smaller than the wind network, and other divergence/convergence centers affected the line integral for the total network. The daily time profile of weighted convergence was examined next; in several cases the cloud development was clearly shown by this parameter. In remaining cases, the variable grid program was applied to the area where the visible cloud and radar echo developed, in order to isolate the time of initiation of the convergence event. With all of these data sources, maps of the divergence field and streamlines over the mesonetwork were used to help locate the development of the clouds.

Visible cloud initiation (event B) was often rather easy to determine to the nearest 4 min. In several cases, there were no clouds in the surface convergence area, and the time of first cumulus appearance was taken as the time of response to the convection. In the other situations, a disorganized and essentially random field of small cumulus clouds grew horizontally and vertically to become non-random in a rather short time interval. Some of these changes were from random cumuli to a line, and others were to a cluster of cloud elements. Panoramic photographs taken from the Field Observing Site (FOS) were sometimes helpful in augmenting the Bolex photographs from the Clewiston, Pahokee, or NCAR Doppler radar sites.

The time of rapid upward visible cloud growth (event C) was also rather easily found from the same film. This time can best be described as when several or many towers are simultaneously growing upward very rapidly; at this

time the cloud line or complex is passing into the stage where it definitely will become a significant raining cloud. Event C was found to the nearest 5 min.

Table 16 shows the time relationships between events A, B, and C for the nine cases whose data were reasonably accurate. The times and dates of event A, the first convergence time, are shown on the left. The interval from first convergence to the time of non-random cumuli (event B) ranged from 10 to 55 min and averaged 25 min, with a standard deviation of 11 min. It was another 35 min until the rapid upward growth stage (event C) was reached, which was 60 min on the average after event A (standard deviation of 13 min). It should be emphasized that all of these systems were clouds that produced radar echoes and significant surface convergence signatures. The interval between convergence and visible cloud growth would be shorter for clouds that never produced radar echoes. Very few, if any, previous studies have been made of the convergence-visible cloud field relation.

b. Time History of Storm Events Normalized to Duration

The preceding lags of visible cloud growth after the initiation of surface convergence were rather variable from case to case. Not shown in Table 16 is the fact that longer time intervals tended to be associated with longer cloud lifetimes. To equalize this effect, the times of events B and C were normalized to the total duration of the storm system. Event A was chosen as the start of the system's lifetime (0%), and the time of dissipation (100%) was found from radar or time-lapse photos. When the nine cases were normalized on this scale, the bottom line of Table 16 shows that event B occurred at an average of 15% through the lifetime of the cloud entity, and event C was at 36%.

It was apparent from these results for visible clouds that normalizing

Table 16. Times of first convergence, first visible clouds, and maximum upward growth of visible clouds for nine cloud entities located in the FACE mesonet network in 1973 and 1975.

Date	First convergence time in EDT (Event A)	Non-random visible clouds, minutes after A (Event B)	Rapid upward growth of visible clouds, minutes after A (Event C)
15 June 1973	1425 EDT	Est. 35 min	Est. 50 min
08 August 1975	1645	Est. 20	45
12 August 1975	Est. 1720	20	60
13 August 1975	Est. 1425	Est. 25	75
18 August 1975	Est. 1345	15	70
19 August 1975	1450	55	100
20 August 1975	Est. 1545	25	75
25 August 1975 (1)	1305	Est. 20	45
25 August 1975 (2)	Est. 1415	10	20
Time (min)	0	25 min	60 min
Normalized time (%)	0	15%	36%

the events to cloud duration was useful in understanding the variations in time lags between the individual cases. Other specific events were then sought which could be identified for the same nine cases shown in Table 16. These additional events are listed in Table 17. Two wind-related milestones were chosen: maximum convergence (event E) and maximum divergence (event I) associated with the cloud system. They were determined with the same types of information as that given earlier for first convergence (event A). Another pair of events was derived from radar: first radar returns from the subject cloud (event D) and maximum radar-estimated rainfall from the cloud entity (event G). The latter was estimated from a combination of the time history graph of radar reflectivity for the mesonet network, and the magnitude of the relevant echo's returns at 5-min intervals. Finally, rain-gage data were considered for two situations. Event F refers to the first rain on the ground, which was detected either by gages or from time-lapse photos of the cloud. Event H was the time when gages measured the maximum rainfall from the cloud, although there were several instances when the clouds moved out of the gage network, which was smaller than the wind mesonet network.

Normalized times for events A to J were found for the nine cases and are shown in Table 18 and diagrammed in Fig. 17. Average duration (events A to J) for these nine cloud entities was 161 min. The individual events B and C, referring to visible cloud development, shown by Table 16 in minutes, are shown now by Table 18 in normalized times. As mentioned earlier, first clouds appeared (event B) on an average of 15% through the duration of the cloud, and rapid upward growth (event C) occurred 36% into the cloud's lifetime. The first radar returns (event D) also occurred 36% through the cloud system, and in some situations occurred earlier than event C. After another 4% of the duration (6 min),

*Table 17. List of events for study of storm duration in FACE mesonetworks*

Event	Description	Data
A	First convergence above background levels	Mesonetwork winds
B	Visible clouds first appear or are no longer randomly distributed	Time lapse photos
C	Visible clouds start rapid upward growth	Time lapse photos
D	First radar returns from cloud entity	Radar
E	Maximum convergence at cloud entity	Mesonetwork winds
F	First rain on ground	Rain gages and/or photos
G	Maximum radar rainfall from cloud entity	Radar
H	Maximum gage-measured rain from cloud	Rain gages
I	Maximum divergence at cloud	Mesonetwork winds
J	Complete dissipation	Radar and/or photos

*Table 18. Normalized times, as percents of total time, when events A to J (in Table 17) occurred for nine cloud entities in the FACE 1973 and 1975 mesonetworks. Times are normalized to storm duration (given in right column), with event A as 0% and event J as 100%. Normalized averages and standard deviations are at bottom of table. Numbers in parentheses refer to events that were out of time order for that cloud entity*

Date	Event										Duration
	A	B	C	D	E	F	G	H	I	J	
15 June 73	0%	29	38	54	(38)	58	58	69	77	100	130 min
8 Aug. 75	0	14	31	(24)	34	38	45	41-52	59	100	145
12 Aug. 75	0	12	38	(36)	(34)	41	62	missing	69	100	160
13 Aug. 75	0	14	42	(41)	(67)	50	72	69-78	86	100	180
18 Aug. 75	0	9	44	(34)	47	(41)	47	56-66	75	100	160
19 Aug. 75	0	23	43	45	51	51	(62)	55-57	81	100	235
20 Aug. 75	0	13	39	39	39	41	62	(54-62)	69	100	195
25 Aug. 75(1)	0	15	33	33	(22)	41	81	missing	(56)	100	135
25 Aug. 75(2)	0	9	18	(14)	27	32	55	missing	59	100	110
Average	0	15	36	36	40	44	60	61	70	100	161
$\sigma$ (n-1 method)	0	7	8	12	14	8	11	10	11	100	38

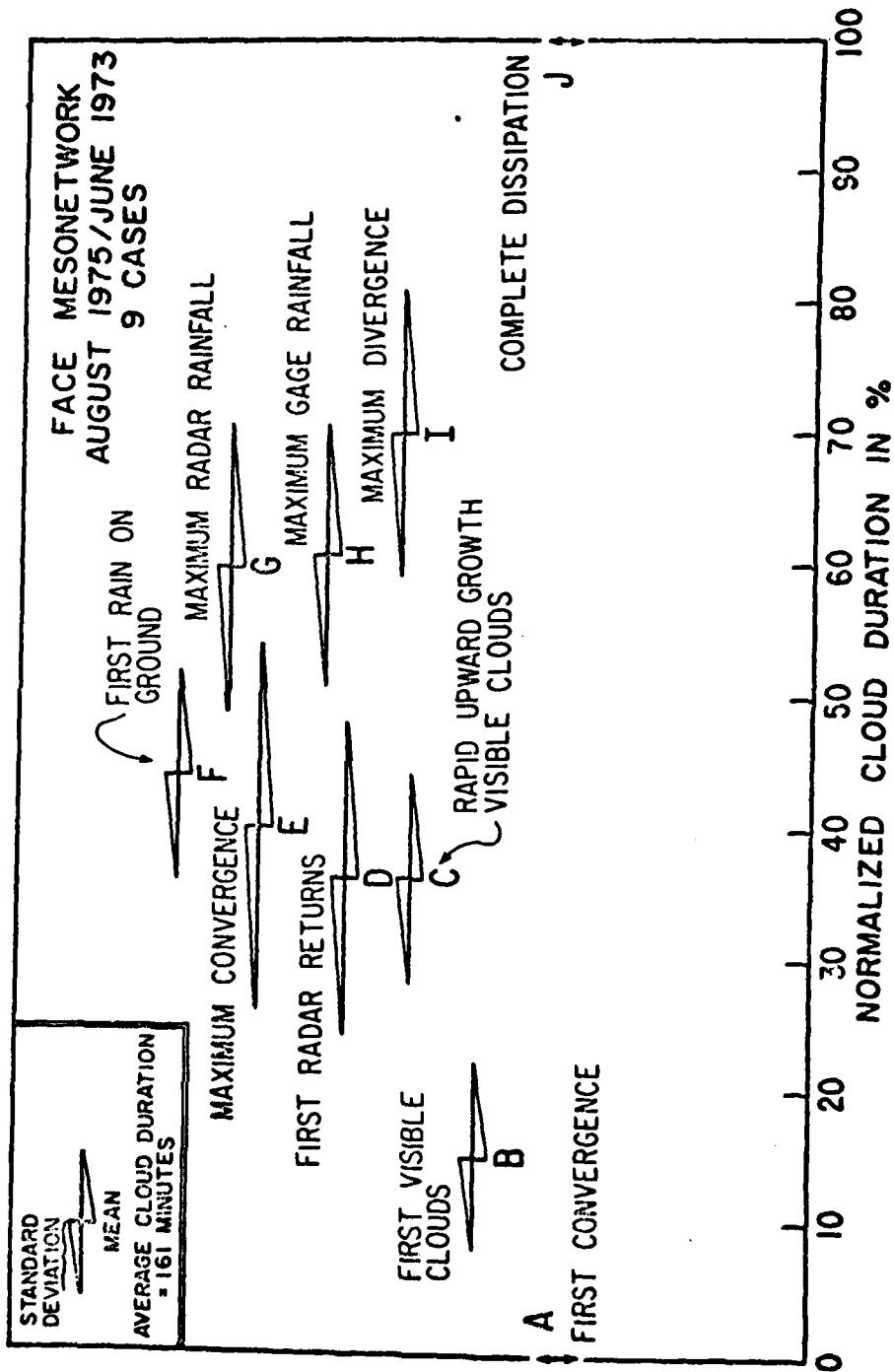


Figure 17. Normalized cloud duration in % for events A to J during 9 cases of cloud entities appearing in FACE mesonet network during August 1975 and June 1973. Mean % of each event is located at center of diamond, and standard deviation is shaded to either side.

maximum convergence occurred (event E), followed 6 min later by first rain on the ground (event F). It is interesting to note that the time interval between first radar and first gage detection of rainfall averaged 13 min. The mature stage of the cloud systems is shown by the next three events. The order usually was maximum radar-estimated rainfall (event G) at 60%, maximum gage-measured rainfall (event H) at 61%, and maximum surface divergence (event I) at 70% of the storm's duration. The dissipation stage from that point to the complete disappearance of the cloud entity (event J) was another 30% of the cloud lifetime, compared with 15% from first convergence to first visible clouds.

A clear indication was given in Table 18 that specific events in a cloud lifetime tended to occur at similar stages of a cloud's evolution when the duration is taken into account by normalizing events to cloud lifetime. How well this relation applied was found by correlating (1) the interval from event A to each event with (2) duration of the cloud entity. Table 19 shows that all correlations are uniformly high for the nine cases given in Tables 16 and 18. That is, the length of time taken by a cloud to reach each stage of its life cycle is highly correlated with how long the cloud will last. This conclusion has obvious and important implications for nowcasting applications. Two factors should be recognized in these high correlation coefficients. One, the clouds in the sample are somewhat larger than the average raining cloud, since they were chosen for their ability to be identified and tracked throughout their duration. They are, however, typical of the more important rain-producing clouds that occurred in August 1975 in the FACE mesonet network. Two, the correlations are not completely independent, since they both count time from event A and use the same duration for normalization.

Table 19. Correlation coefficients between (1) the time interval from Event A to each event and (2) total lifetime of the cloud system. Same nine clouds are used as shown in Table 18

Time between events	Description	Correlation coefficient with duration of cloud
A + B	First visible cloud reaction	0.72
A + C	Rapid upward growth	0.96
A + D	First radar rainfall	0.87
A + E	Maximum convergence	0.86
A + F	First rain on ground	0.90
A + G	Maximum radar rainfall	0.83
A + H	Maximum gage rainfall	0.80
A + I	Maximum divergence	0.95

### c. Merger of Radar Echoes and Visible Clouds

Cloud merger is a major component of cloud growth and interaction. Merger has been evaluated in the past on the basis of radar only, while the evolution and configuration of a merger as detected by other parameters has not been addressed. Radar echo evaluation for the FACE project has recognized that merged echoes produce much more precipitation than unmerged echoes (Simpson et al., 1980). For the FACE program, merger has been described as the joining of two adjacent echoes at the  $2.3 \text{ mm h}^{-1}$  rain rate (Woodley and Sax, 1976) on the WSR-57 10-cm radar operated by the National Hurricane Center (NHC) in Coral Gables. Other FACE radar studies (Simpson et al., 1980; Westcott and Simpson, 1980) have used  $1.0 \text{ mm h}^{-1}$  as a merger criterion in studying frequency distributions and other statistics of mergers, while several other investigations have been made with a definition including the length or separation of echoes before and after merging (Changnon, 1976; Houze and Cheng, 1977).

The data described here were collected during FACE 1975 within range of the NHC radar. When the August radar data were being searched for the cases of convergence related to visible cloud growth, examples were also being sought for radar echo merger. Two separate echoes in or near the mesonet, and in view of the surface time-lapse cameras, were needed for examples. One particularly good case (August 19) and two other less complete cases (August 12 and 25) were found.

The August 19 case occurred over the rain-gage network, and the major events in its time history were given in Tables 16 and 18. First convergence began at 1450 EDT, and the beginning stages of a cloud line became apparent in the visible cloud field at 1545 EDT. By 1615 EDT, visible clouds in this line

had begun to merge at cloud base. It should be emphasized that linking of the clouds at low levels began at this time, and grew to deeper levels over the next hour as the cloud line grew. However, there was no radar echo at this time from the cloud line, and the standard definition of merger as a radar phenomenon had not occurred. A merger of visible clouds had taken place, however, at low altitudes.

Cloud-scale views of radar, rain-gage, and visible cloud data were prepared at 5-min intervals beginning at 1635 EDT and continuing for the next half hour. This area consists of the rain-gage network whose boundary is enclosed by dashed lines in Fig. 2. This region was seen commonly by 16-mm time-lapse cameras on August 19 from the Clewiston and Pahokee Doppler radar sites (Fig. 2). Cloud positions were mapped by the photogrammetric techniques developed for this study and described in detail earlier in Section 2g.

The top of Fig. 18 shows the views from Clewiston and Pahokee of two major clouds, A and B at 1635 EDT. The two are connected at cloud base and slightly above. Note a larger unlabeled cloud mass on the right side of the Pahokee photo. This quite mature cloud is not visible from Clewiston, and is west and southwest of the analysis area. Triangulation of azimuths produced the map of visible clouds in left center. Rain gages measured light precipitation at a few locations in the southwest corner of the analysis area (lower left), while radar (right center) showed an area of echoes of moderate intensity on the southwest side. When the three fields of data were combined (lower right), gage rainfall was found mainly under the maturing cloud mass to the southwest of cloud A. Radar echoes coincided with cloud A and these mature clouds. Overall, then, oldest clouds were on the west side and newer clouds on the east.

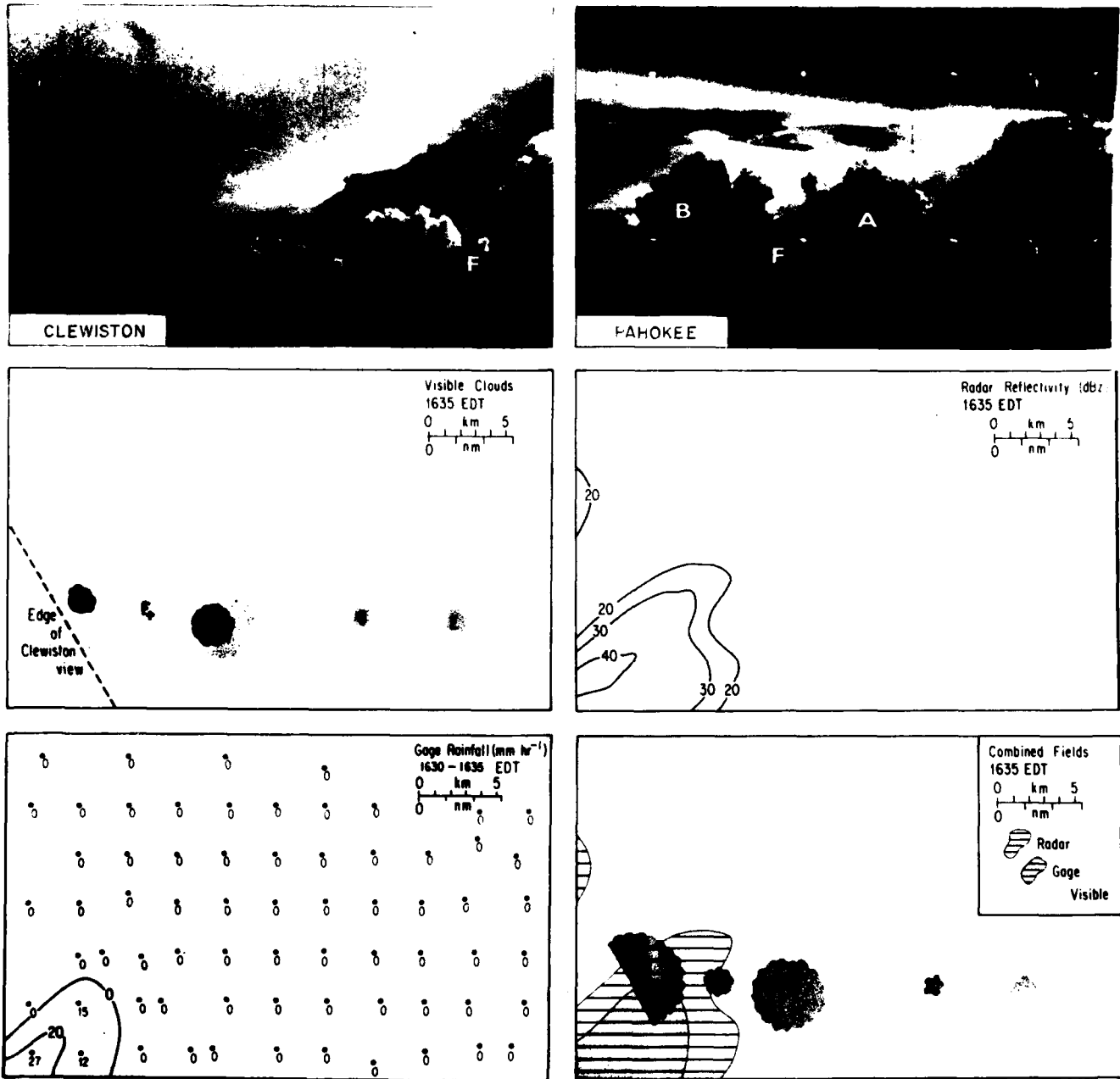


Figure 18. Cloud-scale data on 19 August 1975 in the FACE mesonet network at 1635 EDT. Upper: Clewiston and Pahokee photos at 1635. Left center: map of major visible clouds mapped by triangulation of azimuths from common views at Clewiston and Pahokee. Right center: radar echo pattern from Miami WSR-57. Lower left: rain gage data and subjective isohyet analysis for 5 minute period ending at 1635. Lower right: combined data superimposed for comparison. Shading indicates major visible clouds, dots show rain detected by gages, and horizontal hatching represents radar echoes over 20 dBz.

From 1632 to 1642 EDT, the top height of cloud B was measured rather accurately from the two cameras. Cloud B started near 6 km at 1632 and reached the level of prevailing cirrus near 9.5 km 10 min later. During this period, the rise rate of the tower was increasing from  $2 \text{ m s}^{-1}$  to a maximum of  $12 \text{ m s}^{-1}$  at 1638 EDT. Other clouds in the line appeared visually to grow at a similar rate but were not amenable to as detailed analysis as was cloud B; these rise rates are substantial but not extraordinary for FACE.

By 1645 EDT, major growth had occurred in the analysis area. In Fig. 19 cloud A has become quite mature, while B has a significant new tower growing on the east side (left side of Pahokee photo). Cloud C has continued to grow rapidly, while D has reached the cirrus level and E is well embedded in the cirrus. A major gap (above cloud base) continued to be evident between cloud B and cloud complex C-D-E, especially as seen from Pahokee. However, in the 4 min preceding 1645, the gap between B and C-D-E became several km smaller as new clouds grew to bridge (Simpson et al., 1980) the gap. Not only was the radar echo area at 1645 EDT much larger in the region of cloud B, but a new echo had developed to the east over clouds C, D, and E. Note that the two echoes are completely separate at this time. The area of surface rainfall is nearly as small as 10 min earlier, although the area of radar return has greatly increased.

Major changes occurred during the 5 min ending at 1650 EDT (Fig. 20). Rain gages measured precipitation from the eastern clouds for the first time. Radar at 1650 showed a connection across the gap between the two major echoes. However, the radar merger at 1650 was not at a sufficiently high level of return to be considered a "merger" under FACE definitions using either the  $1.0$  or  $2.3 \text{ mm h}^{-1}$  definition. Three new towers grew in the last 5 min and are visible in the

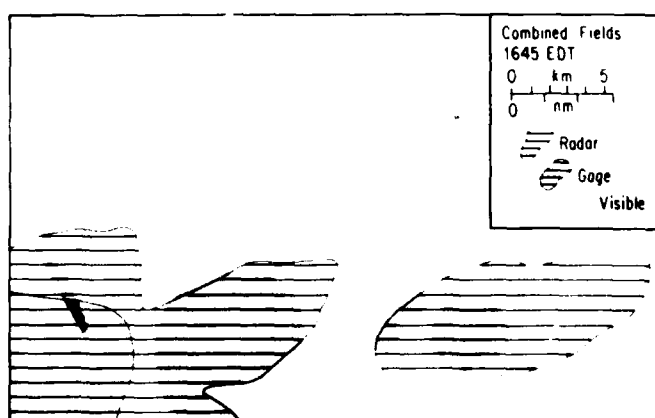
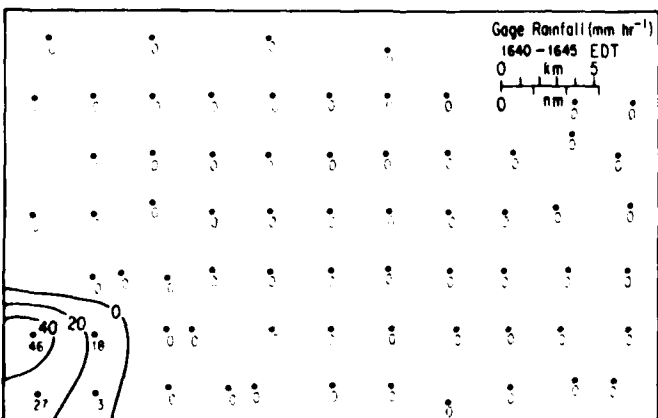
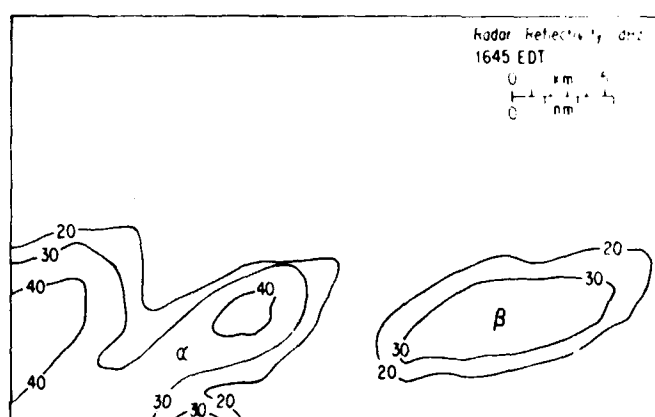
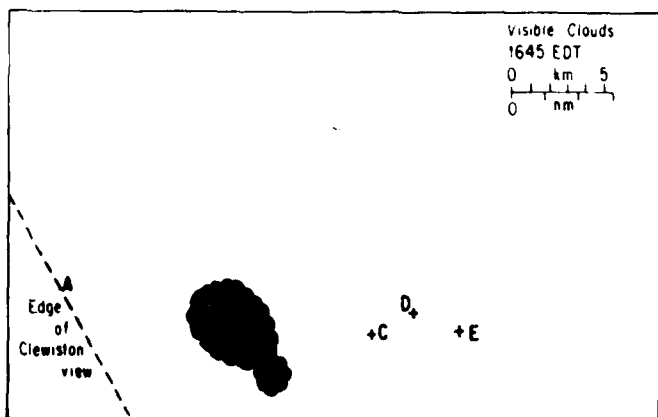
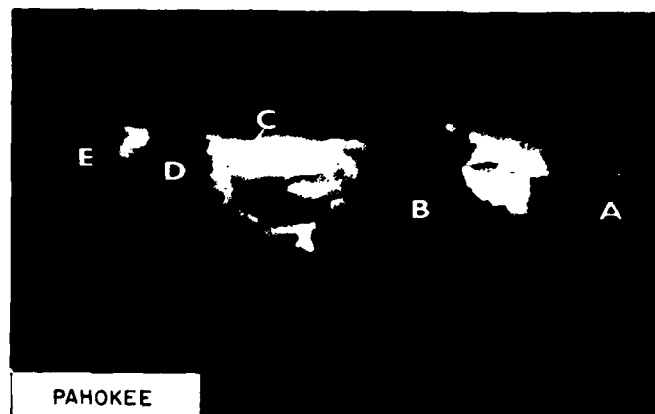


Figure 19. Same as Figure 18 except at 1645 EDT.

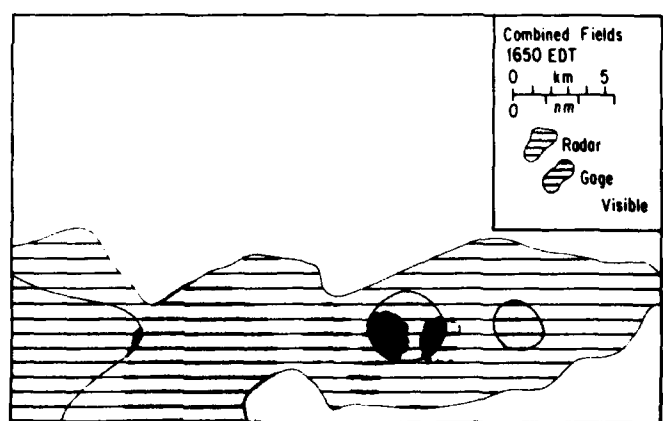
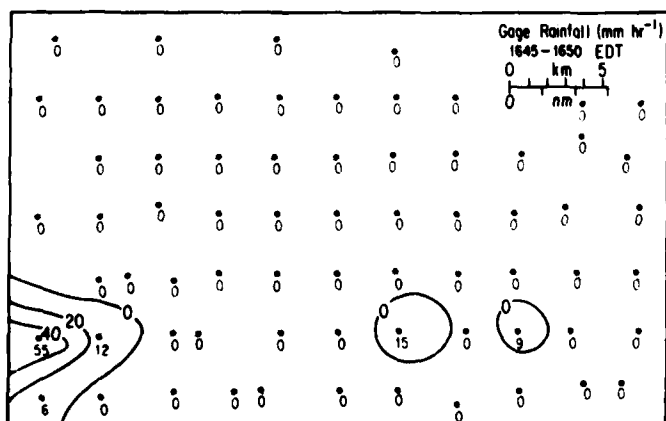
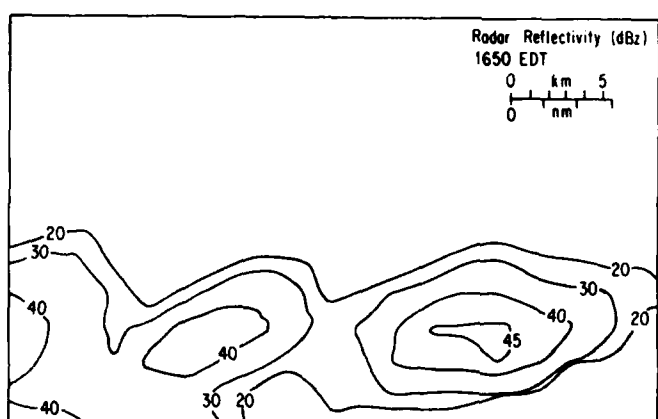
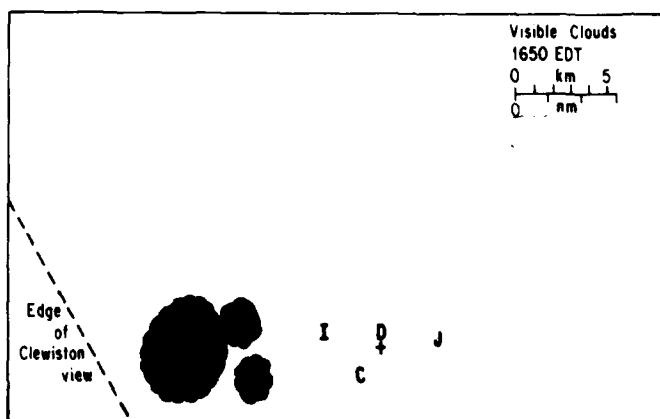
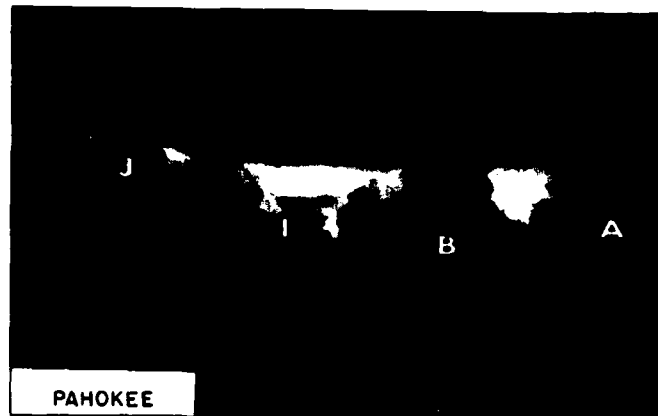
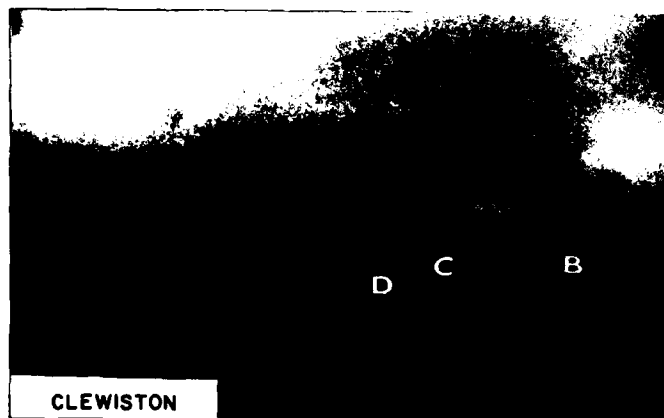


Figure 20. Same as Figure 18 except at 1650 EDT.

Pahokee photo. One was the rather hard, growing cloud I, which rose from cloud base within the last 5 min, from a location where there had previously been no tower. The second tower, on the east (left) side of cloud B, grew rapidly into the cirrus within the last few min from within the body of cloud B on the side toward the gap between B and the eastern clouds. The third tower, J, replaced E in the same location. The only remaining space between visible clouds is above tower I, so that visible clouds have bridged from cloud base to more than halfway to the cirrus level at about 9.5 km.

Merger of both radar echoes and visible clouds to 9 km took place at 1655 EDT (Fig. 21), but gage-measured rainfall was not merged into a line. Radar echo maxima have merged across the gap between the eastern and western echoes that existed at 1650 not only at 20 dBz, but above 35 dBz. Visible clouds also merged at 1655 EDT up to 9 km or higher. There had been a bridge at cloud base between some clouds in the line for nearly an hour, but at 1655 there was a solid row of cumulonimbi extending from cloud base to cirrus level. At 1650, there was some clear sky visible between clouds, but at 1655 only some relatively light areas (marked 1, 2 and 3) remained between major clouds on the Pahokee photo. Separate clouds continued to be mapped at 1655, since the cloud entities could be identified rather well in the time lapse view until then.

The echo merger can be identified as resulting from the following phenomena in the visible cloud field: (1) a new tower grew rapidly upward from cloud base in the location where a gap had been located between visible clouds, which was the echo-free area on radar, (2) a large new tower grew on the side of an older echo toward the gap, (3) a new tower rapidly grew upward to one side of the gap in a place where another cloud tower had located, and (4) the body of a major

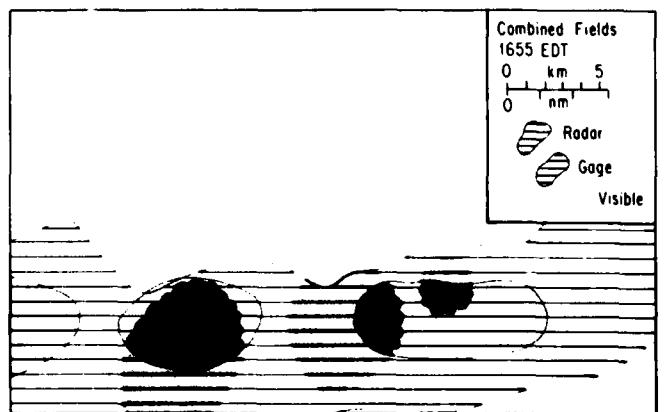
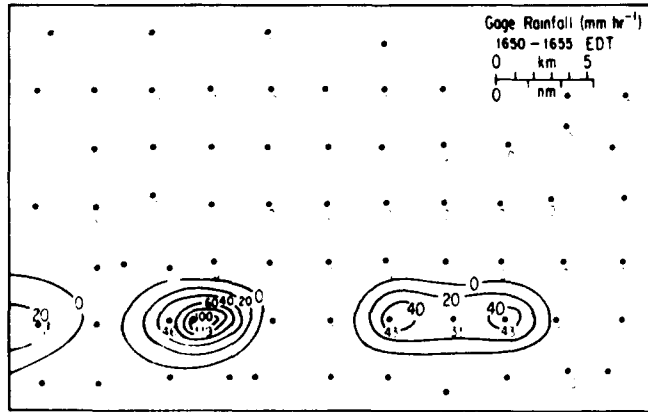
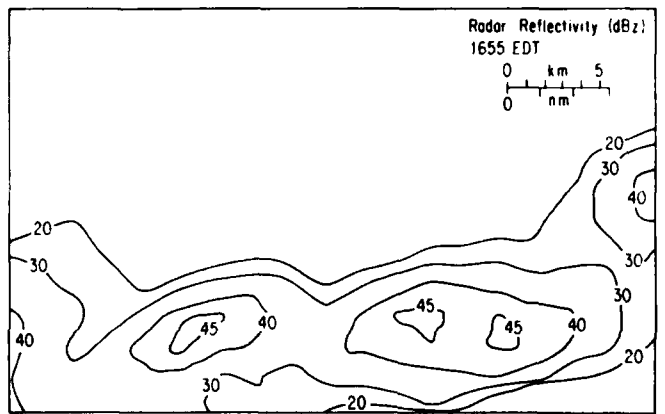
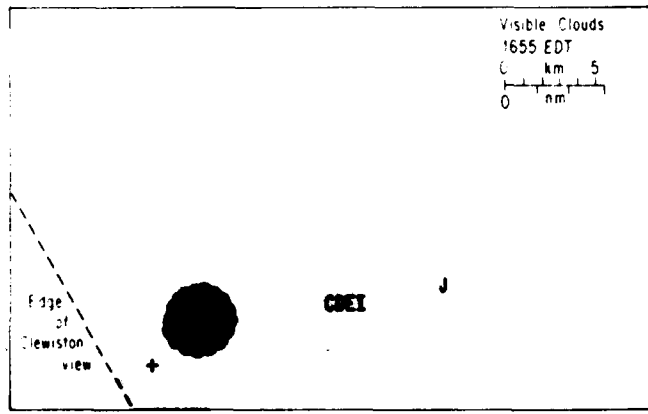


Figure 21. Same as Figure 18 except at 1655 EDT.

cloud on one side of the gap failed to move horizontally, while smaller clouds on the other side moved toward the gap. This combination of new towers growing and moving into the empty space between other clouds produced the radar echo merger.

The rain-gage pattern continued to show separate maxima until the 1705 to 1710 EDT period (Fig. 22), when a continuous line of gages measured rainfall from east to west across the network in a manner similar to that during time of radar merger 10 to 15 min earlier at 1655 EDT (Fig. 21).

Since the August 19 case was the first study of the relation between radar echo merger and other parameters measured concurrently, additional instances were sought in order to consider whether the distance from radar to merger, type of radar, echo size, or meteorological situation affected the relationships shown for August 19. Two other cases of echo merger on August 12 and 25, 1975, were analyzed in much less detail in order to determine whether the August 19 result applied; that is, echo merger coincided with merger of actively-growing visible clouds to above 9 km. The same radar was used in all three cases, and the distance to the mergers was nearly the same. Both August 12 and 25 were presented among the nine cases in Tables 16 and 18.

On August 12, a very strong gust front moved across the mesonet network from the north, with winds gusting to  $15 \text{ m s}^{-1}$  behind the front. When the northerly winds met the prevailing southeasterly flow, a convergence area was formed over the network and new echoes began to form. The new echoes were widely separated at first at 1825 EDT (Fig. 23). The radar echo in the center of the map at this time corresponds to the major but isolated cumulonimbus shown at 1825 EDT in Fig. 24. During the next 10 min, the two radar echoes grew closer to each other. At 1830 EDT, Fig. 24 shows that some growth has occurred in the line of clouds

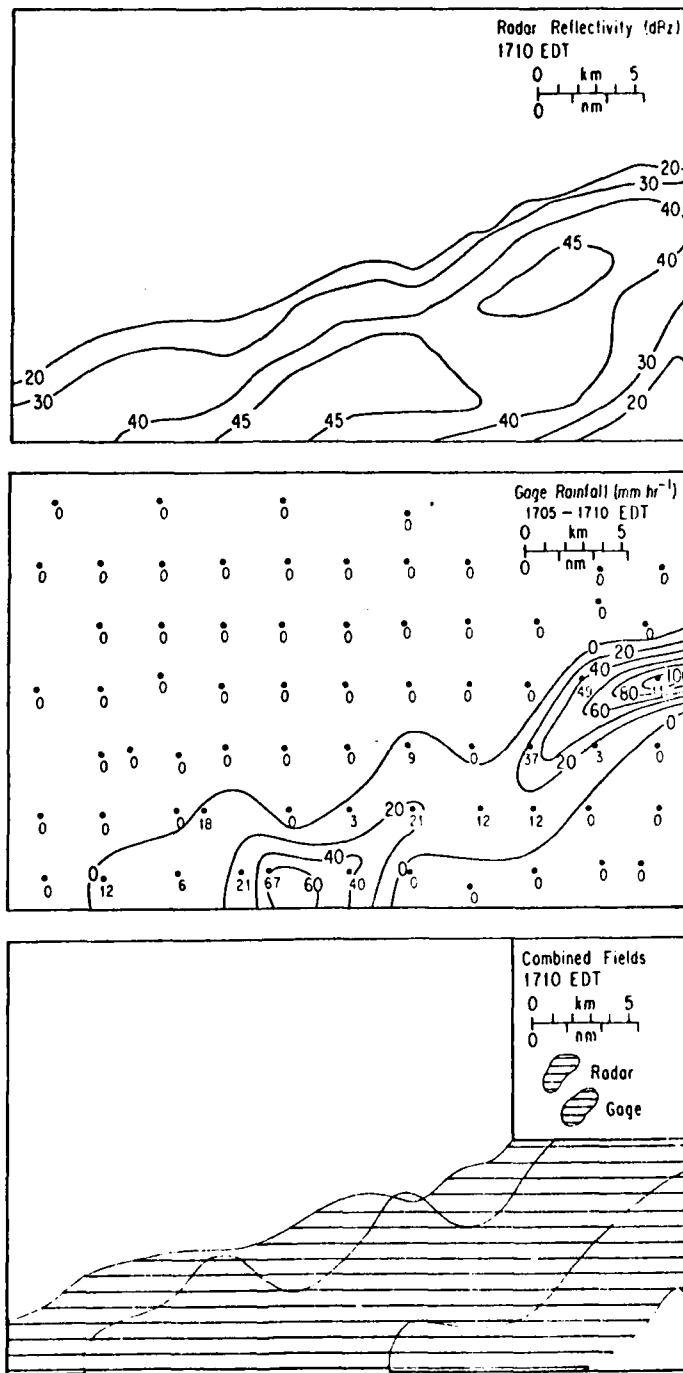


Figure 22. Upper panel: radar echo pattern from Miami WSR-57 at 1710 EDT. Middle panel: rain gage data and isohyet analysis for 1705 to 1710 EDT. Lower panel: combined data superimposed.

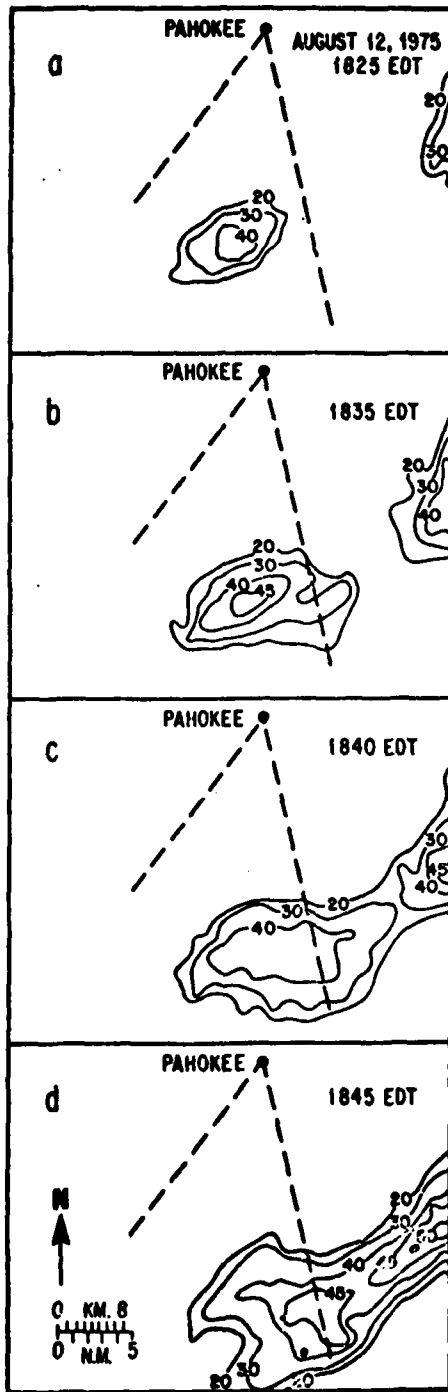


Figure 23. Radar echo pattern (in dBz) over the FACE mesonet network at 4 times on 12 August 1975. Dashed lines show limits of view in photos from Pahokee camera.

AUGUST 12, 1975  
SOUTH FROM PAHOKEE



1825EDT



1830 EDT



1840EDT



1845EDT

Figure 24. Photographs at 4 times on 12 August 1975 from Pahokee time lapse camera looking south into FACE mesonetwork. Limits of view are indicated in Figure 23.

to the left (east) of the main cloud. This line corresponds to the western end of the gap between echoes, and a bridge between visible clouds at cloud base has taken place with the large cumulonimbus clouds to the east, which is outside the photo range in Fig. 24 but is visible in Fig. 25 at 1832 EDT. The bridge between the two large cumulonimbi (Figs. 24, 25) consists of growing clouds joined at cloud base. At 1835 EDT, radar continued to show the two echoes separate (Fig. 23). Five minutes later, radar indicated (Fig. 23) that the echoes had merged at 20 dBz, but not at a high enough level to be considered a radar merger by FACE definitions. Corresponding visible clouds at 1840 (Fig. 24) show that the line had one large cumulonimbus cloud penetrating cirrus and several smaller growing clouds on the left (western side of gap). However, although the clouds in the line at 1840 had merged to a greater height, they had not reached the cirrus level, as their tops are still visible. The eastern cumulonimbus, out of Fig. 24 view, has also penetrated cirrus by 1840 EDT. Five minutes later, echo merger had occurred (Fig. 23). At the same time, visible clouds (Fig. 24) have also merged to cirrus level heights, estimated to be above 12 km, into a solid line. The indication is clear that the gap between echoes was occupied by only small clouds in a line; then the line elements grew upward as the echoes grew together until cumulonimbi had merged when echoes merged.

On August 25, the view of the Field Observing Site (FOS) camera, located on the map in Fig. 2, was moved to the west toward two developing shafts of rain below cloud base. At 1755 EDT, there were two separate radar echoes (Fig. 26). Their cores corresponded well to a pair of rain shafts apparent in the photo taken 2 min later at 1757 and shown in Fig. 27; the clouds are joined at cloud base. The azimuths to the sides of these rain shafts were determined from the photos and transferred to the radar map in Fig. 26.



*Figure 25. Hand-held photograph at 1832 EDT on 12 August 1975 from Fikee looking southeast. Cumulonimbus on left side of photo identifies with large radar echo on east side of Figure 23, and is to left of views of camera in Figure 24 views. The lower bridging clouds on right side of photo are same as clouds on extreme left side of 1830 EDT panel in Figure 24.*

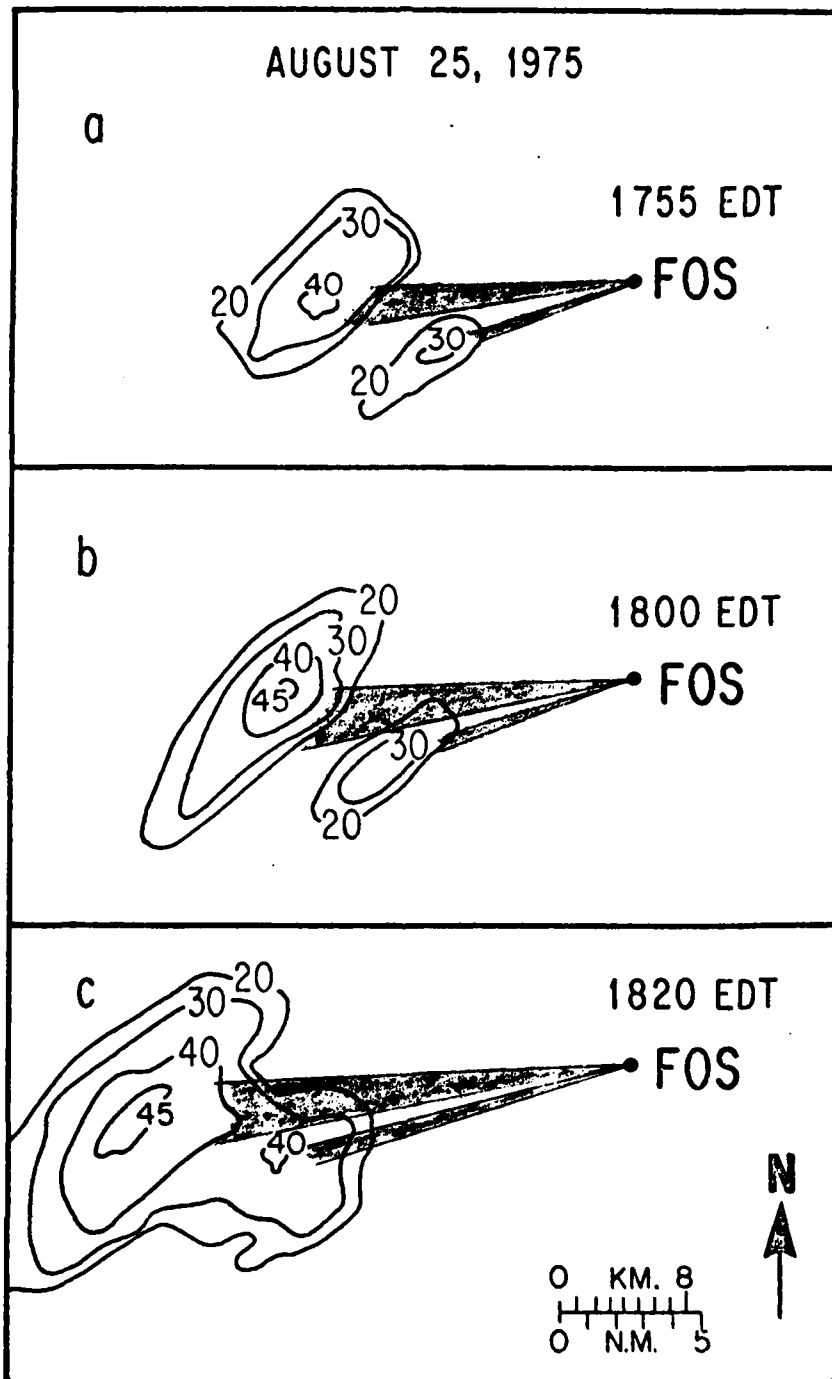


Figure 26. Radar echo patterns (in dBz) over the FACE mesonetwork at 3 times on 25 August 1975. Solid lines enclosing shaded areas indicate angles from FOS camera to the two rain shafts visible in FOS time lapse photographs in Figure 27.

AUGUST 25, 1975  
WEST FROM FOS



1757 EDT



1811 EDT



1818 EDT

*Figure 27. Photographs at 3 times on 25 August 1975 from FOS time lapse camera looking west. Azimuths to rain shafts are indicated in Figure 26.*

At 1800, the radar echoes were larger but continued to be separate. Eleven minutes later at 1811 (Fig. 27), the two shafts continued to be separate but were growing together; clouds were merged to a greater height and the visible cloud structure was quite revealing at this time. A large cumulonimbus extended beyond the top of the photo on the right, a smaller cloud is visible on the left, and a new tower (its age is apparent from the time lapse film) was growing in the center. At 1818 (Fig. 27) the two rain shafts merged, and cloud towers had merged to cirrus heights (about 12 km). The next radar scan, at 1820 (Fig. 26), shows a merged echo above 30 dBz. Radar data were missing between 1800 and 1820, so that merger may have occurred earlier than 1820. Nevertheless, it is likely that tower merger to the cirrus level (1818 EDT) occurred within a few minutes of the radar merger.

In all three cases, August 12, 19 and 25, echo merger at the 1.0 or 2.5 mm  $h^{-1}$  rate occurred at the same time (to the nearest 5 min) as merger of visible clouds to cirrus levels, which in these cases were mainly between 9 and 12 km. Merging of gage-measured rainfall occurred for the August 19 study after another 10 to 15 min. In all cases, the two predecessor radar echoes coincided with separate and distinct cumulonimbi. The visible clouds were, however, bridged or "merged" at cloud base at rather early stages. As the two radar echoes grew, the space between them was filled with growing clouds. Finally, a single cloud or a row of clouds grew rapidly upward between the predecessor clouds. New radar echoes formed in the gap, and radar echo merger at 2.5 mm  $h^{-1}$  occurred within 5 minutes of the time when visible clouds joined into a solid line up to 9 km or higher.

d. Interaction of Cloud-Scale Dynamics with Surface Convergence as Measured by Doppler Radar and Surface Pressure Data

Further understanding of the evolution and interaction of cloud-scale motions and how they influence boundary-layer convergence has been gained by analysis of August 1975 FACE Doppler radar and surface pressure data. Although the sample of cases analyzed has been small to date, the understanding of these clouds has been extensively broadened to help explain some of the processes important in cloud-scale convergence, which is the central focus of this contract report. At present, Doppler analysis of August 25, 1975 has been pursued in detail and will be shown here. The processing methods, computer compilation, and meshing of multi-Doppler data and other details of extraction of reflectivity and velocity from the raw Doppler data have been described in earlier contract reports. The analysis of the August 25 case, when combined with surface pressure data, has led to a more complete understanding of cloud-scale structure, which in turn has stimulated further plans for research with the Doppler and surface pressure data.

As a cloud tower grows vertically, buoyancy exists in the actively rising portion of the cloud, whether it is a natural or a seeded tower. How this buoyancy is communicated to the boundary layer and affects the surface convergence is the subject of differing opinions among researchers. It has been proposed (Simpson, 1980; Cotton and Tripoli, 1979; Fritsch and Chappell, 1979) that the buoyancy of a growing tower is communicated to the boundary layer by enhancement of moist downdrafts which then enhance the surface convergence. Low pressure then forms directly below the rising bubble, and convergence of air into the bubble occurs not only from below but also from the sides, where entrainment of drier environmental air occurs. This cooling initiates the downdraft process, which then develops a more vigorous downdraft both earlier and lower in the cloud.

When these downdrafts interact with the surface air, they increase the surface convergence, and produce new cell growth if the resulting vertical velocity is strong enough. Simpson (1980) amplified this hypothesis as it related to additional buoyancy in the growing cloud tower due to seeding. In this situation, downdraft interaction with the boundary layer would need to be more intense than that formed without seeding, unless there is some optimal timing of downdrafts due to seeding.

Research with Doppler and surface pressure data on August 25, 1975 indicates that the interaction or response of the boundary layer to developing convection is an extremely time-dependent process. A group of convective clouds began (Section 4b) to grow actively on this day in an area of convergence that had formed from interaction of the outflow from Lake Okeechobee to the north and the mean flow over Florida, which was from the southeast. As the clouds began to grow at 1434 EDT, the surface pressure field (Fig. 28) showed a consistent fall, to a maximum decrease of 0.4 mb in the area below the developing convection. The time change of convergence in the vicinity (Fig. 29) shows that convergence responded to the pressure deficit by increasing from  $6 \times 10^{-4} \text{ s}^{-1}$  at 1430 EDT to a maximum value of  $14 \times 10^{-4} \text{ s}^{-1}$  at 1447 EDT.

In Fig. 30 the Doppler data have been analyzed in the vicinity of cell A through the same period. North-south cross sections have been prepared at four times through this area and are shown in the next four figures; the cloud is seen to be growing rapidly during this time series. At 1431 EDT (Fig. 31), when surface pressure and convergence in Figs. 28 and 29 are at their background levels, Doppler data show a cloud with maximum reflectivity at 5 km, and consisting mainly of updrafts. Five minutes later at 1436 EDT (Fig. 32), the cloud has increased in volume and reflectivity levels, as well as maximum

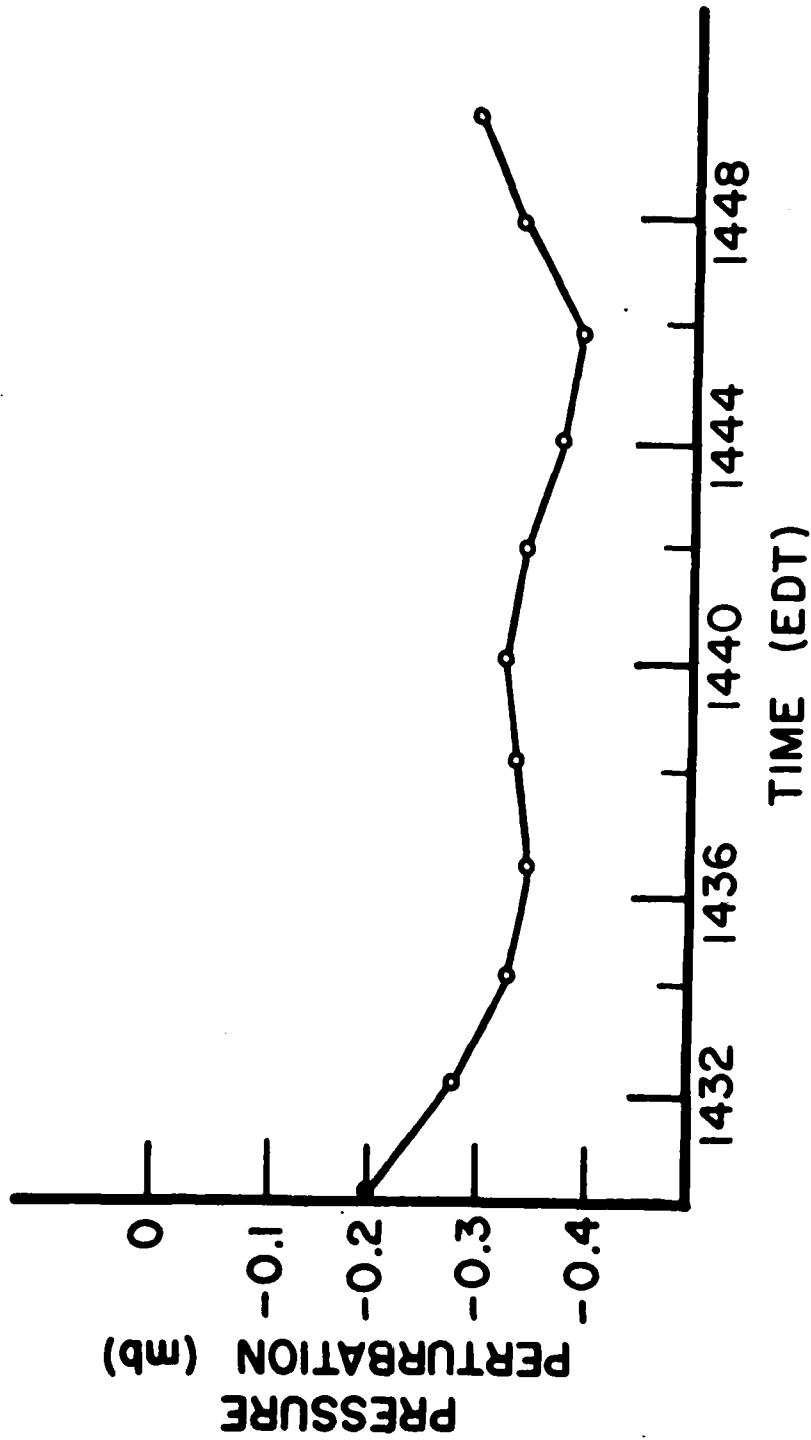


Figure 28. Time series of surface pressure below developing convective system in FACE mesonetwork on 25 August 1975.

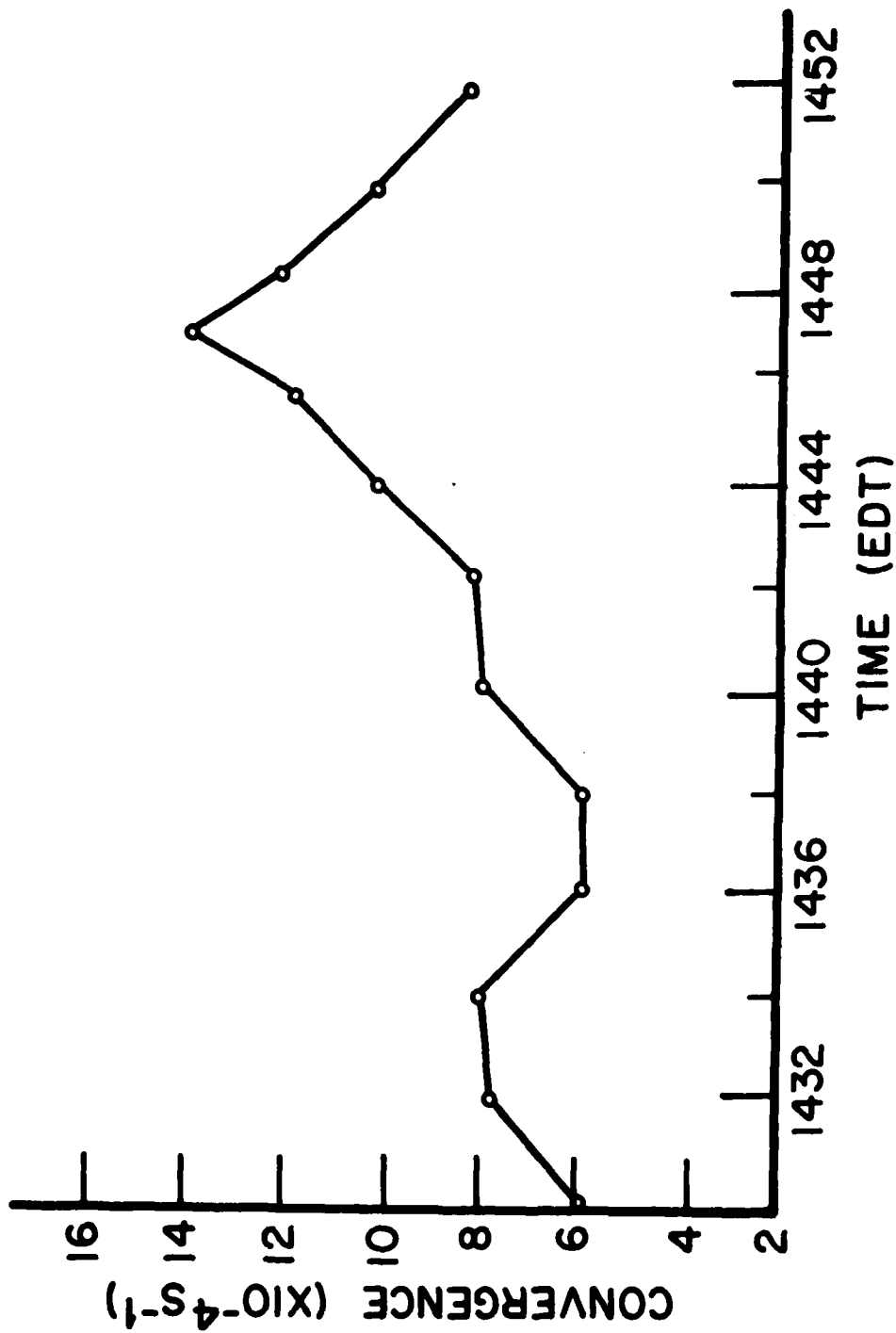


Figure 29. Time series of surface convergence in vicinity of convective system in FACE mesonet on 25 August 1975.

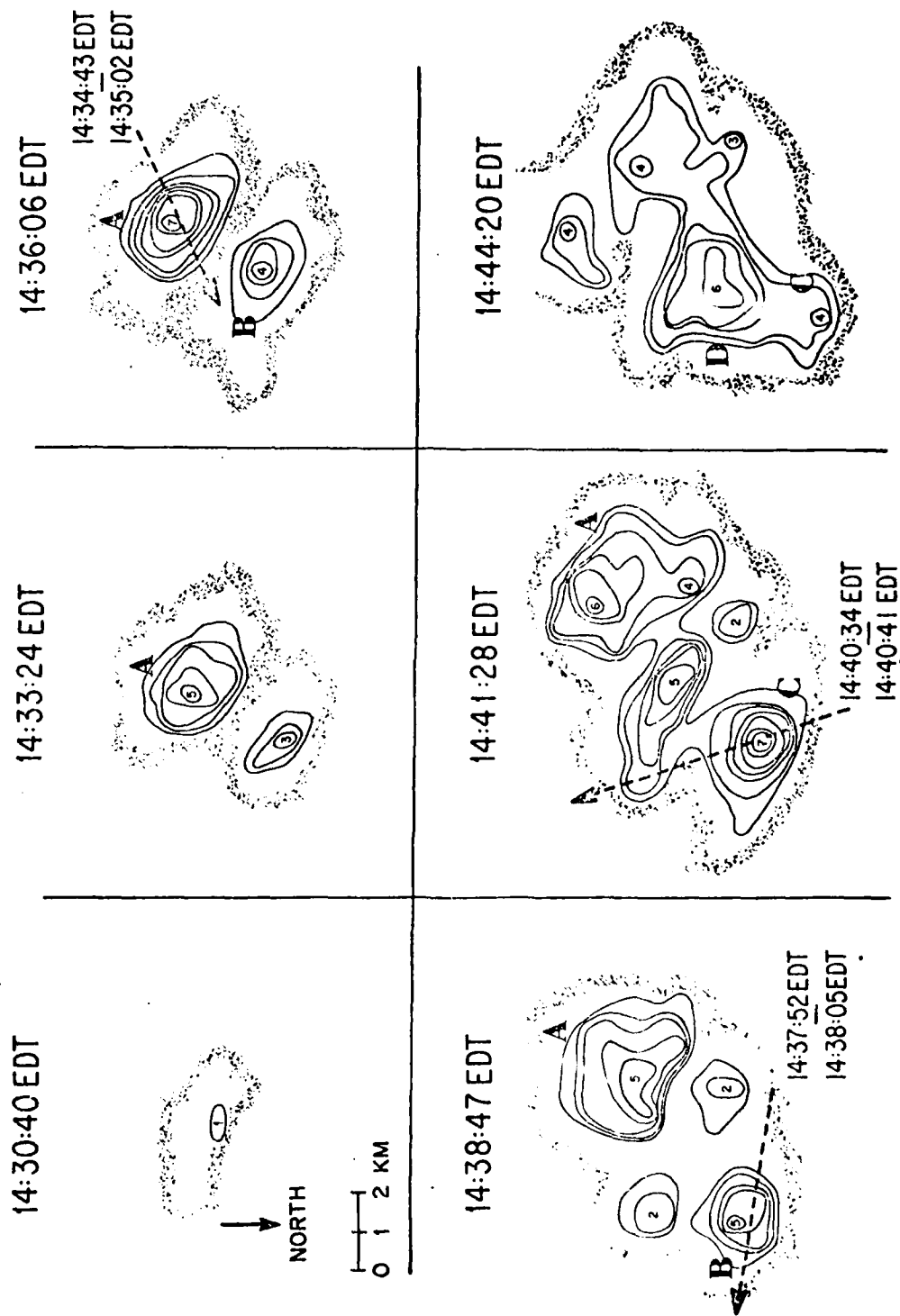


Figure 30. Doppler radar-derived representation of reflectivity fields at 6 km for cloud system studies on 25 August 1975 in the FACE mesonet network. Individual cells are labeled with letters, and reflectivity centers with numbers. Shaded areas show boundaries of reflectivity from radar. Arrows and times represent aircraft traverses through indicated cells (Cunning et al., 1979).



25 AUGUST 1975 1436 EDT  
CELL A

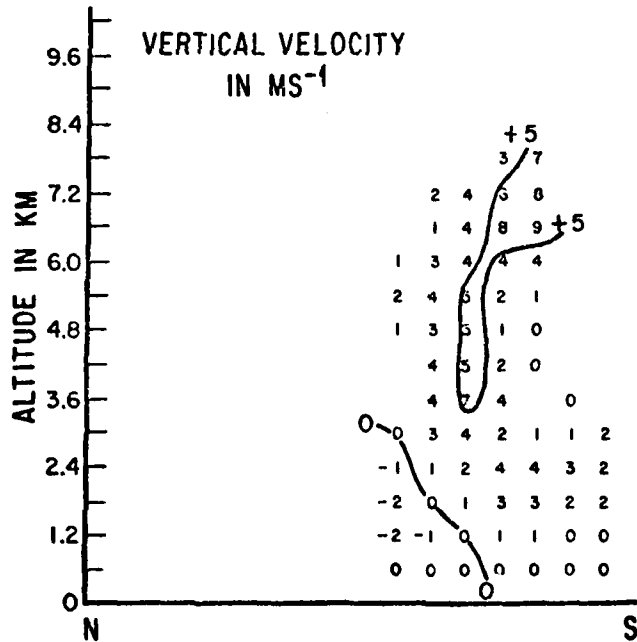
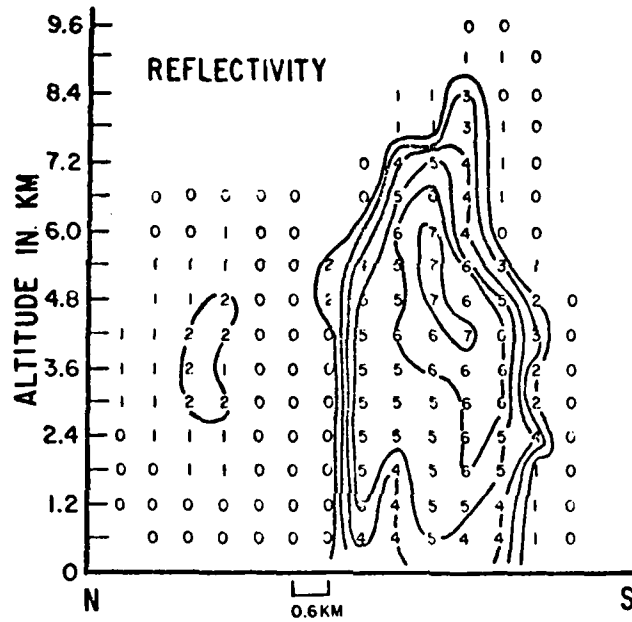


Figure 32. Same as Figure 39, except at 1436 EDT.

upward vertical velocity. The surface pressure has begun to drop at this time (Fig. 28). In another 5 minutes at 1441 EDT (Fig. 33) Doppler data show maximum reflectivities at lower levels and a start of downward motion in two areas of the cloud. By the time of the peak surface convergence at 1447 EDT (Fig. 29), Doppler data (Fig. 34) show that the lower portion of the cells that had induced the pressure perturbation now had either zero or negative vertical velocities, while water contents remained high. This implies that the boundary-layer air that is converging into the storm cannot feed the original cells and is therefore forced to two alternatives. One, there may be some type of boundary layer return circulation, which appears highly unlikely with an active storm overhead. Two, there may be formation of a new cell or cells. The latter appears to have occurred when the new cell D rapidly grew (Fig. 30); this cell was first seen at about 1444 EDT. Cell D grew extremely rapidly and within a short time became the dominant cell within the storm and probably prolonged the storm to a significant degree. The evolution of this storm matched certain descriptions of the pressure perturbation and surface convergence fields in convective storms that were observed and modeled by the National Severe Storms Laboratory in Oklahoma (Lemon, 1976; Barnes, 1978) and the National Hail Research Experiment in Colorado (Foote and Fankhauser, 1973; Koch, 1975).

A general hypothesis of the methods by which convective cells develop and interact in south Florida can be derived from these Doppler and pressure data. First, there must be some type of convergence in the boundary layer for convective cells to form, at least for those that produce radar echoes. This convergence may be established by the sea breeze circulation, lake breeze circulation, down-drafts from other convective systems, differential surface heating, synoptic-scale

25 AUGUST 1975 1441 EDT  
CELL A

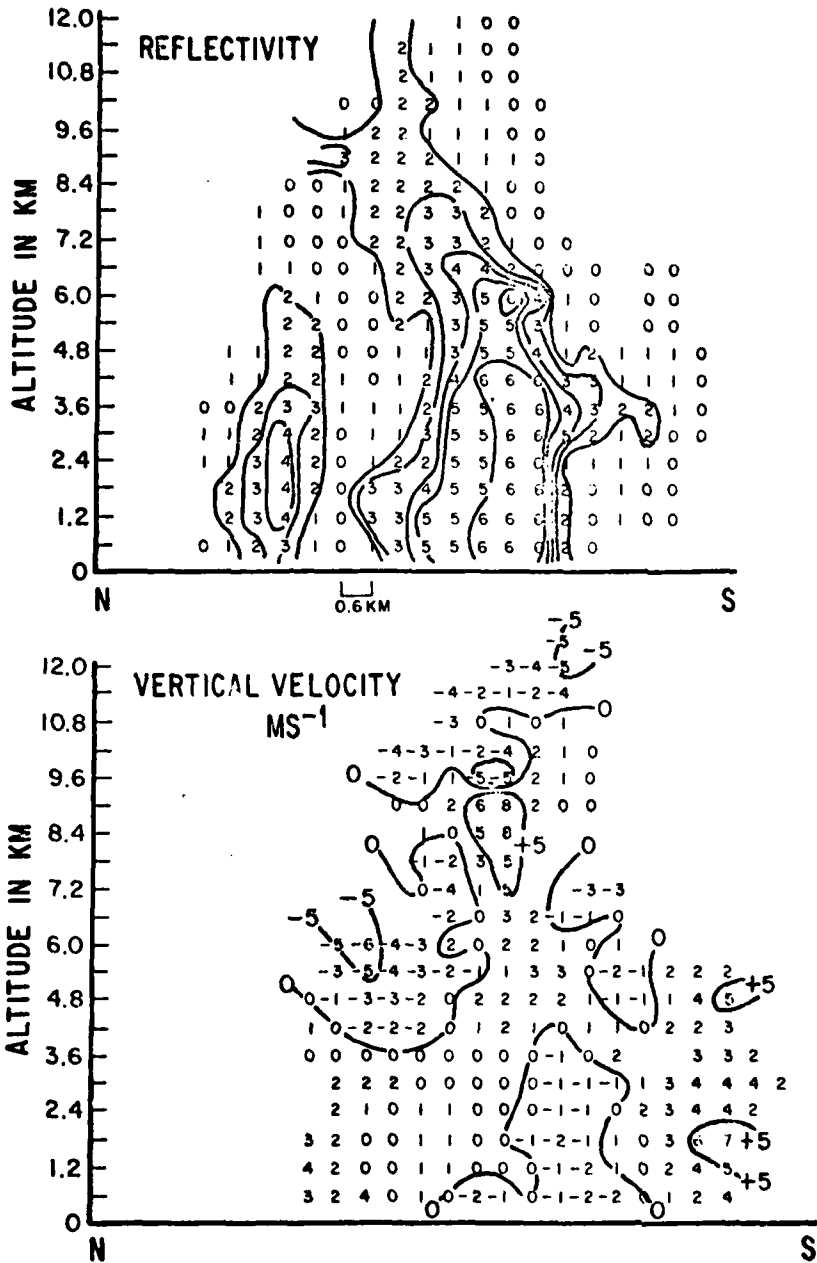


Figure 33. Same as Figure 29, except at 1441 EDT.

25 AUGUST 1975 1447 EDT  
CELL A

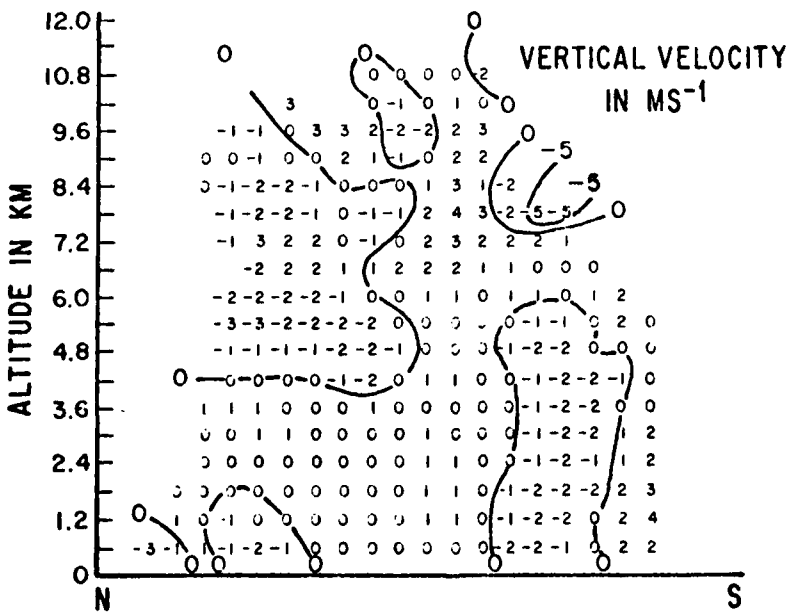
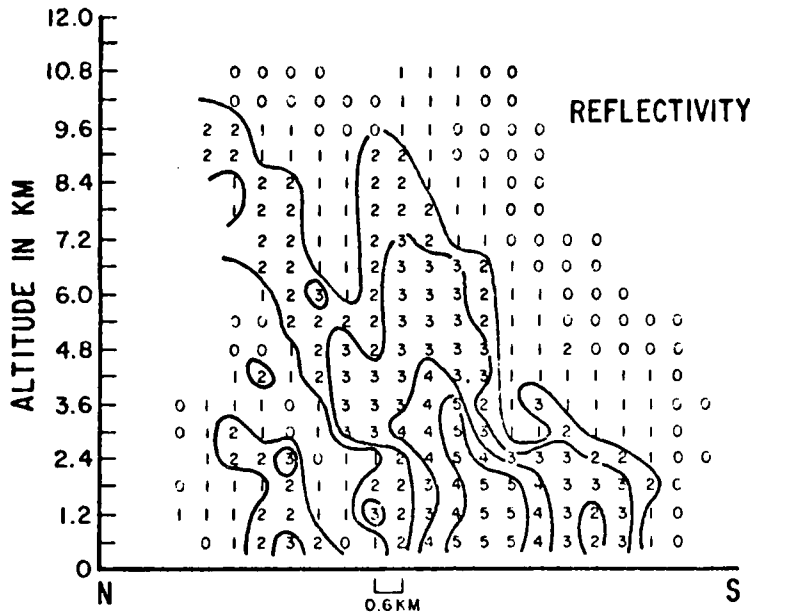


Figure 34. Same as Figure 29, except at 1447 EDT.

circulation, or a number of other possible circulations. Whatever the forcing, however, it appears that the stronger the surface convergence, the greater the likelihood that convective cells will grow and propagate, with the end result being the development of a mesoscale convective system. From the August 25, 1975 case study analysis and from model results found by Tripoli and Cotton (1980), it appears that as the updraft is accelerating, low pressure forms at the surface. The reason for this occurrence is that while the updraft is actively accelerating, it is protected, at least on the upshear side, from entrainment by the high pressure induced by the environmental air interacting with the updraft air. The surface low pressure increases the surface convergence into the region of the developing cells, but according to the August 25 analysis, this response time is 10 to 15 min. In this time frame, though, the cells that induced the pressure perturbation at the surface have become neutral or negatively buoyant in the lower portions of the cloud. The convergent air then cannot feed into the original cells, and the air is forced upward on the periphery of the parent cell. If this process is repeated and strengthened, particularly once the downdrafts have begun to interact with this process, a convective storm has formed. The embryonic storm that formed over the pre-existing convergence zone has been enhanced by the pressure perturbation over and above the prior convergence zone. The surface pressure perturbation may be the key that determines whether a storm evolves into a mesoscale system, by producing or inducing its own mesoscale convergence fields such that it is no longer dependent on the pre-existing convergence. The buoyancy pulse produced by seeding an active tower would be capable of causing additional acceleration and lower surface pressure, and thereby an increase in surface convergence.

## e. Analysis of Boundary Layer Winds

### (1) Introduction

The purpose of this study is to obtain vertical adjustment factors to be applied to the surface FACE mesonetwork winds under varying meteorological conditions and times of day. These adjustment factors will be useful in accounting for the variation of boundary layer winds with height, and permit a more accurate computation of fluxes from cloud base to the surface, when only surface winds are available. Winds were obtained at the Field Observing Site (FOS) in the FACE mesonetwork (Fig. 2), and were measured with theodolite at FOS for 57 radiosonde balloon releases during August 1975.

### (2) Data analysis

Wind speed and direction were considered at the following four levels: 10 ft (3.05 m), 1000 ft (305 m), 2000 ft (610 m), and 3000 ft (915 m). The shear vector, magnitude of direction change, and amount of speed change between levels were calculated for each layer, and for the entire 10- to 3000-ft layer, as well as many other parameters that are listed and described in Table 20.

### (3) Results

#### (a) Mean wind changes by layer

In nearly every category, the wind speed increases with height. The turning of the wind in the vertical is primarily veering; this change is most dominant in the lower two layers (from 10 to 1000 ft, and from 1000 to 2000 ft).

The mean directional changes,  $\overline{\Delta D}_L$ , were found for each of the three layers without respect to time or type of sounding. These overall changes are as follows:  $\overline{\Delta D}_1 = 47^\circ$ ,  $\overline{\Delta D}_2 = 12^\circ$ , and  $\overline{\Delta D}_3 = 18^\circ$ . As expected, the major change was found in layer one. The difference between the magnitude of the changes in layers two and three is not considered significant.

Table 30. Data obtained from FOS winds at 10, 1000, 2000, and 3000 ft

Type of data	Parameter	Description
Shear	$\frac{\partial \bar{V}}{\partial Z}$	Shear vector of wind between levels (e.g., 10 to 1000 ft)
Shear	$\frac{\partial \bar{V}}{\partial Z_{BL}}$	Mean shear vector between 10 and 3000 ft
Shear	$\frac{\partial \bar{V}}{\partial Z_{BL}}$	Mean shear vector for each stratification
Directional	$\overline{\Delta D_{BL}}$	Magnitude of difference between 10 and 3000 ft
Directional	$\overline{\Delta D_L}$	Magnitude of difference between levels
Directional		Turning of wind with height from 10 to 3000 ft
	B	Backing
	V	Veering
	B/V	Backing, then veering
	V/B	Veering, then backing
Directional	$\overline{\Delta D_{BL}}$	Magnitude of mean directional change from 10 to 3000 ft
Directional	$\overline{\Delta D_L}$	Magnitude of mean directional change for each of 3 layers
Directional	$\sigma_{\Delta D_{BL}}$	Standard deviations of changes from 10 to 3000 ft
Speed	$\Delta S_{BL}$	Magnitude and sign of speed change from 10 to 3000 ft
Speed	$\overline{\Delta S_{BL}}$	Magnitude of mean speed change from 10 to 3000 ft
Speed	$\overline{\Delta S_{BL}}$	Magnitude of mean of absolute values of speed change from 10 to 3000 ft
Surface winds	$\overline{V_{SFC}}$	Mean surface vector winds

(b) Stratification by time

When the layer winds were stratified with respect to time, the trends of the mean of the layer shear averages, shown in Table 21, reflect a return to basic flow dominance from 1100 to 1400 EDT after the early morning inversion disappears. With growth of sea breeze and cumulus-scale processes, the combined effect of the Coriolis parameter and inland pressure perturbation results in a marked veering. When convection is ebbing (1700 to 1800 EDT), backing is the dominant turning mode, probably in response to convective overturning and destruction of the original cumulus-initiating mesoscale fields.

The variations in wind direction are larger for all periods than originally expected. The early maxima (1000 to 1100 EDT) probably reflect the effect of large angular turning associated with the fading nocturnal inversion. The maxima from 1400 to 1500, and 1600 to 1700 EDT probably represent variations associated with frictional inflows into mesoscale and cumulus-scale systems.

In every time period, wind speed increases with height. There are two peaks in speed changes through time, but they are not at the same times as the directional change maxima.

(c) Stratification by convective classification

In a study by Brown and Hansen (1978) on water budget characteristics of convection over south Florida, five basic FOS sounding classifications were defined. These classifications established the prevailing thermodynamic character as it relates to cloud types, cloud cover, and air flow in the vicinity of each wind profile. Detailed descriptions by Brown and Hansen (1978) are summarized below:

Category 1. Mixed layer present, with scattered cumuli overhead.

Table 21. Vertical wind variations classified by time of day

Time (EDT)	Number of cases	$\frac{\overline{\partial V}}{\partial Z_{BL}}$	$\overline{\Delta D}_{BL}$	$\sigma_{\Delta D_{BL}}$	$\overline{\Delta S}_{BL}$	$\overline{\Delta S}_{BL}$	Number of cases			
							B	V	B/V	V/B
10-11	11	132 <sup>0</sup> /0.8k	66 <sup>0</sup>	39 <sup>0</sup>	3.7k	3.9k	1	8	0	2
11-12	5	120 /2.9	36	33	7.6	7.6	0	3	0	2
13-14	14	110 /1.6	46	41	3.7	4.3	6	8	0	0
14-15	9	167 /0.6	52	85	2.2	3.8	2	5	0	2
16-17	14	102 /1.3	50	57	3.0	5.4	4	6	0	4
17-18	4	068/3.2	39	38	9.5	9.5	2	0	1	1

Category 2a. Mixed layer present, with broken cumuli overhead. Possible cumulonimbi were near, but no outflow air nearby.

Category 2b. Soundings not belonging to other four categories (other).

Category 3a. "Fresh" outflow air from nearby thunderstorms at FOS.

Category 3b. "Old" outflow air, with surface wind speeds less than 4 to 5  $m s^{-1}$ . High static stability.

Results of stratifying the wind data by these categories are shown in Table 22.

In the absence of nearby convection (category 1), the mean vertical shear vector is from the southeast. As the influence of convection (outflow) becomes more dominant, the mean shear vector swings more to the east and northeast. The mean directional change  $\overline{\Delta D}_{BL}$  is clearly a maximum with "fresh" outflow (category 3a). This category is also noteworthy for the decrease in mean wind speed  $\overline{\Delta S}_{BL}$  with height; this is the only instance of decrease in all of the stratifications. The dominance of an overall veering tendency is also apparent in Table 22.

(d) Stratification by mean low-level Miami winds

The winds observed at 0800 and 2000 EDT at Miami have been routinely weighted and averaged to obtain a mean vector wind from 1000 ft to 700 mb for each day as part of the FACE experiment (Staff, Cumulus Group, 1979). Four wind

Table 22. Vertical wind variation stratified by convective classification

Convective classification	Number of cases	$\frac{\overline{\partial V}}{\partial Z_{BL}}$	$\overline{\Delta D_{BL}}$	$\overline{\Delta S_{BL}}$	$ \overline{\Delta S_{BL}} $	B	Number of cases		
							V	B/V	V/B
1	36	126 <sup>0</sup> /1.2k	53 <sup>0</sup>	3.9k	4.3k	10	20	0	6
2a	6	106 /1.0	22	2.2	3.2	1	3	0	2
2b	5	107 /2.1	19	7.0	7.0	0	3	1	1
3a	3	053 /1.3	109	-2.3	5.7	1	1	0	1
3b	7	093 /2.4	58	6.3	6.6	3	3	0	1

speed classes were defined, and the August 1975 wind profiles from FOS were stratified by these classes. In addition, the mean surface wind  $\overline{V}$  was computed for each class. By using the mean surface wind and the mean of the average shear vectors, a reasonable accounting for turning and speed variation of winds with height in computation of fluxes is obtained. It is recommended that this adjustment be calculated from the wind speed categories in Table 23, since this appears to be the most appropriate form from which to obtain a factor.

Table 23. Vertical wind variations stratified by mean layer vector winds

Mean layer vector wind	Number of cases	$\overline{V}_{SFC}$	$\frac{\overline{\partial V}}{\partial Z_{BL}}$	$\overline{\Delta D_{BL}}$	$\overline{\Delta S_{BL}}$	$ \overline{\Delta S_{BL}} $	Number of cases			
							B	V	B/V	V/B
0 to 4kt	3	0.52 <sup>0</sup> /1.4	262 <sup>0</sup> /1.0k	86 <sup>0</sup>	0.3k	0.3k	0	3	0	0
4 to 8	29	113/1.4	121/1.3	73	2.6	4.6	9	11	1	8
8 to 12	8	074/4.9	118/1.2	27	5.8	5.8	0	6	0	2
more than 12	17	092/6.7	099/2.0	17	6.3	6.4	6	0	0	1

For the cases where the mean 1000 ft - 700 mb layer wind was less than 4 kt, the directional change from 10 to 3000 ft was 210°. As the broad-scale flow increases, directional shear decreases markedly and speeds increase only slightly. The same tendencies persist (Table 23) in the mean directional  $\overline{\Delta D_{BL}}$  and speed  $\overline{\Delta S_{BL}}$  components. The dominant turning tendency is veering. For this August 1975 data set, Table 23 also shows that the predominant direction for high mean winds (> 12 kt) is easterly, while for the largest data sample (4-8 kt) the wind is southeast.

Further research into the vertical structure of moisture and temperature appears to be warranted by the shears apparent in the weak mean layer wind class (0-4 kt). Since light-wind days are observed to be days of well-organized convection over south Florida, the significance of the turning of the wind by almost 180 degrees should be explored further.

AD-A097 553

ILLINOIS STATE WATER SURVEY URBANA

F/G 4/2

LOW-LEVEL CONVERGENCE AND THE PREDICTION OF CONVECTIVE PRECIPIT--ETC(U)

FEB 81 A I WATSON; R L HOLLE; J B CUNNING

NSF-ATM76-08865

UNCLASSIFIED

TR-4

ARO-15529.6-65

NL

3 of 3  
NSA  
787563




END  
DATE  
FILMED  
5-81  
DTC

## 6. CONCLUSIONS

A reliable method has been presented for the prediction of convective precipitation in south Florida. Total area divergence was statistically related to rainfall as derived by radar in a mesoscale region on the order of  $1400 \text{ km}^2$ .

A convergence event is described by the maximum change in total area divergence anytime there is a steady drop of  $25 \times 10^{-6} \text{ s}^{-1}$  for 10 minutes or more. A 5-minute area-averaged divergence field is used for this study, which is further smoothed to remove noise by a 15 minute running mean. Regression statistics are developed for the total ensemble recorded during August 1975 in the FACE field network. Fifty-nine convergence events are found, of which 38 had rainfall. The total ensemble correlation coefficient between convergence and rainfall is  $-.6$ .

It was established that other meteorological factors such as stability, winds, and moisture play important roles affecting changes in the amounts of convective rainfall. The total ensemble is divided according to low-level mean vector wind speed, echo motion, and mid-level moisture. It is found, for south Florida convection, that for slow moving convective systems or during times of weak low-level winds, there is 3 times the amount of rainfall per event with only a 30% increase in convergence. Even more striking is the fact that when mid-level moisture (850-500 mb) is available,  $2 \frac{1}{2}$  times more precipitation is recorded for approximately the same amount of convergence that occurred during dry events. It was also much easier to predict rainfall ( $r = -.76$ ) when mid-level moisture is abundant.

There are several methods of calculating total area divergence. These include the line integral, Bellamy triangles, and the average of divergence values located at gridpoints in a regular array. The Bellamy method was not attempted due to the regular layout of the wind sites which closely

approximated a rectangular grid. The statistical method developed in this study can be applied to wind stations surrounding a forecast area. With the line integral, there is no need for interior sites. Applications of this technique could include the forecasting of precipitation for a metropolitan area, watershed, or agricultural region.

Weighted convergence, a subset of total area divergence, is also used to predict area rainfall. Weighted convergence filters out any positive divergence and only examines convergence in the mesonet network. Weighted convergence reflects what is also seen in the total area divergence relationships, that is, the weaker the low-level wind or slower the movement of the convective system, the stronger the convergence event and heavier the rainfall. When mid-level moisture is high, 2 times more rainfall occurred for approximately the same amount of convergence. A weakness of this system is the fact that a full grid of wind sites is required for the calculation of weighted convergence.

Convective outflow and its reflection in total area divergence was examined and relationships were developed for determining the amount of precipitation from each convective event. For 38 rainfall events, a correlation of .76 was found between the magnitude of the outflow divergence and the precipitation amount. When the ensemble was subdivided, mid-level moisture was found to play little or no role in affecting the outflow and rainfall. When low-level winds were weak, more rain fell with larger amounts of divergence than on days with strong wind flow.

The variable network size study was presented to show how focusing on a convective event by decreasing the network area can improve the chance of total area divergence describing the convective event and predicting rainfall. It was shown that the smaller the convective system, the smaller the network required to record the effects of the system. However, the

importance of the size of the area on these relationships cannot be understated. This technique is highly area-dependent and the strength of total area divergence varies greatly with the size of the region in question. New statistical relationships must be calculated for each constant-size area that is investigated.

When the distances between wind sites were varied, it was shown that the smaller the station separation, the better the description of the actual mesoscale circulations beneath the convective system. Circulations depicted by the 12.9-km spacing showed good agreement with the 6.4-km ("ground truth") spacing. The 19.3-km grid was found to be much too large a scale to record accurate circulations. But when total area divergence is examined, all three scales show good agreement.

Area precipitation efficiencies were calculated for 23 days of August 1975 data. Daily estimates of moisture passing through the boundaries of the meso-network with a thickness equal to the boundary layer depth were compared to precipitation totals. For the total ensemble, an average of 16% efficiency was determined. On days when echo motion was weak or when mid-level moisture was available, significant improvement of area precipitation efficiencies was recorded.

In addition to the rainfall response to convergence, the relationship of visible clouds to surface divergence fields was examined. Nine cases were studied from the FACE 1975 and 1973 mesonetworks when clouds were well-defined visually and located over the wind network. The time interval from first convergence to the time when cumuli responded to the convergence ranged from 10 to 55 minutes, and averaged 25 minutes. It was another 35 minutes until the rapid upward growth of the cloud entity was attained. This appears to be the first study of convergence-visible cloud development lags.

The large variability in these time intervals lead to observing the fact that longer lags were associated with longer cloud lifetimes. To account for this effect, the times of first convergence and of complete dissipation of the cloud entities were found. When the visible cloud events were normalized to the cloud duration, first visible cloud response occurred 15% through the cloud lifetime, while rapid upward growth occurred 36% through the lifetime.

Other specific time-dependent events were then sought which could be rather well-defined from available data. Six other features of rainfall, radar and surface convergence fields were identified. All of them and the visible cloud times were found to have correlation coefficients from 0.72 and 0.96 when the relationship was found between (1) the interval from first convergence to the meteorological event, and (2) duration of the cloud entity. Further research into the usefulness of these rather high capabilities for predicting cloud duration based on early milestones of a cloud's life cycle are planned and appear to be warranted. Since cloud duration often is well related to intensity, size and rainfall production, further research will be conducted on this subject by NOAA for Florida data, as well as for Illinois visible cloud data from VIN.

Cloud merger was studied on 3 days in August 1975 over the FACE meso-network. Past studies have emphasized radar aspects of cloud merger, while these 3 cases were designed to document concomitant changes in other parameters. In all cases, when separate radar echoes were in existence prior to merger, visible clouds also began as separate entities. However, a visible cloud bridge began to develop between the cumulonimbi, beginning at cloud base at a rather early stage. With time, the bridge deepened by new cumuli growing upward in the gap between the cumulonimbi and radar echoes. In all 3 cases, the merging of echoes at the  $2.3 \text{ mm h}^{-1}$  rain rate was coincident (within

5 minutes) with the new clouds between old echoes reaching about 9 to 12 km. At that time, the visible clouds became merged to a solid line or area to the level of cirrus. After another 10 to 15 minutes, the surface rainfall pattern merged from previously separate centers.

Doppler radar and surface pressure data from August 25, 1975 were used to examine the evolution and interaction of cloud-scale motions with the boundary-layer convergence. At first, there must be boundary-layer convergence for convection to form, whether from synoptic-scale forcing or differential surface heating. As shown in the preceding studies of FACE data, the stronger the surface convergence signal, the greater the likelihood that convection will become significant. As the updraft is accelerating, low pressure forms at the surface. Then, surface convergence is increased into the region of the developing cells on the order of 10 to 15 minutes later. By this time, however, the cell that initiated the surface perturbation has lost its original positive buoyancy, and the convergent air is forced upward on the periphery of the parent cell. That is, the embryonic storm has been enhanced by the surface pressure perturbation, which may play a key role in whether a storm evolves into a mesoscale system which no longer depends on the pre-existing convergence.

Vertical adjustment factors to the surface FACE mesonetwork winds were obtained under varying meteorological conditions for August 1975. Most of the directional variations were largest in the first 1000 ft, and speed usually increased with height. Vertical changes were particularly dependent on the age and extent of the mixed layer and the outflow in the lower levels.

Future plans include the investigation of the divergence-rainfall characteristics in the continental environment of east central Illinois where the VIN (University of Virginia-Illinois State Water Survey-NOAA) experiment took place during the summer of 79. Convergence aloft including the boundary layer will be examined in greater detail, and its relationship to surface convergence will be explored. Studies began in Florida, such as the

representativeness of the boundary layer winds by surface winds, moisture flux/precipitation ratios, and time histories of convective clouds through time lapse photography, will be continued with the Illinois data.

## ACKNOWLEDGMENTS

This research was supported by the Army Research Office, Department of Defense, and the Atmospheric Research Section, National Science Foundation, under NSF Grant ATM-78-08865.

Deep appreciation is extended to Dr. Robert Sax, now with the Joseph Oat Corporation, for his advice and guidance during the early stages of this research. Gratitude is also extended to Dr. Bernice Ackerman at the Illinois State Water Survey for her untiring efforts to keep the budget under control and balanced between the three organizations named under this grant. Special thanks also go to Henry Poor of the University of Miami whose programming talents were put to the severest test. Appreciation is also expressed to Harry Cooper for his supervision of the data reduction effort at the University of Virginia. Many thanks go to Jeff Morris who was the focal point for data reduction at NOAA.

Gratitude is also extended to all the other personnel that participated either in the various aspects of data reduction or, most importantly, in the collection of data during the FACE field effort in the summer of 1975.

## REFERENCES

- Achtemeier, G.L., and G.M. Morgan, Jr., 1975: A short-term thunderstorm forecast system: step 1, exploitation of the surface data. Preprints, 9th Conf. Severe Local Storms, Norman, OK, Amer. Meteor. Soc., 18-24.
- Anderson, C.E., and L.W. Uccellini, 1974: Studies of meteorological factors involved in the formation of severe local storms in the northeast Colorado region. Preprints, 8th Conf. Severe Local Storms, Denver, CO, Amer. Meteor. Soc., 84-89.
- Barnes, S.L., 1978: Oklahoma thunderstorms on 29-30 April 1970. Part II: Radar-observed merger of twin hook echoes. Mon. Wea. Rev., 106, 685-696.
- Brown, J.M., and A.R. Hansen, 1978: Water budget of cumulonimbus clusters and of the peninsula scale over south Florida. Final report, Grant no. 04-7-022-44030 from National Hurricane and Experimental Meteorology Laboratory to Iowa State Univ., 220 pp.
- Burpee, R.W., 1979: Peninsula-scale convergence in the south Florida sea breeze. Mon. Wea. Rev., 107, 852-860.
- Byers, H.R., and R.R. Braham, Jr., 1949: The Thunderstorm. U.S. Gov. Printing Office, Wash. DC, 287 pp.
- Changnon, S.A., 1976: Effects of urban areas and echo merging on radar radar echo behavior. J. Appl. Meteor., 15, 561-570.

- Copeland, R.C., and P.L. Hexter, 1957: The association of surface wind convergence with precipitation patterns. Proc. 6th Wea. Radar Conf., Cambridge, MA, Amer. Meteor. Soc., 189-199.
- Cotton, W.R., and G. Tripoli, 1979: Implications of recent three-dimensional simulations of convective clouds to dynamic seeding of clouds over Florida. Preprints, 7th Conf. Inadvertent and Planned Wea. Mod., Banff, Alta., 138-139.
- Cressman, G.P., 1959: An operational objective analysis system. Mon. Wea. Rev., 87, 367-374.
- Fernandez-Partagas, J.J., 1973: Subsynoptic convergence - rainfall relationships based upon 1971 south Florida data. NOAA Tech. Memo. ERL WMPO-9, Boulder, CO, 76 pp.
- Foote, G.B., and J.C. Fankhauser, 1973: Air flow and moisture budget beneath a northeast Colorado hailstorm. J. Appl. Meteor., 12, 1330-1353.
- Fritsch, J.M., and C.F. Chappell, 1979: Three-dimensional numerical simulation of seeded and unseeded convective cloud complexes. Preprints, 7th Conf. Inadvertent and Planned Wea. Mod., Banff, Alta., 136-137.
- Holle, R., J. Cunning, J. Thomas, P. Gannon and L. Teijeiro, 1977: A case study of mesoscale convection and cloud merger over south Florida. Proc. 11th Conf. Hurricanes and Tropical Met., Miami Beach, FL, 428-435.

- Houze, R.A., and G.P. Cheng, 1977: Radar characteristics of tropical convection observed during GATE: mean properties and trends over the summer season. Mon. Wea. Rev., 105, 964-980.
- Johnson, R.H., 1977: Effects of cumulus convection on the structure and growth of the mixed layer over south Florida. Mon. Wea. Rev., 105, 713-724.
- Koch, S.E., 1975: Mesoscale influences upon the intensity of new cells in two severe local storms. Preprints, 9th Conf. Severe Local Storms, Norman, OK, Amer. Meteor. Soc., 105-112.
- Lemon, L.R., 1976: The flanking line, a severe thunderstorm intensification source. J. Atmos. Sci., 33, 686-694.
- Merceret, F.J., R.L. Holle and J.B. Cuning, 1980: Classification of meteorological radar echoes by their state of motion during FACE 1970 through 1978 - procedures and results. NOAA Tech. Rept. ERL 411 - NHEML 3, Miami, FL, 9 pp.
- Simpson, J., 1980: Downdrafts as linkages in dynamic cumulus seeding effects. J. Appl. Meteor., 19, 477-487.
- Simpson, J., N.E. Westcott, R.J. Clerman and R.A. Pielke, 1980: On cumulus mergers. Archiv für Meteorologie Geophysik und Bioklimatologie, Series A, 29, 1-40.

Staff, Cumulus Group, 1976: 1975 Florida Area Cumulus Experiment (FACE):  
operational summary. NOAA Tech. Memo. ERL WMPO-28, Boulder, CO, 186 pp.

Staff, Cumulus Group, 1979: 1978 Florida Area Cumulus Experiment (FACE):  
operational summary and data inventory. NOAA Tech. Memo. ERL NHEML-4,  
Coral Gables, FL, 262 pp.

Tripoli, G.J., and W.R. Cotton, 1980: A numerical investigation of several  
factors contributing to the observed variable intensity of deep convection  
over south Florida. J. Appl. Meteor., 19, 1037-1063.

Ulanski, S.L., and M. Garstang, 1978: The role of surface divergence and  
vorticity in the life cycle of convective rainfall. Part I: Observations  
and analysis. J. Atmos. Sci., 35, 1047-1062.

Westcott, N.E., and J. Simpson, 1980: Population study of radar echoes over  
south Florida. Submitted to J. Appl. Meteor.

Wiggert, V., and G.F. Andrews, 1974: Digitizing, recording, and computer  
processing weather radar data at the Experimental Meteorology Laboratory.  
NOAA Tech. Memo. ERL WMPO-17, Boulder, CO, 70 pp.

Woodley, W.L., 1970: Precipitation results from a pyrotechnic cumulus  
seeding experiment. J. Appl. Meteor., 9, 242-257.

Woodley, W.L., and R.I. Sax, 1976: The Florida area cumulus experiment:  
rationale, design, procedures, results, and future course. NOAA Tech.  
Rept. ERL 354-WMPO 6, Boulder, CO, 204 pp.

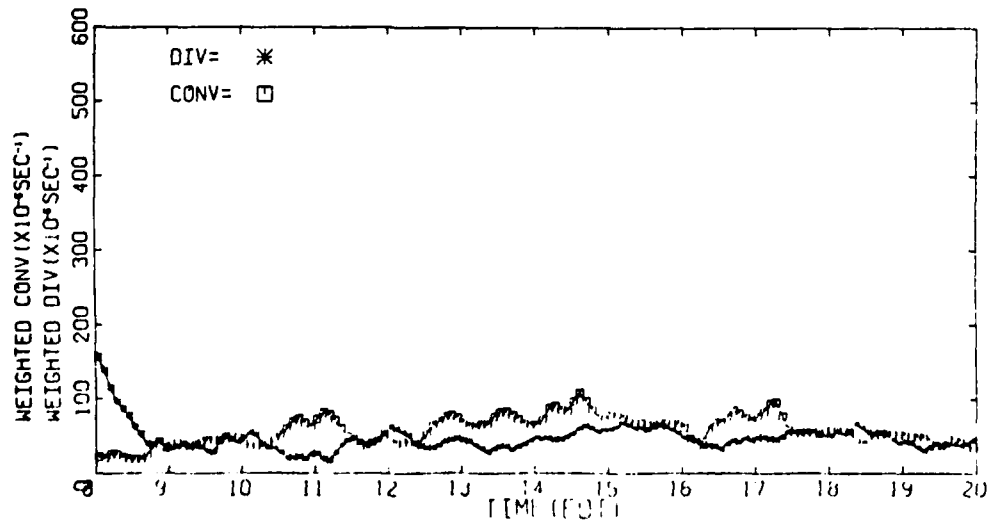
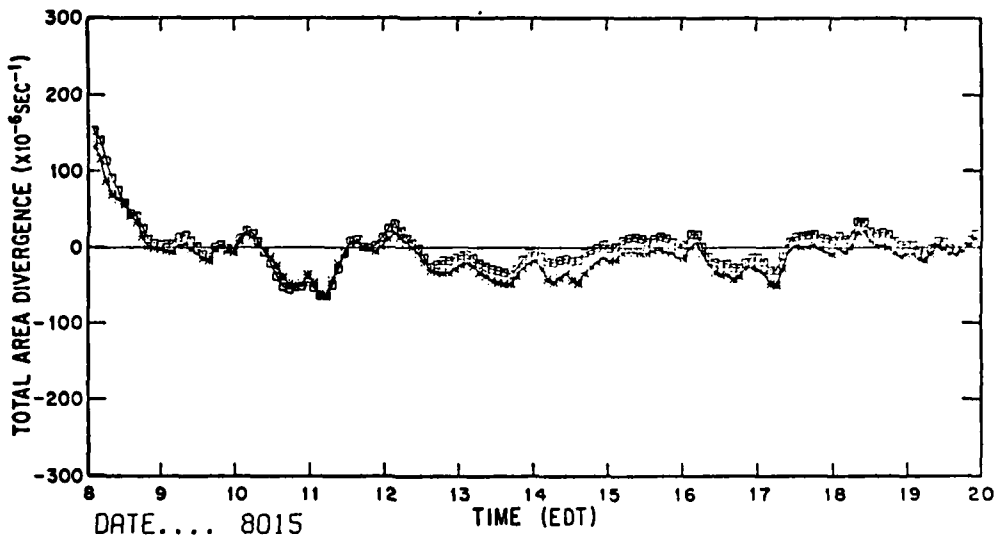
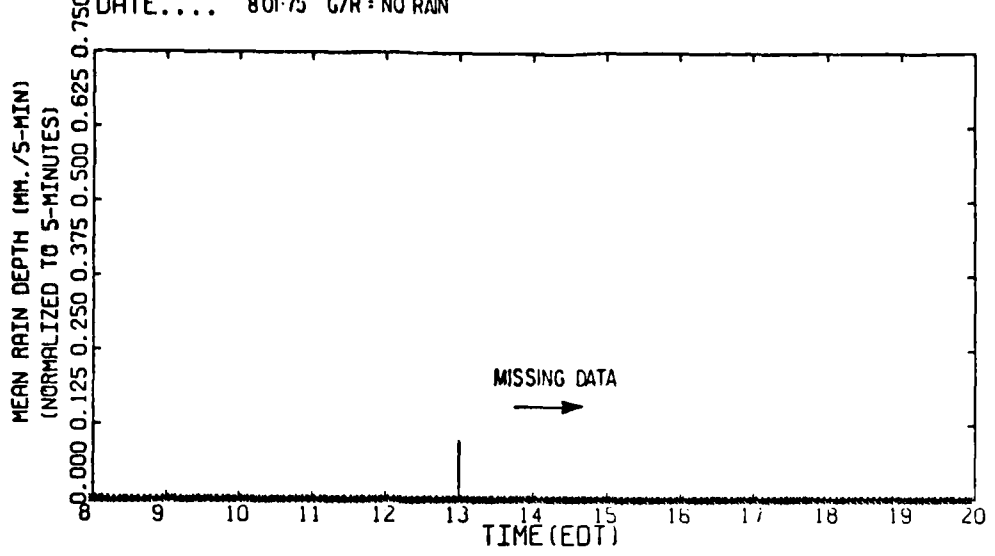
Woodley, W.L., J. Simpson, R. Biondini and J. Jordan, 1977: Rainfall results,  
1970-1975: Florida Area Cumulus Experiment. Science, 195, 735-742.

## APPENDIX

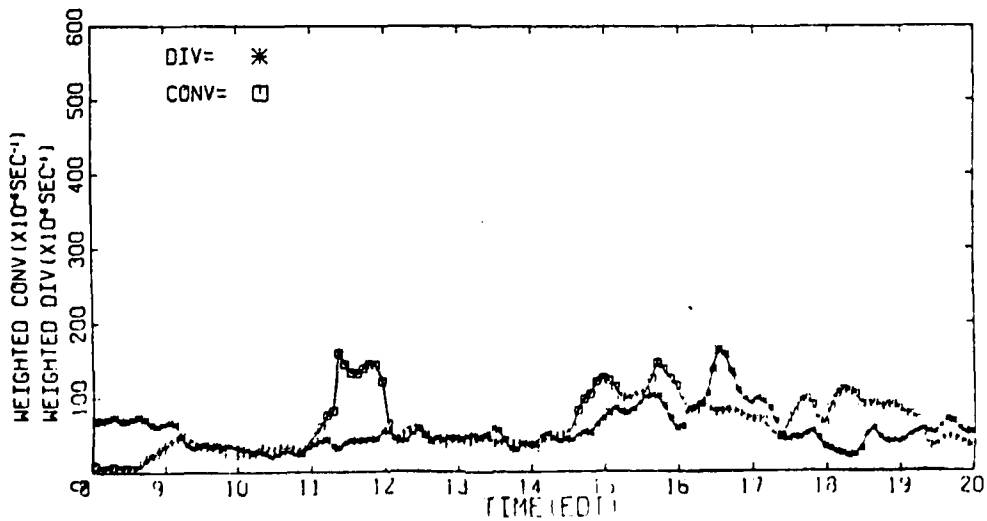
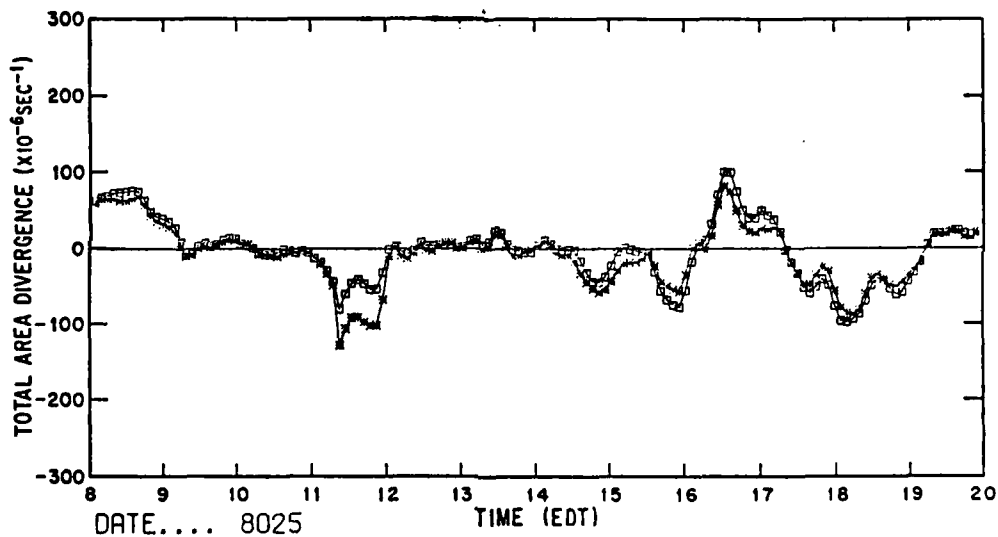
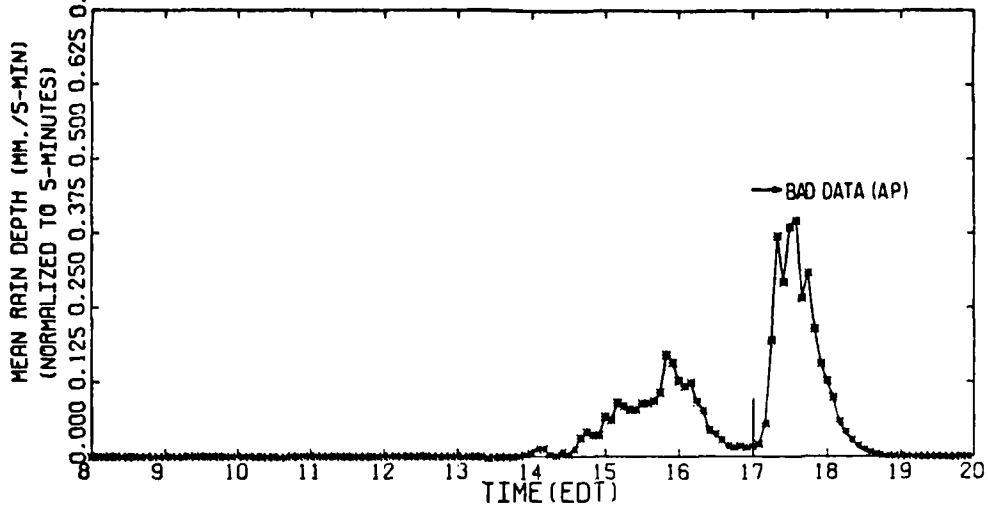
The Appendix includes FACE mesonetwork radar and wind data for 30 days of August 1975. The following time histories are presented.

1. Rain depth for the mesonetwork for each 5 min period. A gage to radar (G/R) correction is given but not applied to the time series. Periods of missing data are also shown.
2. Total area divergence for each 5 min period. The squares define the time history of line integral divergence while the stars are applied to area averaged divergence. Both methods are calculated through the use of an objective analysis scheme.
3. Weighted divergence/convergence for each 5 min period.

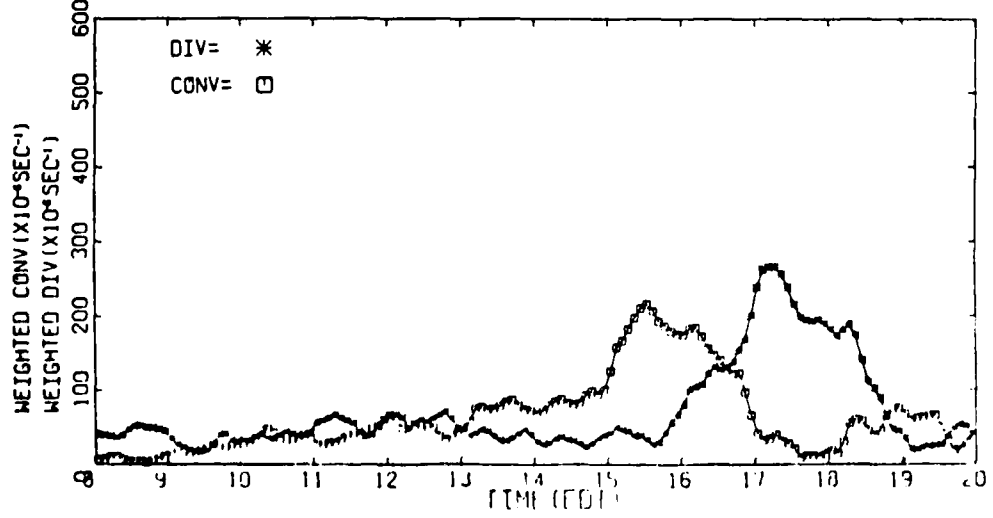
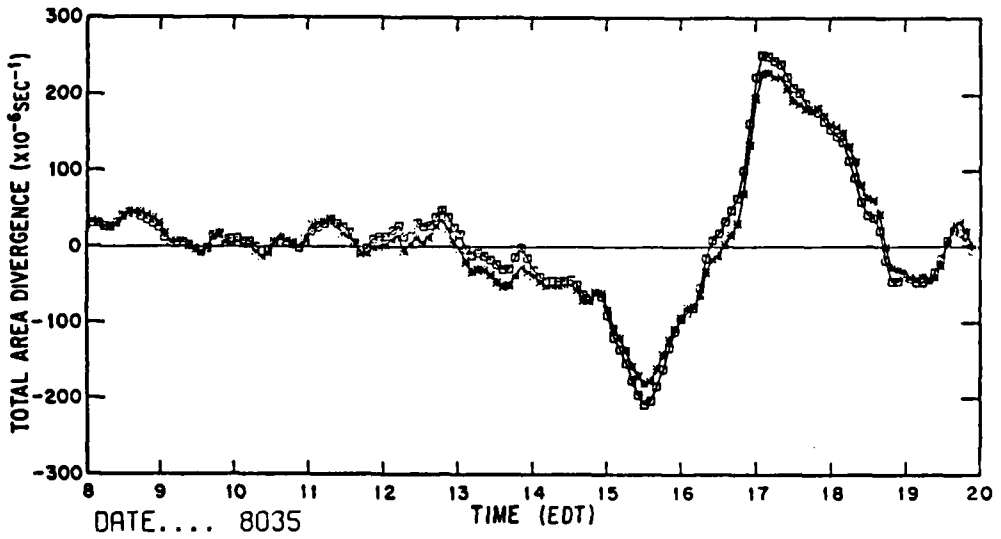
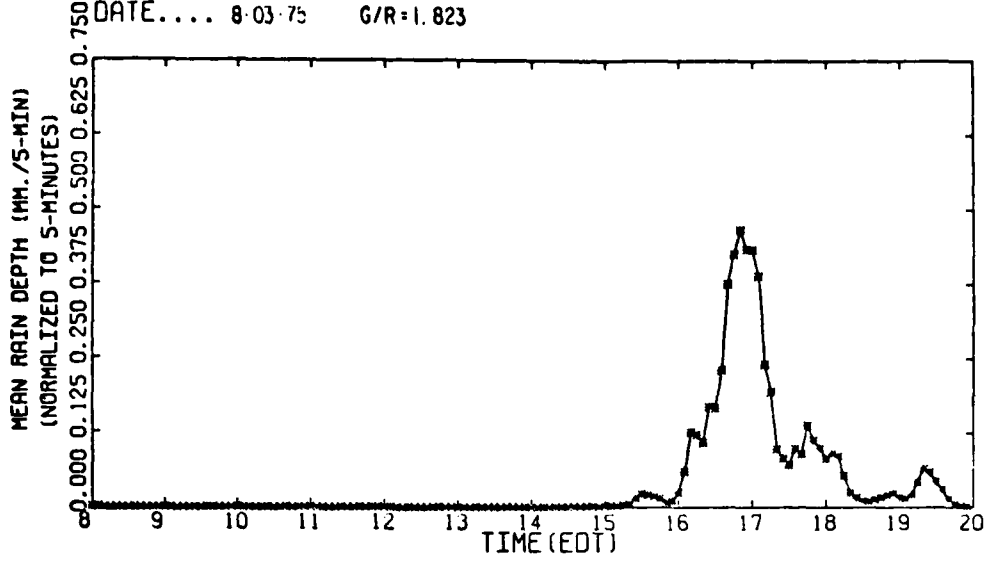
DATE.... 80175 G/R = NO RAIN



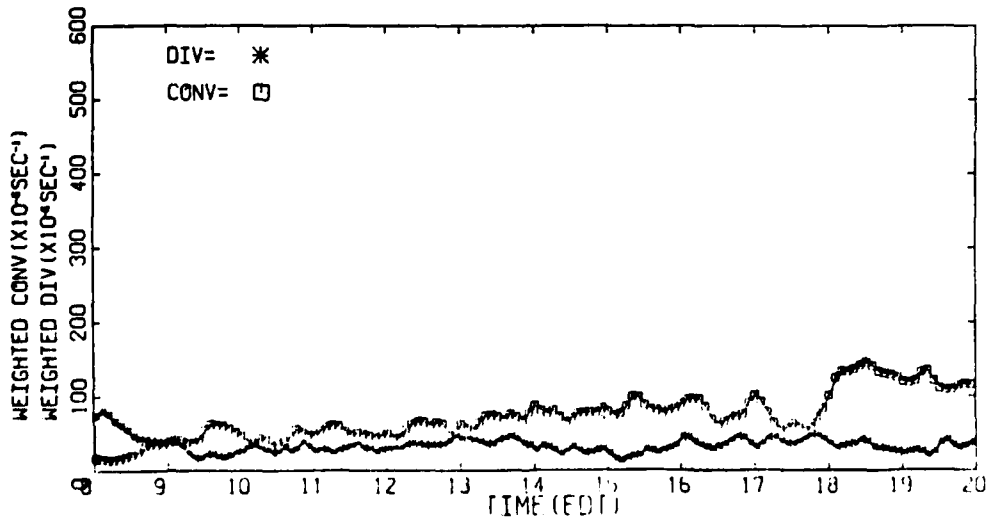
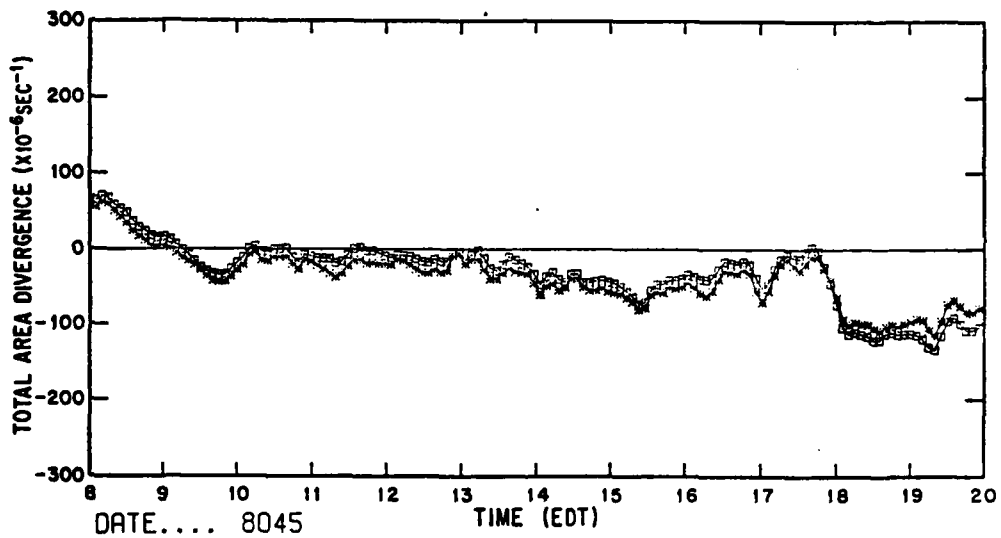
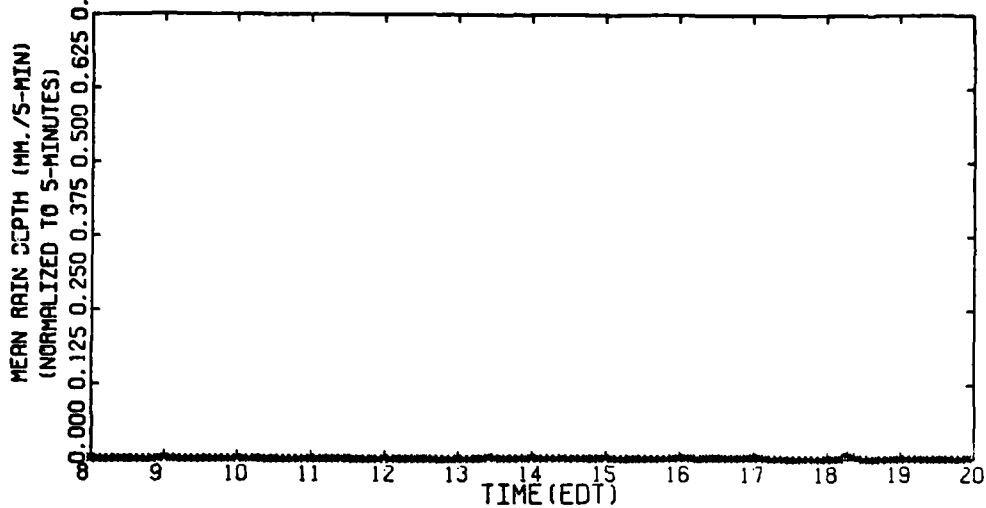
DATE.... 8 02-75 G/R =0.764



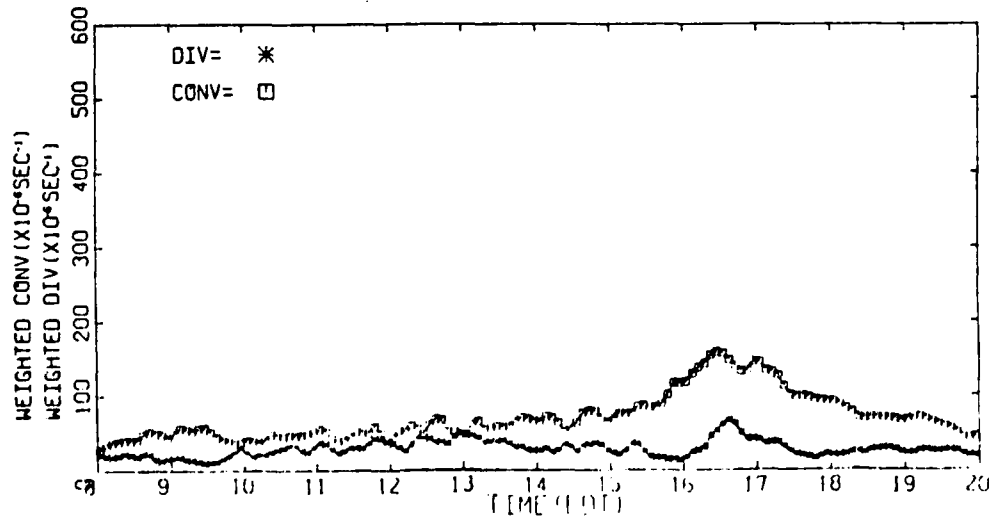
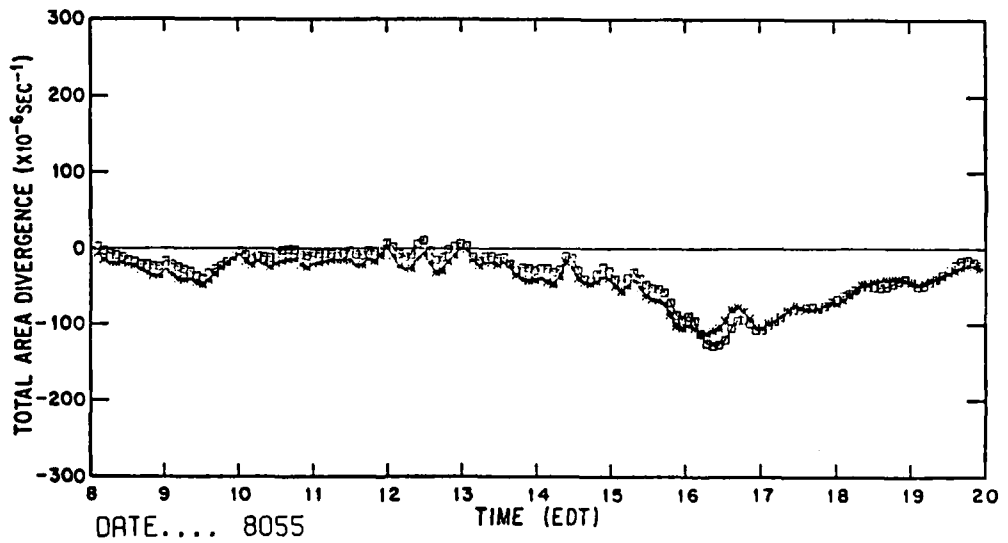
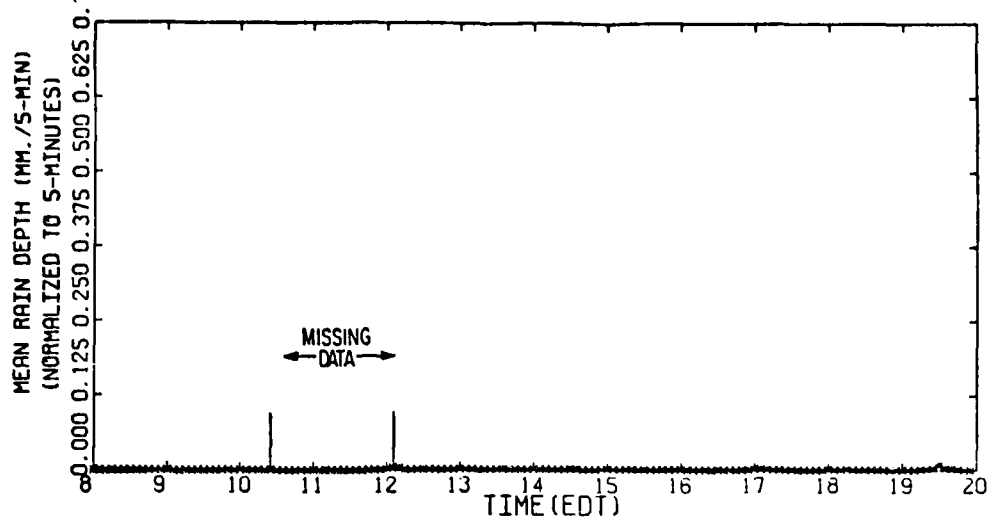
DATE.... 8-03-75 G/R=1.823



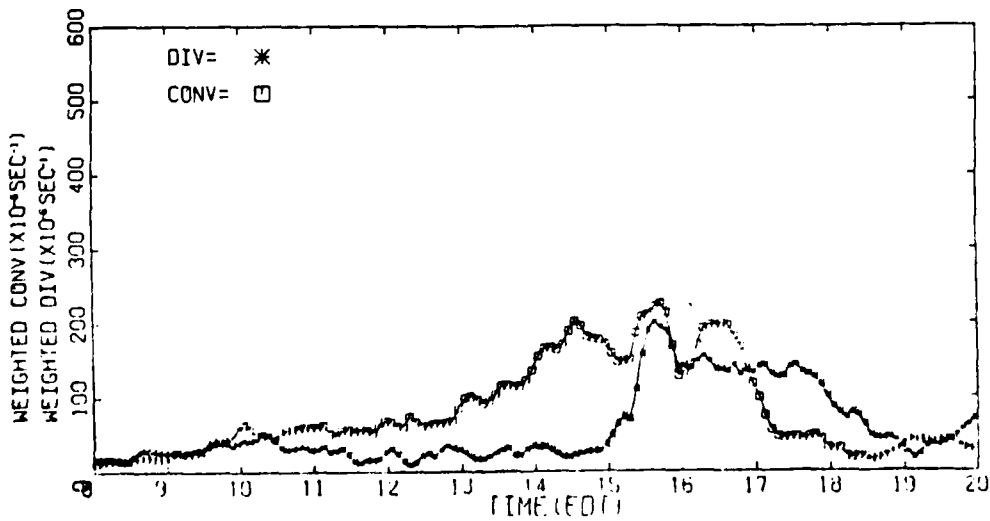
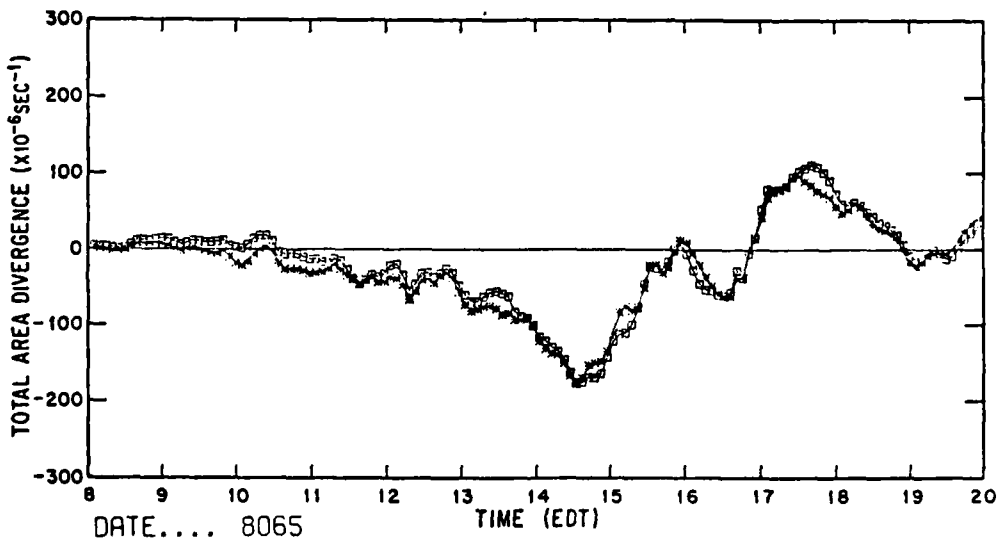
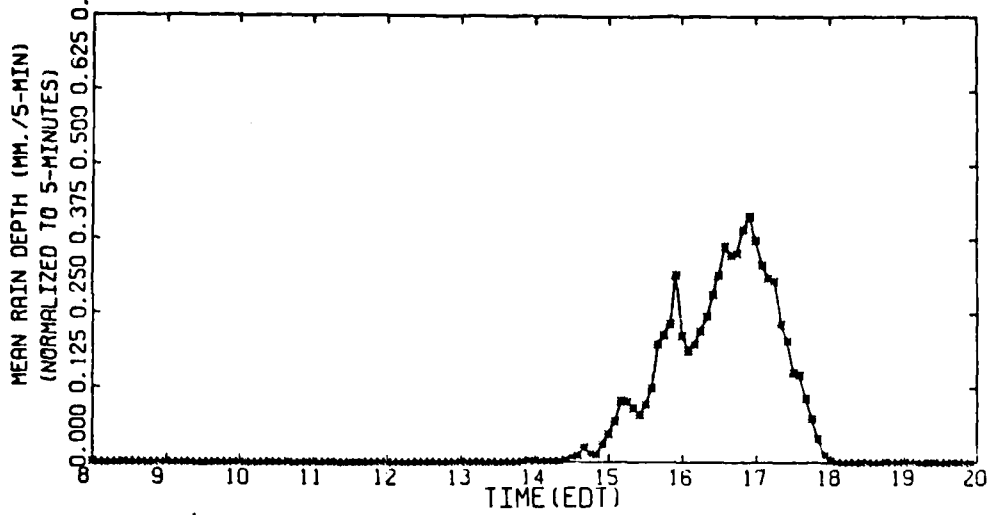
DATE.... 80475 G/R=1.364



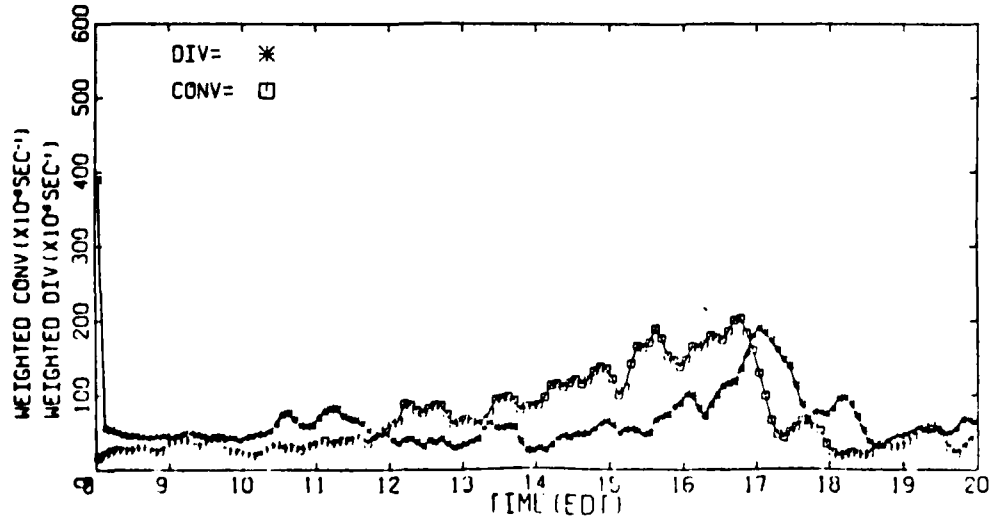
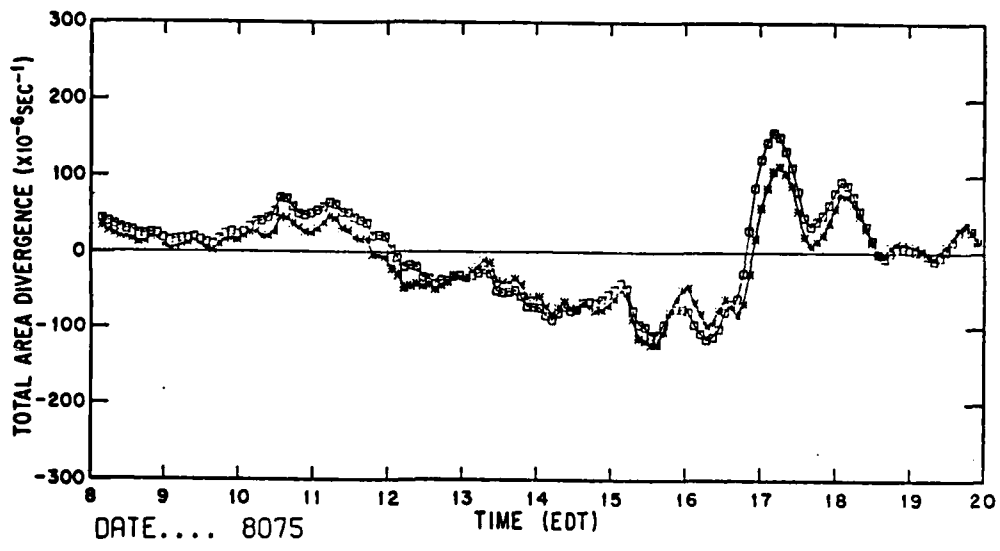
DATE.... 80575 G/R: NO RAIN



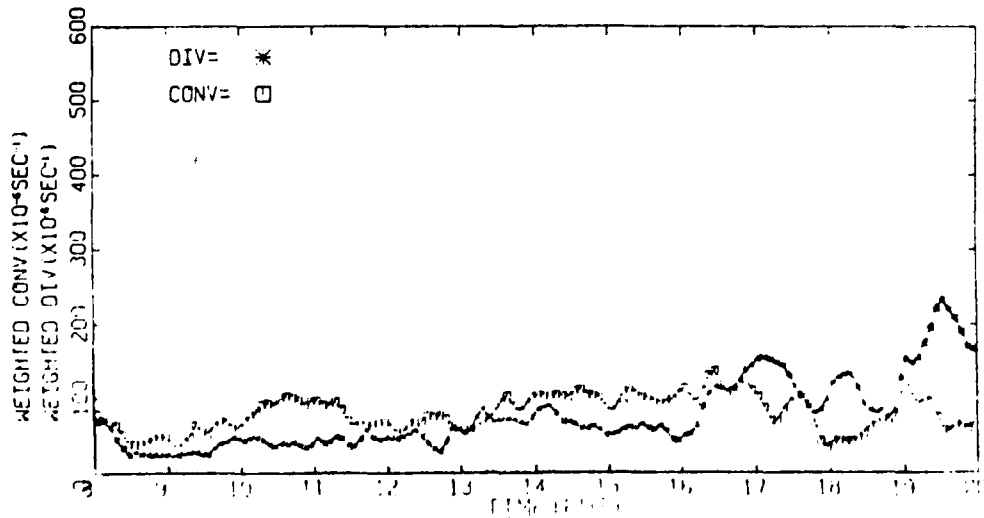
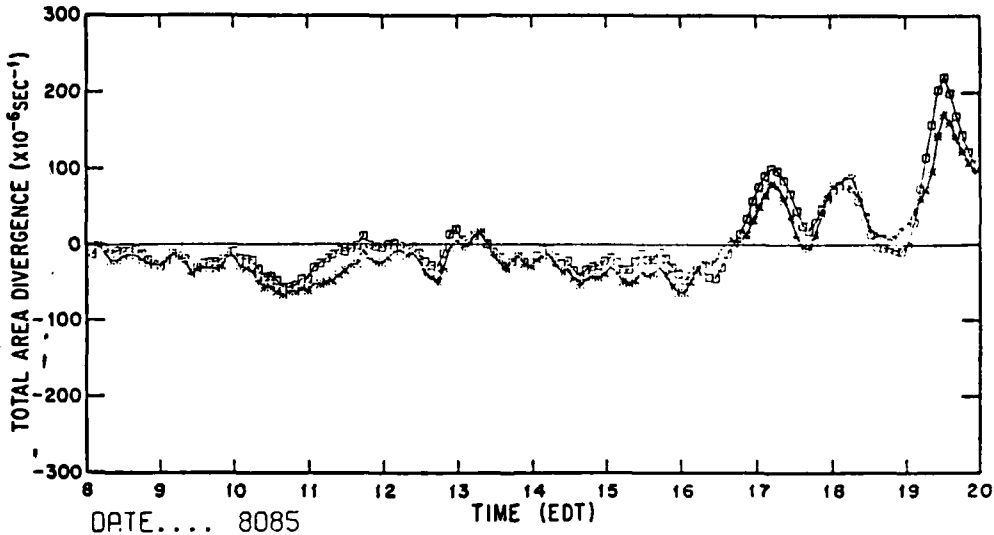
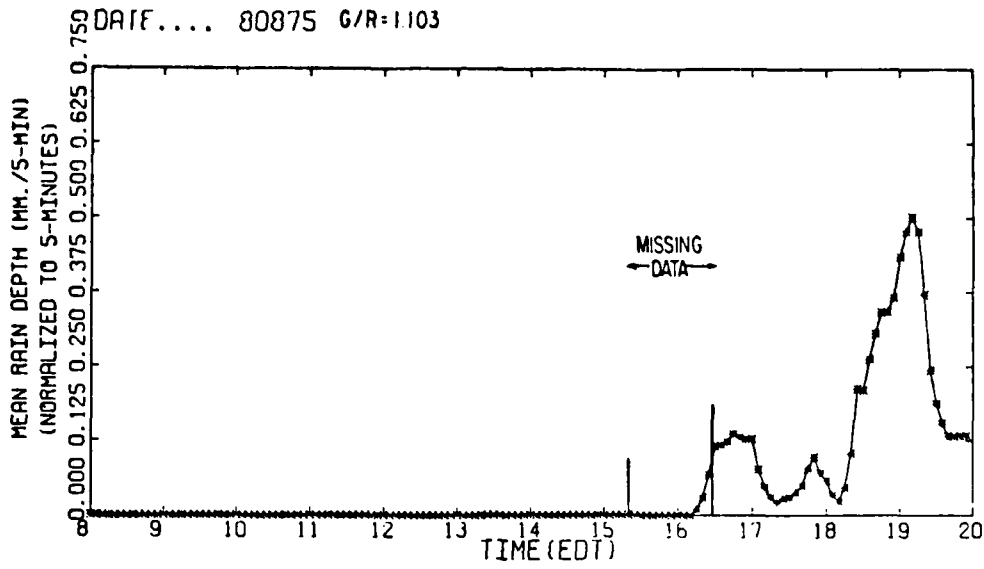
DATE.... 80675 G/R=0.905



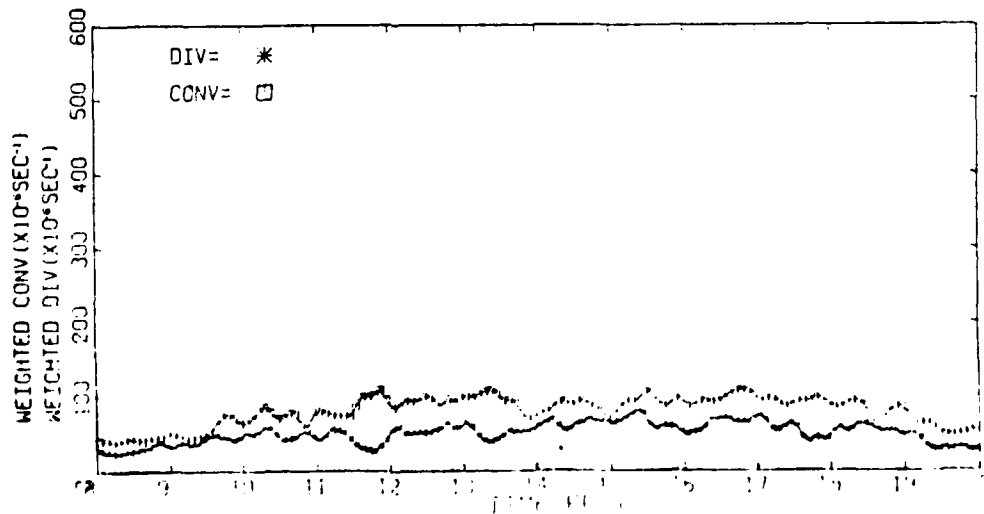
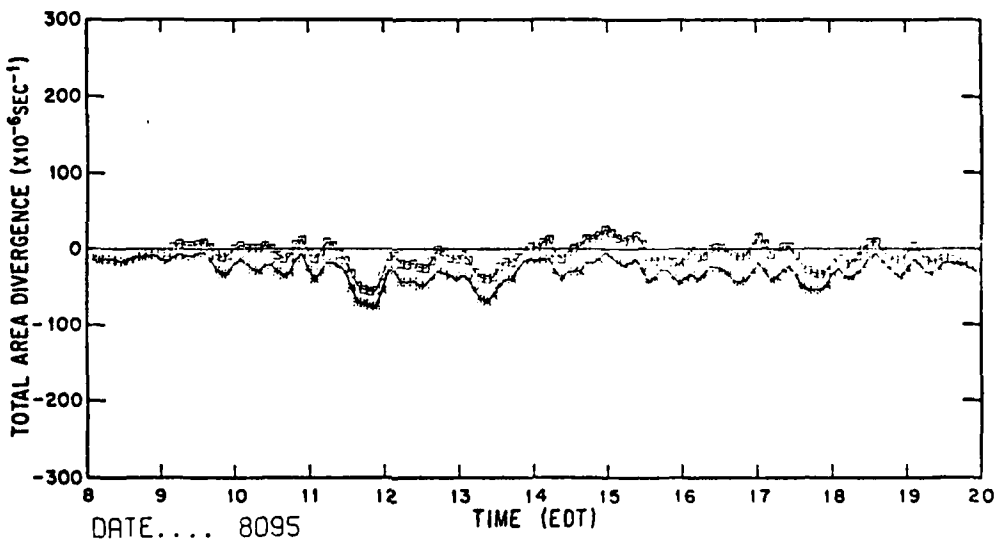
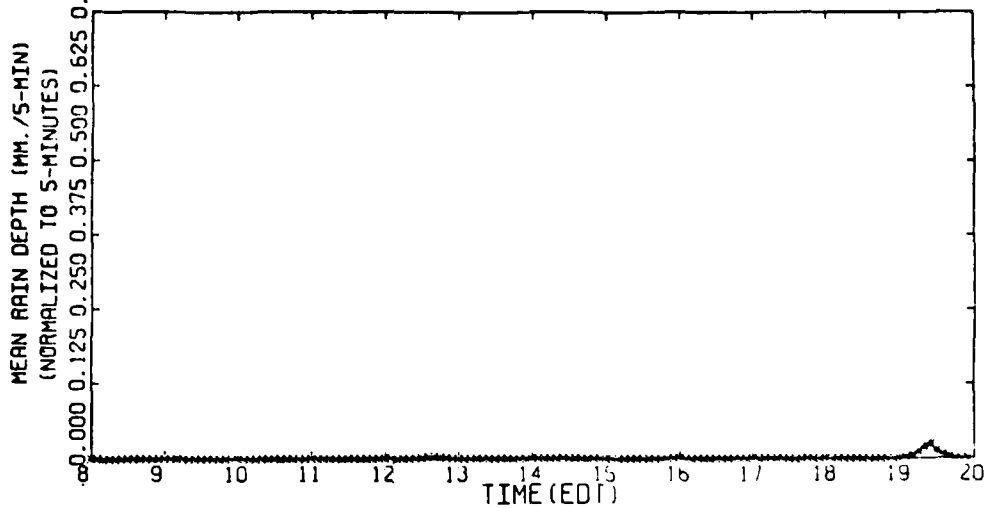
NO RADAR DATA  
7 AUG 75



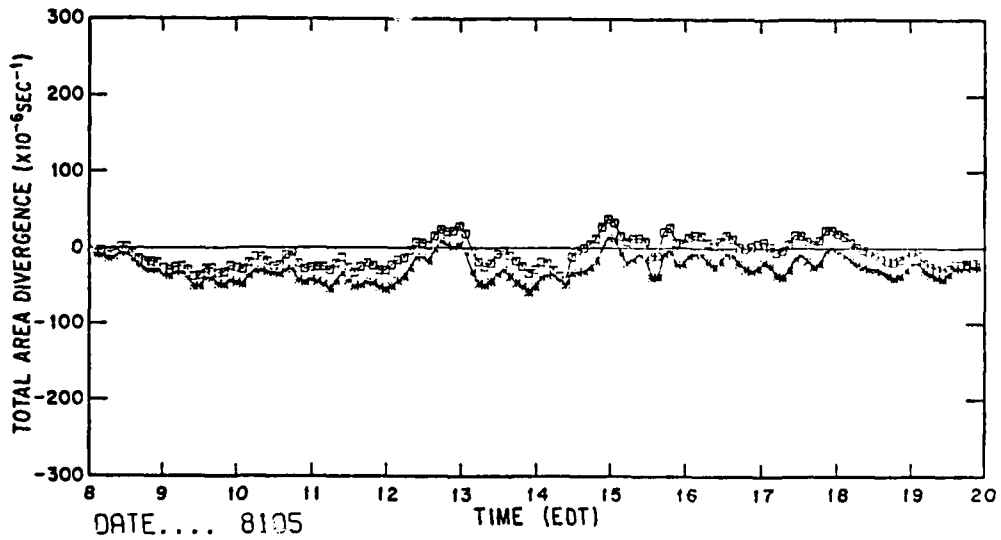
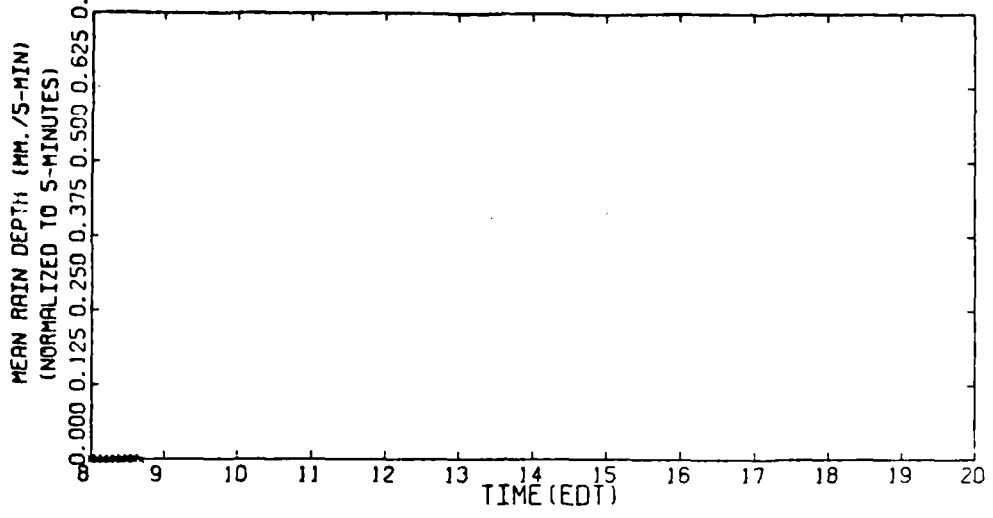
DATE.... 80875 G/R=1.103



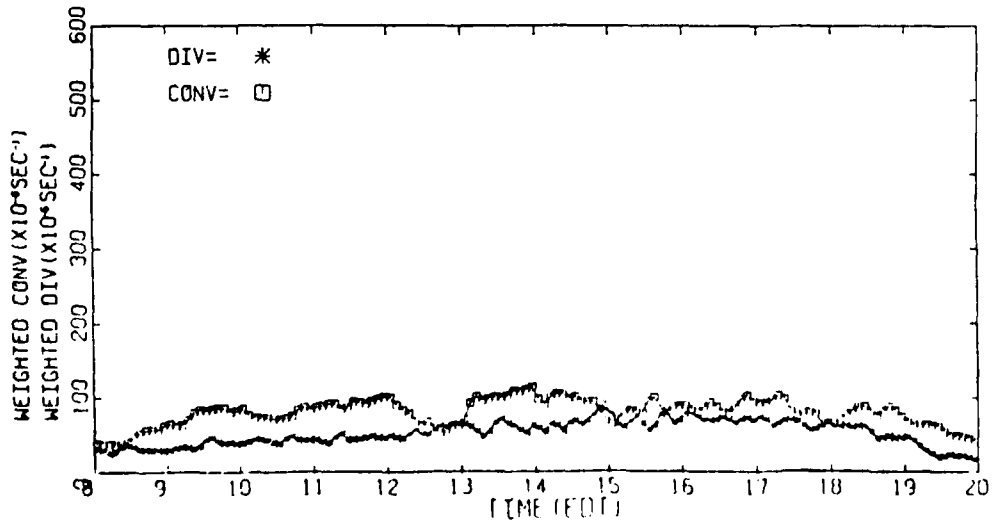
DATE.... 80975 G/R=1.0



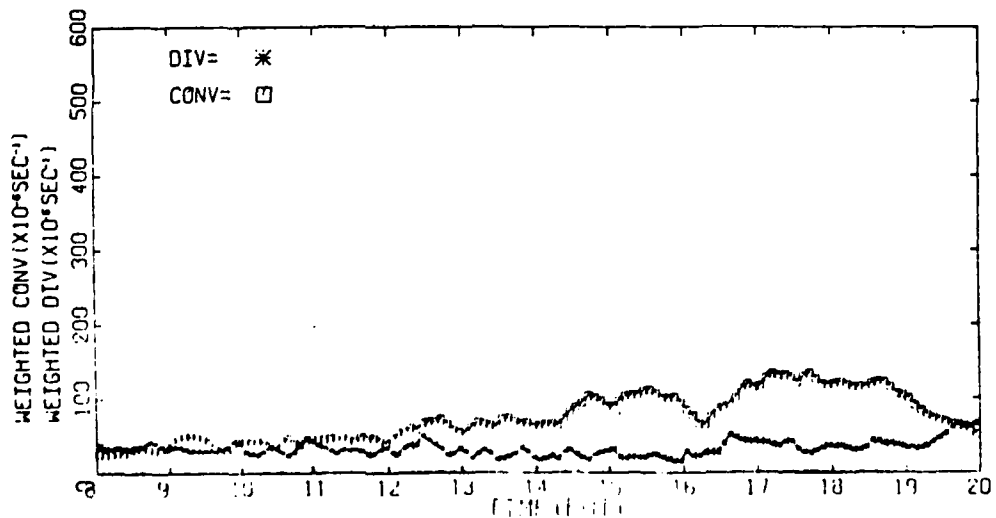
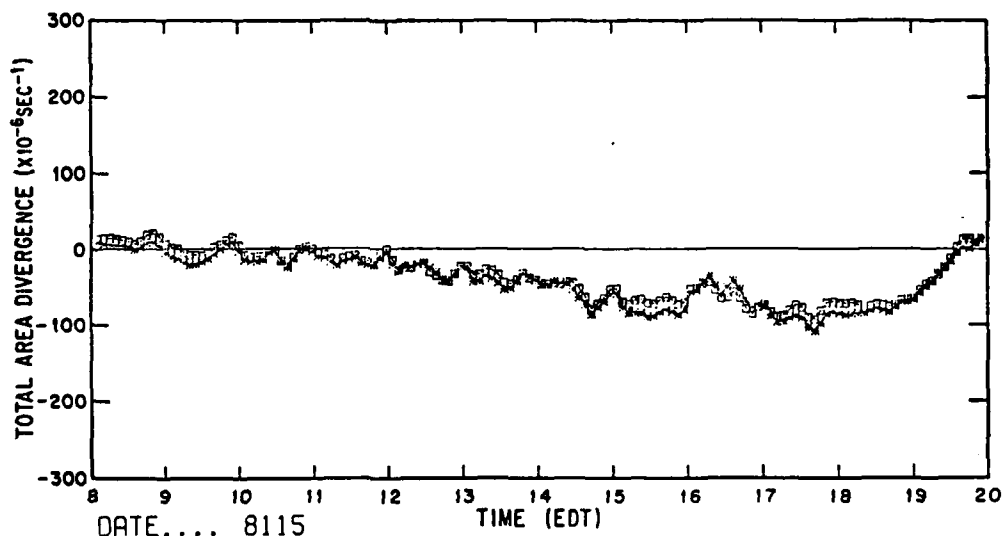
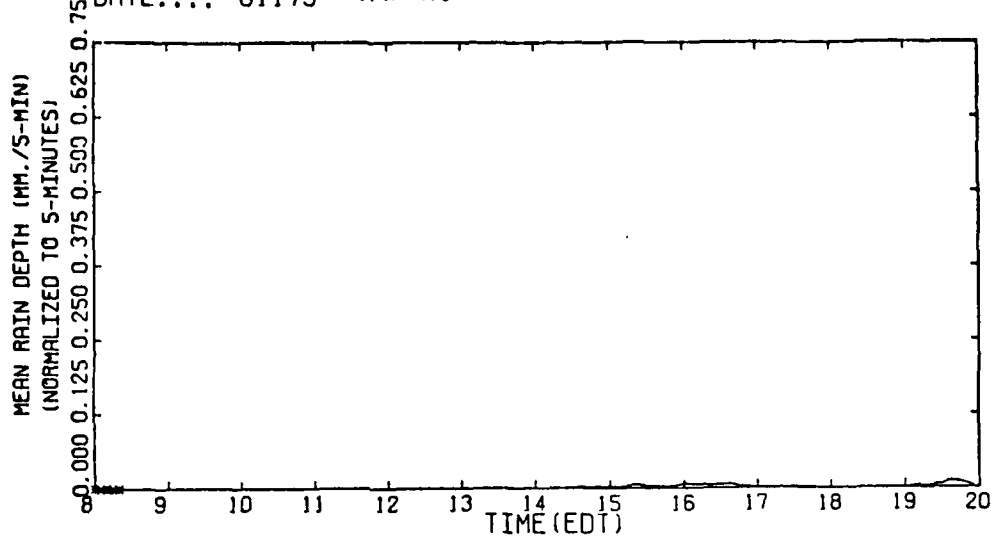
DATE.... 81075 G/R = NO RAIN



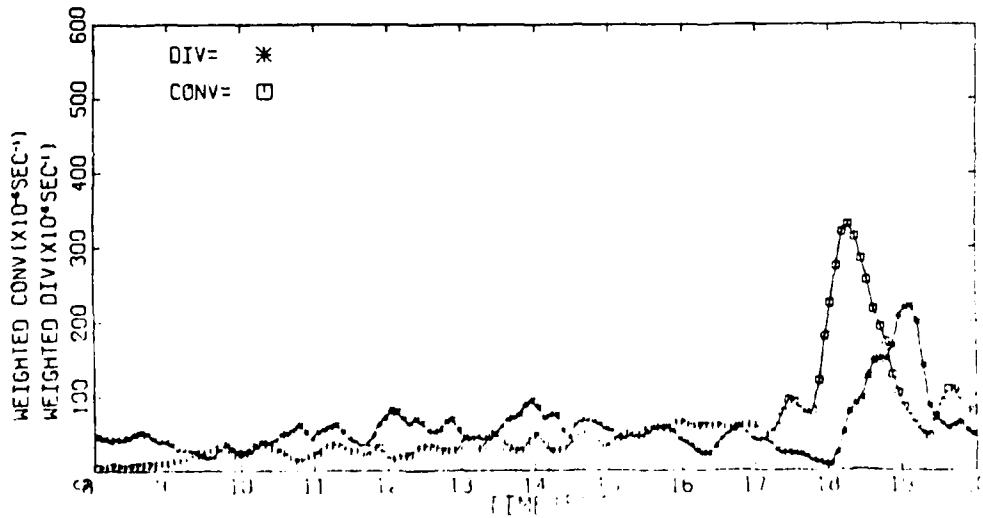
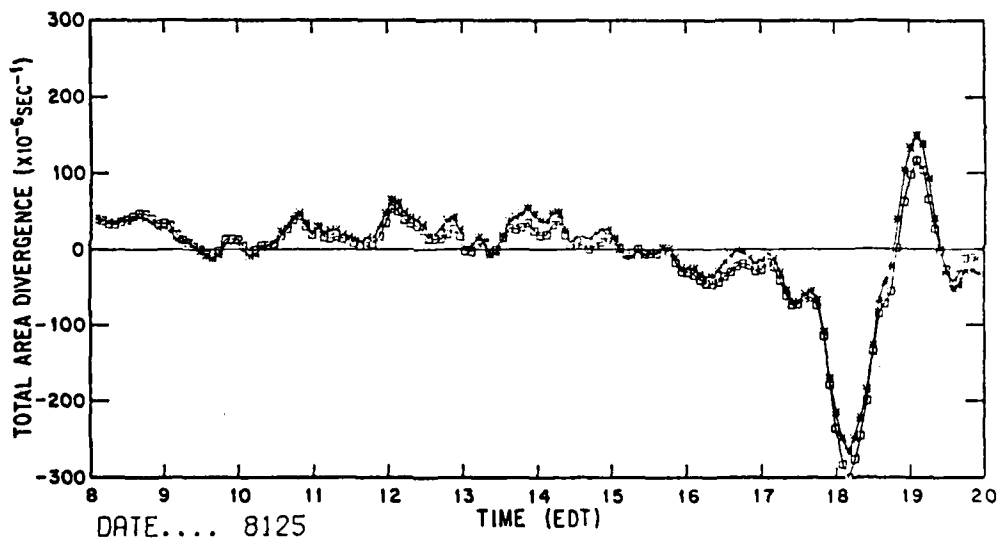
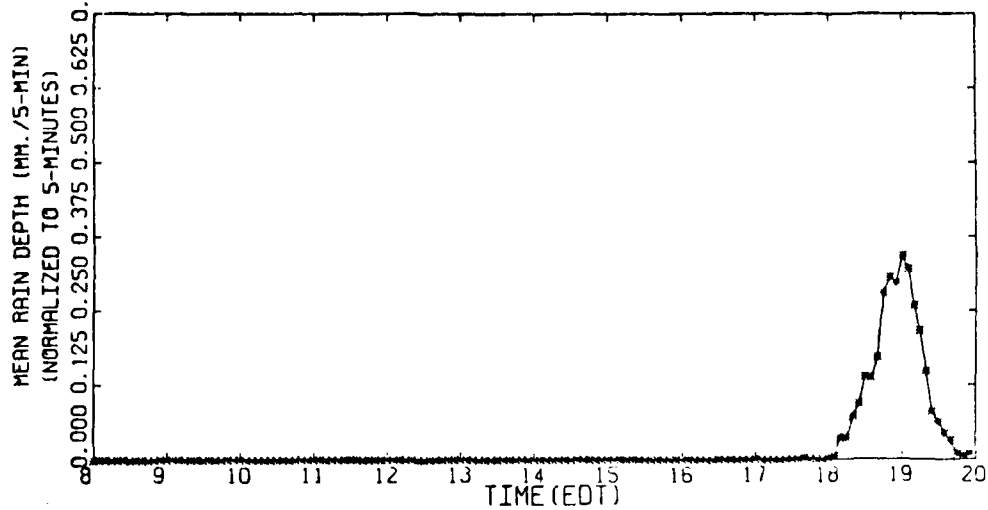
DATE.... 8105



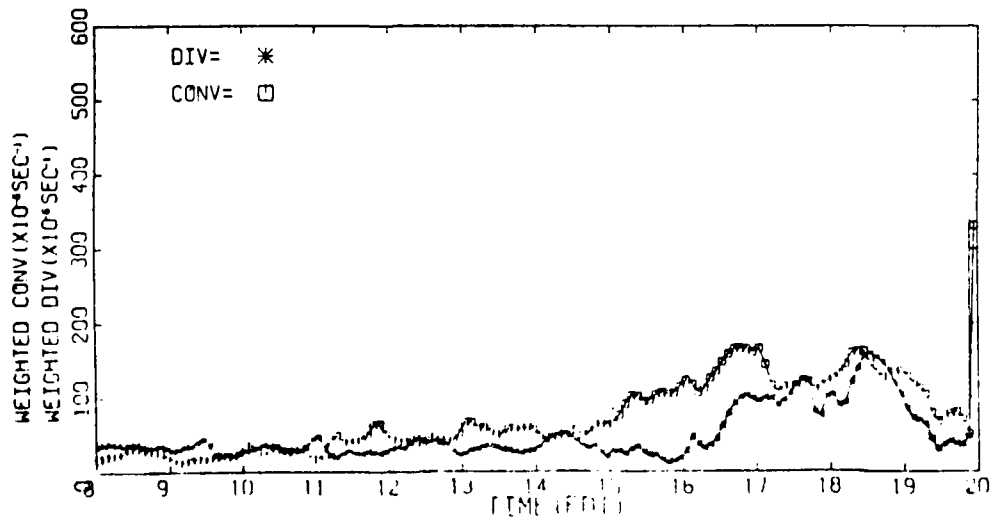
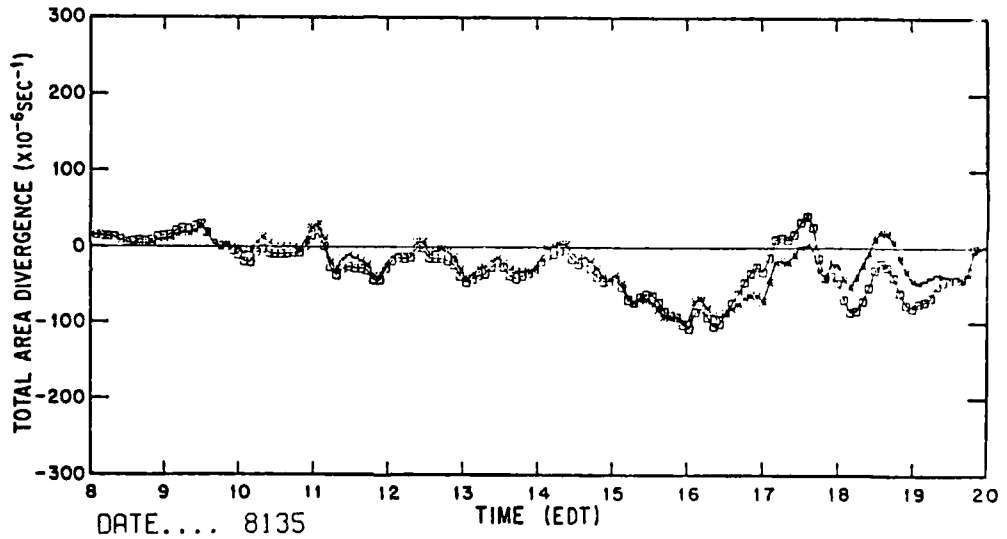
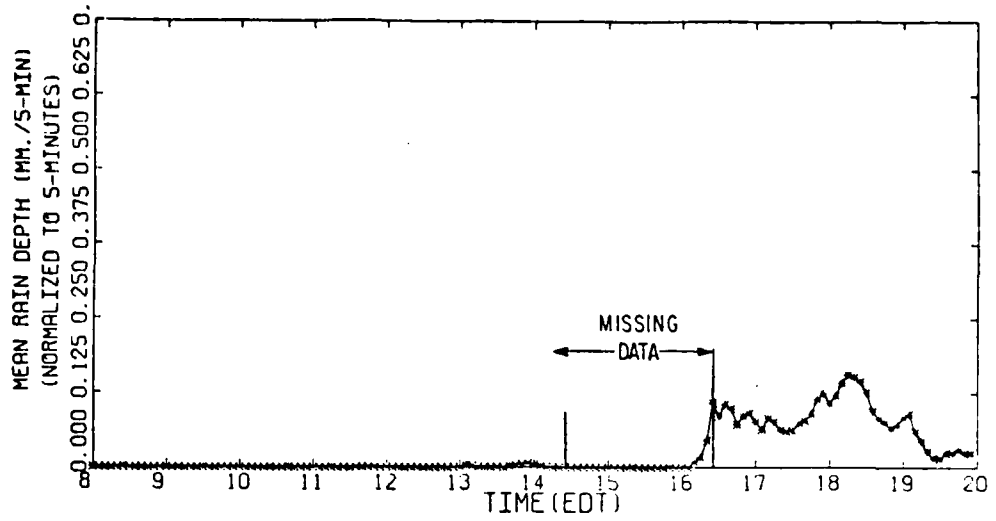
DATE.... 81175 G/R=1.0



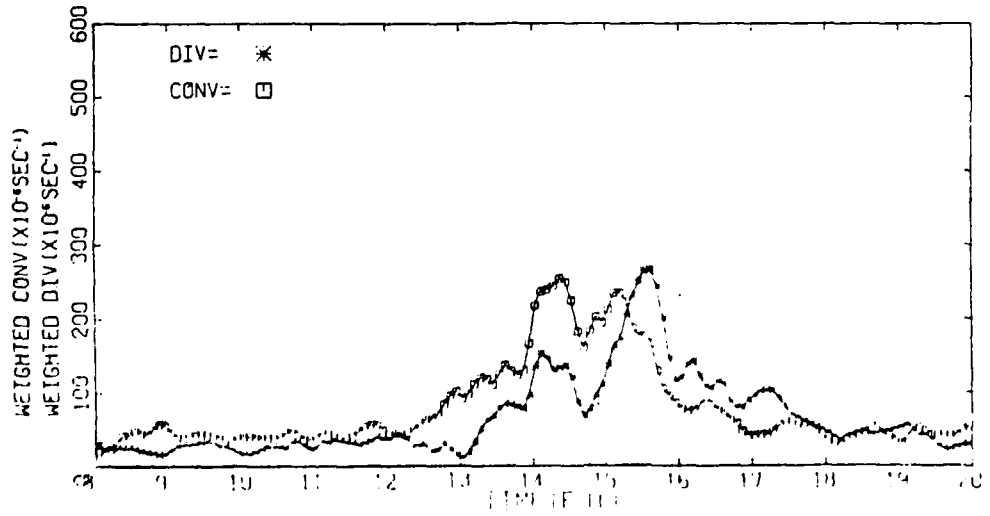
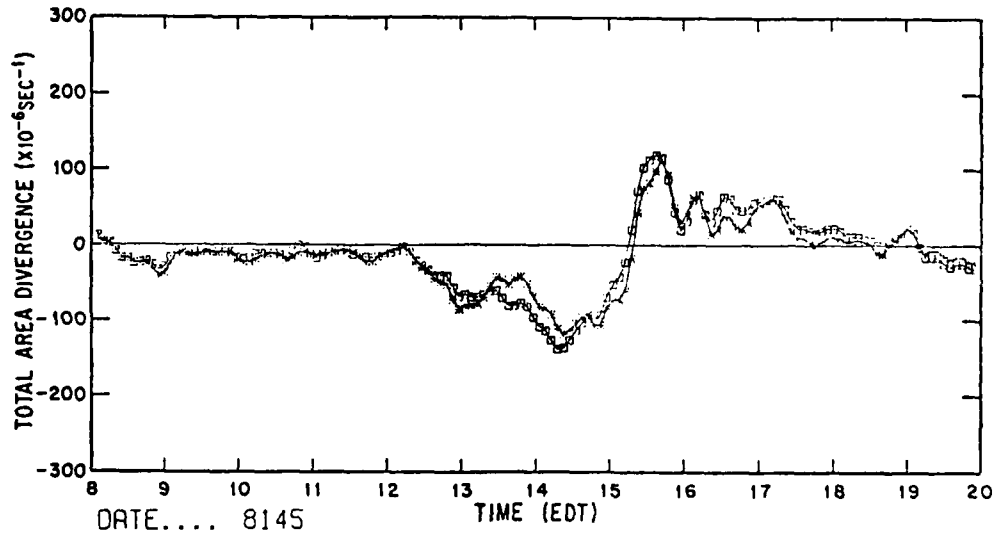
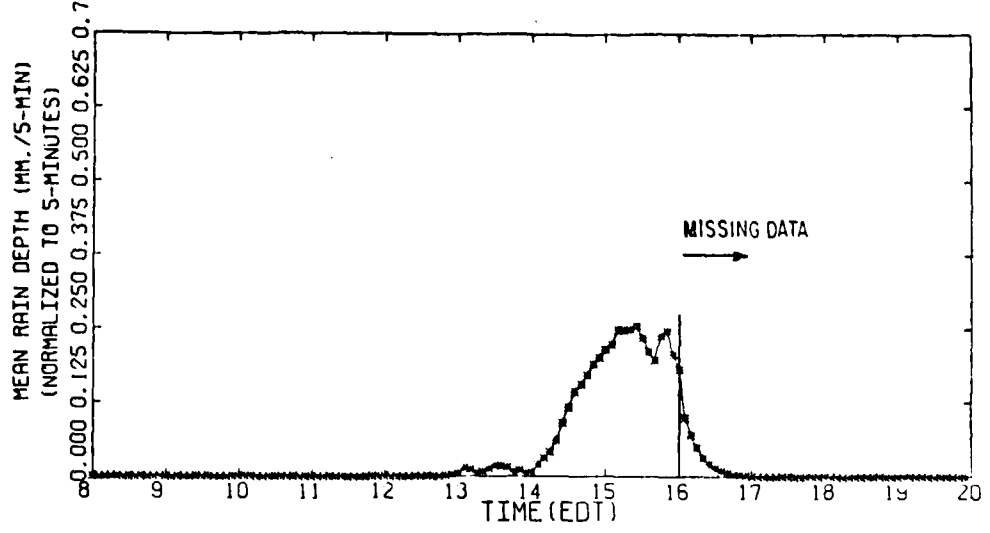
DATE.... 81275 G/R =.794



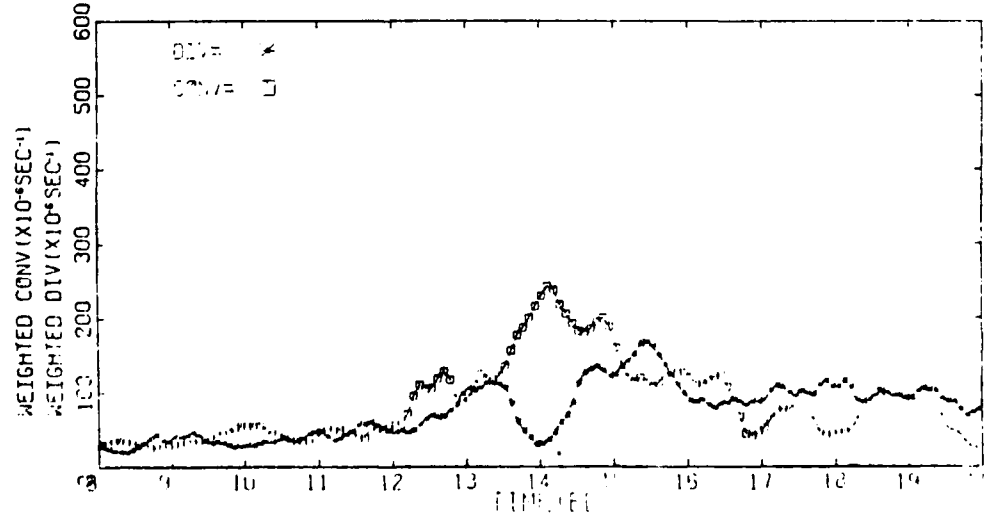
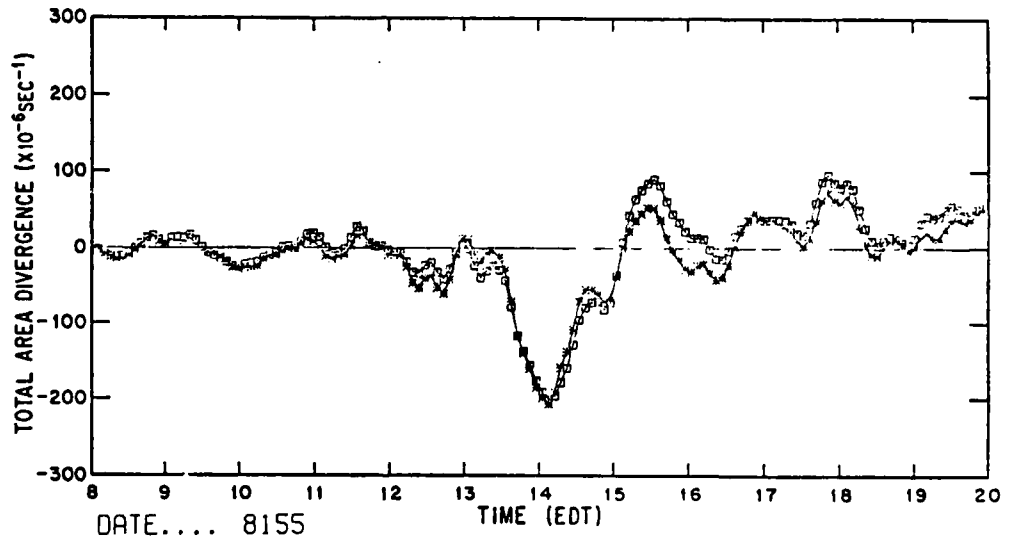
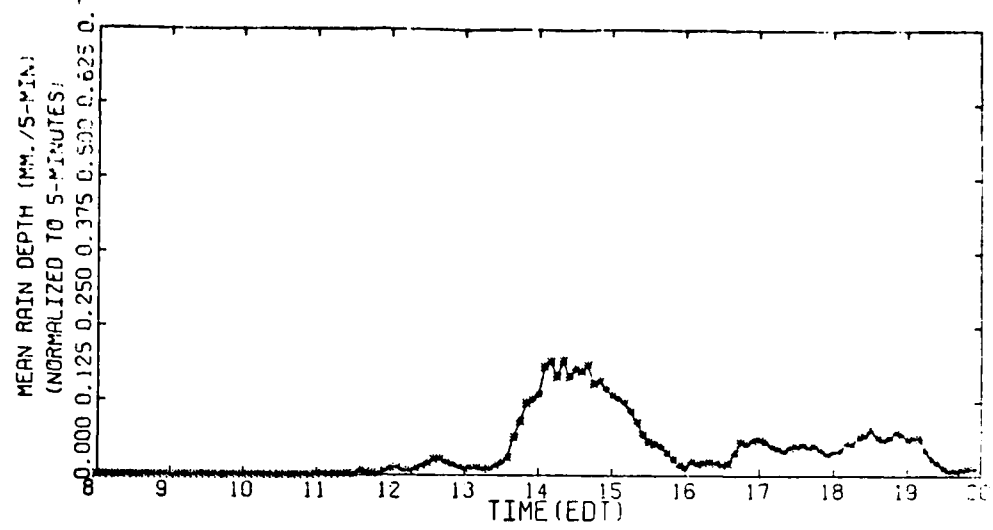
DATE.... 81375 G/R: NOT ENOUGH RADAR DATA



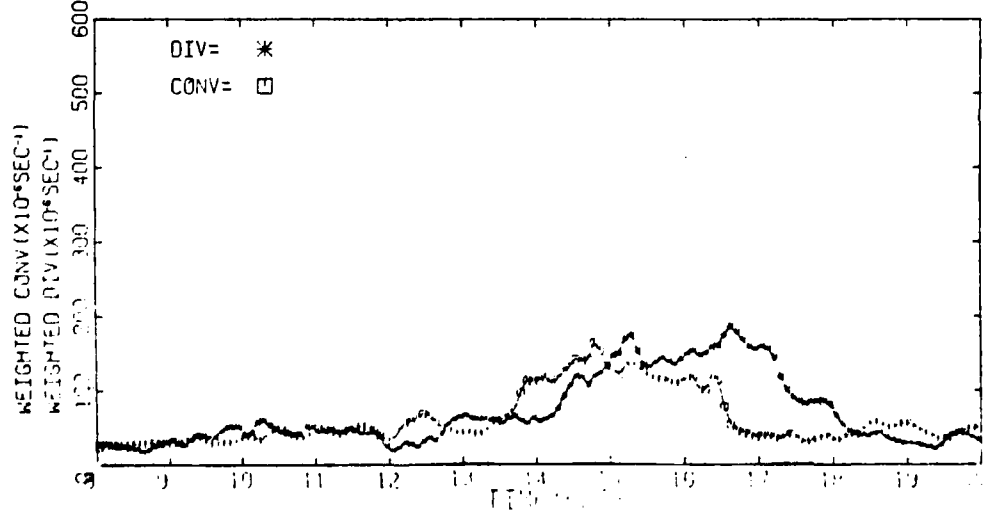
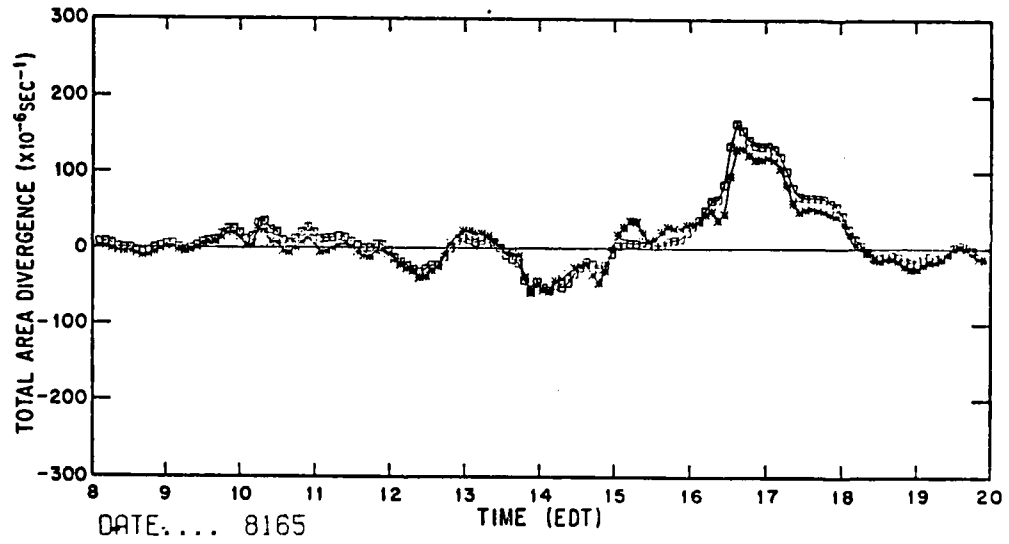
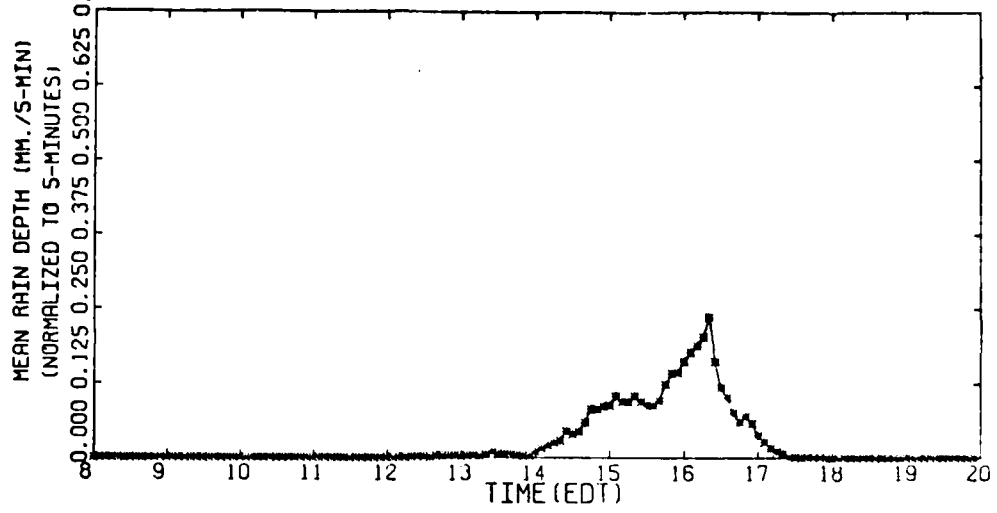
DATE.... 81475 G/R :1.628



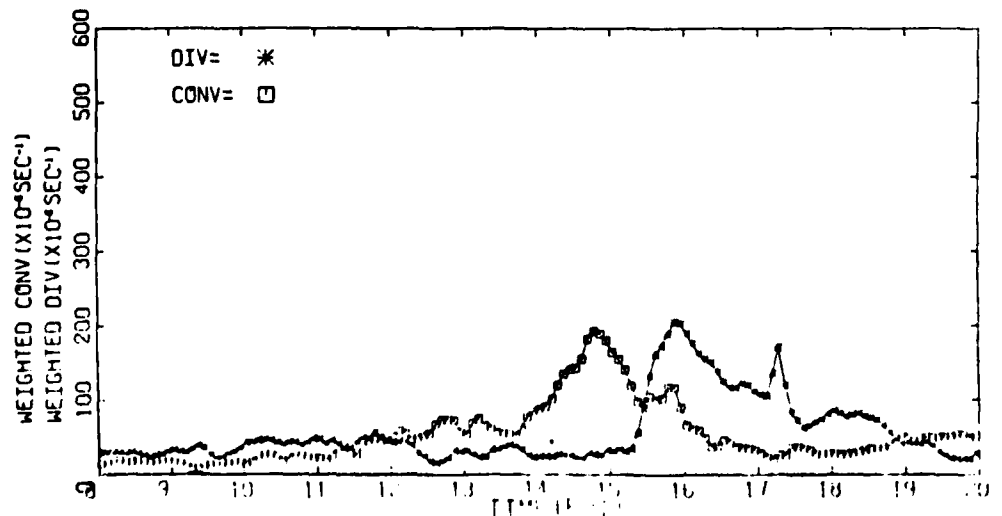
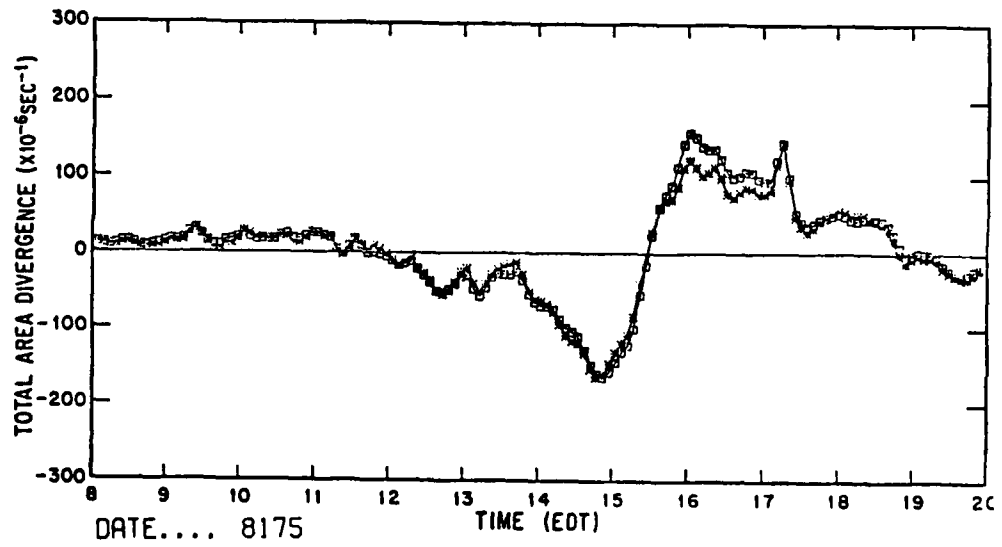
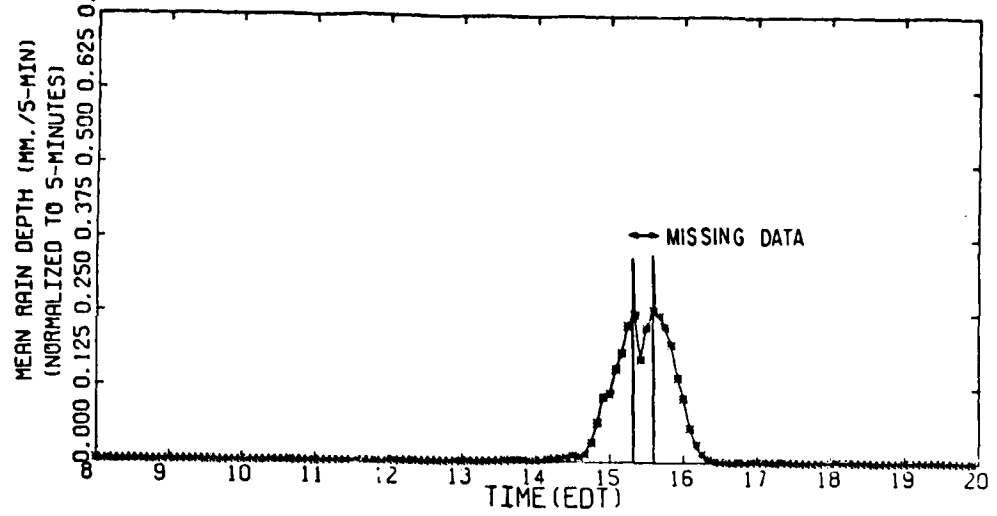
DATE.... 81575 G/R=1.857



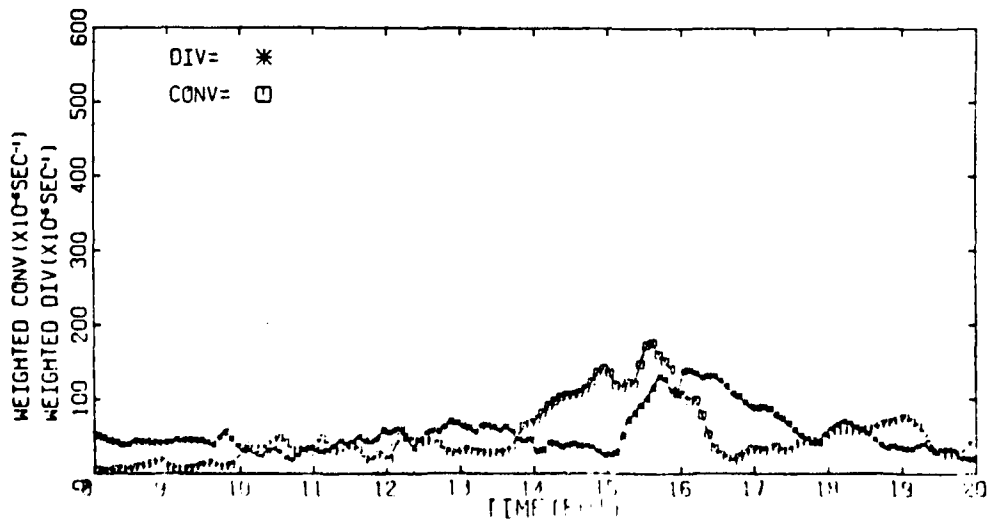
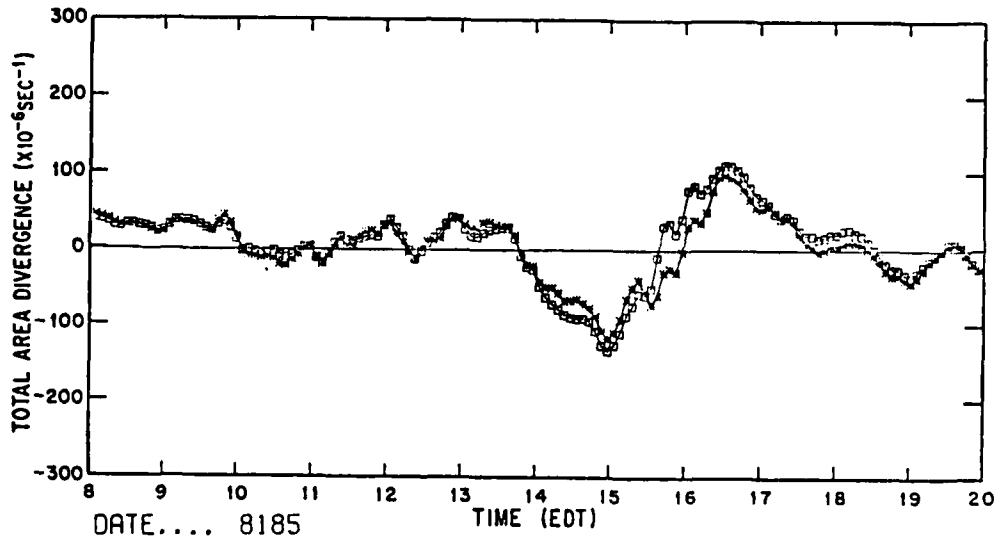
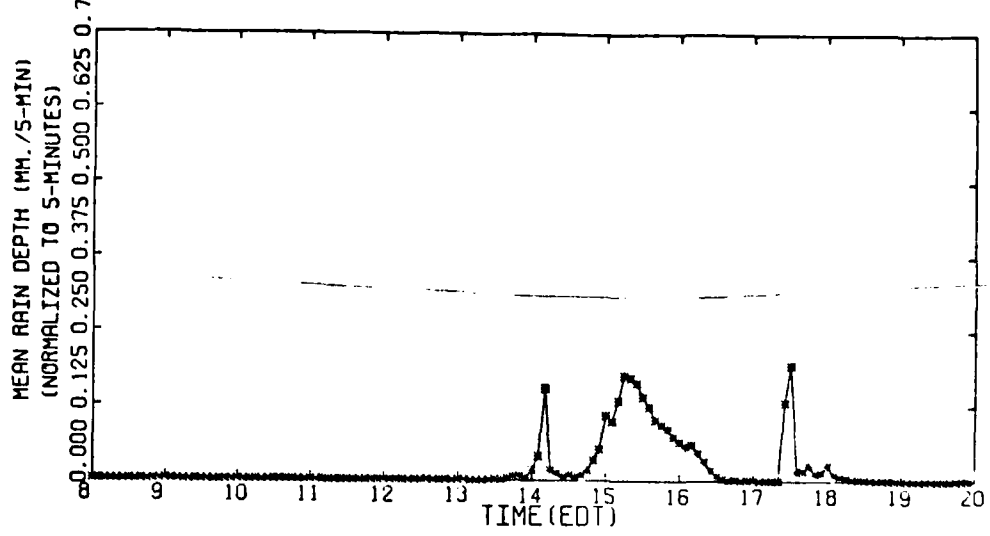
DATE.... 81675 G/R=1.476



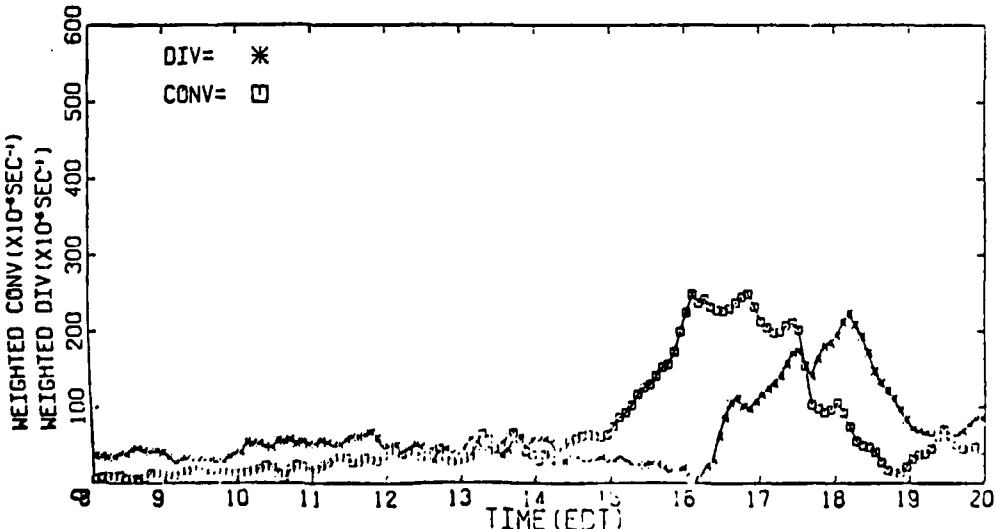
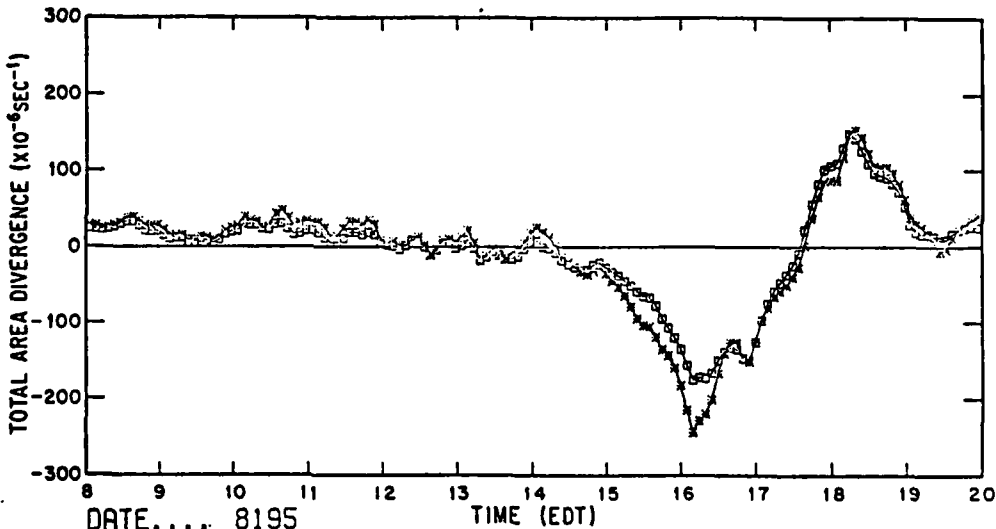
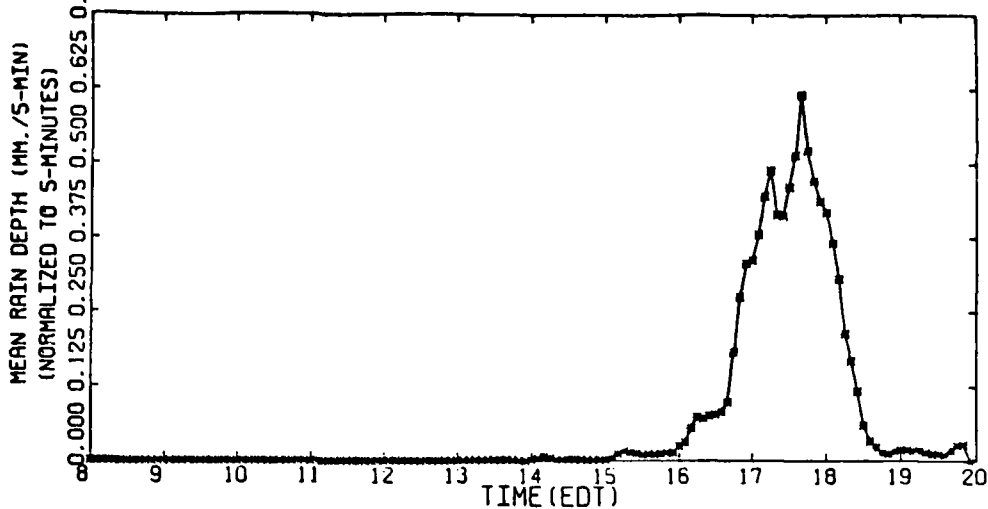
DATE.... 81775 G/R= 3.026



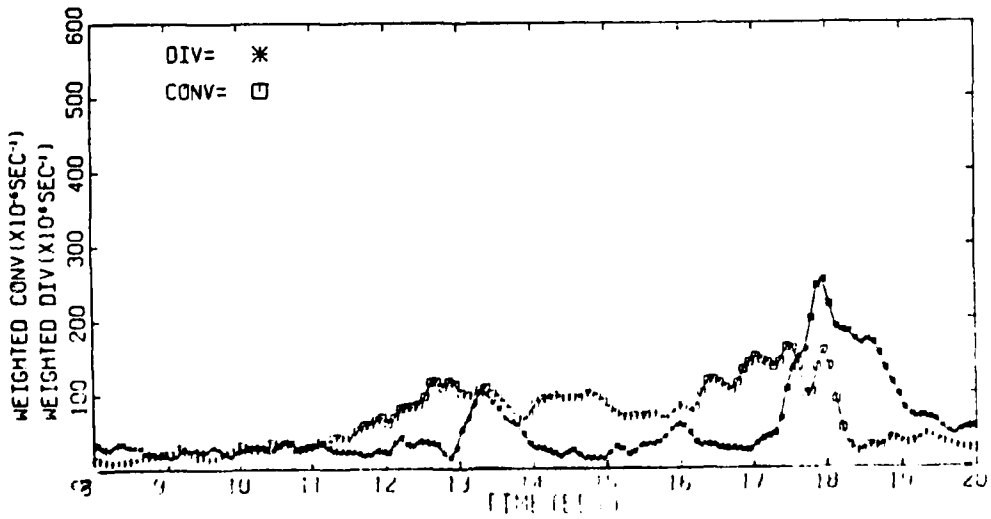
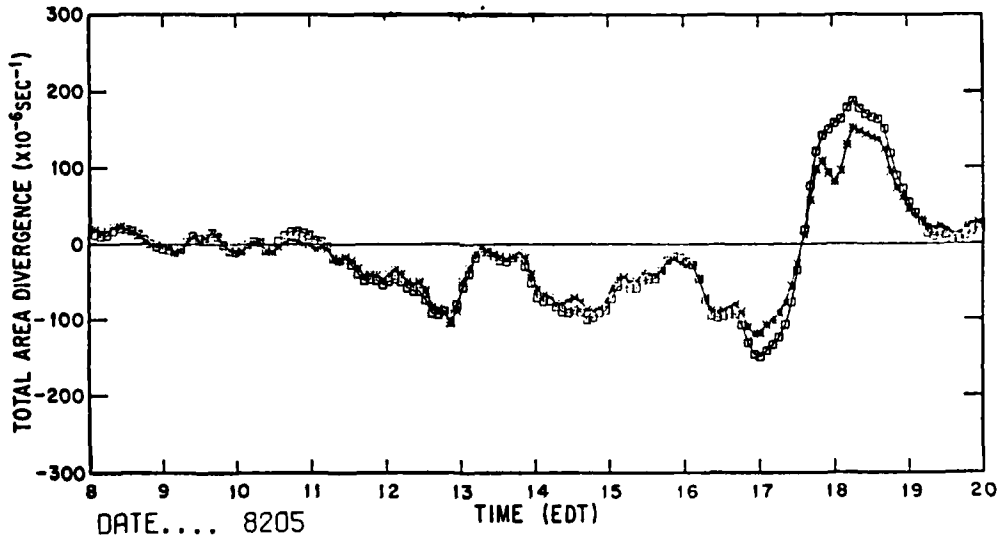
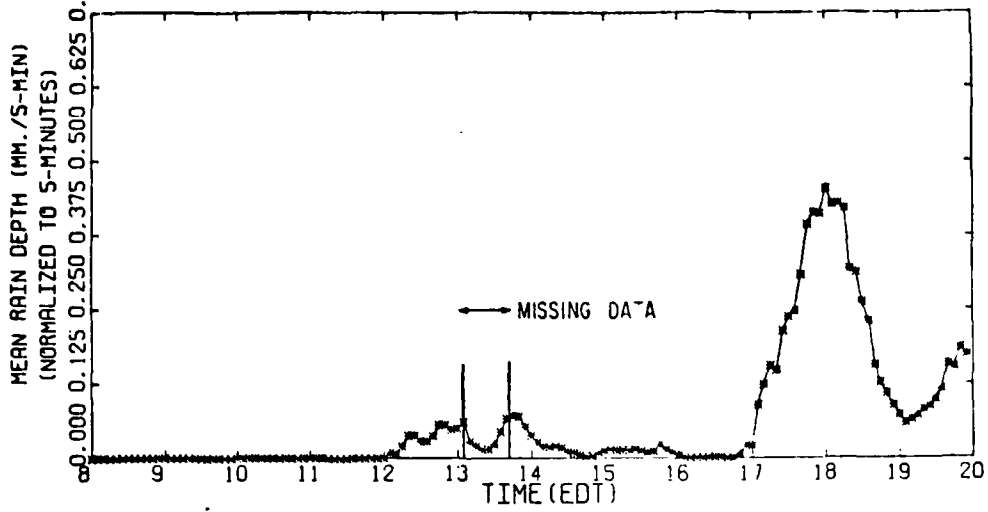
DATE.... 81875 G/R=1.709



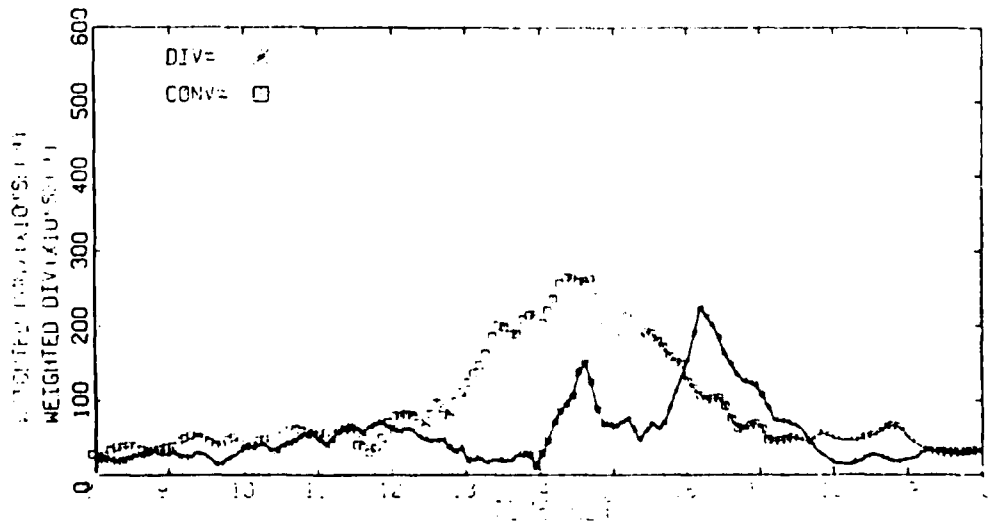
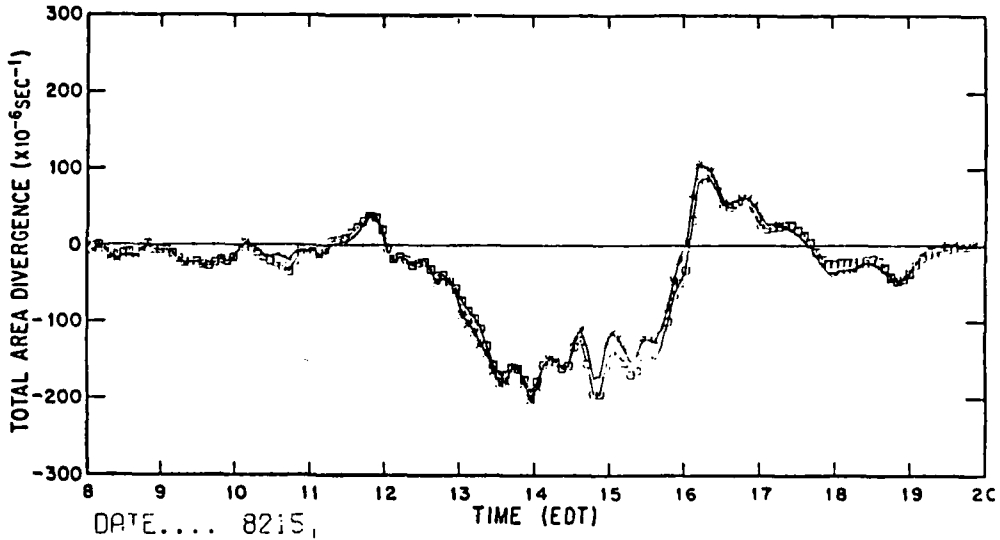
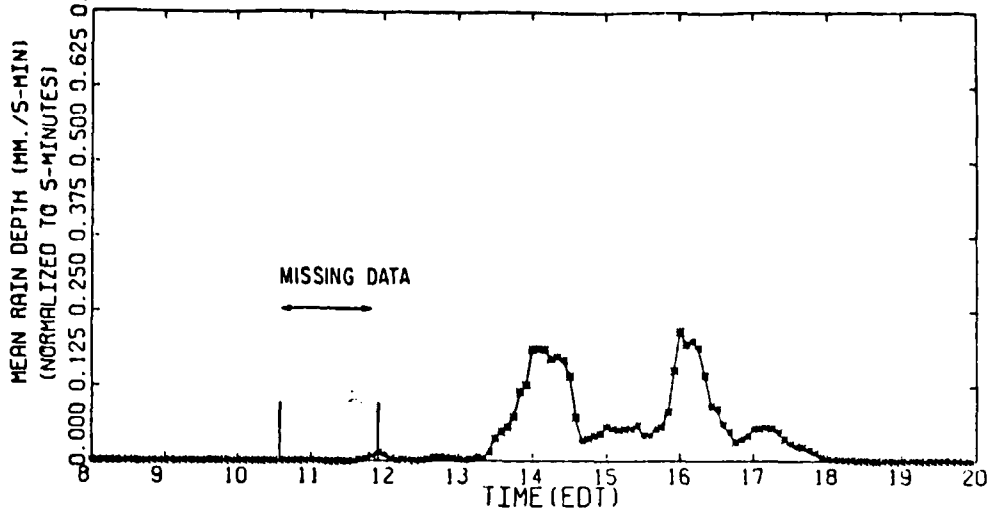
DATE.... 81975 G/R:1.969



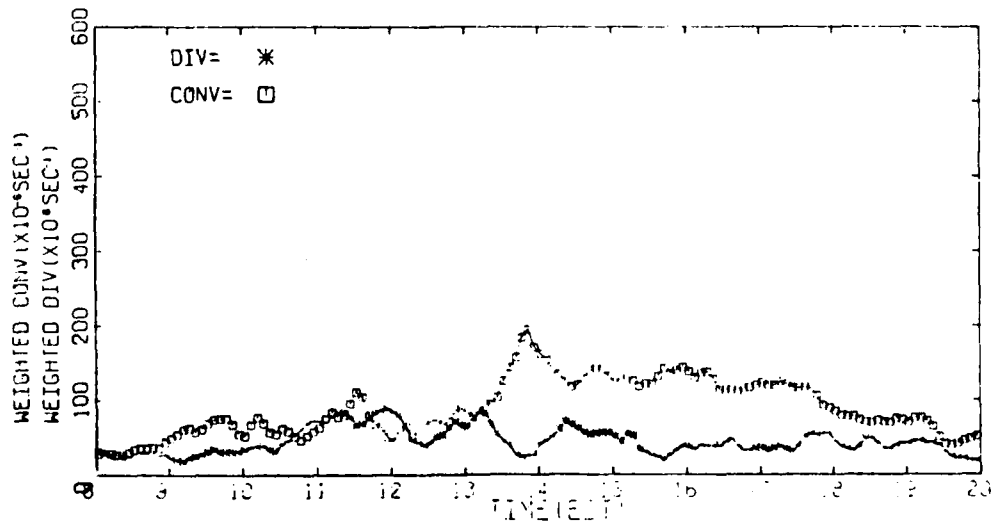
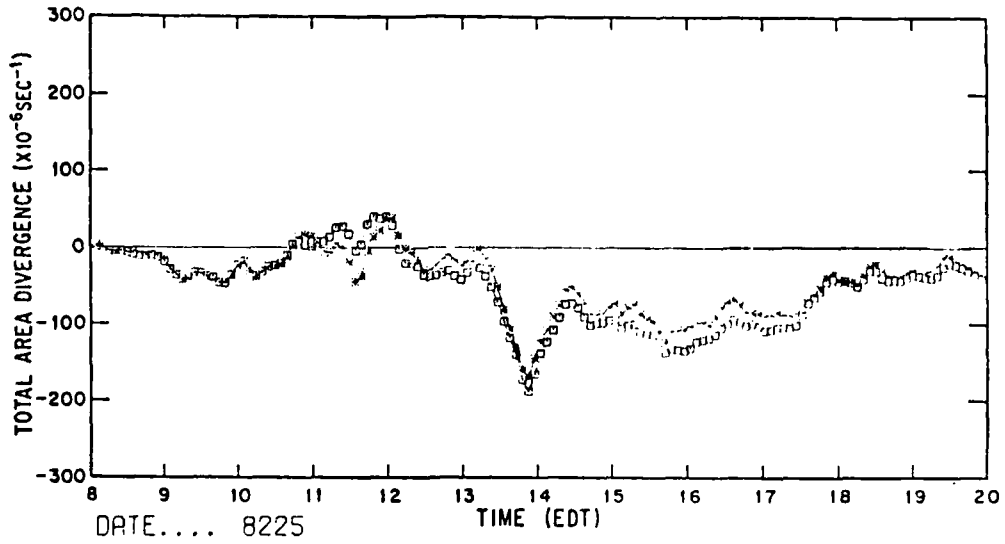
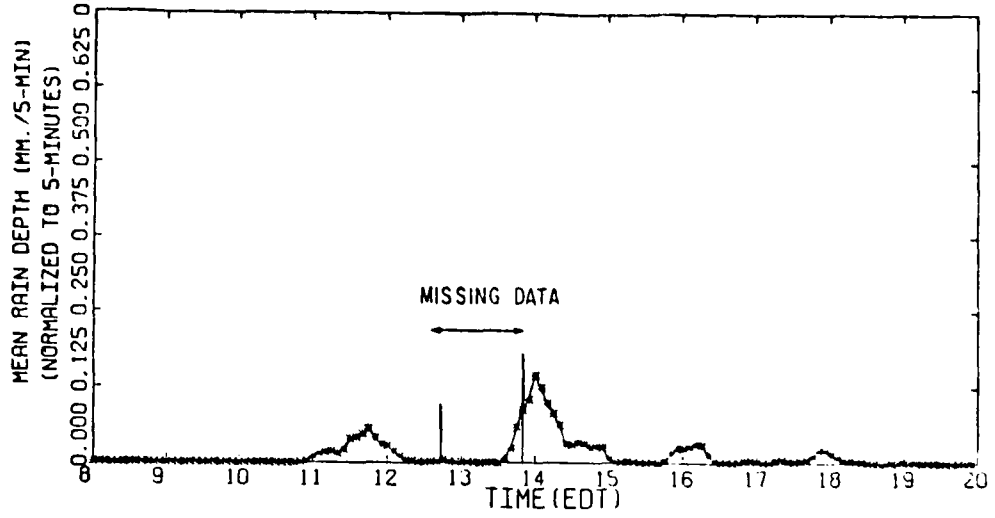
DATE.... 82075 G/R = 1.787



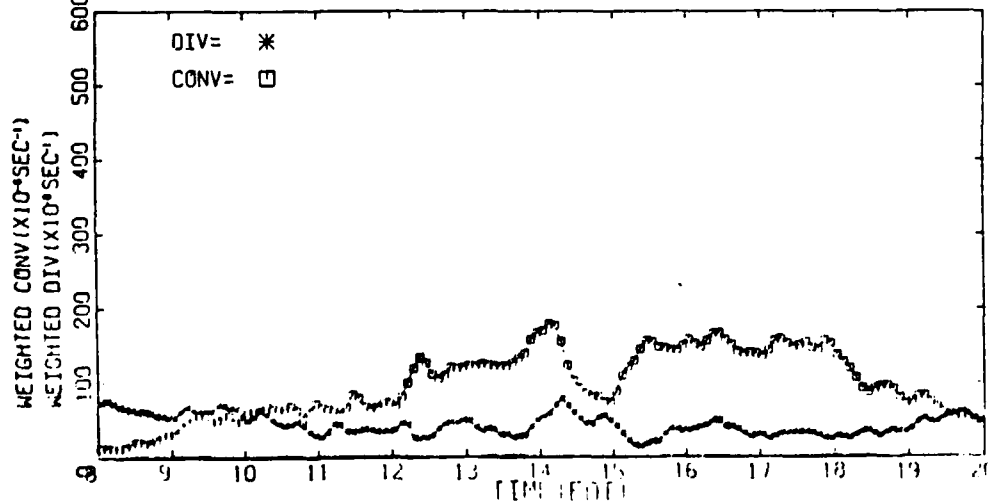
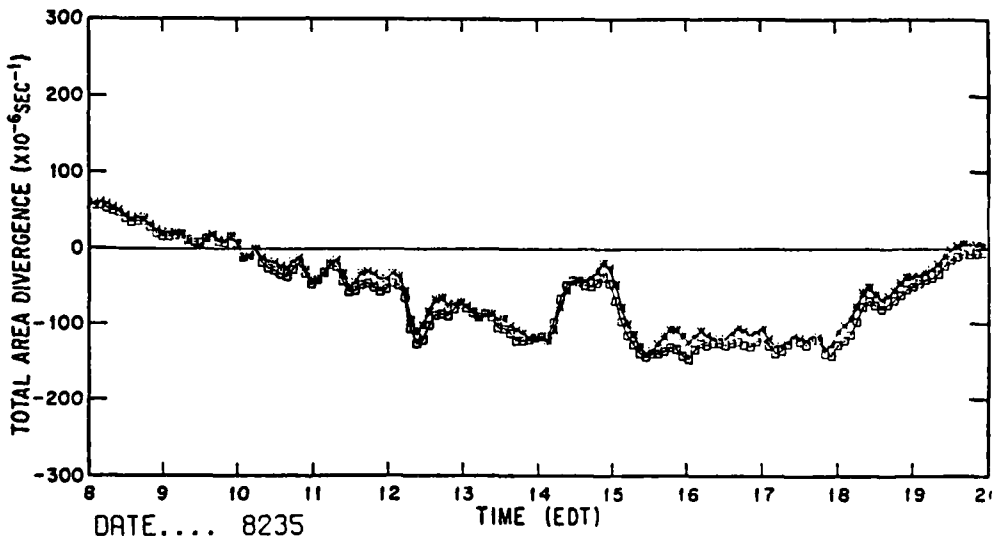
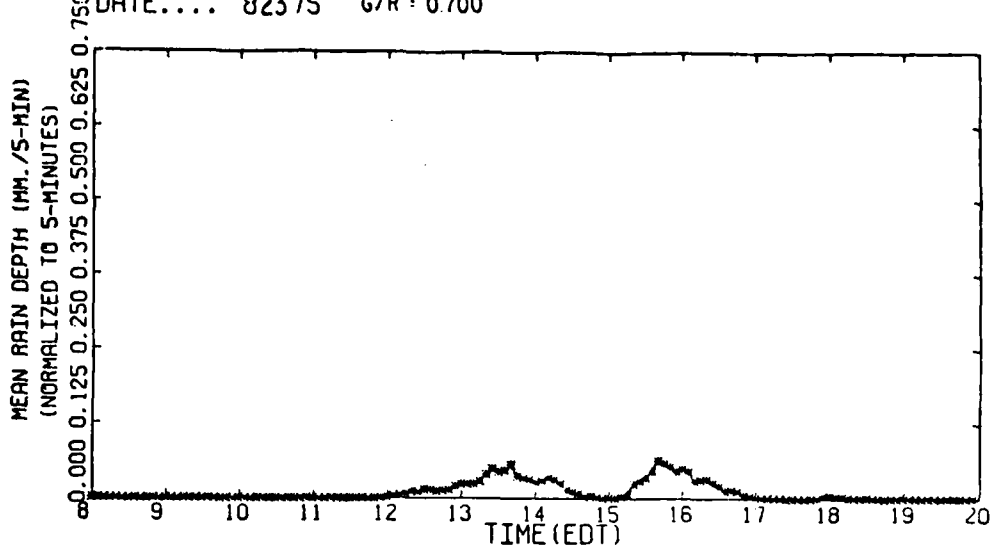
DATE.... 82175 G/R = 0.513



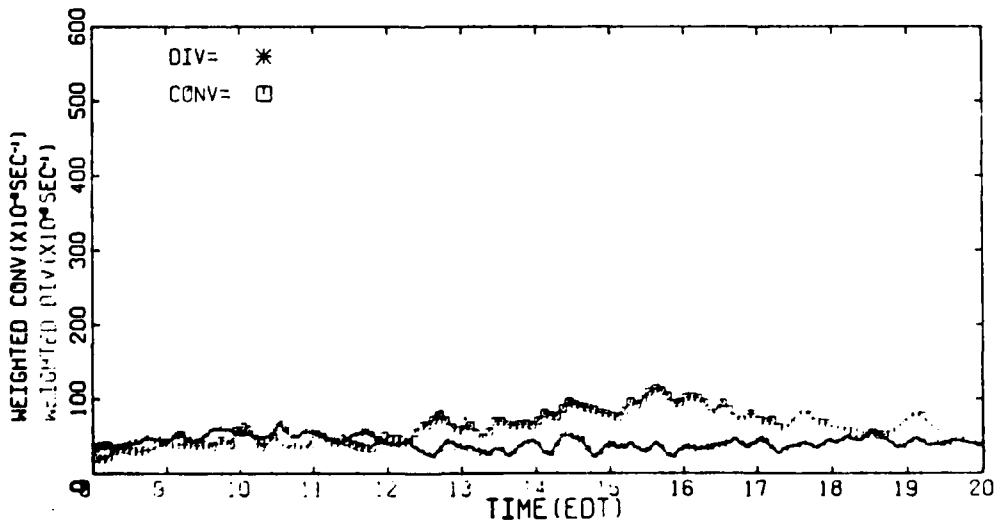
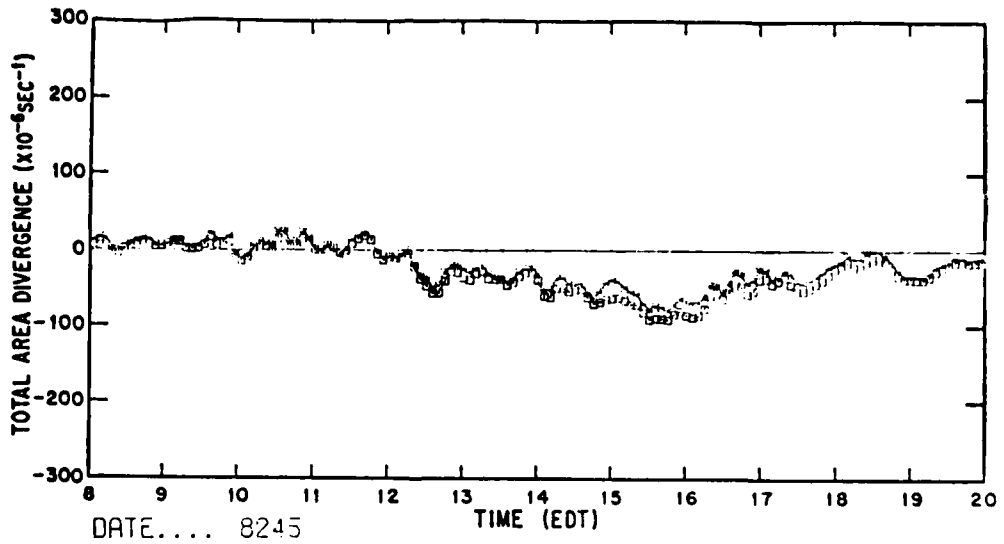
DATE.... 82275 G/R = 0.607



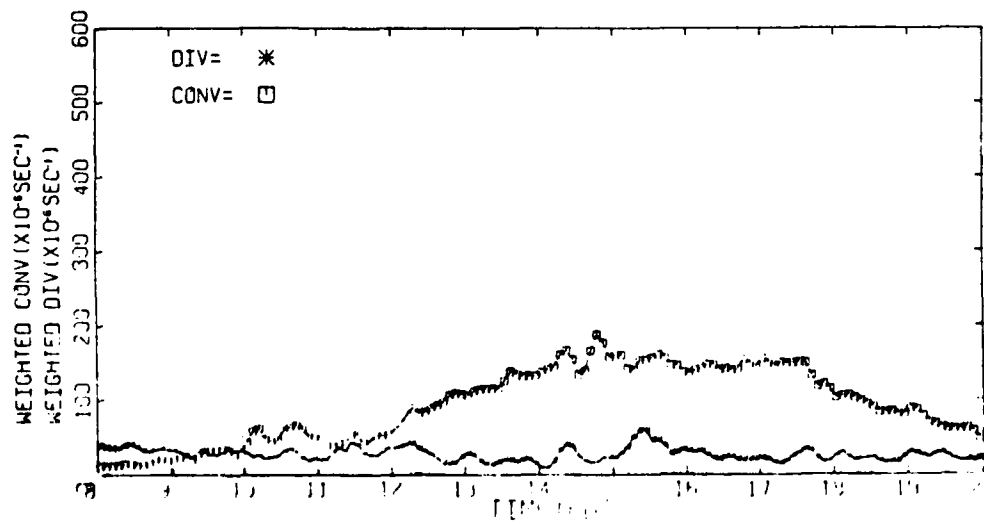
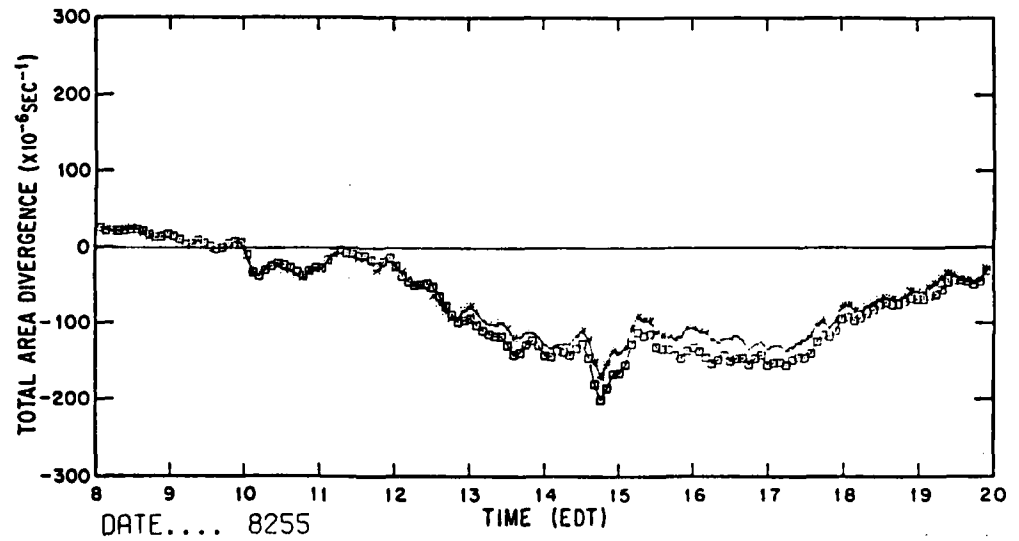
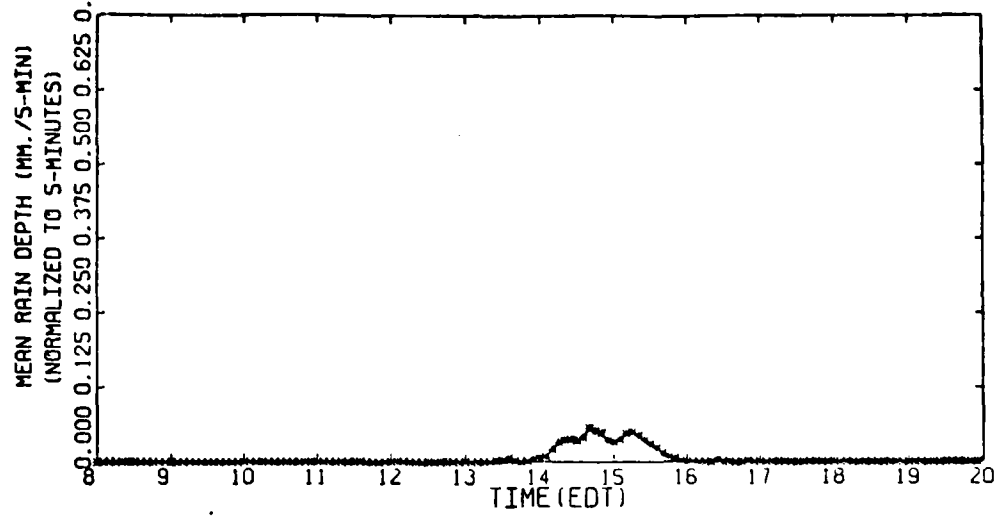
DATE.... 82375 G/R : 0.700



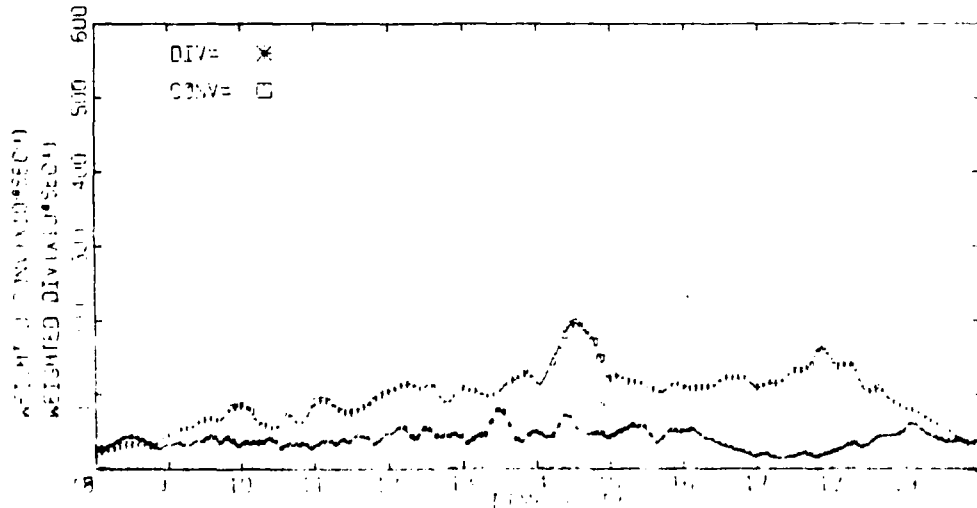
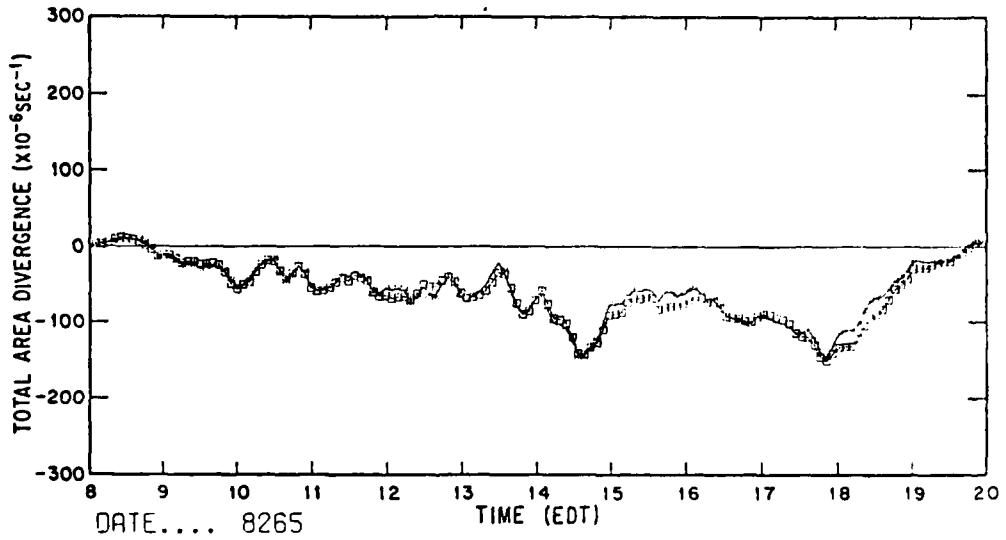
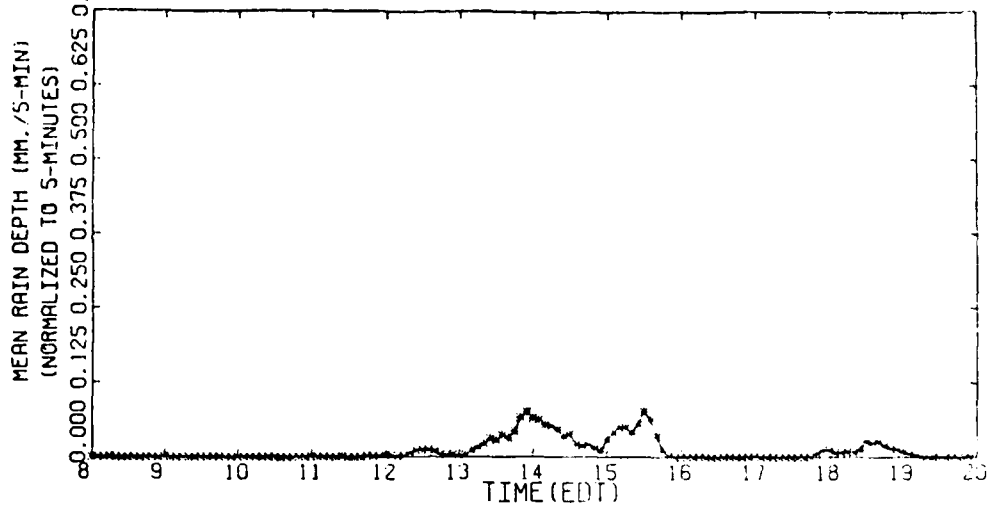
NO RAIN  
24 AUG 75



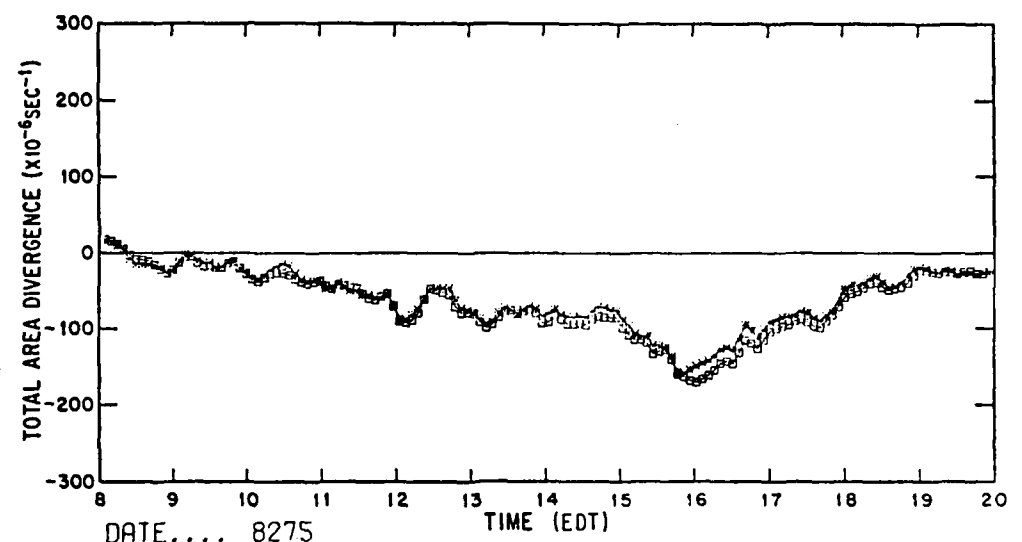
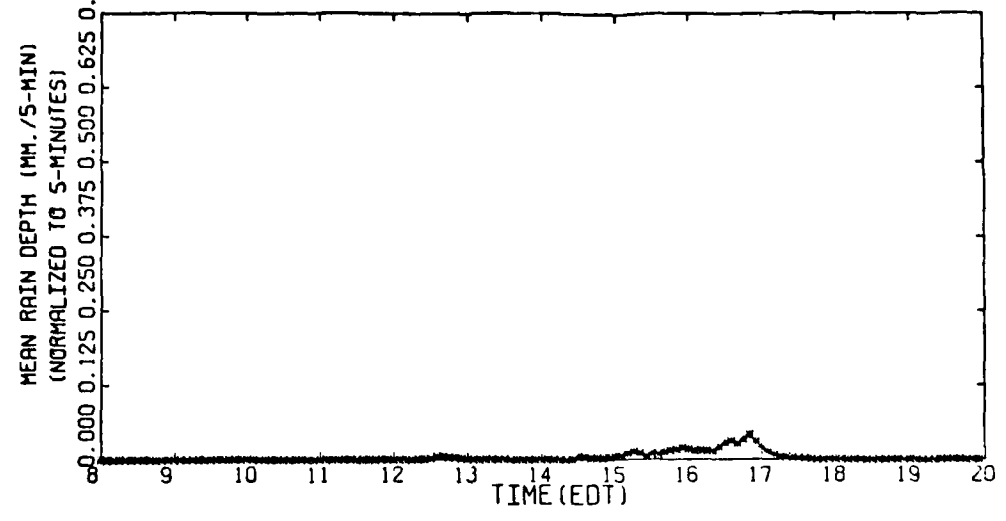
DATE.... 82575 G/R: 0.818



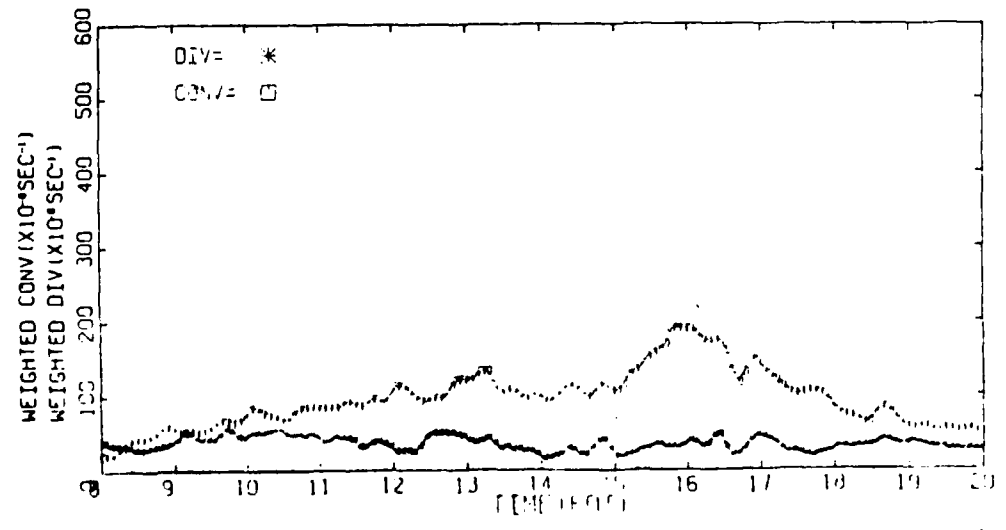
DATE.... 8265 G/R = 0.785



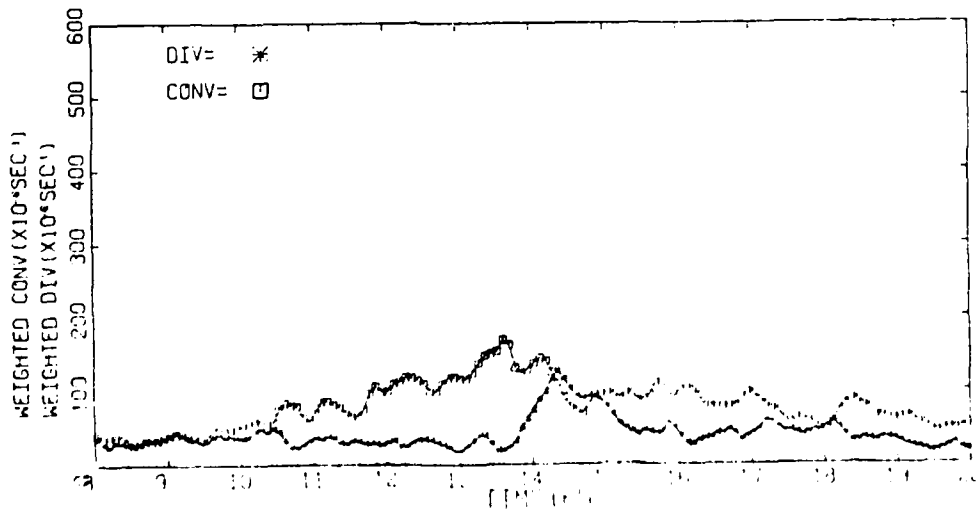
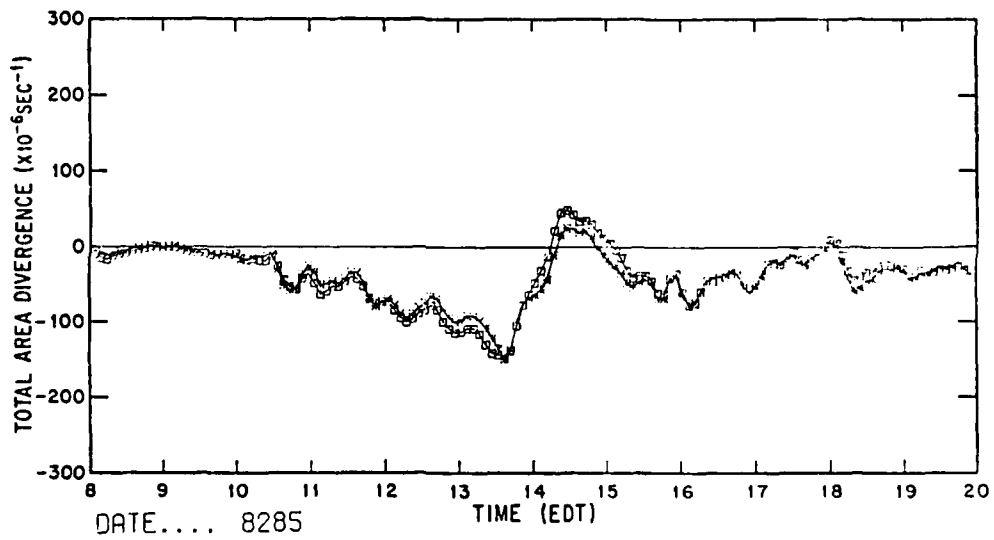
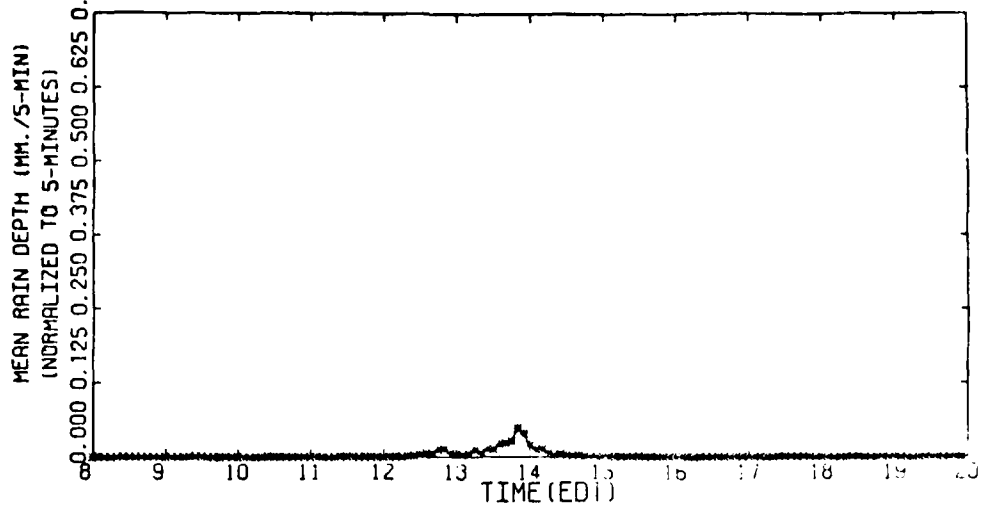
DATE.... 82775 G/R-0.785



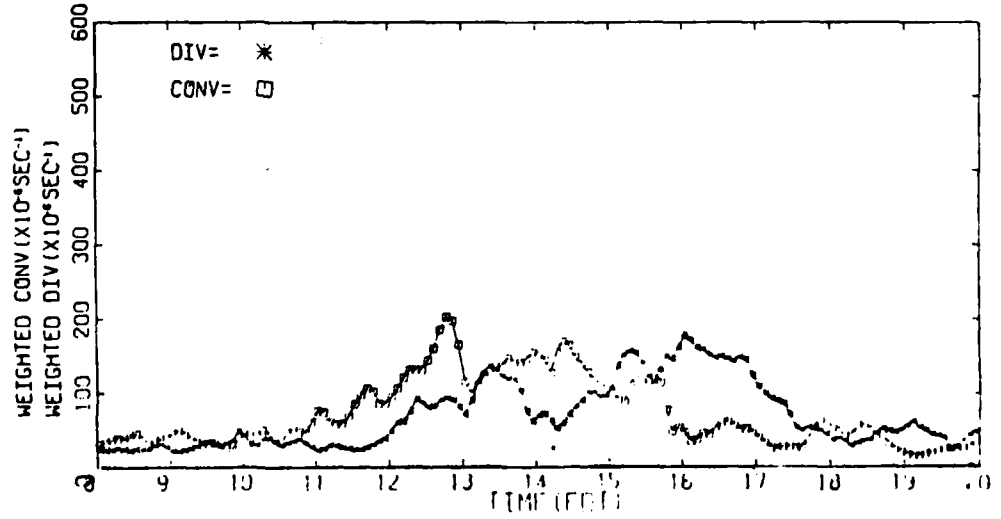
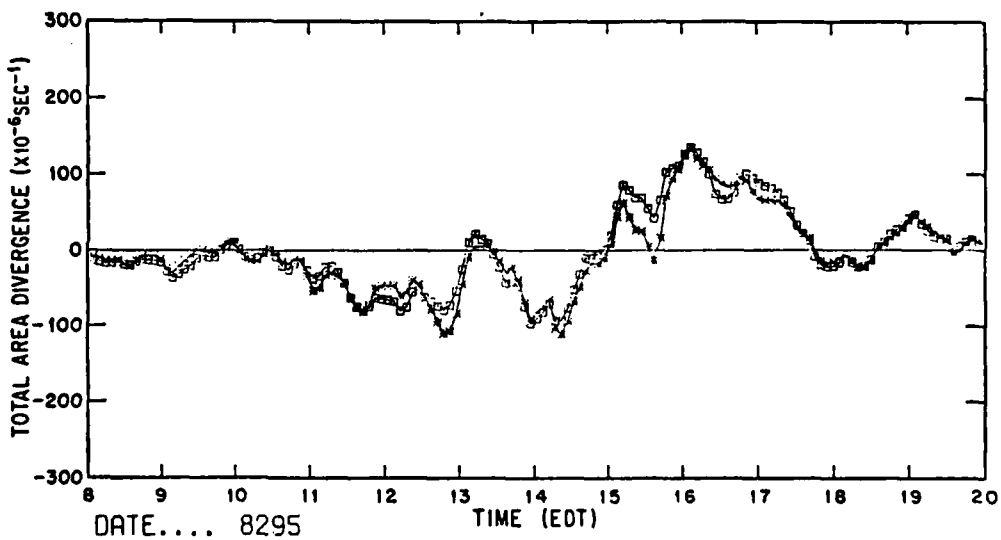
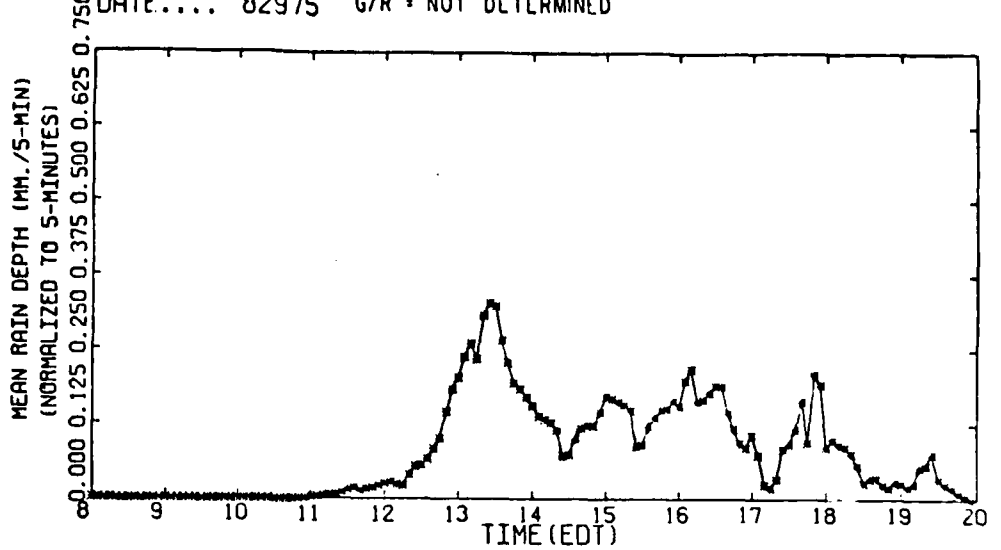
DATE.... 8275



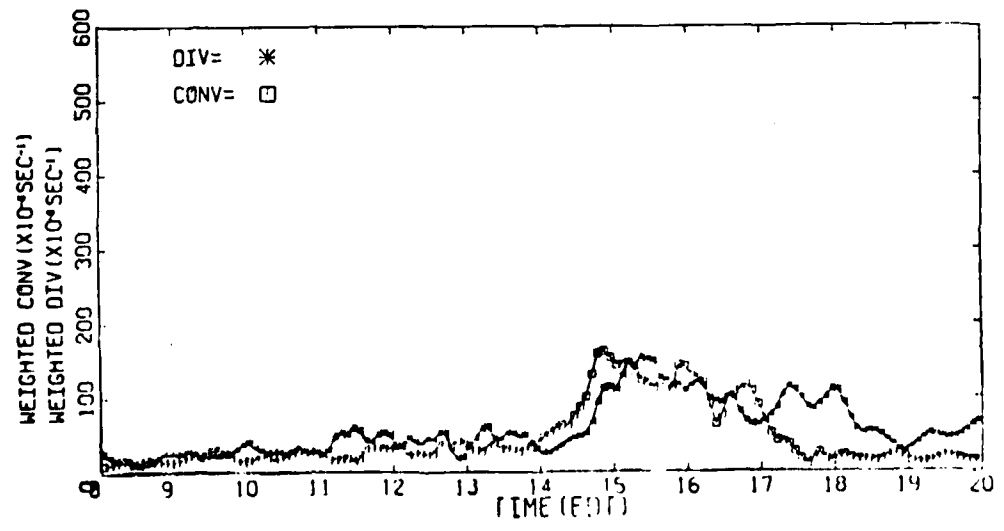
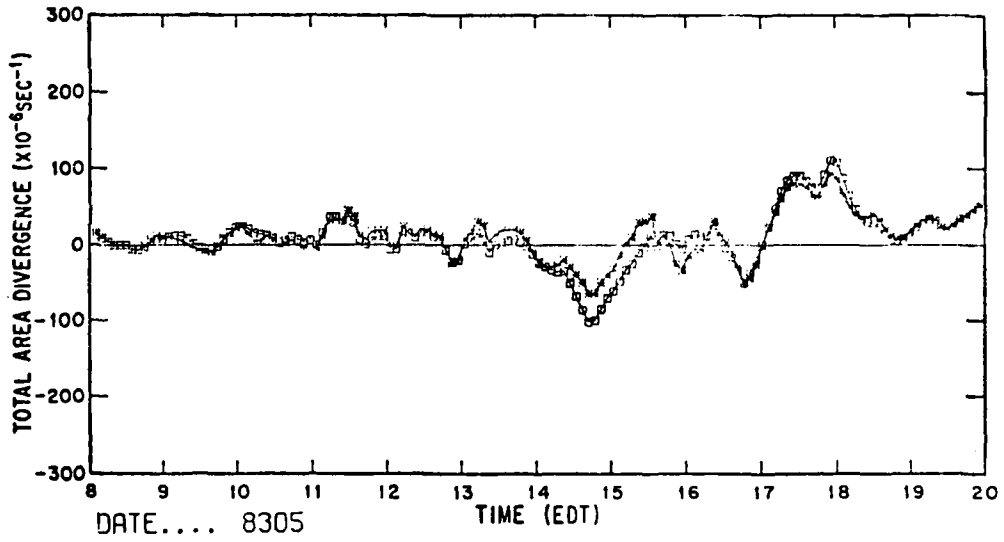
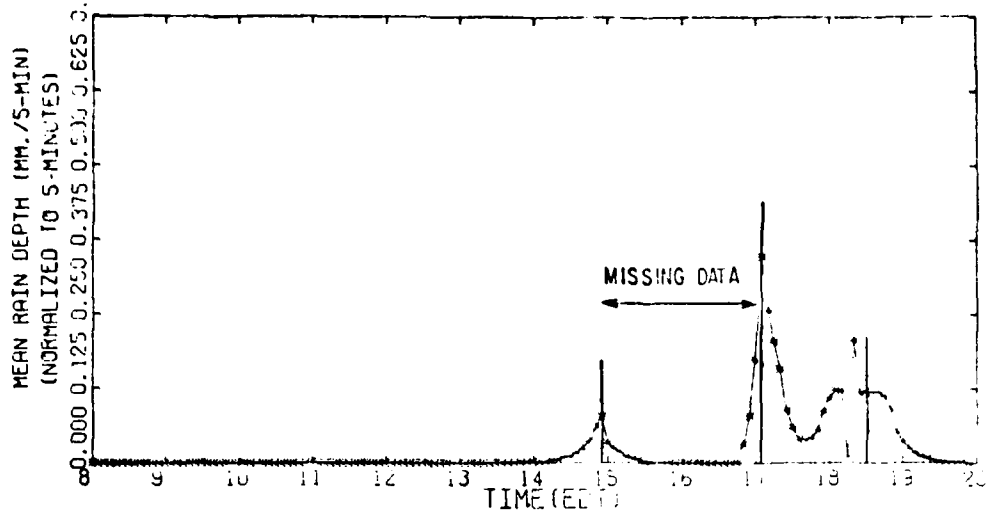
DATE.... 82875 G/R=0.785



DATE.... 82975 G/R = NOT DETERMINED



DATE.... 8305 G/R = NOT DETERMINED



**DATA  
FILM**